Silicon Photomultipliers and Monolithic Scintillators for Time-of-Flight PET

Proefschrift

ter verkrijging van de graad van doctor
aan de Technische Universiteit Delft;
op gezag van de Rector Magnificus prof. ir. K. Ch. A. M. Luyben
voorzitter van het College voor Promoties

in het openbaar te verdedigen
op dinstag 16 oktober 2012 om 15:00 uur

door
Stefan SEIFERT

Diplom Physiker
Technische Universität Chemnitz
geboren te Schlema (German Democratic Republic)

Dit proefschrift is goedgekeurd door de promotor:
Prof. dr. F. J. Beekman

Copromotor:
Dr. ir. D. R. Schaart

Samenstelling promotiecommissie:

Rector Magnificus, voorzitter
Prof. dr. F. J. Beekman, ... Technische Universiteit Delft, promotor
Dr. ir. D. R. Schaart, ... Technische Universiteit Delft, copromotor
Prof. dr. J. S. Karp, ... University of Pennsylvania
Prof. dr. F. Verzijlbergen, ... Erasmus Medical Center Rotterdam
Prof. dr. H. Löhner, ... Rijksuniversiteit Groningen
Prof. dr. ir. E. Charbon, ... Technische Universiteit Delft
Dr.–Ing. V. Schulz, ... Philips Research Europe–Aachen
Prof. dr. H. Th. Wolterbeek, ... Technische Universiteit Delft, reservelid

For my parents

The most exciting phrase to hear in science, the one that heralds new discoveries, is not "Eureka!" but "That's funny...".

Isaac Asimov

Table of Contents

1 Introduction

Abstract – In this chapter, a brief overview of nuclear medical imaging (NMI) techniques, in particular positron emission tomography (PET), is given. Both topics, NMI and PET, are far too broad to be covered to any significant extent in the scope of this introduction and this chapter is by no means intended to give a complete or balanced review of more than six decades of research in NMI instrumentation. Instead, the following text will highlight those fundamental principles and important conceptual ideas that are deemed to be of importance in the development of γ-radiation detectors for time-of-flight (TOF) PET, the subject matter of the research described in the remainder of this work. Consequently, the majority of the topics are discussed in the context of TOF PET even though some of them (such as image reconstruction techniques or the influence of certain noise sources) may be applicable to other (nuclear) medical imaging modalities as well. For a more complete review on the subjects of NIM and emission tomography the interested reader may refer to one of the many excellent book titles on these subjects, e.g. (Cherry *et al.* 2003, Wernick and Aarsvold 2004a).

1.1. Nuclear medical imaging

The field of nuclear medicine can be described in general terms as the application of radioactive substances to diagnose, visualize, or treat disease. One branch of nuclear medicine is nuclear medical imaging (NMI), i.e. the application of radioactive isotopes with the aim to visualize physiological processes. To this end a certain fraction of the molecules of a radiopharmaceutical is labeled with a radioactive isotope. These radiopharmaceuticals are designed to specifically target certain features of interest within a subject. In this regard, one often speaks of *radiolabeled molecular imaging probes* (RMIPs) or *tracers*. The targeting behavior of RMIPs allows to acquire information about specific features of interest by measuring the radiation that is emitted upon the decay of the labeling isotopes.

The fact that nuclear medical imaging techniques visualize the tracer distribution implies that the image contrast and thus the information that is visualized are determined by regional differences in the kinematics of the tracer uptake rather than by anatomic differences. Specifically the possibility to obtain contrast between similar or identical tissue based on certain functional properties of the tissue is the main reason for the success of nuclear medical imaging in both, clinical (human) and preclinical (animal), medical imaging.

Furthermore, the tracer principle makes nuclear medical imaging extremely versatile in its application. There are a number of elements with isotopes that are suitable for NMI (see Table 1.1 from Wernick and Aarsvold (2004b) for some examples) and each of these isotopes can in principle be incorporated in an indefinite number of different chemical compounds. Nevertheless, the development of new tracer materials for specific applications is a challenging task, as the requirements on tracer materials are very demanding. Some of the key prerequisites for a NMI tracer are:

- non-toxicity
- rapid and strong localization to specific target area
- week localization to non-specific sites
- high rate of clearance from the blood plasma to reduce background (unless required otherwise by the application)
- high specific activity to avoid saturation of the target sites

Table 1.1. Some isotopes of importance for SPECT and PET tracers (Wernick and Aarsvold 2004b).

SPECT-Isotopes	Half-Life	PET-Isotopes	Half-Life
^{67}Ga	78.3 h	^{11}C	20.4 min
^{99}mTc	6.02 h	^{13}N	9.96 min
^{111}In	2.83 days	^{15}O	124 s
^{123}I	13.2 h	^{18}F	110 min
^{131}I	8.02 days	^{82}Rb	1.25 min
^{201}Tl	73.1 h		

The principle of RMIPs may be best illustrated by considering the examples of two commonly used compounds: ^{99m}Tc-Methylene Diphosphonate (MDP), and ^{18}F-fluoro-deoxy-glucose (FDG). ^{99m}Tc-MDP is a tracer that is routinely used in so-called *single photon emission computed tomography* (SPECT) scans. This tracer is chemically adsorbed onto the surface of hydroxyapatite as well as incorporated into the crystalline structure of hydroxyapatite (Kanishi 1993) which makes up about 50% of the bone mass. The fact that this happens primarily during osteogenesis (i.e. the production of bone) makes ^{99m}Tc-MDP and excellent tracer to monitor abnormal bone growth due to infection, inflammation, fracture, or bone cancer.

   ^{18}F-FDG is the most prominent tracer in positron emission tomography (PET). The targeting mechanism of ^{18}F-FDG is based on the fact that its chemical structure is very similar the structure of glucose. As a result, the kinetics of FDG in an organism are essentially the same as for glucose up until the delivery to individual cells. In contrast to glucose, however, FDG cannot be broken down by the cell metabolism and it will remain until the radioactive decay of ^{18}F (^{18}F $\rightarrow$ ^{18}O $+ \beta^+$). Thus, once administered FDG will accumulate within regions with high glucose uptake. This makes ^{18}F-FDG interesting in oncology as many types of cancer show an abnormally high glucose metabolism and ^{18}F-FDG is routinely used in cancer diagnostics, staging, and restaging. It is also used in other fields, where the cellular glucose uptake is of interest such as cardiology or functional brain imaging.

   In order to be able to estimate the tracer distribution a number of γ-photons that are emitted upon the decay of the radioactive isotopes need to be detected along with information regarding their point of emission (i.e. directional information). For the most accurate estimate of the tracer distribution one should aim to detect as many γ-photons as possible with as much information regarding their origin as possible. The simultaneous maximization of scanner sensitivity and the (average) information per detected γ-photons has proven to be a challenging optimization task as these two demands lead to competing requirements for many scanner characteristics.

1.2.   Emission Tomography

   As mentioned in above text, in nuclear medical imaging information regarding the distribution of radiolabeled molecular imaging probes is obtained by measuring a number of emitted γ-photons. In practice this is most often done under many different observation angles which allows for the 3-dimensional reconstruction of the tracer distribution. This is known as *emission tomography*. Emission tomography comprises two major techniques: *single photon emission computed tomography* (SPECT) and *positron emission tomography* (PET). The key point that differentiates these two techniques is the means by which directional information is obtained for measured γ-photons.

   In SPECT the γ-photons are physically collimated using dense materials with high atomic numbers (e.g. Pb, W, or Au). Thus, the point of emission of a single

detected γ-photon can be determined to be within the bounds a certain *volume of response* (VOR) based on its localization on a detector and the geometry of the collimator as illustrated in Figure 1.1. The design of the collimator has direct consequences for the performance of a SPECT system. It can be adjusted in order to balance different requirements for specific tasks. For example decreasing the diameter of the collimator bores may increases the spatial resolution but will decrease the system sensitivity. A further example is that a magnification factor on the projection of γ-photons onto the detectors (see Figure 1.1) can be incorporated (and adjusted) by using pinhole collimators. This can greatly enhance the spatial resolution (Beekman and van der Have 2007) but it does reduce the so-called *field of view* (i.e. the imaged volume) which is why the greatest benefit of pinhole collimators arises for the imaging of small volumes (e.g. for dedicated small animal systems, or for human cardiac or brain imaging (Rogulski *et al.* 1993, Goorden *et al.* 2009)).

Conversely, PET utilizes tracers that incorporate isotopes which decay via β^+-emission, viz. via emission of a positron. An emitted positron travels a short distance before it annihilates with an electron available in the surrounding medium. The distance between the point of emission of the position and the point of annihilation is commonly referred to as the *positron range*. The electron-positron annihilation results in the emission of a pair of γ-photons each carrying the energy equivalent to the electron/positron rest mass (511 keV). The emission of these two *annihilation photons* happens "back-to-back", i.e. the angle between their propagation directions is ~180˚. Due to this correlation between γ-photons originating from the same annihilation event a VOR can be determined for a pair of annihilation photons based on the coordinates of their detection, as illustrated in Figure 1.2.

Both, SPECT and PET have their individual, distinct advantages, drawbacks, and challenges. How strongly these matters need to be weighed when comparing the two techniques strongly depends on the desired application. In many cases, however, the applicability of either technique is constrained by the availability of suitable tracers. In what follows the focus will be on PET for clinical applications.

1.3. Positron Emission Tomography

1.3.1. General Aspects of PET Imaging

As stated in section 1.2 PET relies on the detection of annihilation photons pairs in order to obtain directional information on the detected photons. Thus a PET scanner must facilitate the simultaneous, position-resolved detection of γ-photons on opposing sides of the volume of interest. Therefore, the simplest PET scanner geometry consists of a pair of planar γ-detectors. However, as will be made clear shortly this geometry does not allow for tomographic reconstruction of the tracer distribution per se due to the limited angular coverage. In order to facilitate a 3d-reconstruction of the tracer distribution such a detector pair must be rotated around a patient in order to acquire data from
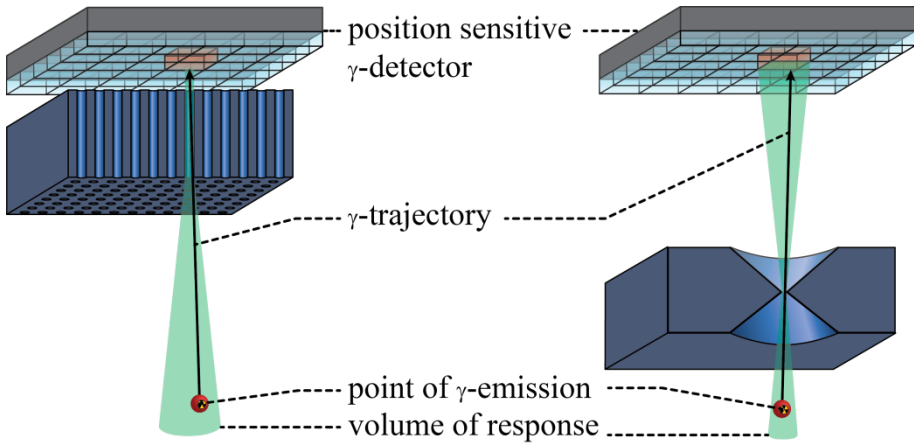
Figure 1.1. Operating principle of single photon emission tomography. An emitted γ-photon reaches the position sensitive γ-detector after passing a parallel hole collimator (left) or pinhole collimator (right). A volume of response is constructed based on the position of detection and the collimator geometry.
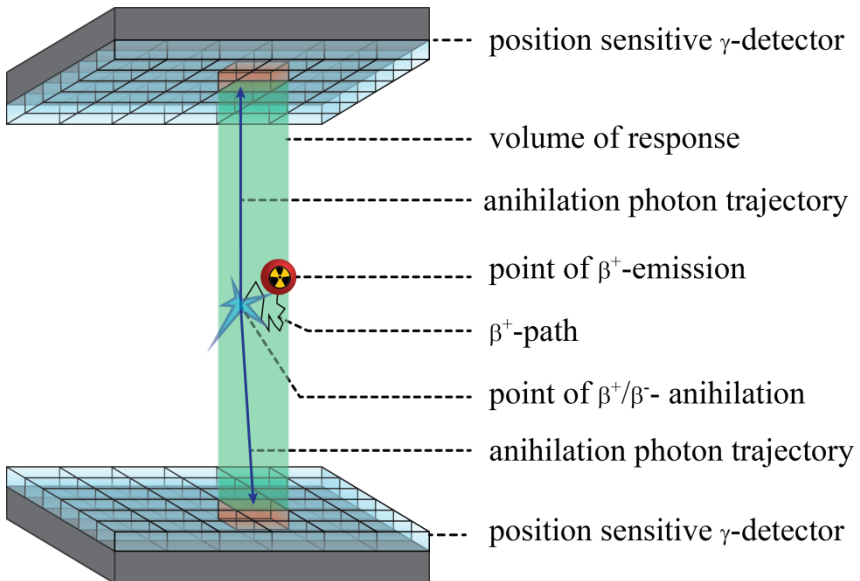
Figure 1.2. Operating principle of positron emission tomography. An positron annihilates after thermalization and a detector pair is triggered by the resulting annihilation photons. A volume of response is constructed based on the position of the detectors.

sufficient number of observation angles. The sequential measurement under different angles is a very inefficient process. This is a major drawback as the amount of activity in the target area is limited. Nevertheless, planar scanners are still being used in applications that do not require tomographic reconstruction (e.g. diagnostic screening) and/or in areas that pose restrictions on the scanner geometry (e.g. Pawelke *et al.* 1996, Parodi *et al.* 2005).

An approach that is more efficient in terms of its γ-detection probability is to surround the targeted volume with ring-like detector assemblies. In this geometry all data that is necessary for tomographic reconstruction is acquired simultaneously. This has the additional advantage, that the detector geometry can be determined more accurately from calibration measurements as the detectors remain static. This feature is beneficial for the quality of the reconstructed image, as the detector geometry is an important parameter in all reconstruction algorithms (see section 1.3.4). Additionally, corrections for the changing activity due to the finite half-life and metabolic changes are much simpler as all observation angles are effected equality. For these reasons, essentially all modern PET scanners are built in a closed-ring-geometry.

The individual detected γ-photons, which are commonly referred to as *single events* or *singles,* must be sorted into annihilation pairs. To this end a time stamp is created for each detected γ-photon. Two γ-photons are considered to form an annihilation pair if they are detected within a small time window. In this respect one also speaks of a *coincidence event*.

1.3.2.   Random Coincidences

As the width of the coincidence acceptance window τ is finite, it is possible that γ-photons that originate from different annihilation events are falsely classified as annihilation pairs. Such misclassified pairs are denoted as *accidental* or *random* coincidences as opposed to *true* events (see also Figure 1.3). The rate of occurrence of random events, which is commonly referred to as *random rate* r_{rnd}, for a given detector pair λ is given by

$$r_{\mathrm{rnd}} = 2\tau r_{\mathrm{single},\lambda 1} r_{\mathrm{single},\lambda 2} \,, \tag{1.1}$$

where $r_{\mathrm{single},\lambda 1}$ and $r_{\mathrm{single},\lambda 2}$ are the singles count rates for the two respective detectors. Consequently, r_{rnd} and the corresponding noise contribution can be reduced by keeping τ as small as possible.

The minimum width of the coincidence time window τ for a given PET system is in part determined by the accuracy with which the time difference between two single events can be measured–the so-called *coincidence resolving time* (CRT). Furthermore, the dimensions of the imaged object pose a lower limit on τ as annihilation photons might arrive at the respective detectors with a small time difference, depending on their point of emission. Reducing τ below the maximum time-of-flight (TOF) difference that could occur for a given object would result in a reduction of the number of true events along with the number of randoms and would thus not be beneficial. Yet, a CRT that is significantly smaller than the maximum TOF difference for a given object is still beneficial as
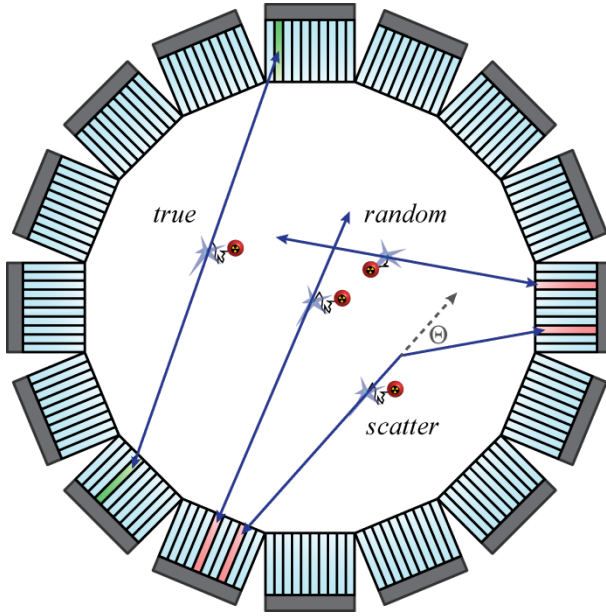
Figure 1.3. Illustration of true, random, and scattered coincidence events.

will be described in section 1.3.6.

1.3.3.   Scatter

A further important phenomenon in PET is Compton scattering of γ-photons. Compton scattering arises from the non-elastic interaction between a γ-photon and an atom. As illustrated in Figure 1.3, a γ-photon with energy E is deflected from its original trajectory by a scatter angle Θ while transferring some of its energy to one of the atomic electrons, which is ejected as a result. The relation between Θ and the energy of the scattered photon E_{sc} is given by the laws of conservation of momentum and energy (e.g. Knoll 2000):

$$E_{sc} = \frac{E}{1 + \dfrac{E}{m_0 c^2}\left(1 - \cos\Theta\right)}\,, \tag{1.2}$$

where $m_0 c^2$ corresponds to the rest mass of the ejected electron, implying that $E/m_0 c^2 = 1$ for unscattered annihilation photons. In principle, Θ can assume all values in between 0 and π. Still, the distribution of Θ is not isotropic. The details of this distribution are discussed in many textbooks (e.g. Knoll 2000). For this work it is important to note that forward scatter (i.e. scatter events with small Θ) is preferred for 511 keV γ-photons.

Detected annihilation pairs of which one or both γ-photons were subject to Compton scatter before detection have lost most of the information regarding the position of their emission and therefore contribute to the image noise and background in a similar way as random coincidences (see section 1.3.5.2). The

relation between energy and scatter angle (1.2) suggests that in principle some of the directional information of the detected γ-photons could be retrieved by an accurate measurement of the γ-photon energy. Yet, the energy resolution of state of the art PET detectors is in the order of 10% at best. This relates to a scatter angle of ~ 27° which covers most of the field of view. Still, the relation (1.2) allows the rejection of γ-photons for which Θ exceeds a certain threshold. A good energy resolution thus is essential for PET detectors to discriminate scattered γ-photons.

1.3.4.   Principles of Image Reconstruction

It was stated earlier that in emission tomography one aims to estimate the tracer distribution from a set of measurements of the emitted γ-photons. This process is known as image reconstruction. In order to highlight the basic principles of image reconstruction it will be assumed that the deteriorating effects of position range, noncollinearity and scattering of γ-photons are negligible (see also section 1.3.5.1). In practice all these simplifications are violated and state of the art image reconstruction techniques take these contributions into account. In general the reconstruction problem is formulated in terms of a transformation from the so-called *projection space,* (i.e. the space containing the measurement data) to the *image space* (i.e. the volume of interest containing the 3d tracer distribution).

Before focusing on the image reconstruction process it will be helpful to introduce a formal definition of *volume of response* (VOR) and the related concept of the line of response (LOR). The VOR is defined such that it encompasses all possible positions of tracer isotopes for which the emission of a positron can lead to the absorption of both γ-photons of a corresponding annihilation pair in the two detector elements. Under the above mentioned simplifications the VOR is confined by the lines connecting the bounds of the detector elements (see also Figure 1.2). Evidently, the so defined VOR reduces to a line, viz. the LOR, as the dimensions of the detector elements approach zero.

This definition implies that each LOR is associated with a unique pair of detector coordinates (and vice versa). Thus, such a coordinate pair represents one unique point $\mathbf{\Lambda}$ in the projection space. The activity that is "seen" by the detector pair at $\mathbf{\Lambda}$ corresponds to the integrated activity along the LOR. It follows that the expected number of detected coincidence events at measured $\mathbf{\Lambda}$ is proportional to the (weighted) line integral of the activity along the corresponding LOR:

$$\bar{n}(\mathbf{\Lambda}) = \int_{LOR} S(\mathbf{L}\,|\,\mathbf{\Lambda})\rho(\mathbf{L})d\mathbf{L}, \qquad (1.3)$$

where $\rho(\mathbf{L})$ denotes the tracer density at the image space coordinate $\mathbf{L}$ and $S(\mathbf{L}|\mathbf{\Lambda})$ denotes the effective local detector sensitivity at $\mathbf{\Lambda}$ for annihilation photon emissions from $\mathbf{L}$. Accordingly, for a pair of finite sized detector elements one can express the expected number of coincidence events $\bar{n}$ as the

activity integral over the VOR.

In practice most often the continuous functions $\rho(\mathbf{L})$, $\bar{n}(\mathbf{\Lambda})$, and $S(\mathbf{L}|\mathbf{\Lambda})$ are replaced by respective discrete representations. That is that the projection space is subdivided into a number of finite area elements (*pixels*). Similarly, the image space is sectioned into volume elements (*voxels*). The relation between the (mean) projection data and the image space tracer distribution can then conveniently be expressed in terms a of a matrix multiplication:

$$\bar{\mathbf{n}} = \mathbf{S} \times \mathbf{\rho}, \qquad\qquad (1.4)$$

where the vector $\bar{\mathbf{n}} = \begin{bmatrix} \bar{n}_1 \dots \bar{n}_\Lambda \end{bmatrix}^{\mathrm{T}}$ comprises the expected number of coincidences for each of the Λ detector pixels and the vector $\mathbf{\rho} = \begin{bmatrix} \rho_1 \dots \rho_L \end{bmatrix}^{\mathrm{T}}$ is composed by the total activity in each image space voxel. $\mathbf{S}$ is a $\Lambda \times L$ matrix that is commonly referred to as the *system matrix*. Its matrix elements $\mathbf{S}_{\lambda,l}$ represent the average probability of the λth detector pixel to detect an annihilation photon emitted from the lth voxel.

The relations (1.3) and (1.4) offer the means to reformulate the task of image reconstruction in terms of the inversion problem to the corresponding expression. Image reconstruction techniques that utilize this relation in order to calculate the tracer distribution directly from the measured projection data are commonly referred to as analytical reconstruction methods. A formalism, which has found widespread application, is so-called backprojection (Colsher 1980). In this method it is assumed that all voxels along a given LOR are contributing equally to the line integral measured by the corresponding detector pair. In essence this means that the value measured by the detector pair is projected as a constant value along the corresponding LOR; hence the name backprojection. The intensity value for an individual voxel is obtained by integration over all LORs that intersect the voxel.

In order to illustrate this method, Figure 1.4 shows the backprojected image of a 2-dimentional tracer distribution. It can be observed that the reconstructed image resembles the original tracer distribution closer and closer as LORs of more and more different angles are taken into account. However, in the same figure furthermore a specific drawback of simple backprojection is apparent. This method results in a blurring of the image data. It can be shown that the blurring that is introduced by the backprojection is equivalent to a convolution of the image data with a cone shaped filter function $h(x,y) = (x^2+y^2)^{-1/2}$. Still, as the shape of this filter is known, it can be removed by applying an appropriate inversed filter to either projection or image data in which case one speaks of *filtered backprojection* (FBP) or *backprojection filtering* (BPF) as illustrated in Figure 1.5.

Furthermore, Figure 1.4 and Figure 1.5 highlight, that a certain number of projection angles is required for an accurate reconstruction. Consequently the image space is constraint to those voxels for which the number of possible projections per voxel is sufficiently large. This volume is often referred to as the *field of view (FOV)* of the scanner.
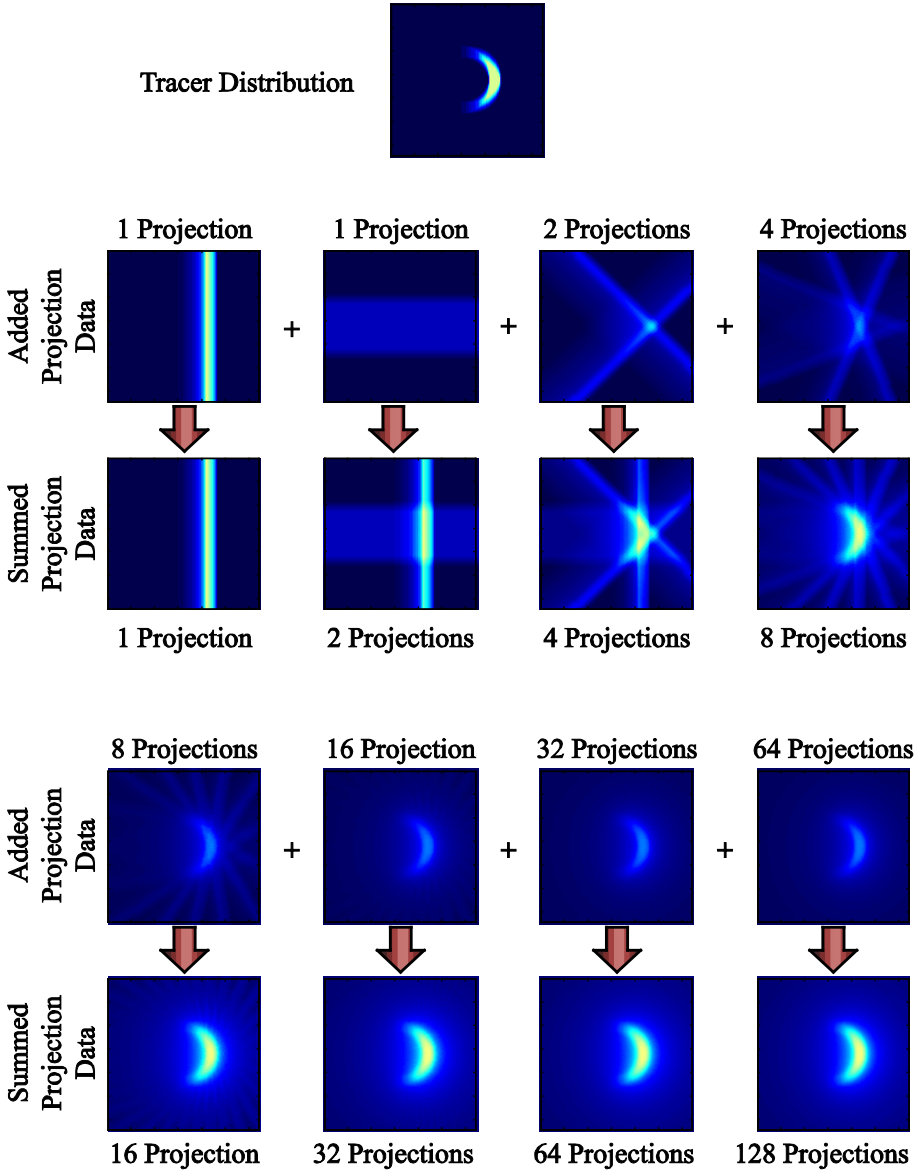
Figure 1.4. Illustration of the reconstruction of a 2d tracer distribution (top) using a simple backprojection algorithm. The pictures show the evolution of the reconstructed image as more and more projections are taken into account from top left to bottom right.

Tracer Distribution

Added Projection Data

1 Projection	1 Projection	2 Projections	4 Projections

Summed Projection Data

1 Projection	2 Projections	4 Projections	8 Projections

Added Projection Data

8 Projections	16 Projection	32 Projections	64 Projections

Summed Projection Data

16 Projection	32 Projections	64 Projections	128 Projections
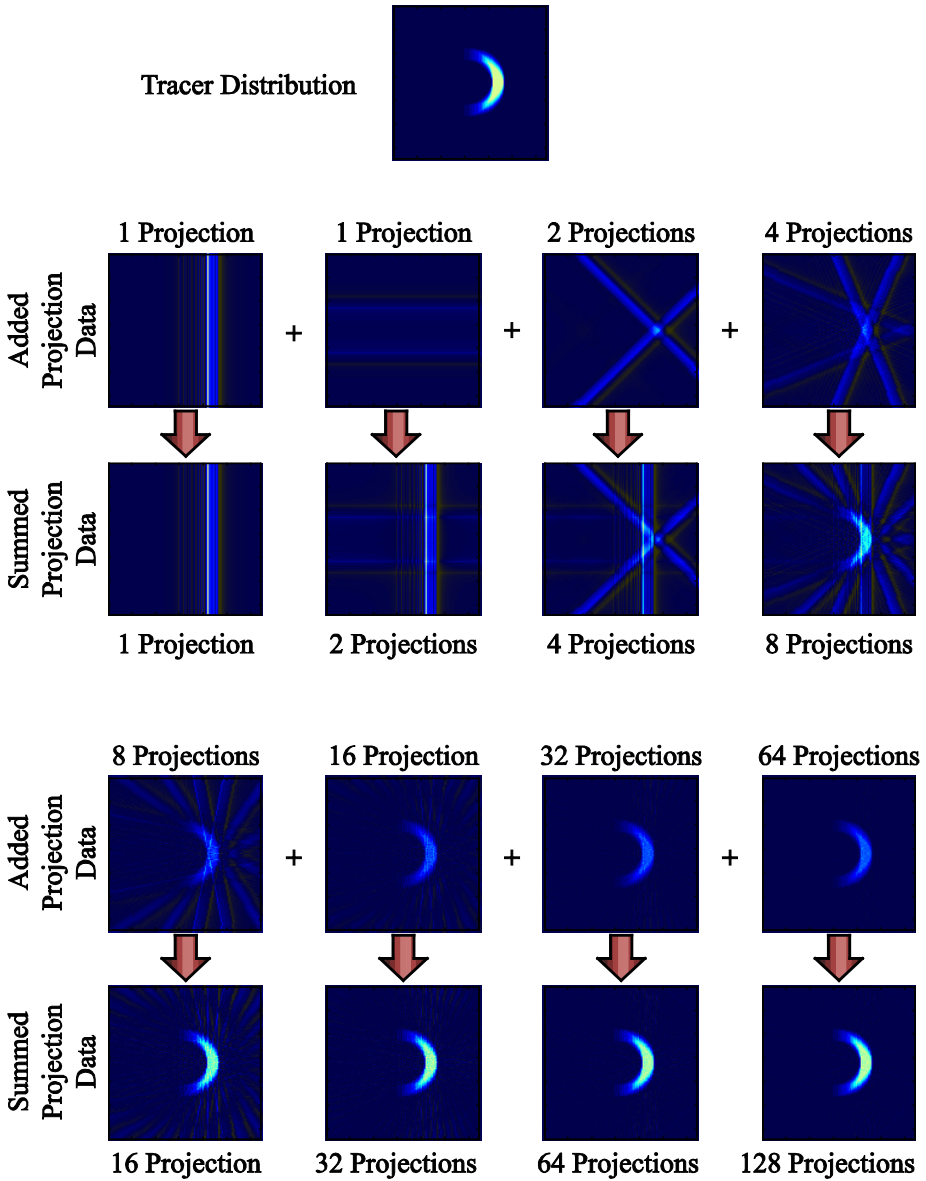
Figure 1.5. Illustration of the reconstruction of a 2d tracer distribution (top) using a filtered backprojection. The pictures show the evolution of the reconstructed image as more and more projections are taken into account from top left to bottom right.

The methods described so far assumed that the measured projection data is identical to the expectation value $\bar{\mathbf{n}}$. This, however, is generally not the case and analytical reconstruction methods such as FPB suffer if the recoded data is noisy. This is a particular problem as the data acquisition in all ET modalities is at least associated with the contribution of statistical noise as explained in section 1.3.5. Furthermore, the incorporation of physical effects such as position range, noncollinearity and scattering of γ-photons into analytical models can be problematic or prevent an explicit formulation of the reconstruction problem entirely. In order to tackle the difficulties of noisy data and the detector physics so-called iterative reconstruction algorithms are often better suited.

The starting point for an iterative image reconstruction algorithm is an assumed tracer distribution $\boldsymbol{\rho}$. For this distribution the expected projection data $\bar{\mathbf{n}}$ is calculated using (1.4). This (*forward*) *projected* image is then compared to the measured projection data. Subsequently, $\boldsymbol{\rho}$ is updated based on this comparison. This process is repeated until some predefined criterion (often a fixed number of iterations) is met. The advantage of this method is that the estimate of the activity in a certain voxel implicitly makes use of the estimated activity in other voxels in the image. This is especially useful in mitigating the deteriorating effect of the inherent noise in the data. A drawback is that the repeated forward and back projection of the data is computationally costly. Nevertheless, iterative reconstruction algorithms are becoming more and more popular as the gain in image quality often justifies the additional computational expense and because computational power has become exponentially cheaper over the years.

Amongst the most widely used iterative reconstruction techniques are algorithms based on Maximum-Likelihood Expectation-Maximization (ML-EM) (Vardi *et al.* 1985). In these algorithms the calculated expectation values $\bar{\mathbf{n}}$ are treated as statistical variables under assumption of a certain noise model (e.g. Poisson distribution of the $\bar{n}_\lambda$). This allows for the calculation of the probability to measure a certain $\mathbf{n}$ for a given tracer distribution. This in return facilitates the evaluation of the likelihood for an assumed tracer distribution $\boldsymbol{\rho}$ under consideration of a given, measured $\mathbf{n}$. A reconstructed tracer distribution is then considered to be a good representation of the true tracer distribution if it maximizes this likelihood (under consideration of certain regularity conditions).

1.3.5.   Image Quality

As the purpose of a PET scanner is the visualization of tracer distributions the figure-of-merit when evaluating its performance is the quality of the produced images. Here, the *image quality* should be understood in terms of the performance of an observer (e.g. a radiologist) to perform a certain task (e.g. the diagnose of carcinoma or metastasis) (Swets 1988). In other words, the image quality and, therefore, the performance of a PET system are observer- and task dependent. This is clearly problematic for a qualitative assessment of the image quality and scanner performance as the evaluation for a single task in principle requires a trial with a large number of human observers. Alternatively, human

observers might be simulated by so-called *model-observers* however, in this case, the performance measure is weighted by how closely the model observer resembles the performance of its human counterpart (e.g. Barrett *et al.* 1993). Regardless, a detailed discussion on the topic of *model-observers* is considered to be beyond the scope of this work.

In general one can differentiate four phenomena that may deteriorate the image quality: the image noise, bias, the spatial resolution of the image, and the occurrence of so-called artifacts. Image noise can be defined in terms of the uncertainty of the intensity value assigned to individual voxels in the image whereas a bias can be understood as a systematic difference between the estimated and the true activity distribution. The spatial resolution is commonly defined in terms of the width of the reconstructed image of a point like activity distribution (assuming a negligible noise contribution).

Artifacts are features that appear in the reconstructed image but are not a direct representation of the true activity distribution. The occurrence of artifacts can in most cases be avoided by a proper scanner calibration and by the implementation of the reconstruction algorithm. As these issues are not the subject matter of this work the matter of artifacts in the image will not be discussed in detail. However, it should be noted, that it may be an important issue in the practical application of clinical PET where artifacts must be avoided as they introduce a severe risk of misdiagnosis.

The extent to which noise, bias or spatial resolution influence the success rate of an observer strongly depends on the task the observer is required to perform. Observer tasks can be classified into two groups: *detection* and *quantitation*. A detection task requires an observer to decide if a certain feature is present in an image or not while quantitation requires the measurement of the tracer uptake in a *region of interest* (ROI). Quantitation often requires the observer to decide on the ROI based on the PET image data and is generally the more demanding of the two classes of observer tasks. For example, the observer performance may hardly be influenced by the blurring of the image or by a bias in the image data when detecting individual, spatially well separated features. Conversely, a blurry image hampers the accurate determination of the ROI and a remaining bias in the image data leads to false estimates on the total activity contained in the ROI.

Nevertheless, in the following discourse the most important factors that influence the image quality of a PET system are highlighted under the premise that effects that lessen the success rate of an observer for a certain task will be deteriorating for any other task as well yet (possibly) to a different extent.

1.3.5.1.   Spatial Resolution.

The definition of the spatial resolution as the broadening of a point like activity distribution in the reconstructed image in principle includes possible effects of the image reconstruction itself (see also section 1.3.4). However, for the following discussion it will be assumed that the reconstruction algorithm is ideal in the sense that it makes the best possible use of the information contained in the projection data.

Under this premise the finite spatial resolution is a direct consequence of the fact that the approximations that were used to derive the simplified concept of the LOR are never fulfilled in practice. That is that always the projection from a VOR with a finite diameter is measured at a given pair of detector coordinates. The VOR was defined in section 1.3.4 for two given detector elements to encompass all possible positions of tracer isotopes for which the emission of a positron can lead to the absorption of both γ-photons of a corresponding annihilation pair in the two detector elements. For a measured (true) coincidence the so defined VOR can be understood as a measure for the uncertainty of the distance between the position of the nucleus that emitted the positron and the presumed LOR, which in most cases corresponds to the center axis of VOR. This uncertainty is projected back into the image upon reconstruction.

One factor that contributes to the diameter of the VOR and thus the spatial resolution is the fact that positrons need to thermalize before annihilation with respective electrons can occur. Consequently, the annihilations take place a certain distance away from the nucleus. This distance is known as the *positron range*. The positron range is a function of the initial energy of the positrons and it thus depends on the labeling isotopes in the tracer. It furthermore depends on the electron density of the surrounding medium. Typically, the positron range distribution is sharply peaked with pronounced tails with a FWHM in the order of 0.1 mm for ^{18}F up to 0.5 mm ^{15}O and a FWTM in the order of 1 mm up to 4 mm for the two respective materials (Levin and Hoffman 1999).

An additional contribution to the image spatial resolution arises from the fact that the angle Θ between the propagation directions of annihilation photons is not exactly 180˚. This annihilation photon *noncollinearity*, i.e. the deviation of the Θ from 180˚, is typically <1˚ and depends on the momenta of the positron and the electron upon anihilation (Beringer and Montgomery 1942). The influence of the noncollinearity on the system resolution depends on the system diameter. It can vary from 0.2 mm for small systems (10 cm bore diameter) to 1.8 mm for large (80 mm) diameter systems (Levin and Hoffman 1999).

Furthermore, it is clear that the diameter of a VOR increases as the effective area of the detectors that define the VOR is increased. This effective area is determined by the accuracy with which the detectors can resolve the γ-interaction position, i.e. the detector spatial resolution, in the plane perpendicular to the presumed LOR. Most modern PET scanners employ segmented scintillation crystals in order to resolve the position of individual γ-interactions (see also section 1.3.8.4). Consequently, the detector spatial
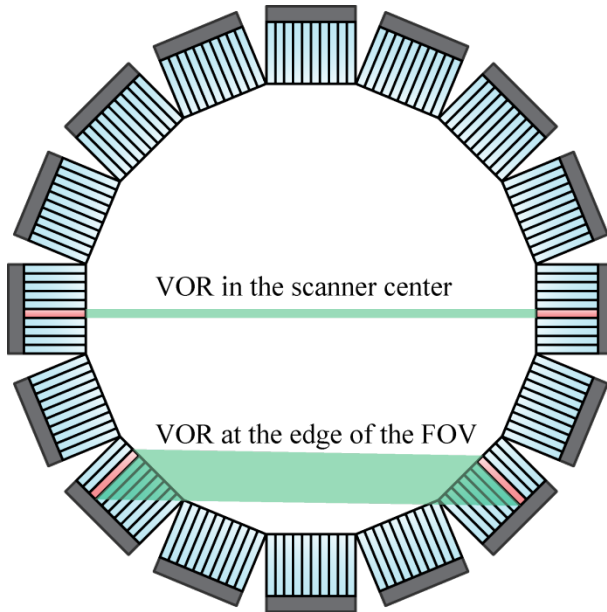
Figure 1.6. Illustration of the so-called parallax error, i.e. the broadening of the volume of response (VOR) at the edges of the scanners field of view (FOV) due to the depth interaction of the γ-photons within the crystal elements that define the VOR.

resolution for VORs that cross the FOV close to the detector center this is limited by the diameter of individual of crystal elements in the detector which are in the order of 4 mm[1].

This however, changes for VORs that are located in peripheral regions of the FOV. This is illustrated in Figure 1.6. The crystal elements in current PET detectors are typically much larger in the radial direction (20 mm up to 30 mm) than their diameter in axial and transversal directions. Thus, the effective area of the crystal element in the plane perpendicular to the presumed LOR increases as a crystal is irradiated under a larger angle of incidence. The resulting VOR appears elongated in the radial direction resulting in deterioration of the spatial resolution along the same axis. This asymmetric deterioration of the spatial resolution for off-center positions in PET scanners is known as *parallax error*. One possible remedy to the parallax error is to determine the *depth of interaction* (DOI) of the γ-photon in the scintillation crystal (see also section 1.3.8.4) as DOI information offers the means to constrain the VOR in the radial direction (e.g. MacDonald and Dahlbom 1998).

---

[1] Philips GEMINI TF PET/CT 2012
http://www.healthcare.philips.com/de_de/products/nuclearmedicine/products/geminitf/, or
Siemens Biograph mCT 2012 http://www.medical.siemens.com/

1.3.5.2.   *Image Noise and Bias*

The respective impacts of image noise and bias on the image quality can be very different. Naturally, most tasks are the more difficult the noisier a given image is. A biased estimate of the activity distribution is mostly problematic in quantitative PET imaging. Nevertheless, the two effects are closely related, as both are to a large extend determined by the contributions of random events and scattered γ-photons.

Both random events and scattered γ-photons increase the observed number of counts in the projection data without adding information. It is easy to see that such a systematic offset in the projection data leads to a corresponding bias in the image data. In principle it is possible to apply corrections for the bias caused by randoms (e.g., Hoffman *et al.* 1981, Casey and Hoffman 1986, Brasse *et al.* 2005) and scattered photons (e.g., Barney *et al.* 1991, Cherry and Sung-Cheng 1995, Ollinger 1996). However, in practice, it is often not trivial to estimate the magnitude of these effects accurately and the remaining bias can still be problematic.

A further consequence of the contribution of randoms and scattered events is that they increase the noise in the image. In this work the term *image noise* is defined such as to include all effects that increase the uncertainty on the reconstructed voxel values. The noise in a given image voxel is commonly expressed in terms of a *signal to noise ratio* (SNR), which is defined as the expected signal intensity divided by the expected standard deviation on the signal.

Evidently, the image noise originates from noisy measured projection data. The measurement of annihilation photon pairs is a probabilistic counting process. This counting process is commonly assumed to follow a Poisson or a normal distribution which implies that the standard deviation σ_λ on the measured value n_λ of a given projection data pixel is $\sqrt{n_\lambda}$. The SNR for a given pixel is thus $\bar{n}_\lambda^{1/2}$ without the contribution of randoms or scatter (i.e. all n_λ counts are trues). This statistical noise contribution poses a lower limit on the image noise, as the number of measured true coincidences is limited by the amount of activity that can safely be administered to a patient and by the sensitivity of the system.

As randoms and scattered events are added to n_λ, the corresponding pixel noise increases accordingly whereas the number of trues remains constant. In consequence the SNR deteriorates. An additional effect of Compton scatter is that γ-photons that otherwise might have been detected by one of the detector elements in the scanner may be scattered onto a trajectory that cannot lead to its detection. If this happens to one or both annihilation photons that are emitted along certain LOR this potential true event is "lost" thus reducing the number of true events detected along this LOR and further deteriorating the SNR. The scatter probability varies for different patient tissue types as described in section 1.3.7. This inhomogeneous scatter probability can be problematic if not treated properly in the reconstruction (Barney *et al.* 1991, Watson 2000).

The combined effect of statistical noise, random coincidences, and Compton

scatter is often summarized by expressing the number of counts contributing to a certain region of interest in so-called noise equivalent counts (*NEC*). *NEC* are defined as the number of counts that lead to the same SNR in the reconstructed image as a measurement that contains statistical noise only. In first order approximation the *NEC* can be expressed as (Strother *et al.* 1990)

$$NEC = \frac{T^2}{\left(T + S_{\text{FOV}} + R_{\text{VOF}}\right)}, \tag{1.5}$$

where T is the number of true counts in the FOV. S_{FOV} represents the number of scattered events and R_{FOV} equals the number randoms (i.e., r_{rnd} integrated over the measurement time).

The significance of this definition of *NEC* is best exemplified by considering the effect of increasing the total activity in the FOV, in first instance neglecting the effects of Compton scatter. The increase of the activity leads to a proportional increase of the count rates of singles and true coincidences. Consequently, R_{FOV} increases quadratically, according to (1.1). This means that the *NEC* starts to saturate for $R_{\text{FOV}}/T \gg 1$. Taking other effects such as scatter and the dead time of the detectors into account the number of NEC will even drop for higher activities.

At this point it may be important to recall that voxel values in a back projected image correspond to the weighted sum of corresponding projection data. Consequently, the variance on the voxel value is given by a (weighted) sum of the variances of the all projection data that contributes to this voxel whereas the (average) signal for the voxel corresponds to the total activity contained in the corresponding volume. This is pointed out, as it imposes a practical limit on the spatial resolution as subdividing the image space into smaller voxels results in less counts per voxels and thus a smaller SNR (for a constant *T*, S_{FOV} and R_{FOV}).

Furthermore, it should be noted, that the noise amplitude on individual voxels is not independent in a statistical sense as the reconstruction introduces a covariance between the voxel values in the image. Depending on the reconstruction method this can be troublesome as it may lead to "lumpy" backgrounds in the images which can complicate detection tasks and the interpretation of the image.

1.3.6. Time-of-Flight (TOF) Information.

As explained in section 1.3.2, a small coincidence resolving time (*CRT*) of a PET system is required to minimize the number of randoms that contribute to the image. Additional benefits can be achieved if the CRT is in the order ~1 ns or smaller by making effective use of so called *time-of-flight* (TOF) information. TOF PET utilizes the fact that the distance *d* between the point of emission of an annihilation photon pair and the midpoint of the presumed LOR is measurable as a difference in their arrival time Δt at the corresponding detectors:

$$d = \frac{c}{2}\Delta t, \tag{1.6}$$

where c is the speed of light. The accuracy Δd with which the annihilation position along the LOR can be determined is thus given by (Anger 1966)

$$\Delta d = \frac{c}{2} CRT \ . \tag{1.7}$$

It is clear that Δd must at least be smaller than the diameter of the FOV in order to make use of *TOF* information. In this case, for a given annihilation event the likelihood for each voxel along the LOR (or within the VOR) to contain the point of emission can be calculated based on the measured time difference. During reconstruction this likelihood can be used as a weighting factor for the back projection of measurement data into the image space. This effectively constrains the data that contribute to a certain voxel to those projections that originate from a volume with a diameter in the order of Δd.

One benefit of reducing the size of the image space volume from which projection data is accepted becomes clear if one realizes that without TOF information the variance on the number of counts in a given projection data pixel n_λ is shared by all voxels along the corresponding VOR. With TOF information, however, a given voxel only shares the counting uncertainty of the subset of those counts in n_λ that originated from a range of $\sim\Delta d$ along the VOR. This noise reduction due to TOF information affects all counting noise (i.e, trues, random, and scatter counts). The magnitude of this noise reduction can be estimated considering a uniform activity distribution within a cylinder with diameter D in the center of the FOV. In this simplified model random and scatter events are distributed uniformly in both, image and projection space. Assuming a linear transformation between projection and image space (as, e.g. a backprojection operator), the improvement on the *SNR* that is achieved using TOF information with respect to non-TOF reconstruction can be expressed as the ratio (Moses 2003, Conti 2006, 2011)

$$\frac{SNR_{\text{TOF}}}{SNR_{\text{nonTOF}}} \cong \sqrt{\frac{D}{\Delta d}} \ . \tag{1.8}$$

For accuracy, it should be noted, that iterative reconstruction methods are nonlinear transformations. Still, estimating the TOF benefit under more realistic conditions (including nonhomogenous activity distributions, Compton scatter and randoms) indicate performance improvements in the same order of magnitude (Surti *et al.* 2006, Karp *et al.* 2008).

The above reasoning regarding the reduction of the data that is allowed to contribute to a certain partial volume in the image furthermore implies that the relative contributions of random and scatter data are reduced, when using TOF information. Consequently, this leads to a reduced background in the image (viz. reduced bias), faster conversion of iterative reconstruction methods, and improved contrast recovery (Karp *et al.* 2008).

1.3.7.   Attenuation Correction and Multi-Modality Imaging

In section 1.3.4 it was explained that an accurate tomographic reconstruction of the tracer distribution requires exact knowledge of the system matrix **S**. The

matrix elements $S_{\lambda,l}$ are defined to give the probability of the λth detector pair to detect both annihilation photon emitted from the lth voxel. This definition includes all effects that influence the detection probability of annihilation photon pairs. In consequence, $S_{\lambda,l}$ changes as an object that increases the fraction of scatter is placed in the corresponding LOR . This is clearly problematic for clinical PET. The scatter probability depends on the density and effective atomic number of the different tissue types. The exact location and dimensions of the different tissue types and in consequence the system matrix **S** are unique to each patient.

A practical solution to this dilemma is to determine **S** for a "bare" PET system and to apply an *attenuation correction* for real patient data (Lewellen and Karp 2004). This correction is facilitated by the symmetry of the propagation of the two annihilation photons and the fact that the combined scatter probability of the two γ-photons is independent on the point of emission along a given LOR. The uncorrected **S** can be obtained in a relatively straight forward manner, e.g. by performing calibration measurements, by means of Monte-Carlo simulations, or by a combination of the two.

A number of methods to obtain the attenuation correction data, also called attenuation maps, are based on the acquisition of transmission data using γ-radiation from an external γ-radiation source which is rotated around the scanner FOV (Carroll *et al.* 1983, Karp *et al.* 1995, Watson *et al.* 2001). An alternative to these methods is to acquire X-ray computed tomography (CT) data and to compute an attenuation map by correcting for the difference in energy of the transmitted photons.

The approach to combine PET and CT data has the added advantage, that the different *imaging modalities* yield different, complementary information: PET visualizes physiological processes whereas CT visualizes the anatomy of the subject. Thus the combination of PET and CT data allows for the localization for the physiological processes in the context of anatomical features of the patient, which is a desirable feature for many diagnostic tasks. Consequently, nowadays the overwhelming majority of commercially available PET systems are integrated with a CT scanner.

Nevertheless, CT utilizes ionizing radiation and therefore adds to the total radiation dose received by a patient. The added dose due to the CT depends on the acquisition protocol. It is in the order of 7 mS – 20 mS and thus in the same order or larger than the dose received during a typical ^{18}F-FDG PET scan (7 mS) (Watson *et al.* 2004, Brix *et al.* 2005, IAEA 2012). Furthermore, a truly simultaneous acquisition of PET and CT data is not feasible (Watson *et al.* 2004) which complicates the matter of alignment, or *co-registration,* of the acquired data.

A recent development is to utilize magnetic resonance (MR) tomography instead of CT data. MR imaging does not use ionizing radiation and thus PET/MR delivers a significantly lower effective radiation dose than a comparable PET/CT scan. Furthermore, the application of solid state

photosensors and MR-compatible materials in PET detectors facilitates the simultaneous acquisition of PET/MR data (Catana *et al.* 2008, Judenhofer *et al.* 2008, Pichler *et al.* 2008). This does not only simplify the co-registration of the PET/MR data but also offers the possibility to correct the PET data for patient movements based on MR data using fast acquisition protocol (Tsoumpas *et al.* 2010, Catana *et al.* 2011, King *et al.* 2012).

1.3.8. γ-detectors for (TOF) PET

1.3.8.1. Detector Requirements

The considerations regarding the image quality made in the previous sections can be translated into a number of requirements that are essential for γ-detectors for clinical PET.

An essential requirement for PET detectors is a high capture efficiency ε for annihilation photons, which can be understood as the probability that a 511 keV γ-photon impinging on the detector is registered and recognized as a having the appropriate energy. It is clear, that for a system employing detectors with lower ε (yet otherwise identical properties) a higher total activity is required in the FOV in order to obtain an equal coincidence count rate. What is more, is that at equal coincidence count rate a lower ε means that a larger fraction of the detected coincidences is caused by random events. This is because the singles rate is proportional to ε whereas the detection of true coincidences events scales with ε^2 since the measurement of each annihilation event requires the detection of two photons. In short, the higher ε the higher is the NEC at equal activity.

The advantage of using TOF information was discussed in detail in section 1.3.6. As the time resolution of a PET system is directly limited by the timing performance of the γ-detectors, it is clear that a small CRT is a highly desirable PET detector property. Moreover, PET detectors should offer an as good as possible energy resolution in order to discriminate scattered γ-photons. This is important as the contribution of scattered photons to the image reduces the NEC and may introduce a bias in the image (see section 1.3.5.2).

Furthermore, the accuracy with witch the interaction position of detected γ-photons can be determined is of importance. Yet, as mentioned in section 1.3.5.1, the positron range and the noncollinearity contribute significantly to the system spatial resolution. Thus, improvements of the detector spatial resolution become progressively less effective as it becomes better than the combined effect of positron range and noncollinearity, which is in the order of 0.8 mm FWHM to 2 mm FWHM for ^{18}F for ring diameters ranging from 20 cm to 80 cm (Levin and Hoffman 1999). For a constant spatial resolution throughout the FOV the detectors should furthermore provide DOI information (see section 1.3.5.1).

Additional requirements are scalability, low power consumption, MR-compatibility, and cost effectiveness. A class of γ-detector with the potential to perform well in all these areas is constituted by scintillation detectors. Scintillation detectors combine a conversion material, viz. the scintillator, and a

photosensor to create an electronic signal for an ionizing particle impinging on the detector. To date, the detectors in all commercial PET scanners and the overwhelming majority of detector concepts currently under investigation for application in (TOF) PET employ scintillation detectors.

1.3.8.2.   Scintillation Materials

Scintillators are materials that convert the energy carried by an ionizing particle (e.g. a 511 keV γ-photon) into a number of low energy photons that are typically in the visible spectral range. For an ideal scintillator the number of *scintillation photons N* is proportional to the energy *E* deposited by the ionizing particle in the scintillator upon the interaction. The constant of proportionality is commonly referred to as *light yield Y*. It should be noted that this proportionality is only fulfilled in approximation for realistic scintillators (e.g. Pidol *et al.* 2004, Kapusta *et al.* 2005, Owens *et al.* 2007). A high scintillation light yield is essential for suitable energy, timing, and spatial resolution. In Table 1.2 some important scintillation materials that are in principle suitable for application in PET are summarized together with properties that are of importance for the detector performance.

One prerequisite for a PET detector is a high detection efficiency for 511 keV γ-photons. The detection efficiency of a scintillation detector depends on the thickness of the scintillator and its so-called *attenuation length*. As the energy resolution, the timing performance and the spatial resolution deteriorate with the

Table 1.2. Scintillators for suitable for application in PET and their most important properties according to (van Eijk 2002) and references therein.

	density (g/cm^3)	Z_{eff}	atten. length (mm)	P_{ph} eff (%)	hygro-scopic	Y (ph/MeV)	decay time (ns)	λ_{max} (nm)
NaI:Tl	3.67	51	29.1	17	Yes	41000	230	410
LaCl$_3$:Ce	3.86	60	27.8	14	Yes	46000	25	330
LaBr$_3$:Ce	5.3	47	21.3	13	Yes	70000[1]	15[2]	358
Bi$_4$Ge$_3$O$_{12}$ (BGO)	7.1	74	10.4	40	No	9000	300	480
Lu$_2$SiO$_5$:Ce (LSO)	7.4	66	11.4	32	No	26000	40	420
Gd$_2$SiO$_5$:Ce (GSO)	6.7	59	14.1	25	No	8000	60	440
LuAlO$_3$:Ce (LUAP)	8.3	65	10.5	30	No	12000	18	365
Lu$_2$Si$_2$O$_7$:Ce (LPS)	6.2	64	14.1	29	No	30000	30	380

[1] according to (de Haas and Dorenbos 2008)
[2] according to (Glodo *et al.* 2005)

thickness of the scintillator scintillators with a small attenuation length are preferable. This in turn requires dense materials with a high effective atomic number Z_{eff}.

The use of dense, high-Z_{eff} materials offers the additional benefit that the average volume of the scintillator in which a 511 keV γ-photon deposits its energy is relatively small. This is because the probability for γ-photon interaction via photo effect scales with Z_{eff} and the mean free path of Compton scattered photons is the smaller the denser the material and the larger its Z_{eff}. A small average volume of energy deposition is advantageous especially for detectors utilizing small scintillation crystals as an event might be mis-positioned or not registered at all if only a portion of the energy is deposited in a single crystal element. In consequence, scintillation detectors optimized for PET application almost exclusively utilize inorganic scintillation crystals.

A further requirement on the scintillator properties is a fast time profile of the scintillation pulse following the γ-absorption. The distribution of the emission times of scintillation photons constitutes a major contribution to the intrinsic limit on the timing resolution that can be achieved with a given scintillation detector (see also chapters 5 and 6). Thus scintillation materials that exhibit fast rise and decay times of the emitted light pulse are required for optimum timing. Furthermore, fast scintillators are required to avoid so-called pulse pile up which may reduce the detector performance at high (singles) count rates.

Other properties such as the so-called intrinsic energy resolution, wavelength of maximum emission intensity λ_{max}, the probability for self-absorption and reemission of scintillation photons, the refractive index of the material, or its sensitivity to moisture (hygrocopicity) are often considered to be of less importance. Still, those properties may have a significant influence on the detector performance and the applicability of the scintillator in a PET system and should therefore be taken into account in a comparison of different scintillation materials.

1.3.8.3.   *Photosensors*

The properties of the photosensor are equally important for the performance of the scintillation detector as the characteristics of the scintillator. One important sensor property is its contribution to the overall photon detection efficiency (PDE). Here, we define the photon detection efficiency as the probability that a given scintillation photon emitted by the scintillator causes a corresponding electronic signal at the detector (van Dam *et al.* 2010). The contribution of the photosensor to the detector PDE can be expressed as the product of geometrical efficiency η_{geom}, optical efficiency η_{opt}, and internal quantum efficiency (QE).

The geometric efficiency is given by the ratio of active sensor area to the total sensor area coupled to the scintillator. The optical efficiency describes the probability for a given photon that impinges on the active sensor area to be transmitted to the active volume of the photosensor. In the simplest case this is

determined by the probability for a photon to be reflected at the sensor surface. Yet, most photosensors are equipped with a protective layer or a transparent casing and the reflection and transmission properties of all optical layers have to be taken into account. Lastly, the internal quantum efficiency defines the probability with which a photon that is absorbed the active volume of the sensor triggers an electronic signal.

It is pointed out that the optical efficiency and internal quantum efficiency both vary with the wavelength of the scintillation photons. It is therefore desirable to obtain a good match between the emission spectrum and the product of η_{opt} and the QE. It should also be noted that η_{opt} is not strictly a photosensor property as it depends on the refractive index of the scintillator and the optical coupling medium at the interface as well as the angular distribution of scintillation photons (e.g. Knapitsch *et al.* 2011).

The number of detected scintillation photons in a PET detector is typically in the order of a few thousand photons per scintillation event. The corresponding charge of the same number of electrons would be in the order of 0.1 fC – 1 fC which is difficult to measure without severe degradation due to electronic noise. Thus, photosensors for application in PET must provide an internal gain to avoid this issue. Furthermore, the timing characteristics of the sensor must allow accurate time stamping of scintillation events. The timing properties of photosensor are determined by the so-called signal transit time spread TTS and the time profile of the electronic signal caused by a single photon (see also chapters 5 and 6).

One type of photosensor that combines a high gain, with good timing properties and photon detection efficiency is the photomultiplier tube (PMT). PMTs were first introduced in the 1930's (Zworykin *et al.* 1936) and have found widespread application since. Consequently, the technology is mature, reliable and cost-effective. To date, PMTs are employed in the majority of commercial PET systems.

The operating principle of a PMT is illustrated in (see Figure 1.7). A PMT consist of an evacuated body (usually a glass tube) with a photocathode positioned behind an entrance window. A photon impinging on the photocathode may create a free electron by external photoemission. This electron is subsequently accelerated in the electric field between the photocathode and the first dynode stage. The kinetic energy of the photo-electron as it reaches the first dynode is thus determined by the voltage difference between cathode and dynode, which is typically in the order of 100 V. Upon impact of the photoelectron on the dynode a number of secondary electrons (typically ~10) are emitted. These secondary electrons are accelerated towards the next dynode stage leading to a further multiplication and so forth.

PMTs typically have about 10 dynode stages which require a total bias voltage (cathode to anode voltage difference) of 1 kV – 2.5 kV. The total gain is the order of 10^6 electrons per initial photoelectron. The PDE of conventional PMTs (for perpendicular incident photons in air) is typically 20% – 30% at the
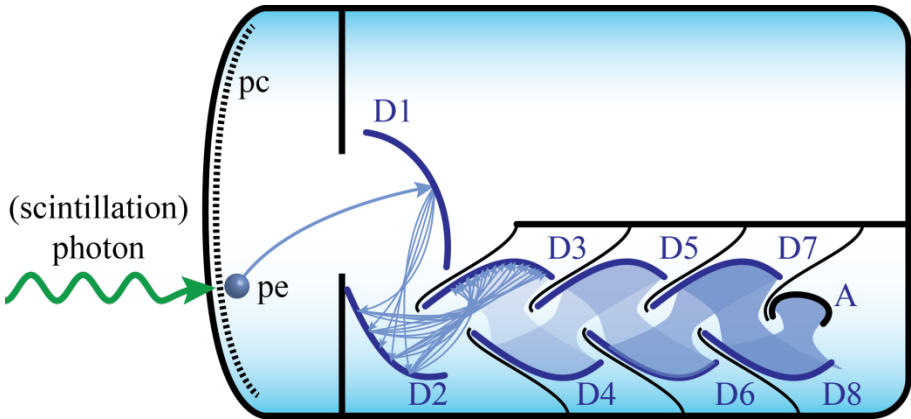
Figure 1.7. Schematic illustrating the principle of operation of a photomultiplier tube. An incoming photon releases a photoelectron (pe) from the photocathode (pc). The photoelectron is focused on the first dynode stage (D1) where its impact creates a number of secondary electrons. Further amplification takes place in subsequent dynode stages D2 ... D8. The signal charge is collected at the anode (A).

wavelength of maximum sensitivity. The TTS depends on the size of the cathode and the geometry of the dynode structure. Typical values for the TTS are in the order of 0.2 ns – 1 ns (FWHM)

The possibly largest disadvantage of PMTs is that the multiplication mechanism relies on the propagation of electrons over considerable distances. Consequently the performance of PMTs is sensitive to external magnetic fields making PMTs incompatible with MR imaging. This particular problem is avoided by solid state (semiconductor) photosensors with internal gain such as avalanche photodiodes (APDs). APDs are in essence photodiodes that operate at large reverse bias (300 V – 400 V). This results in large electric field in the depletion region of the diode. In this field charge carriers that are created upon absorption of a scintillation photon are accelerated may gain sufficient energy to lead to additional ionizations in depletion region thus creating an avalanche of charge carriers.

The gain that results from the avalanche process depends on the electric field strength in the depletion region and hence the applied bias. Values in the order of 100 – 1000 can be achieved. That means that the gain of APDs is considerably smaller than for PMTs. This is partially mitigated by the fact that APDs exhibit a substantially larger QE (>90 %). Yet, also the response of APDs is relatively slow (~10 ns signal rise time) because of the large diode capacitance. In combination with the small gain this leads to an inferior timing resolution in comparison to scintillation detectors employing conventional PMTs. Still, the timing resolution achievable with APDs can be sufficient for
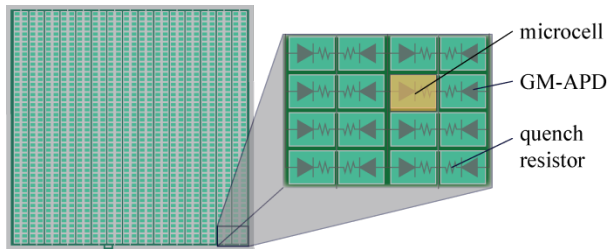
Figure 1.8. Illustration of an SiPM. The inset shows a zoom on 4 × 4 microcells. Each micorcelll is composed of a GM-APD and a resistor for passive quenching, which is indicated by the symbols in the inset.

non-TOF PET and APDs have found application in scanners with small bore diameter (e.g. dedicated small animal PET; Ziegler *et al.* 2000, Berard *et al.* 2009, Bergeron *et al.* 2009a, Bergeron *et al.* 2009b) and the first clinical PET/MR system (Siemens Biograph™ mMR[2]).

A relatively new development in the field of solid state photosensor overcomes the issues of the low gain and the slow response of APDs. So-called silicon photomultipliers (SiPMs)–also referred to as multi-pixel photon counters (MPPCs) or solid state photomultipliers (SSPMs)–are composed by a large number $(10^2 - 10^4)$ of ADPs operated at a bias voltage beyond the so-called break down voltage of the device (Buzhan *et al.* 2003, Otte *et al.* 2005, Dolgoshein *et al.* 2006, Korpar *et al.* 2008, Renker 2009). In this regime a triggered avalanche becomes self-sustaining and the break down spreads throughout the entire diode resulting in a much higher gain (10^5-10^6).

The break down across the entire diode means that the avalanche current is saturated and thus independent on the number of initial charge carriers. ADPs operated in this regime are referred to as Geiger mode APDs (GM-APDs). As the avalanche is self-sustaining a quenching circuit is required. In the simplest case this is a resistor, the so-called quench resistor, in series with the GM-APD. The combination of APD and quenching circuit forms the basic building block of SiPMs and often referred to as micro cell. In order to obtain a (semi) proportional light sensor many microcells are operated in parallel in SiPMs (see Figure 1.8). A detailed description of the operating principle of SiPMs can be found in chapter 2.

The timing properties of SiPMs are comparable to those of fast PMTs. Depending on the device architecture, the TTS of individual microcells can be much smaller than < 100 ps (Cova *et al.* 1987, Cova *et al.* 1989) (FWHM). For commercially available SiPMs the TTS is in the order of 300 ps (FWHM) (Ronzhin *et al.*). The single photon signal rise time can be in the order of 1 ns – 2 ns.

In consequence, SiPMs may appear to be the ideal replacement for conventional PMTs in scintillation detectors for application in PET. Yet the

---

[2]   Siemens 2012 http://www.medical.siemens.com/webapp/wcs/stores

application of SiPMs can be challenging. Due to large terminal capacitance (100 pF – 400 pF) and the architecture of the microcells SiPMs are far from ideal current sources which can be problematic for signal handling and noise suppression (see also Chapter 2). Furthermore, SiPMs exhibit a substantial amount of so-called *dark counts*, *cross talk,* and *after pulsing* (Du and Retiere 2008, Retiere *et al.* 2009, Eckert *et al.* 2010), which may deteriorate the detector performance.

1.3.8.4. *Detector Assembly*

For the performance of a scintillation detector it is important that scintillation photons are collected efficiently and fast at the active area of the photosensor. As scintillation photons are emitted isotropically in all directions it is in general beneficial to cover crystal surfaces that are not directly coupled to a photosensor with a reflective material. Further improvement of the light collection can be achieved by the surface finish of the crystals (rough/etched vs. polished) and the optical coupling between the crystal and the sensor.

Several different types of reflective materials are currently used in PET detectors. In detector research PTFE (Teflon) or similar materials (e.g. Spectralon®) are often employed as a "golden standard". These materials exhibit a high reflectivity (>98%) in a broad spectral range. Yet, they also require a certain thickness (up to ~1 mm) to achieve such high reflectivity which can lead to severely compromised system sensitivity especially for systems that employ small crystal elements. In consequence other reflectors, such as thin reflective foils, reflective coatings (based on e.g. Al, or Ag), white paint or TiO_2 loaded epoxy are often employed.

A further design aspect of PET detectors concerns the encoding of the (axial and transversal) position of the γ-interaction. One way to realize position encoding is to use scintillation crystals with a small footprint (e.g. 4 mm × 4 mm). In order to maintain sufficient system sensitivity a number of such crystals are tightly packed into a scintillator block. For the same reason the thickness of these scintillator blocks is commonly chosen to be in the order of or larger than 2 × the attenuation length of the scintillator material (2 cm – 3 cm).

The position decoding is done by identifying the crystal that had been "hit" by the γ-photon. The conceptual simplest for crystal identification scheme is so-called *1-to-1-coupling*, i.e. a small photosensor is attached to each crystal element. Historically, this approach was not feasible as PMTs of a small enough size were not available, while possible alternatives (multi-anode PMTs or micro channel plates) were either too costly or inferior in performance (APDs). However, the emergence of SiPMs may make this concept a viable alternative.

The need for a large number of small photosensors can be circumvented by allowing the light from a single crystal element to spread over multiple detectors. This can be achieved by using spatially designed light guides or by using incomplete saw cuts in a crystal block. These light sharing schemes are designed such that a scintillation event in a given scintillation crystal leads to a

unique intensity ratio on the attached photosensors. Thus, for a typical scintillator matrix of 8 × 8 pixels coupled to 4 PMTs the number of channels is reduced by a factor of 8.

One drawback of pixelated block detectors is that scintillation photons undergo a large number of reflections before reaching the photosensor. As each interaction at the crystal surface may also lead to the loss of the scintillation photon this geometry is not beneficial for the photon collection efficiently of the detector. What is more is that the average number of reflections and the path length distribution for scintillation photons depend on the distance between the γ-interaction point and the photosensor. This degrades both the energy and the timing resolution of the detector. A further disadvantage of pixelated block detectors is that even for high-Z materials the majority of 511 keV photons interact via Compton scattering. The scattered photon may leave the crystal be absorbed in a neighboring crystal element, in which case the positioning may become difficult.

These issues are avoided by using monolithic scintillation crystals (~ 20 mm × 20 mm × 20 mm) that are read out by pixelated photosensors (Bruyndonckx *et al.* 2006, Maas *et al.* 2006). As each interaction position leads to a unique light distribution on the photosensor the interaction position can be estimated based on the intensities measured by the individual pixels, e.g. using statistical methods (Maas *et al.* 2008, van Dam *et al.* 2011a) or calibrated Neural Networks (Bruyndonckx *et al.* 2004).

An additional benefit of this concept is that the light distribution also contains information on the distance between photosensor and the γ-interaction point, i.e. the DOI (Maas *et al.* 2009, van Dam *et al.* 2011b). This information can be used to reduce the parallax error (see section 1.3.5.1). For conventional, pixelated crystal detectors DOI information can only be obtained by introducing substantial design changes (e.g. Karp and Daubewitherspoon 1987, Moses and Derenzo 1994). However, these proposed concepts to obtain DOI information for pixelated detector blocks compromise the collection efficiency for scintillation photons and/or the timing properties of the detector.

1.4.   Thesis Research Objectives

The quality of the images acquired with any give PET system crucially depends on how accurately the tracer distribution can be reconstructed from the acquired PET data. This accuracy is fundamentally limited by the number of detected (true) annihilation photon pairs, the ratio between true and random coincidences, and the accuracy with which each γ-photon can be localized in space and time. All these limiting factors are largely determined by the properties of the employed γ-photon detectors.

In this respect, the parameters of interest are the γ-detection efficiency, the energy resolution, the spatial resolution, the coincidence resolving time, and depth of interaction resolution. It is often the case that improvements in one of these areas degrade the detectors capabilities in one or more of the remaining

Table 1.3. Properties of γ-detectors currently employed in state of the art TOF PET scanners.

System	Scintillator/ Photosensor	Crystal element dimensions (mm³)	Energy Res.	Spatial Resolution / at distance from center	CRT (ps)
Philips Gemini TruFlight	LYSO/PMT	4 × 4 × 22	11.5% [1]	4.8 mm / 1 cm 5.0 mm / 10 cm [1]	585 [1]
Siemens Biograph TruePoint	LSO/PMT	4 × 4 × 20	11% [2]	4.4 mm / 1 cm 5.0 mm / 10 cm [3]	550 [2]

[1] according to Surti *et al.* (2007)

[2] according to Lois *et al.* (2010)

[3] according to Jakoby *et al.* (2009)

ones. For example, crystal elements with a very small diameter might be favorable in terms of spatial resolution, yet at the same time this might degrade the detection efficiency, energy and timing resolution.

Evidently, a detector that performs very well in some areas but poorly in others is not suitable for application in PET. In consequence, a large portion of PET detector development is dedicated to finding the optimum compromise between competing requirements. This is reflected in the performance of state of the art TOF PET detectors (see Table 1.3). Neither the energy resolution, nor the spatial resolution, nor the CRT are truly outstanding, yet the combination of an energy resolution of 11%, ~5 mm spatial resolution and a CRT of 550 ps (FWHM) is difficult to achieve at a system level.

The research conducted in the scope of this thesis is dedicated to the investigation of innovative detector concepts and new materials that facilitate significant improvements of the energy resolution, spatial resolution, and timing resolution with respect to state of the art PET detectors. One important aspect in this regard is the application of monolithic scintillation crystals in γ-detectors for TOF PET. Furthermore, the benefits of using the recently discovered fast and bright scintillation material $LaBr_3$:Ce are explored. A specific focus of this research is directed towards SiPMs in order to further the understanding of these light sensors, to optimize their readout and to investigate the feasibility of their application in TOF PET detectors.

1.5. Thesis outline

In chapter 2 an equivalent circuit model for SiPMs is presented and compared to measurements. The model is discussed in terms of its implications for read out electronics and the consequences for the signal linearity. The measurements

presented in chapter 3 highlight the potential scintillation detectors based on LaBr$_3$:Ce and SiPMs for applications that require accurate timing, e.g. TOF PET.

Chapter 4 describes the measurements of scintillation pulse shape of two fast scintillators, namely LYSO:Ce and LaBr$_3$:Ce. The scintillation pulse shape constitutes an important input parameter for theoretic models aimed to predict the timing resolution of scintillation detectors. Such a model is developed in chapter 5. Furthermore, this chapter details validation measurements that were performed with detectors utilizing LaBr$_3$:Ce and LSYO:Ce crystals.

A different approach to assess the timing performance of a given scintillation detector is described in chapter 6. The timing resolution of a scintillation detector is ultimately limited by the statistical nature of the detection of scintillation photons. This imposed limit is described in a detailed statistical model. The model predictions are compared to values known from literature and its implications for the future development of (digital) SiPMs are discussed.

In chapters 7 and 8 two scintillation detectors based on monolithic scintillation crystals and SiPMs arrays are characterized. The detector described in chapter 7 utilizes LYSO and the first commercially available SiPM array. The experimental setup and the methods to characterize the detector are presented and the spatial resolution, the ability to correct for the DOI, and the energy and timing resolutions obtained with the detector are discussed. Chapter 8 describes the characterization of a detector comprising a LaBr$_3$:Ce crystal and an advanced SiPM array in terms of its spatial resolution, its energy resolution and its timing performance. Furthermore a detailed discussion of the bias in the position estimation is presented.

Lastly, the most important findings of the research conducted in the scope of this thesis are summarized in the concluding chapter of this work. These results are discussed in the context of recent or imminent technological progress and the implications of these developments for future TOF PET detectors are considered.

References

Anger H O 1966 Survey of Radioisotope Cameras *Isa T* **5** 311-&

Barney J S, Rogers J G, Harrop R and Hoverath H 1991 Object Shape Dependent Scatter Simulations for Pet *IEEE Trans. Nucl. Sci.* **38** 719-725

Barrett H H, Yao J, Rolland J P and Myers K J 1993 Model Observers for Assessment of Image Quality *P Natl Acad Sci USA* **90** 9758-9765

Beekman F and van der Have F 2007 The pinhole: gateway to ultra-high-resolution three-dimensional radionuclide imaging *Eur J Nucl Med Mol I* **34** 151-161

Berard P, Bergeron M, Pepin C M, Cadorette J, Tetrault M A, Viscogliosi N, Fontaine R, Dautet H, Davies M, Deschamps P and Lecomte R 2009 LabPET II, a Novel 64-channel APD-based PET Detector Module with

Individual Pixel Readout Achieving Submillimetric Spatial Resolution *IEEE Nuclear Science Symposium and Medical Imaging Conference (2008 NSS/MIC)* (Dresden) 4730-4735

Bergeron M, Cadorette J, Beaudoin J F, Lepage M D, Robert G, Selivanov V, Tetrault M A, Viscogliosi N, Norenberg J P, Fontaine R and Lecomte R 2009a Performance Evaluation of the LabPET APD-Based Digital PET Scanner *IEEE Trans. Nucl. Sci.* **56** 10-16

Bergeron M, Cadorette J, Beaudoin J F, Tetrault M A, Viscogliosi N, Selivanov V, Lepage M D, Robert G, Norenberg J P, Fontaine R and Lecomte R 2009b Imaging Performance of the LabPET (TM) APD-based Digital PET Scanner *IEEE Nuclear Science Symposium and Medical Imaging Conference (2008 NSS/MIC)* (Dresden) 3116-3120

Beringer R and Montgomery C G 1942 The angular distribution of positron annihilation radiation *Phys Rev* **61** 222-224

Brasse D, Kinahan P E, Lartizien C, Comtat C, Casey M and Michel C 2005 Correction methods for random coincidences in fully 3D whole-body PET: Impact on data and image quality *J Nucl Med* **46** 859-867

Brix G, Lechel U, Glatting G, Ziegler S I, Munzing W, Muller S P and Beyer T 2005 Radiation exposure of patients undergoing whole-body dual-modality F-18-FDG PET/CT examinations *J Nucl Med* **46** 608-613

Bruyndonckx P, Leonard S, Tavernier S, Lemaitre C, Devroede O, Wu Y B and Krieguer M 2004 Neural network-based position estimators for PET detectors using monolithic LSO blocks *IEEE Trans. Nucl. Sci.* **51** 2520-2525

Bruyndonckx P, Lemaitre C, Leonard S, Schaart D R, van der Laan D J, Maas M C, Bevroede O, Wu Y B, Krieguer M and Tavernier S 2006 Initial characterization of a nonpixelated scintillator detector in a PET prototype demonstrator *IEEE Trans. Nucl. Sci.* **53** 2543-2548

Buzhan P, Dolgoshein B, Filatov L, Ilyin A, Kantzerov V, Kaplin V, Karakash A, Kayumov F, Klemin S, Popova E and Smirnov S 2003 Silicon photomultiplier and its possible applications *Nucl Instrum Meth A* **504** 48-52

Carroll L R, Kretz P and Orcutt G 1983 The Orbiting Rod Source - Improving Performance in Pet Transmission Correction Scans *J Nucl Med* **24** P11-P11

Casey M E and Hoffman E J 1986 Quantitation in Positron Emission Computed-Tomography .7. A Technique to Reduce Noise in Accidental Coincidence Measurements and Coincidence Efficiency Calibration *J Comput Assist Tomo* **10** 845-850

Catana C, Procissi D, Wu Y B, Judenhofer M S, Qi J Y, Pichler B J, Jacobs R E and Cherry S R 2008 Simultaneous in vivo positron emission tomography and magnetic resonance imaging *P Natl Acad Sci USA* **105** 3705-3710

Catana C, Benner T, van der Kouwe A, Byars L, Hamm M, Chonde D B, Michel C J, El Fakhri G, Schmand M and Sorensen G 2011 MRI-Assisted PET Motion Correction for Neurologic Studies in an Integrated MR-PET

Scanner *J Nucl Med* **52** 154-161

Cherry S R and Sung-Cheng H 1995 Effects of scatter on model parameter estimates in 3D PET studies of the human brain *IEEE Trans. Nucl. Sci.* **42** 1174-1179

Cherry S R, Sorenson J A and Phelps M E 2003 *Physics in nuclear medicine* (Philadelphia, PA: Saunders)

Colsher J G 1980 Fully 3-Dimensional Positron Emission Tomography *Phys Med Biol* **25** 103-115

Conti M 2006 Effect of randoms on signal-to-noise ratio in TOF PET *IEEE Trans. Nucl. Sci.* **53** 1188-1193

Conti M 2011 Focus on time-of-flight PET: the benefits of improved time resolution *Eur J Nucl Med Mol I* **38** 1147-1157

Cova S, Ripamonti G and Lacaita A 1987 Avalanche Semiconductor Detector for Single Optical Photons with a Time Resolution of 60 Ps *Nucl Instrum Meth A* **253** 482-487

Cova S, Lacaita A, Ghioni M, Ripamonti G and Louis T A 1989 20-Ps Timing Resolution with Single-Photon Avalanche-Diodes *Rev Sci Instrum* **60** 1104-1110

de Haas J T M and Dorenbos P 2008 Advances in yield calibration of scintillators *IEEE Trans. Nucl. Sci.* **55** 1086-1092

Dolgoshein B, Balagura V, Buzhan P, Danilov M, Filatov L, Garutti E, Groll M, Ilyin A, Kantserov V, Kaplin V, Karakash A, Kayumov F, Klemin S, Korbel V, Meyer H, Mizuk R, Morgunov V, Novikov E, Pakhlov P, Popova E, Rusinov V, Sefkow F, Tarkovsky E and Tikhomirov I 2006 Status report on silicon photomultiplier development and its applications *Nucl Instrum Meth A* **563** 368-376

Du Y and Retiere F 2008 After-pulsing and cross-talk in multi-pixel photon counters *Nucl Instrum Meth A* **596** 396-401

Eckert P, Schultz-Coulon H C, Shen W, Stamen R and Tadday A 2010 Characterisation studies of silicon photomultipliers *Nucl Instrum Meth A* **620** 217-226

Glodo J, Moses W W, Higgins W M, van Loef E V D, Wong P, Derenzo S E, Weber M J and Shah K S 2005 Effects of Ce concentration on scintillation properties of LaBr$_3$:Ce *IEEE Trans. Nucl. Sci.* **52** 1805-1808

Goorden M C, Rentmeester M C M and Beekman F J 2009 Theoretical Analysis of Multi-Pinhole Brain SPECT *Ieee Nucl Sci Conf R* 3311-3313

Hoffman E J, Huang S C, Phelps M E and Kuhl D E 1981 Quantitation in Positron Emission Computed-Tomography .4. Effect of Accidental Coincidences *J Comput Assist Tomo* **5** 391-400

IAEA 2012 *Radiation Protection of Patients (RPOP)* Available: https://rpop.iaea.org/RPOP/RPoP/Content/InformationFor/HealthProfessio nals/6_OtherClinicalSpecialities/PETCTscan.htm#PETCT_FAQ01

Jakoby B W, Bercier Y, Watson C C, Bendriem B and Townsend D W 2009 Performance Characteristics of a New LSO PET/CT Scanner With Extended Axial Field-of-View and PSF Reconstruction *IEEE Trans. Nucl.*

Sci. **56** 633-639

Judenhofer M S, Wehrl H F, Newport D F, Catana C, Siegel S B, Becker M, Thielscher A, Kneilling M, Lichy M P, Eichner M, Klingel K, Reischl G, Widmaier S, Rocken M, Nutt R E, Machulla H J, Uludag K, Cherry S R, Claussen C D and Pichler B J 2008 Simultaneous PET-MRI: a new approach for functional and morphological imaging *Nat Med* **14** 459-465

Kanishi D 1993 Tc-99m-Mdp Accumulation Mechanisms in Bone *Oral Surgery Oral Medicine Oral Pathology Oral Radiology and Endodontics* **75** 239-246

Kapusta M, Szupryczynski P, Melcher C L, Moszyński M, Balcerzyk M, Carey A A, Czamacki W, Spurrier M A and Syntfeld A 2005 Non-proportionality and thermoluminescence of LSO : Ce *IEEE Trans. Nucl. Sci.* **52** 1098-1104

Karp J S and Daubewitherspoon M E 1987 Depth-of-Interaction Determination in Nai(Tl) and Bgo Scintillation Crystals Using a Temperature-Gradient *Nucl Instrum Meth A* **260** 509-517

Karp J S, Muehllehner G, Qu H and Yan X H 1995 Singles Transmission in Volume-Imaging Pet with a Cs-137 Source *Phys Med Biol* **40** 929-944

Karp J S, Surti S, Daube-Witherspoon M E and Muehllehner G 2008 Benefit of time-of-flight in PET: Experimental and clinical results *J Nucl Med* **49** 462-470

King A P, Buerger C, Tsoumpas C, Marsden P K and Schaeffter T 2012 Thoracic respiratory motion estimation from MRI using a statistical model and a 2-D image navigator *Med Image Anal* **16** 252-264

Knapitsch A, Auffray E, Fabjan C W, Leclercq J L, Lecoq P, Letartre X and Seassal C 2011 Photonic crystals: A novel approach to enhance the light output of scintillation based detectors *Nucl Instrum Meth A* **628** 385-388

Knoll G F 2000 *Radiation detection and measurement* (New York: Wiley)

Korpar S, Dolenec R, Hara K, Iijima T, Krizan P, Mazuka Y, Pestotnik R, Stanovnik A and Yamaoka M 2008 Measurement of Cherenkov photons with silicon photomultipliers *Nucl Instrum Meth A* **594** 13-17

Levin C S and Hoffman E J 1999 Calculation of positron range and its effect on the fundamental limit of positron emission tomography system spatial resolution *Phys Med Biol* **44** 781-799

Lewellen T and Karp J 2004 *Emission Tomography* Chapter Chapter 10 - PET Systems ed N W Miles, Ph.D, and P D John N. Aarsvold (San Diego: Academic Press) pp 179-194

Lois C, Jakoby B W, Long M J, Hubner K F, Barker D W, Casey M E, Conti M, Panin V Y, Kadrmas D J and Townsend D W 2010 An Assessment of the Impact of Incorporating Time-of-Flight Information into Clinical PET/CT Imaging *J Nucl Med* **51** 237-245

Maas M C, van der Laan D J, Schaart D R, Huizenga J, Brouwer J C, Bruyndonckx P, Leonard S, Lemaitre C and van Eijk C W E 2006 Experimental characterization of monolithic-crystal small animal PET detectors read out by APD arrays *IEEE Trans. Nucl. Sci.* **53** 1071-1077

Maas M C, Schaart D R, van der Laan D J, van Dam H T, Huizenga J, Brouwer J C, Bruyndonckx P, Lemaitre C and van Eijk C W E 2008 Signal to noise ratio of APD-based monolithic scintillator detectors for high resolution PET *IEEE Trans. Nucl. Sci.* **55** 842-852

Maas M C, Schaart D R, van der Laan D J, Bruyndonckx P, Lemaitre C, Beekman F J and van Eijk C W E 2009 Monolithic scintillator PET detectors with intrinsic depth-of-interaction correction *Phys Med Biol* **54** 1893-1908

MacDonald L R and Dahlbom M 1998 Parallax correction in PET using depth of interaction information *IEEE Trans. Nucl. Sci.* **45** 2232-2237

Moses W W and Derenzo S E 1994 Design Studies for a Pet Detector Module Using a Pin Photodiode to Measure Depth of Interaction *IEEE Trans. Nucl. Sci.* **41** 1441-1445

Moses W W 2003 Time of flight in PET revisited *IEEE Trans. Nucl. Sci.* **50** 1325-1330

Ollinger J M 1996 Model-based scatter correction for fully 3D PET *Phys Med Biol* **41** 153

Otte A N, Barral J, Dolgoshein B, Hose J, Klemin S, Lorenz E, Mirzoyan R, Popova E and Teshima M 2005 A test of silicon photomultipliers as readout for PET *Nucl Instrum Meth A* **545** 705-715

Owens A, Bos A J J, Brandenburg S, Dorenbos P, Drozdowski W, Ostendorf R W, Quarati F, Webb A and Welter E 2007 The hard X-ray response of Ce-doped lanthanum halide scintillators *Nucl Instrum Meth A* **574** 158-162

Parodi K, Ponisch F and Enghardt W 2005 Experimental study on the feasibility of in-beam PET for accurate monitoring of proton therapy *IEEE Trans. Nucl. Sci.* **52** 778-786

Pawelke J, Byars L, Enghardt W, Fromm W D, Geissel H, Hasch B G, Lauckner K, Manfrass P, Schardt D and Sobiella M 1996 The investigation of different cameras for in-beam PET imaging *Phys Med Biol* **41** 279-296

Pichler B J, Wehrl H F and Judenhofer M S 2008 Latest advances in molecular imaging instrumentation *J Nucl Med* **49** 5S-23S

Pidol L, Kahn-Harari A, Viana B, Virey E, Ferrand B, Dorenbos P, de Haas J T M and van Eijk C W E 2004 High efficiency of lutetium silicate scintillators, Ce-doped LPS, and LYSO crystals *IEEE Trans. Nucl. Sci.* **51** 1084-1087

Renker D 2009 New developments on photosensors for particle physics *Nucl Instrum Meth A* **598** 207-212

Retiere F, Du Y, Foreman S, Kitching P, Kostin A, Lindner T, Low M, Masliah P, Moult I, Oser S, Tanaka H and Vacheret A 2009 Characterization of Multi Pixel Photon Counters for T2K Near Detector *Nucl Instrum Meth A* **610** 378-380

Rogulski M M, Barber H B, Barrett H H, Shoemaker R L and Woolfenden J M 1993 Ultra-High-Resolution Brain Spect Imaging - Simulation Results *IEEE Trans. Nucl. Sci.* **40** 1123-1129

Ronzhin A, Albrow M, Byrum K, Demarteau M, Los S, May E, Ramberg E, Va'vra J and Zatserklyaniy A 2010 Tests of timing properties of silicon

photomultipliers *Nucl Instrum Meth A* **616** 38-44

Strother S C, Casey M E and Hoffman E J 1990 Measuring Pet Scanner Sensitivity - Relating Countrates to Image Signal-to-Noise Ratios Using Noise Equivalent Counts *IEEE Trans. Nucl. Sci.* **37** 783-788

Surti S, Karp J S, Popescu L A, Daube-Witherspoon M E and Werner M 2006 Investigation of time-of-flight benefit for fully 3-D PET *IEEE Transactions on Medical Imaging* **25** 529-538

Surti S, Kuhn A, Werner M E, Perkins A E, Kolthammer J and Karp J S 2007 Performance of philips gemini TF PET/CT scanner with special consideration for its time-of-flight imaging capabilities *J Nucl Med* **48** 471-480

Swets J A 1988 Measuring the Accuracy of Diagnostic Systems *Science* **240** 1285-1293

Tsoumpas C, Mackewn J E, Halsted P, King A P, Buerger C, Totman J J, Schaeffter T and Marsden P K 2010 Simultaneous PET-MR acquisition and MR-derived motion fields for correction of non-rigid motion in PET *Ann Nucl Med* **24** 745-750

van Dam H T, Seifert S, Vinke R, Dendooven D, Löhner H, Beekman F J and Schaart D R 2010 A Comprehensive Model of the Response of Silicon Photomultipliers *IEEE Trans. Nucl. Sci.* **57** 2254-2266

van Dam H T, Seifert S, Vinke R, Dendooven P, Löhner H, Beekman F J and Schaart D R 2011a Improved Nearest Neighbor Methods for Gamma Photon Interaction Position Determination in Monolithic Scintillator PET Detectors *IEEE Trans. Nucl. Sci.* **58** 2139-2147

van Dam H T, Seifert S, Vinke R, Dendooven P, Löhner H, Beekman F J and Schaart D R 2011b A practical method for depth of interaction determination in monolithic scintillator PET detectors *Phys Med Biol* **56** 4135-4145

van Eijk C W E 2002 Inorganic scintillators in medical imaging *Phys Med Biol* **47** R85-R106

Vardi Y, Shepp L A and Kaufman L 1985 A Statistical Model for Positron Emission Tomography *J Am Stat Assoc* **80** 8-20

Watson C C 2000 New, faster, image-based scatter correction for 3D PET *IEEE Trans. Nucl. Sci.* **47** 1587-1594

Watson C C, Eriksson L, Casey M E, Jones W F, Moyers J C, Miller S, Hamill J, Van Lingen A, Bendriem B and Nutt R 2001 Design and performance of collimated coincidence point sources for simultaneous transmission measurements in 3-D PET *IEEE Trans. Nucl. Sci.* **48** 673-679

Watson C C, Townsend D W and Bendriem B 2004 *Emission Tomography* Chapter Chapter 11 - PET/CT Syatems ed N W Miles, Ph.D, and P D John N. Aarsvold (San Diego: Academic Press) pp 195-212

Wernick M N and Aarsvold J N 2004a *Emission Tomography* (San Diego: Academic Press)

Wernick M N and Aarsvold J N 2004b *Emission Tomography* Chapter 2:

Introduction to Emission Tomography ed N W Miles, Ph.D, and P D John
N. Aarsvold (San Diego: Academic Press) pp 11-23

Ziegler S I, Pichler B J, Boening G, Rafecas H, Bieler S, Pimpl W, Lorenz E and
Schwaiger M 2000 MadPET: High resolution animal pet with avalanche
photodiode arrays and LSO crystals. *J Nucl Med* **41** 20p-20p

Zworykin V K, Morton G A and Malter L 1936 The Secondary Emission Multiplier-
A New Electronic Device *Proceedings of the Institute of Radio Engineers*
24 351-375

2   Simulation of Silicon Photomultiplier Signals

   Abstract— In a silicon photomultiplier (SiPM), also referred to as multi-pixel photon counter (MPPC), many Geiger-mode avalanche photodiodes (GM-APDs) are connected in parallel so as to combine the photon counting capabilities of each of these so-called microcells into a proportional light sensor. The discharge of a single microcell is relatively well understood and electronic models exist to simulate this process. In this paper we introduce an extended model that is able to simulate the simultaneous discharge of multiple cells. This model is used to predict the SiPM signal in response to fast light pulses as a function of the number of fired cells, taking into account the influence of the input impedance of the SiPM preamplifier. The model predicts that the electronic signal is not proportional to the number of fired cells if the preamplifier input impedance is not zero. This effect becomes more important for SiPMs with lower parasitic capacitance (which otherwise is a favorable property). The model is validated by comparing its predictions to experimental data obtained with two different SiPMs (Hamamatsu S10362-11-25u and Hamamatsu S10362-33-25c) illuminated with ps laser pulses. The experimental results are in good agreement with the model predictions.

2.1.   Introduction

Silicon photomultipliers (SiPMs), also referred to as multi-pixel photon counters (MPPCs), are a relatively new and promising class of solid-state, low-level light sensors with potential in a multitude of applications such as high-energy physics, astronomy, biomolecular imaging, and medical imaging (Bondarenko *et al.* 2000, Buzhan *et al.* 2003, Otte *et al.* 2005, Dolgoshein *et al.* 2006) SiPMs are comprised of many, tiny, self-quenching Geiger-mode avalanche photodiodes (GM-APDs), all connected in parallel. A consequence of the Geiger-mode operation of the APDs is that their individual signals do not carry any information about the intensity of the detected light. However, the massive parallel connection of these so-called microcells, their small dimensions, their dense packaging, and their short recovery times (20 ns to 150 ns (Burr and Wang 2007, Uozumi 2007)) allow for a nearly proportional response if the light intensity is not too high, i.e., if the probability that more than one photon hits a single microcell within its recovery time is negligible (Buzhan *et al.* 2001).

For a thorough analysis and interpretation of SiPM signals a detailed understanding of the discharge process and of the influence of the front-end electronics is compulsory. A powerful method to achieve this is the utilization of equivalent-circuit models that describe the physical discharge and quenching processes. Such models have already been developed for individual GM-ADPs (Haitz 1964, Cova *et al.* 1996) and for single cells firing within a SiPM (Pavlov *et al.* 2005, Corsi *et al.* 2007, Wangerin *et al.* 2008).

In this paper we introduce an extended model that allows for the simulation of the simultaneous firing of multiple microcells in a SiPM. We will show that such a multi-cell model is necessary to adequately describe the operation of a SiPM since its instantaneous electronic properties are a function of the number of cells firing. We will furthermore demonstrate that this results in an influence of the input impedance of the front-end electronics on the proportionality of the SiPM signal. The results obtained from these simulations are validated by comparison to experimental data obtained with two different SiPMs (Hamamatsu S10362-11-25u and Hamamatsu S10362-33-25c).

2.2.   Methods and Materials

2.2.1.   Simulation Model

The equivalent circuit simulating the discharge of N_f cells in a SiPM consisting of a total number of N_{tot} microcells is illustrated in Figure 2.1. The dashed lines in Figure 2.1 separate the circuit into an active part (left), representing a number of Nf fired microcells in parallel; a passive component (middle), representing the remaining, $N_p = N_{tot} - N_f$ unfired microcells; and a parasitic capacitance C_g (right), which equals the sum of the parasitic capacitances of the N_{tot} cells connected in parallel. The resistor and capacitor values in the active and passive part of the circuit are given by:
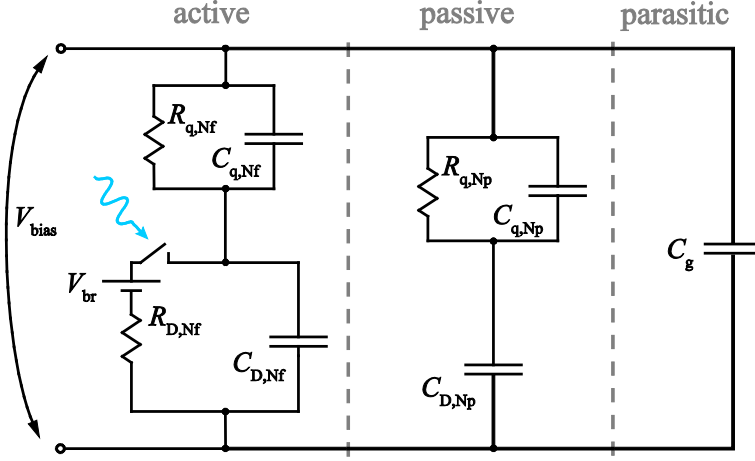
Figure 2.1. Equivalent circuit for the discharge of N_f microcells in a SiPM (symbols are explained section 2.2.1).

$$C_{\mathrm{D,Nf}} = C_{\mathrm{D}} \cdot N_{\mathrm{f}}, \quad R_{\mathrm{q,Nf}} = R_{\mathrm{q}} / N_{\mathrm{f}}, \quad C_{\mathrm{q,Nf}} = C_{\mathrm{q}} \cdot N_{\mathrm{f}},.$$

$$C_{\mathrm{D,Np}} = C_{\mathrm{D}} \cdot N_{\mathrm{p}}, \quad R_{\mathrm{q,Np}} = R_{\mathrm{q}} / N_{\mathrm{p}}, \quad C_{\mathrm{q,Np}} = C_{\mathrm{q}} \cdot N_{\mathrm{p}}, \quad (2.1)$$

$$\text{and } R_{\mathrm{D,\,Nf}} = R_{\mathrm{D}} / N_{\mathrm{f}},$$

where C_{D} is the capacitance of the reverse-biased diode, R_{D} is the series resistance of the microplasma in the avalanche, R_{q} is the quench resistor and C_{q} is its associated stray capacitance, all for an individual microcell. For the special case of $N_{\mathrm{f}} = 1$ the equivalent circuit is similar to the ones used by Pavlov *et al.* (2005) and Corsi *et al.* (2007) to simulate the signal for a single fired cell in a SiPM.

In addition to the possibility to simulate signals for more than one fired cell, the circuit presented in Figure 2.1 also differs from the latter two models in the way in which the signal charge is generated. Pavlov and Corsi both employ a current source, whilst in the present work the avalanche following a breakdown event is modeled by the voltage source V_{br}, the resistor R_{S}, and a switch. This is in accordance with the works by Haitz (1964) and Cova *et al.* (1996), which deal with breakdown events in individual diodes, rather than arrays of GM-APDs in a SiPM.

The switch is implemented such that it closes at a preset time t_0 marking the start of a breakdown event. The switch then monitors the microplasma current I_{D} through the diode (i.e. through R_{D} and V_{br}) and opens if I_{D} drops below a predefined threshold current $I_{\mathrm{q,Nf}}$, thus quenching the avalanche. $I_{\mathrm{q,Nf}}$ is determined by the average quenching current of an individual microcell I_{q} and the number of fired cells:

$$I_{\mathrm{q,Nf}} = I_{\mathrm{q}} \cdot N_{\mathrm{f}}. \quad (2.2)$$
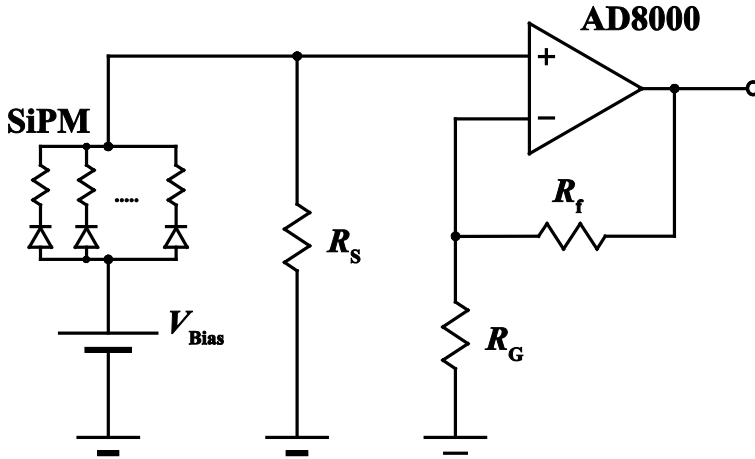
Figure 2.2. Simplified diagram of the circuit used in the simulations and experiments. The circuit includes a voltage source V_{Bias} for SiPM biasing, the shunt resistor R_S, and a preamplifier based on the AD8000 opamp. Note that in this configuration V_{Bias} has to be negative to ensure that the SiPM is reverse biased.

2.2.2.   Simulations

All electronic simulations in this work were performed with LTspice[1], a circuit simulation engine based on Berkeley SPICE 3f4[2]. In a first simulation aimed at the direct comparison of simulated and measured pulse traces, a transient analysis was performed on the circuit shown in Figure 2.2. This circuit consists of the SiPM model discussed in section 2.2.1, a shunt resistor R_S, and a preamplification stage. The values of the shunt resistor and the resistors that determine the amplifier gain (R_f and R_G in Figure 2.2), as well as the operational amplifier (opamp) type (AD8000 from Analog Devices) were chosen to match the ones used in the present experiments (see section 2.2.3). A SPICE model for the AD8000 opamp is available from the manufacturer. The model parameters for the SiPM electronic model were determined in separate experiments as described in section 2.2.4.

The influence of the shunt resistor R_S and the microplasma series resistance R_D on the SiPM signal was investigated in a second set of simulations. Here, the amplifier was omitted to exclude its potential influence on the signal (e.g. due to its finite bandwidth) and the signal charge was determined directly from the integral of the current through R_S.

---

[1] Linear Technology Corporation 2009;
   http://www.linear.com/designtools/software/#LTspice
[2] EECS, University of California, Berkeley 1993;
   http://bwrc.eecs.berkeley.edu/Classes/icbook/SPICE/

In a third series of simulations, performed to derive the transfer function of a single cell, the switch was removed from the SiPM model and the voltage source was replaced by an ideal current source generating an AC signal. AC analyses in the frequency range between 100 kHz and 1 GHz were performed for different values of the shunt resistor R_S. Again, no amplifier was included. The -3dB points were determined by linear interpolation between the two data points just above and below the -3dB level. The error margin for this procedure is estimated as the distance between these two data points.

2.2.3. Experimental Setup

All experiments were performed with two different SiPMs, viz. the MPPC-S10362-11-25u and the MPPC-S10362-33-25c by Hamamatsu Photonics K.K. (denoted as MPPC-11 and MPPC-33, respectively, in the remainder of this work). The SiPMs were operated at 21°C and at a bias voltage of V_{Bias} = -71.10 V in the case of the MPPC-11 and V_{Bias} = -68.82 V in the case of the MPPC-33. These are the operating voltages recommended by the manufacturer, corresponding to 2.30 V (MPPC-11) and 1.52 V (MPPC-33) over breakdown (often also denoted as over-voltage). The dark count rates f_d, measured under these conditions are 250 kHz for the MPPC-11 and 2.2 MHz for the MPPC-33. f_d is defined here as the frequency of occurrence of a pulse with a peak height of least 0.5 times the average single cell signal. The cross talk and after pulsing probability at these conditions are reported to be 0.1% and 30%, respectively (Yamamoto *et al.* 2007).

The setup used to determine the SiPM response to ps laser pulses is shown in Figure 2.3. A SiPM was illuminated with a Hamamatsu PLP-04 laser (average pulse duration 50 ps, 10 kHz repetition rate). The laser light was fed via a fiber optic cable into a dark box. The diameter of the laser spot at the SiPM position was about 2 cm. The intensity of the light was regulated with neutral density filters. A 30%-to-70% beam splitter was used to couple a photodiode into the beam for monitoring the laser intensity.

The SiPM current was converted by a shunt resistor R_S into a voltage that was subsequently amplified by a high-bandwidth voltage amplifier (made in-house on the basis of the AD8000 current feedback opamp, see Figure 2.2). This circuit layout was chosen because it allows for easy control of the impedance seen by the SiPM. The amplifier gain was adjusted to achieve similar output amplitudes with the two shunt resistors used in this work (287 V/A for R_S = 50 Ω and 295 V/A for R_S = 100 Ω, respectively). The amplified signals were sampled using an Aqciris DC282 fast 10-bit digitizer at a sampling rate of 8 GS/s. The digitizer and the pulsed laser were simultaneously triggered by an external clock generator. Since both the amplifier gain and the value of R_S were known, the signal charge could be determined from the integral of the recorded trace. The time window for the integration Δt_i was chosen to match the SiPM pulses (Δt_i = 40 ns for MPPC-11 and R_S = 50 Ω; Δt_i = 60 ns for MPPC-11 and R_S = 100 Ω; Δt_i = 120 ns for MPPC-33 and R_S = 50 Ω; and Δt_i = 210 ns for MPPC-33 and R_S = 100 Ω).
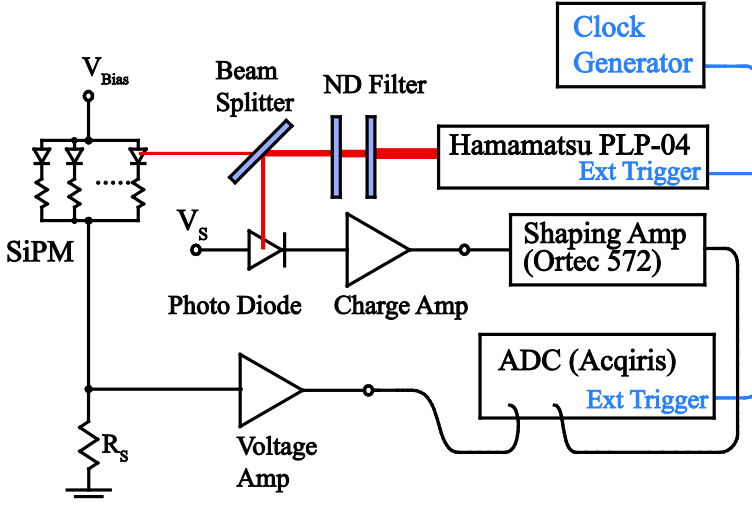
Figure 2.3. The setup used to record the SiPM response to ps laser pulses. The reverse biased SiPM (V_{Bias} = -71.10 V for MPPC-11 and V_{Bias} = -68.82 V for MPPC-33) is illuminated with attenuated laser pulses. The signal is recorded over the shunt resistor R_S and digitized with a fast digitizer. Further details are given in the text.

In experiments in which the laser intensity was of interest, the signal of the abovementioned photodiode was shaped using an Ortec 572A shaping amplifier (shaping time 500 ns, gain 25) and the shaped signal was digitized simultaneously with the SiPM signal using the same digitizer. In these cases the sample rate for both signals was reduced to 4 GS/s.

2.2.4. Determination of the Model Parameters

The input parameters for the model described in section 2.2.1 were determined for each of the two SiPMs. Since the total number of microcells is known for both devices (1600 for the MPPC-11 and 14400 for the MPPC-33, respectively), the value of R_q can readily be obtained from the IV-curve of the forward-biased SiPM.

The sum of the two capacitors C_q and C_D can be determined if the charge Q_C per fired cell and the breakdown voltage V_{br} are known (Cova *et al.* 1996):

$$Q_C = \frac{R_q}{R_q + R_D}(V_{bias} - V_{br})(C_D + C_q)$$

$$\approx (V_{bias} - V_{br})(C_D + C_q).$$

(2.3)

For a fixed bias voltage, Q_C can be obtained by applying a linear fit to the peak positions in a signal charge histogram recorded at low light intensity (see Figure 2.4 for an example) with the setup described in section 2.2.2. V_{br} can be determined by repeating these measurements at different bias voltages and
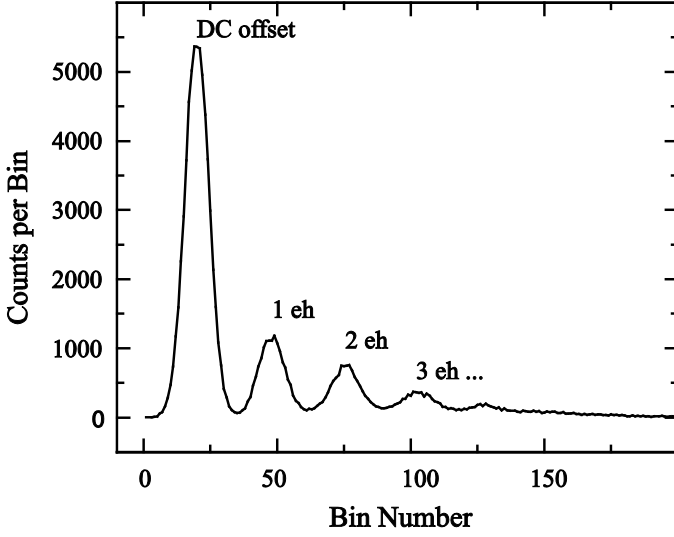
Figure 2.4. Signal charge histogram measured with MPPC-11 at a bias voltage of -71.10 V showing single, double, and triple electron-hole (eh) pair peaks. The bin size is 1.7 fC.

extrapolating $Q_C(V_{br})$ to zero.

A procedure to separate the sum of the capacitances C_D and C_q into its individual components and to determine C_g has been given by Corsi *et al.* (2007). The complex impedance $Z(\omega)$ of the reverse-biased SiPM is measured in a dark box with a precision LCR-meter (Agilent 4282A) at a signal frequency of $\omega = 1$ MHz. Since the bias applied (-40 V) is well below the breakdown voltage, no cells are fired and the equivalent circuit for the SiPM is reduced to the passive (plus parasitic) component with $N_p = N_{tot}$, see Figure 2.1 and equation (2.1). $Z(\omega)$ can then be expressed as

$$Z^{-1}(\omega) = \left(\frac{1}{G_\omega} \| \frac{1}{i\omega C_\omega} \right)^{-1} = G_\omega + i\omega C_\omega$$

$$= \left[\left(R_{q,Np} \| \frac{1}{i\omega C_{q,Np}} + \frac{1}{i\omega C_{D,Np}} \right) \| \frac{1}{i\omega C_g} \right]^{-1},$$

(2.4)

where G_ω and C_ω are the measured parallel conductance and capacitance of the SiPM, respectively, at the signal frequency ω. Equation (2.4) can be rewritten to derive the following expressions[3] for C_D and C_g:

---

[3] The equations for C_D and C_g published by Corsi *et al* (2007) contain two errors. Firstly the denominator under the square root in equation (2.5) contains R_q^2 instead of R_q, which would leave this equation with unbalanced units. Secondly the sign of the last term in equation (2.6) is reversed.

$$C_D = \sqrt{\frac{1 + \omega^2 (C_D + C_q)^2 R_q^2}{\omega^2 N_{tot} R_q}} \cdot G_\omega \quad \text{and} \tag{2.5}$$

$$C_g = C_\omega - N_{tot} C_D + \frac{\omega^2 C_D{}^2 R_q^2 N_{tot} (C_D + C_q)}{1 + \omega^2 R_q^2 (C_D + C_q)^2}. \tag{2.6}$$

2.3. Results and Discussion

2.3.1. SiPM Model Parameters

The model parameters determined for MPPC-11 and MPPC-33 are summarized in Table 2.1. The measured capacitance of the individual diodes and the quench resistors' stray capacitance are similar for the two SiPMs investigated. This is expected, as the pitch between the microcells and the area of the diodes are the same for both devices. However, the nine times larger total area of MPPC-33 results in a parasitic capacitance much larger than that of MPPC-11.

A value for the average quenching current I_q is not readily available through measurement on a SiPM. Yet, a reasonable estimate can be made based on the quench resistor values and the voltage over breakdown V_{ob} during normal operation of the device. After an avalanche is triggered, the initially large microplasma current will drop and approach an asymptotic value I_f due to the presence of the quench resistor (Cova *et al.* 1996):

$$I_f = \frac{V_{ob}}{R_q + R_D} \approx \frac{V_{ob}}{R_q}, \tag{2.7}$$

where the approximation is justified since R_q typically has a value of several hundred kΩ while R_D lies within the range between 500 Ω and a few kΩ (Cova *et al.* 1996).

For the operation of a SiPM it is imperative, that every avalanche is quenched properly and therefore R_q must be chosen such that I_f is well below I_q. On the other hand, R_q should be chosen as small as possible to ensure fast recovery times. Therefore I_q should be larger, but not much larger than If in a properly designed SiPM. Using the values presented in Table 2.1, If can be calculated to be 13 µA for the MPPC-11 and 6 µA for the MPPC-33. Based on these values, I_q was set to 30 µA. This value was chosen for both detectors, since the individual GM APDs that compose the two devices should essentially be the same.

The determination of the microplasma series resistance R_D poses a similar problem. Since a direct measurement of the voltage drop over a diode within an individual microcell is not feasible, the only remaining possibility is a determination from the signal rise time τ_r, via the relation (Cova *et al.* 1996):

Table 2.1. Summary of the model parameters determined experimentally for MPPC-11 and MPPC-33. The Error margins indicate 95% confidence intervals.

		MPPC-11	MPPC-33
V_{br}	(V)	68.8 ± 1.5	67.3 ± 0.9
C_D	(fF)	15.0 ± 1.2	15.4 ± 0.4
C_q	(fF)	4.3 ± 1.2	3.4 ± 0.4
R_q	(kΩ)	179 ± 1	268 ± 2
C_g	(pF)	7.5 ± 1.9	59 ± 5
R_d	(kΩ)	1	1
I_q	(μA)	30	30

$$\tau_r = (C_{D,Nf} + C_{q,Nf}) \cdot \frac{R_{D,Nf} \cdot R_{q,Nf}}{R_{D,Nf} + R_{q,Nf}} = (C_D + C_q) \cdot \frac{R_D \cdot R_q}{R_D + R_q}$$

$$\approx (C_D + C_q) \cdot R_D. \tag{2.8}$$

There are, however, additional factors influencing the rise time of the measured signal, such as the finite bandwidth of the amplifier and the digitizer as well as inductances in the signal chain, which prevent a direct extraction of the value of R_D. For all matters discussed in this work, however, the influence of R_D is very small. Figure 2.5 illustrates that varying R_D within a range of 500 Ω to 5 kΩ has only very little effect on the simulated signal shape. This also underlines the difficulty of determining R_D from a measured signal. In Figure 2.6 the signal charge obtained from the simulated data, using $N_f = 1000$ for MPPC-11 and $N_f = 5000$ for MPPC-33, is plotted as a function of R_D. The output signal charge is expressed in terms of the equivalent number of fired cells N_f^e, defined as the ratio of the total signal charge and the charge due to a single firing microcell. Also in this figure, the change with R_D is small, compared to the deviation of the measured N_f^e from N_f with increasing shunt resistor R_S. The latter effect will be discussed later on in this paper. In the remaining simulations presented in this work a value of 1 kΩ was assumed for R_D.

2.3.2.   Comparison of Simulations and Measured Data

Figure 2.7 and Figure 2.8 show some experimentally recorded traces for different combinations of SiPMs and shunt resistors and for different laser intensities. These are compared to traces simulated for the same conditions and with N_f matching the equivalent number of fired cells obtained from the pulse integral of the corresponding measured trace. The figures show that both pulse height and pulse shape are reproduced well by the simulations, especially around the initial decay of the pulses. These parts of the traces are governed by the low-pass characteristics of the circuit formed by the combination of the SiPM and the shunt resistor R_S.
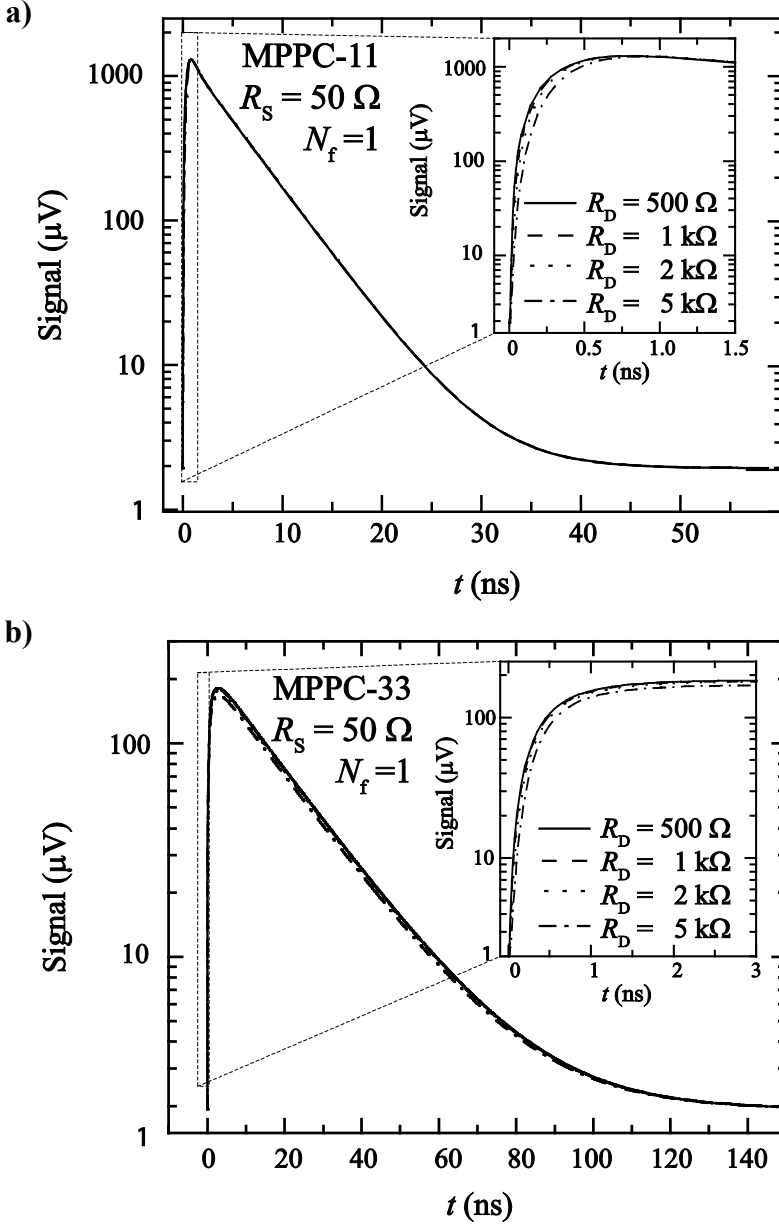
Figure 2.5. Simulated signal as a function of the microplasma series resistance. For both devices, the MPPC-11 (a) and the MPPC-33 (b), the observed changes are marginal when varying R_D from 500 Ω to 5 kΩ. The insets show the initial parts of the pulses.

a)

b)

Figure 2.6. Equivalent number of fired cells N_f^e obtained from the simulated data, for a true number of fired cells N_f = 1000 for MPPC-11(a) and for N_f = 5000 for MPPC-33 (b), as a function of R_D.

The -3dB point of this low pass filter can be obtained from the simulated transfer function of the circuit (SiPM model plus R_S). The time constant τ_{-3dB} corresponding to the frequency at the -3dB point f_{-3dB} then corresponds very well to the pulse decay times τ_d obtained by fitting an exponential function to the measured curve (see Table 2.2). The error margins for τ_d were estimated from the 95% confidence intervals of the fits to the measured data.

Starting from about 20 ns – 50 ns after the light pulse, however, the measured traces start to deviate from the predicted ones. This can be attributed to afterpulsing of some of the fired cells, which is not taken into account by the simulations and which leads to the observed slower decay.

A slight mismatch also remains in the rising edges, which, in all measurements, is somewhat slower than predicted by the simulations (see Table 2.3). There are a number of potential reasons for this mismatch. One possibility is the presence of inductances in the signal chain which limit the bandwidth of the overall circuit. Simulations with a modified SiPM model show that an inductance of a few nH in series with the SiPM could already decrease the rise time to the observed value. A second possible reason is that differences between the signal transient times of different microcells could lead to an increase in the effective signal rise time, as the signals from many fired cells are being summed. These differences, however, are expected to be in the order of a few hundred ps due to the relatively small dimensions of the devices and are therefore expected to be too small to be the sole reason for the observed increase in rise time. Thirdly, also the choice of R_D has some influence on the simulated signal rise times. However, this influence is small for a large range of resistor values (see Figure 2.6).

Table 2.2. Comparison of the measured SiPM signal decay time τd and the characteristic time constants associated with the -3dB points in the SiPM signal transfer functions.

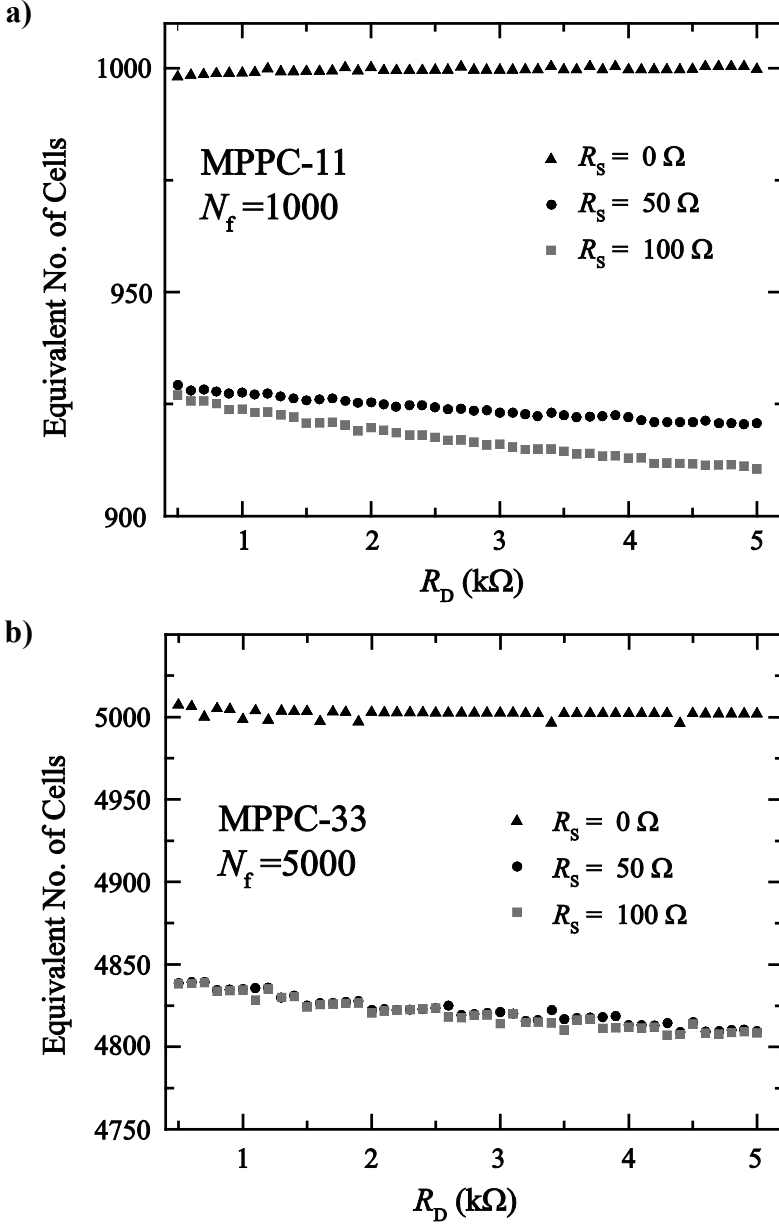|		MPPC-11		MPPC-33	
		R_S=50 Ω	R_S=100 Ω	R_S=50 Ω	R_S=100 Ω
τ_d	(ns)	4.66 ± 0.12	5.92 ± 0.16	18.55 ± 0.20	34.13 ± 0.16
f_{-3dB}	(MHz)	34.52 ± 0.08	26.50 ± 0.07	8.95 ± 0.022	5.03 ± 0.012
τ_{-3dB}	(ns)	4.61 ± 0.011	6.00 ± 0.016	17.78 ± 0.05	31.66 ± 0.08

Table 2.3. Comparison of the 10%-90% rise time obtained from the measured data (t_{m10-90}) and from the simulated traces (t_{s10-90}).

		MPPC-11		MPPC-33	
		R_S=50 Ω	RS=100 Ω	R_S=50 Ω	R_S=100 Ω
t_{m10-90}	(ns)	1.2 ± 0.2	1.2 ± 0.2	2.0 ± 0.2	2.2 ± 0.2
t_{s10-90}	(ns)	0.4 ± 0.05	0.5 ± 0.05	1.2 ± 0.05	1.4 ± 0.05
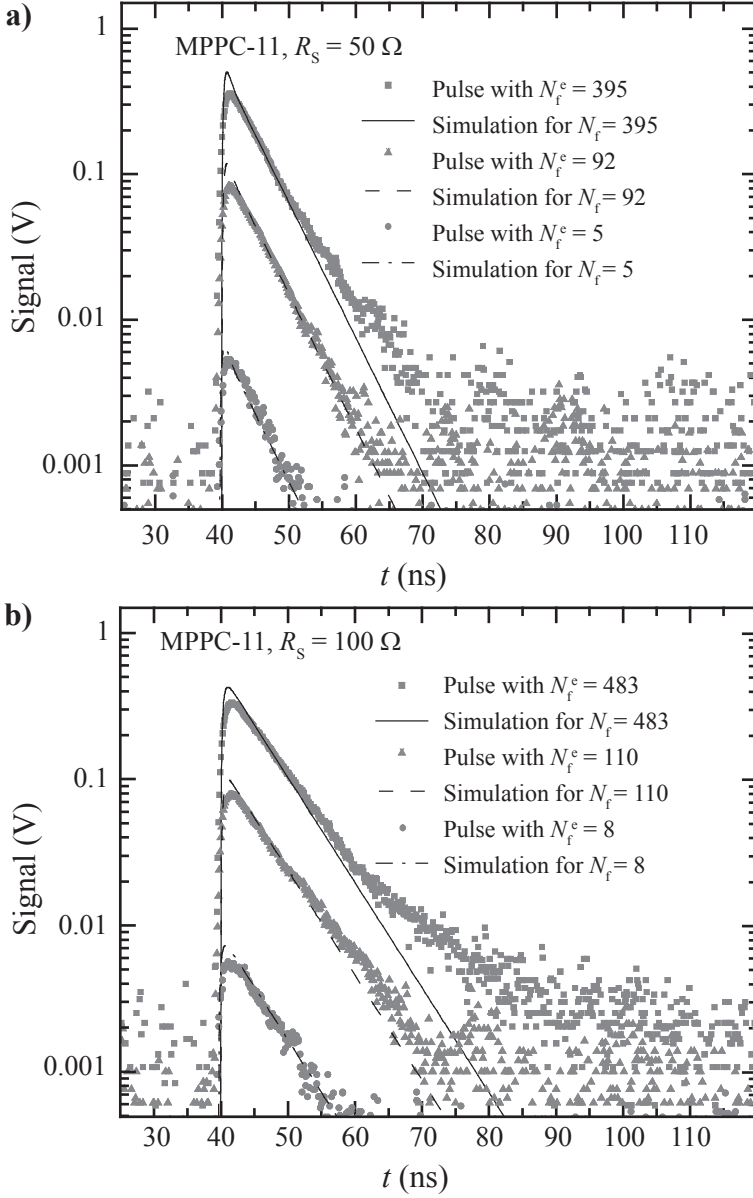
Figure 2.7. Examples of simulated and measured pulse traces of the MPPC-11 in combination with different shunt resistors: $R_S = 50\ \Omega$ (a), and $R_S = 100\ \Omega$ (b). The SiPM was illuminated with ~50 ps laser pulses of different intensity. The equivalent number of fired cells was calculated from the pulse integrals and the single cell gain.
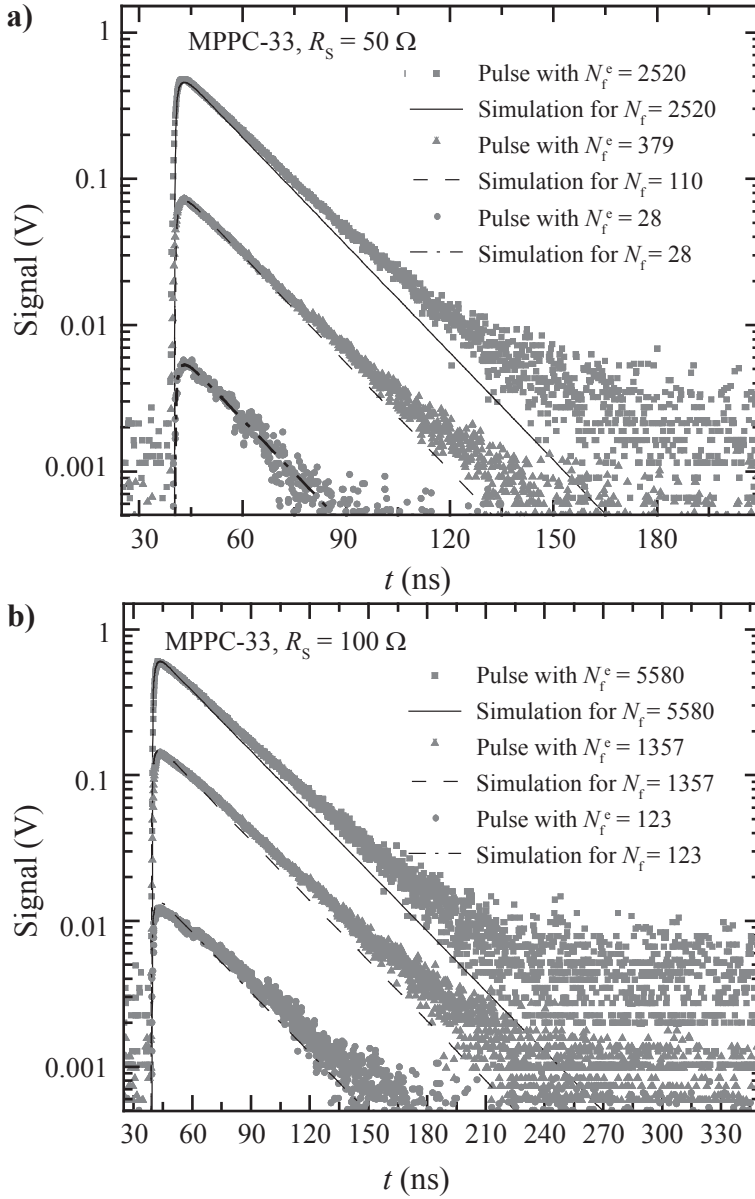
Figure 2.8. Examples of simulated and measured pulse traces of the MPPC-33 in combination with different shunt resistors: $R_S = 50\,\Omega$ (a), and $R_S = 100\,\Omega$ (b). The SiPM was illuminated with ~50 ps laser pulses of different intensity. The equivalent number of fired cells was calculated from the pulse integrals and the single cell gain.
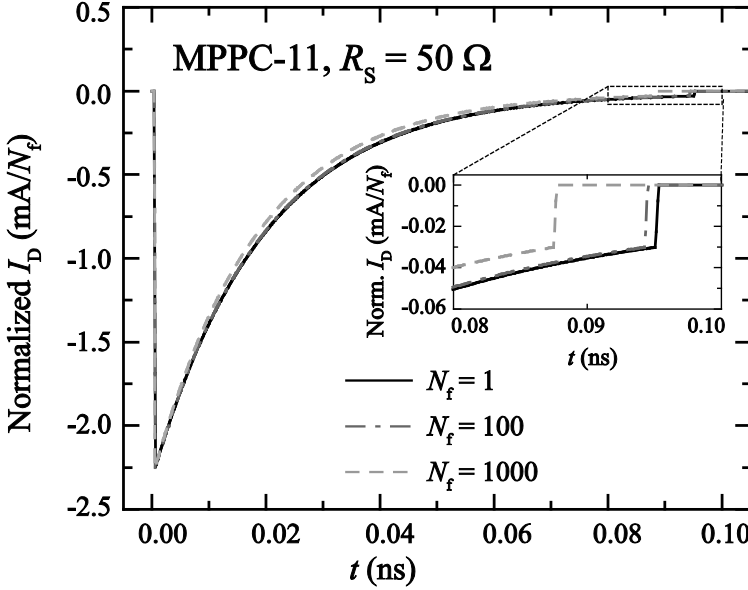
Figure 2.9. Simulated microplasma current I_D for different N_f. I_D is normalized to N_f. The inset depicts a zoom on the tail of the pulses, where the avalanches are quenched.

A further prediction of the model concerns the signal generation. The parallel combination of firing microcells leads to a decrease of both $R_{q,Nf}$ and $R_{D,Nf}$ with increasing number of fired cells. Since both resistors decrease at the same rate, the ratio between $R_{D,Nf}$ and the quench resistor also remains constant, as long as the load impedance is zero. This, however, changes, when the resistor R_S is added in series. Now, an increase in the number of fired cells changes the ratio between $R_{D,Nf}$ and the effective quench resistor $R_{q,Nf} + R_S$. The resulting effect is the same, as if the quench resistor of the individual cells was increased. The result is an earlier average quenching time. This is illustrated in Figure 2.9, where the normalized microplasma current I_D is shown for an increasing number of fired cells.

It should be noted, that the time constant associated with the decay of the avalanche current is mainly determined by R_D (since $R_{D,Nf} \ll R_{q,Nf} + R_S$ remains true, also for larger N_f). Therefore, it may not be immediately obvious why the quenching threshold should be reached earlier as N_f increases. The answer lies in the fact that the avalanche current does not decay to zero but to the asymptotic value given in equation (2.7), which is governed by the quench resistor value. As the quench resistor effectively increases, this asymptotic value decreases, and since the avalanche decays towards a lower asymptotic value, it reaches the quenching threshold on average earlier.

The decrease of the average quenching time with increasing N_f decreases the charge per fired cell and, therefore, the signal is no longer proportional to N_f.

This behavior is illustrated in Figure 2.10, which shows the simulated output signal as a function of the number of fired cells for different shunt resistor values R_S. Both SiPMs exhibit a distinct deviation from proportionality if the input impedance of the front-end electronics is not zero. This electronic non-proportionality is most pronounced for MPPC-11: at 1000 fired cells and with $R_S = 50\ \Omega$ the deviation is 7%, compared to only 1% for MPPC-33 under the same conditions.

This difference between the two SiPMs is examined in more detail in Figure 2.11, in which the equivalent number of fired cells N_f^e is plotted against R_S for a fixed number of fired cells ($N_f = 1000$). For both SiPMs, N_f^e decreases quickly as R_S is increased above zero, until an asymptotic value is approached. In Figure 2.11.a) it is apparent that this happens at much lower R_S for MPPC-33 than for MPPC-11. One cause of this difference is the difference in total SiPM capacitance. The capacitances of MPPC-11 and MPPC-33 can be estimated from the values given in Table 2.1 to be ~11 pF and ~99 pF, respectively, at high frequencies, and ~32 pF and ~281 pF, respectively, at low frequencies. The SiPM capacitance, however, constitutes a finite impedance at any of the frequencies within the signal spectrum and, since it is in parallel to R_S, this impedance limits the shunt resistor's influence on the quenching process. This can be illustrated by increasing the parasitic capacitance C_g (and thus the total capacitance) in the MPPC-11 model. Figure 2.11.b) shows that this leads to a significant reduction of the observed non-proportionality indeed.

A second reason for the electronic non-proportionality to be more pronounced for MPPC-11 than for MPPC-33 is the fact that MPPC-11 has a smaller quench resistor value R_q (see Table 2.1). This means that, relative to R_q, the increase of the effective quench resistance with N_f is larger if all other conditions are the same. This is demonstrated by changing R_q in the MPPC-11 model from 179 kΩ to 268 kΩ (i.e. the same value as for the MPPC-33). This slightly reduces the electronic non-proportionality. As can be seen in Figure 2.11.b), however, this effect is much smaller than the change due to the added capacitance.

The predicted electronic non-proportionality can also be found in the experimental data. In Figure 2.12 the signals of MPPC-11 (a) and MPPC-33 (b) are plotted against the intensity of the exciting laser pulses for two different shunt resistor values. For each data point in this figure, both the signal charge and the laser pulse intensity were averaged over at least 2000 pulses.

a)

b)
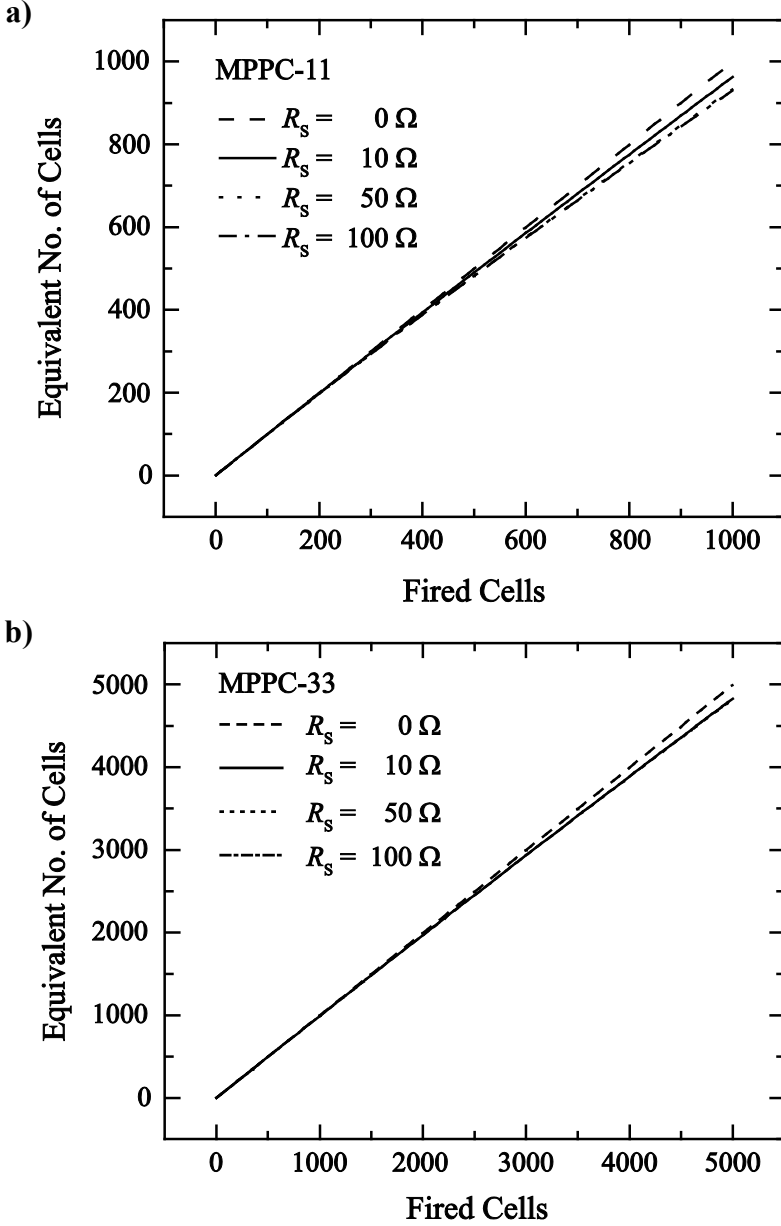
Figure 2.10. Predicted SiPM signal, normalized to the single cell charge, as a function of the true number of fired cells, for (a) MPPC-11 and (b) MPPC-33. Both SiPMs show an increasing deviation of the equivalent number of fired cells from the true value of N_f with increasing N_f. Please note that the lines for $R_S = 50 \ \Omega$ and $R_S = 100 \ \Omega$ overlap in both figures.

a)

b)
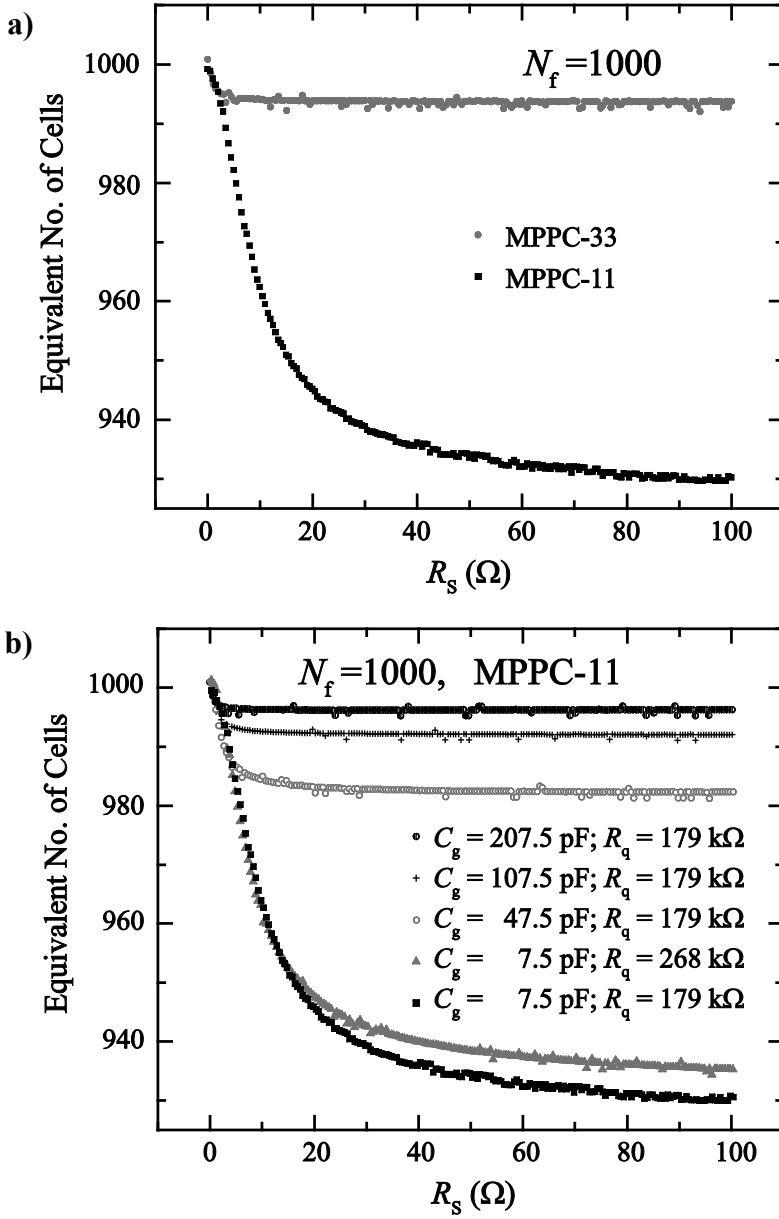
Figure 2.11. SiPM signal, normalized to the single cell charge plotted against R_S for MPPC-11 at a fixed number of 1000 fired cells (a) in comparison to MPPC-33 and (b) as a function of C_g and for two different values for R_q (179 kΩ, corresponding to MPPC-11, and 268 kΩ, corresponding to MPPC-33, respectively).

Unfortunately, the interpretation of these measurements is complicated by the intrinsic non-proportionality of the SiPM response to optical stimulation (Buzhan *et al.* 2001). However, for light pulses of much shorter duration than the GM-APD recharge time a simple statistical model can be used to describe the relationship between the number of fired cells N_f and the intensity of the exciting light pulse (Buzhan *et al.* 2001):

$$N_f = N_{tot}\left[1 - \exp\left(-\frac{\xi \cdot I}{N_{tot}}\right)\right],\tag{2.9}$$

where ξ is the constant of proportionality between the measured laser intensity I and the number of triggered cells, given that all cells are fully charged at the time. It is comprised of the photon detection efficiency of the device, the cross talk probability and a constant of proportionality between I and the number of photons arriving at the sensor. ξ can be determined by fitting this saturation model to the experimental data. Since equation (2.9) does not take into account electronic non-proportionality, the fit was performed using only the data points corresponding to up to 80 equivalent fired cells for MPPC-11 and up to 500 equivalent fired cells for MPPC-33 (as indicated by the dotted circles in Figure 2.12). In this range the calculated electronic non-proportionality is smaller than 0.5% for both detectors.

Extrapolation of these fits (dashed lines in Figure 2.12) shows that the measured signals for both SiPMs and for both shunt resistor values are indeed smaller than would be expected if only optical SiPM saturation were considered. Also the fact that the observed deviation is much stronger for the smaller MPPC-11 with smaller associated capacitance is in agreement with our model. Here it should be noted that the same procedure applied to data obtained with a transimpedance amplifier with very low input impedance yielded good agreement between the extrapolation and the measured data (Seifert *et al.* 2008).

The solid lines in Figure 2.12 depict the correction of the extrapolation of N_f for the electronic non-proportionality, as predicted by the simulations. The graphs indicate that the simulations actually underestimate the magnitude of the electronic non-proportionality. This might be linked, again, to the neglected inductances of the SiPM and of the electronics used in the experiments. Inductances in the signal chain can increase the impedance at signal frequencies, which in return would increase the deviation from proportionality. This is plausible as the impedance seen by the SiPM in the signal frequency band is only a few Ω, so small absolute changes can have a large influence on the observed behavior.
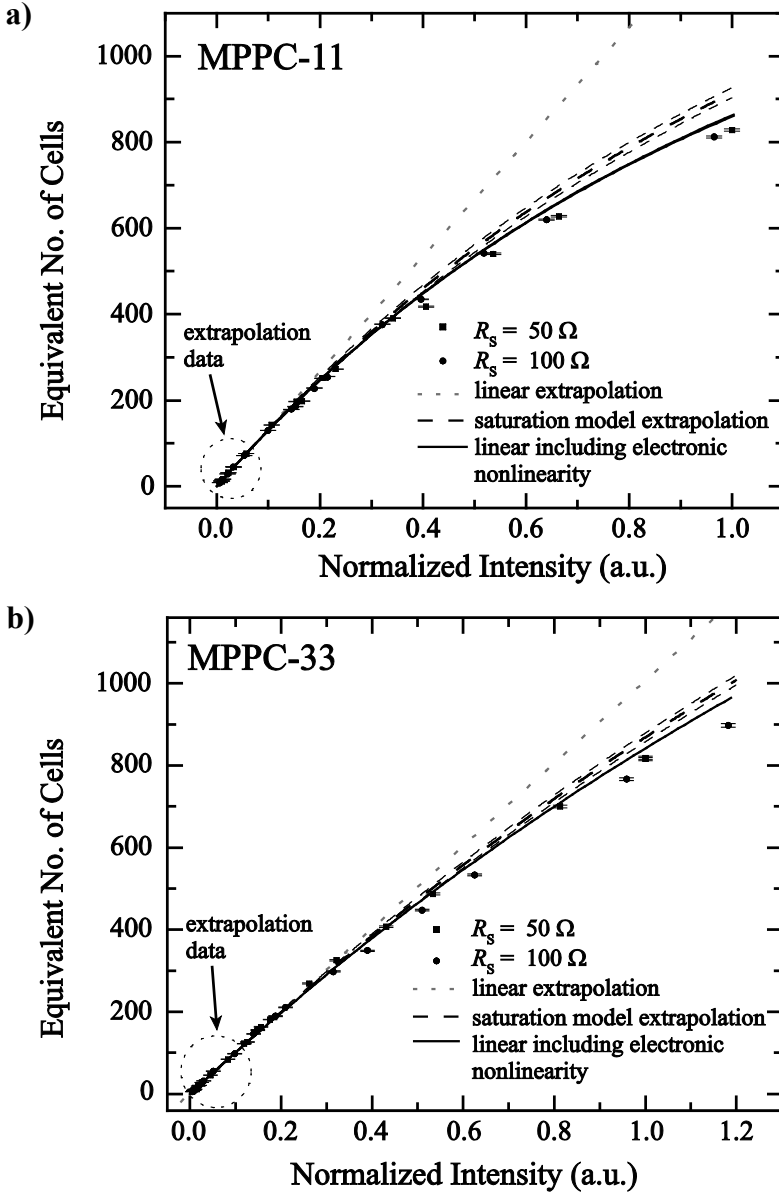
Figure 2.12. Signals of (a) MPPC-11 and (b) MPPC-33 plotted against the relative intensity of the exciting laser pulse. The dotted red line is a linear extrapolation of the data points at the low light intensity. The dashed line constitutes the extrapolation of the SiPM signals below 80 (MPPC-11) and 500 (MPPC-33) equivalent fired cells with the corresponding 95% prediction intervals, taking into account optical SiPM saturation. The solid lines depict the correction of the extrapolated curve for the electronic non-proportionality.

2.4.   Conclusions

An improved electronic model for the simulation of the simultaneous firing of multiple microcells in a SiPM has been introduced in this paper. The necessary model parameters were determined experimentally for two different SiPMs (Hamamatsu S10362-11-25u and Hamamatsu S10362-33-25c). Comparison of simulated and measured signals of these SiPMs was shown to yield excellent agreement.

Furthermore, it has been shown that the model can be an important tool for the interpretation of the SiPM response to instantaneous light pulses and for the development of front-end electronics. This was illustrated by predicting the effect of the preamplifier input impedance on the proportionality of the SiPM signal. The electronic signal was shown to be non-proportional to the number of fired cells unless the preamplifier input impedance equals zero. Again, these predictions were confirmed by experiments.

Although the assumption of simultaneous triggering of the microcells might seem a limitation of the proposed multicell model, its practical use is not necessarily limited to the case of instantaneous excitation. In fact, the model can easily be adapted to simulate the response to a light pulse of finite duration (such as a scintillation pulse). This can be done by placing a number of active subcircuits in parallel and closing the corresponding switches according to a predefined trigger schedule determined by the probabilities of photon arrival and absorption, avalanche triggering, crosstalk and afterpulsing (which can e.g. be obtained by Monte Carlo simulation).

Each of the active subcircuits may represent any number of fired cells, which allows for a grouping of cells that may greatly reduce the necessary number of circuit elements and thus the computational expense of such a simulation. Cells may be grouped if they a) are fired within a small time window (smaller than the avalanching time) and b) are not fired again until they are completely recharged. If the second condition is not met for a given cell, it could be treated as a single cell in order to properly account for the influence of the cell recovery time on subsequent discharges. The realization of such a model and an investigation as to how accurately it predicts recovery times and scintillation pulses is currently in progress.

References

Bondarenko G, Buzhan P, Dolgoshein B, Golovin V, Guschin E, Ilyin A, Kaplin V, Karakash A, Klanner R, Pokachalov V, Popova E and Smirnov K 2000 Limited Geiger-mode microcell silicon photodiode: new results *Nucl Instrum Meth A* **442** 187-192

Burr K C and Wang G C 2007 Scintillation detection using 3 mm x 3 mm silicon photomultipliers *IEEE Nuclear Science Symposium and Medical Imaging Conference (2007 NSS/MIC)* (Honolulu, Hawaii) 975-982

Buzhan P, Dolgoshein B, Ilyin A, Kantserov V, Kaplin V, Karakash A, Pleshko A, Popova E, Smirnov S, Volkov Y, Filatov L, Klemin S and Kayumov F 2001 An advanced study of silicon photomultiplier *ICFA Instumentation Bulletin* **32** 28-42

Buzhan P, Dolgoshein B, Filatov L, Ilyin A, Kantzerov V, Kaplin V, Karakash A, Kayumov F, Klemin S, Popova E and Smirnov S 2003 Silicon photomultiplier and its possible applications *Nucl Instrum Meth A* **504** 48-52

Corsi F, Dragone A, Marzocca C, Del Guerra A, Delizia P, Dinu N, Piemonte C, Boscardin M and Dalla Betta G F 2007 Modelling a silicon photomultiplier (SiPM) as a signal source for optimum front-end design *Nucl Instrum Meth A* **572** 416-418

Cova S, Ghioni M, Lacaita A, Samori C and Zappa F 1996 Avalanche photodiodes and quenching circuits for single-photon detection *Appl Optics* **35** 1956-1976

Dolgoshein B, Balagura V, Buzhan P, Danilov M, Filatov L, Garutti E, Groll M, Ilyin A, Kantserov V, Kaplin V, Karakash A, Kayumov F, Klemin S, Korbel V, Meyer H, Mizuk R, Morgunov V, Novikov E, Pakhlov P, Popova E, Rusinov V, Sefkow F, Tarkovsky E and Tikhomirov I 2006 Status report on silicon photomultiplier development and its applications *Nucl Instrum Meth A* **563** 368-376

Haitz R H 1964 Model for Electrical Behavior of Microplasma *J Appl Phys* **35** 1370-&

Otte A N, Barral J, Dolgoshein B, Hose J, Klemin S, Lorenz E, Mirzoyan R, Popova E and Teshima M 2005 A test of silicon photomultipliers as readout for PET *Nucl Instrum Meth A* **545** 705-715

Pavlov N, Maehlum G and Meier D 2005 Gamma spectroscopy using a silicon photomultiplier and a scintillator *IEEE Nuclear Science Symposium and Medical Imaging Conference (2005 NSS/MIC)* (Puerto Rico) 173-180

Seifert S, Schaart D R, van Dam H T, Huizenga J, Vinke R, Dendooven P, Löhner H and Beekman F J 2008 A High Bandwidth Preamplifier for SiPM-Based TOF PET Scintillation Detectors *IEEE Nuclear Science Symposium and Medical Imaging Conference (2008 NSS/MIC)* (Dresden) 891-894

Uozumi S 2007 Study and Development of Multi Pixel Photon Counter for the GLD Calorimeter Readout *Proc. Int. workshop on new photon-detectors (PD07)* (Kobe, Japan) 022

Wangerin K A, Wang G C, Kim C and Danon Y 2008 Passive Electrical Model of Silicon Photomultipliers *IEEE Nuclear Science Symposium and Medical Imaging Conference (2008 NSS/MIC)* (Dresden) 4172-4179

Yamamoto K, Yamamura K, Sato K, Kamakura S, Ota T, Suzuki H and Ohsuka S 2007 Development of multi-pixel photon counter (MPPC) *IEEE Nuclear Science Symposium and Medical Imaging Conference (2007 NSS/MIC)* (Honolulu, Hawaii) 1511-1515

3 LaBr₃:Ce and SiPMs for Time-of-Flight PET: Achieving 100 ps Coincidence Resolving Time

Abstract - The use of time-of-flight (TOF) information in positron emission tomography (PET) enables significant improvement in image noise properties and, therefore, lesion detection. Silicon photomultipliers (SiPMs) are solid-state photosensors that have several advantages over photomultiplier tubes (PMTs). SiPMs are small, essentially transparent to 511 keV gamma rays, and insensitive to magnetic fields. This enables novel detector designs aimed at e.g. compactness, high resolution, depth-of-interaction (DOI) correction, and MRI-compatibility. The goal of the present work is to study the timing performance of SiPMs in combination with LaBr₃:5%Ce, a relatively new scintillator with promising characteristics for TOF-PET. Measurements were performed with two, bare, 3 mm × 3 mm × 5 mm LaBr₃:5%Ce crystals, each coupled to a 3 mm × 3 mm SiPM. Using a ²²Na point source placed at various positions in between the two detectors, a coincidence resolving time (CRT) of ~100 ps FWHM for 511 keV annihilation photon pairs was achieved, corresponding to a TOF positioning resolution of ~15 mm FWHM. At the same time, pulse height spectra with well-resolved full-energy peaks were obtained. To our knowledge this is the best CRT reported for SiPM-based scintillation detectors to date. It is concluded that SiPM-based scintillation detectors can provide timing resolutions at least as good as detectors based on PMTs.

3.1.   Introduction

The use of time-of-flight (TOF) information in positron emission tomography (PET) has recently been demonstrated to enable significant improvement in image noise properties and, therefore, lesion detection, especially in heavier patients (Kuhn *et al.* 2006, Moses 2007, Surti *et al.* 2007, Kadrmas *et al.* 2009). This warrants further research into TOF-capable PET scintillation detectors, in particular with the aim to obtain better timing resolution.

The relatively new inorganic scintillator $LaBr_3$:Ce has high potential for TOF-PET (Kuhn *et al.* 2006). Commercial-grade $LaBr_3$:5%Ce has a fast decay time of ~16 ns (Bizarri and Dorenbos 2007), a high light yield of ~70.000 photons/MeV (de Haas and Dorenbos 2008), an excellent energy resolution of ~2.6% FWHM at 662 keV (Drozdowski *et al.* 2007), a mass density of 5.1 g cm-3 (Higgins *et al.* 2006), and an effective atomic number of 46.9 (van Eijk 2002). To optimally benefit from the advantages of $LaBr_3$:Ce in a PET detector, the scintillation light should be read out using a photosensor with fast response and high photodetection efficiency (PDE) at the $LaBr_3$:Ce emission wavelengths (~380 nm).

Excellent coincidence resolving times (CRTs) have already been demonstrated with $LaBr_3$:Ce crystals of various dimensions and Ce concentrations, coupled to fast photomultiplier tubes (PMTs) (Kuhn *et al.* 2005 , Glodo *et al.* 2006, Kyba *et al.* 2008). However, silicon photomultipliers (SiPMs) are turning into a promising alternative for PMTs as of recently (Antich *et al.* 1997, Bondarenko *et al.* 2000, Golovin and Saveliev 2004, Britvitch *et al.* 2007, Herbert *et al.* 2007, McElroy *et al.* 2007, Musienko *et al.* 2007, Renker 2007, Yamamoto *et al.* 2007, Lewellen 2008). Similar to PMTs, SiPMs have a gain in the order of ~106. In addition, these solid-state devices are much more compact and essentially transparent to 511 keV gamma rays. This enables novel detector designs aimed at, for example, compactness, high resolution, depth-of-interaction (DOI) correction, etc. (España *et al.* 2008, Llosá *et al.* 2008, Schaart *et al.* 2008a, Shibuya *et al.* 2008, Song *et al.* 2008, Kolb *et al.* 2008 , Schaart *et al.* 2009, Pestotnik *et al.* 2010). Moreover, in contrast with PMTs, SiPMs are compatible with magnetic fields, a feature that is very interesting in light of recent endeavours to combine PET and MRI into hybrid imaging devices (Shao *et al.* 1997, Catana *et al.* 2006, Judenhofer *et al.* 2008, Townsend 2008).

The goal of the present work is to study the timing performance of commercially available, 3 mm × 3 mm SiPMs in combination with $LaBr_3$:5%Ce for TOF-PET. We use relatively small $LaBr_3$:5%Ce crystals to minimize time walk due to the variation of photon path lengths with the position-of-interaction. However, when using larger crystals one may attempt to achieve similarly good timing resolution by applying a position-of-interaction correction to the timing information (Moses and Derenzo 1999, Shibuya *et al.* 2008, Vinke *et al.* 2008, 2010).

3.2. **Materials and Methods**

3.2.1. **Detectors**

Measurements were performed with two, identical, SiPM-based scintillation detectors. In each detector a bare, 3 mm × 3 mm × 5 mm LaBr$_3$:5%Ce crystal (Saint-Gobain BrilLanCe 380) was enclosed in a reflective casing made from Spectralon, a PTFE-based material with a reflectivity specified to be better than 98% at 380 nm, i.e., the wavelength of maximum emission of LaBr$_3$:5%Ce. A 3 mm × 3 mm SiPM (Hamamatsu MPPC-S10362-33-050C) was coupled directly to each of the LaBr$_3$:Ce crystals using a transparent silicone encapsulation gel (Lightspan LS-3252). Each SiPM consists of an array of 3600 self-quenched Geiger Mode Avalanche Photodiodes at a pitch of 50 μm. Both SiPMs were operated at ~2.0 V above their breakdown voltages, which were measured to be ~69.7 V and ~70. V, respectively. All experiments were performed at room temperature and in a dry atmosphere to protect the hygroscopic LaBr$_3$:Ce crystals.

3.2.2. **Measurement setup**

Figure 3.1 shows a schematic representation of the measurement setup. The two detectors and a ^{22}Na point source (Isotope Products Laboratories, active volume $\varnothing$ 0.5 mm ×1 mm) were mounted on an optical rail, such that the source could be placed at various positions x in between the two detectors.

The SiPM charge pulses were converted to voltage pulses by means of 15 Ω shunt resistors and fed into voltage preamplifiers made in-house. Each preamplifier consisted of two, cascaded amplification stages, as indicated in Figure 3.1. The first amplification stage (gain ~13) consisted of a Texas Instruments OPA847 opamp in non-inverting configuration with a feedback resistor of 270 Ω and a 22 Ω resistor to ground. The second stage (gain ~5) consisted of an AC-coupled monolithic microwave integrated circuit (MMIC) low noise amplifier (Avago Technologies MGA-61563). Care was taken to minimize the total length of the leads between the SiPM and the preamplifier (< 1 cm).

In the timing experiments, the signals of the first amplification stages were used to obtain a coincidence trigger, by feeding them into LeCroy 825 leading edge discriminators (LEDs) and connecting the discriminator outputs to a LeCroy 465 coincidence unit. The signals of the first amplification stages were also used to determine the two pulse heights of each coincident pulse pair. This was done by feeding these signals into a CAEN N568B multi-channel shaping amplifier (shaping time 100 ns) connected to a CAEN V785 multi-channel, peak-sensitive ADC.

The pulses from the secondary amplification stages of the two preamplifiers were digitized by two, synchronized, Acqiris DC282 fast sampling ADCs. Both ADCs were operated at the maximum sampling rate of 8 GS/s and at 10 bit resolution. The synchronization clock jitter between the two ADCs is specified to be ≤ 1 ps. The trigger for the two synchronized ADCs was provided by the
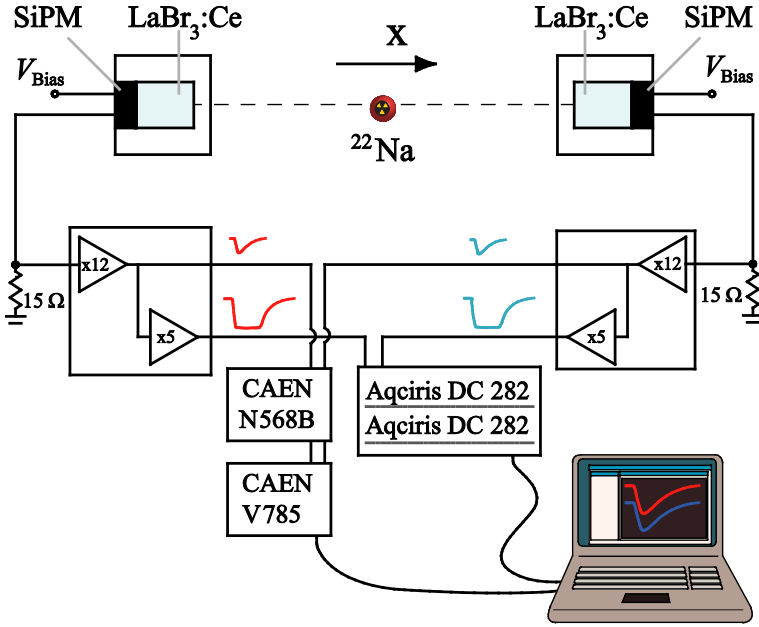
Figure 3.1. Schematic overview of the experimental setup. See text for explanation.

above-mentioned LeCroy 465 coincidence unit. The gain of the secondary amplification stages was chosen such that the ADC input range (set to 500 mV) corresponded to only ~12.5% of the amplitude of a 511 keV pulse. As the optimum trigger threshold for timing lies within this portion of the pulse rising edge, this approach minimizes the contribution of ADC noise to the overall signal-to-noise ratio of the digitized (partial) pulse traces. The traces of each coincident pulse pair were stored in a PC, together with the corresponding pulse heights recorded by the CAEN V785 ADC. The stored data were subsequently used for offline, digital time pickoff as described in section 3.2.3.

Experiments were also performed by irradiating the detectors with a ^{22}Na source and feeding the signals from the first amplification stages of the preamplifiers directly into the Acqiris ADCs, using an ADC input range larger than the maximum pulse amplitude and applying no coincidence condition. About 10^5 full pulse traces thus acquired were stored for offline analysis of the pulse shape and energy content.

3.2.3. Digital time pickoff

A selection of digitized pulse traces for timing analysis was performed using the pulse height information recorded by the CAEN V785 ADCs. Only events with energies between ~490 keV and ~532 keV were accepted, corresponding to the full-width-at-tenth-maximum (FWTM) of the full-energy peak. Time stamps
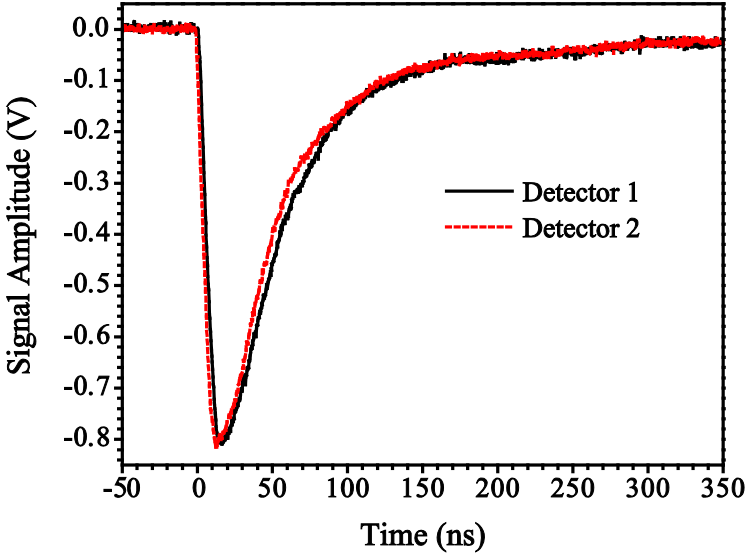
Figure 3.2. Typical digitized pulse traces of the two detectors, measured with 511 keV photons. The average 10% – 90% rise time of the recorded 511 keV pulses equals ~9 ns

were subsequently derived by interpolating each trace with a cubic spline and determining the intersection of the interpolated data with a fixed threshold relative to the baseline, set at ~9 times the pulse height of a single photon pulse. The baseline was determined for each trace individually as the average signal in the region between ~1.2 ns and ~0.2 ns before the onset of the pulse.

3.3. Results

3.3.1. Pulse shape

Figure 3.2 shows some typical examples of 511 keV pulse traces from the two detectors. These were obtained by feeding the outputs of the first amplification stages of the preamplifiers directly into the Acqiris DC282 ADCs. The average 10% - 90% rise time of the pulses in the full-energy peak equals ~9 ns. As the pulse shape equals the convolution of the scintillation light pulse and the SiPM response, the rise time is primarily determined by the low pass (i.e. integrating) characteristics of the SiPM and the scintillation decay time. The influence of the high-bandwidth preamplifiers and other electronics on the pulse rise time is expected to be negligible in our measurements.

3.3.2. Timing spectra

Figure 3.3 shows the timing spectra obtained with the [22]Na point source located at positions x_1 = -20 mm ± 0.25 mm (green diamonds), x_2 = 0 mm ± 0.25 mm (black squares), and x_3 = 20 mm ± 0.25 mm (blue circles). These spectra were obtained using the digital time pickoff method described in section 3.2.3,
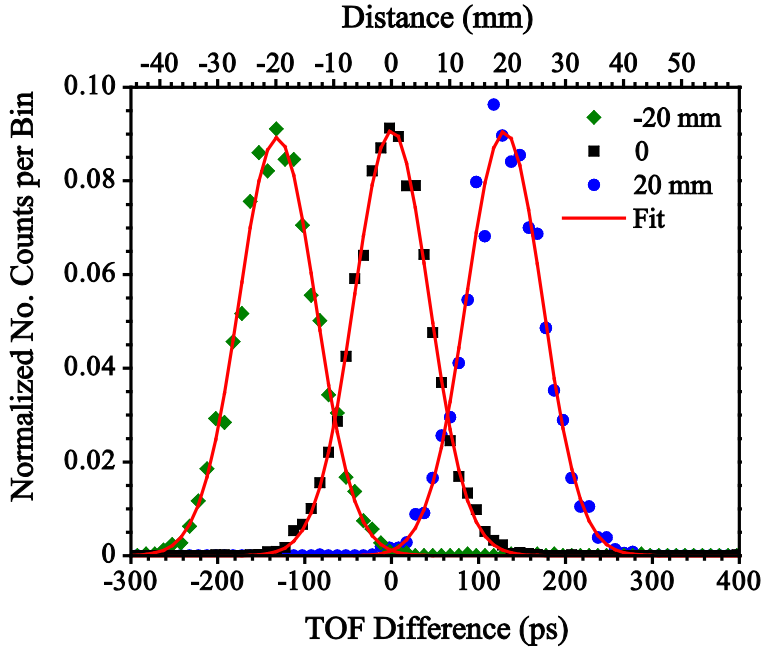
Figure 3.3. Timing spectra recorded with two 3 mm × 3 mm × 5 mm LaBr₃:Ce crystals read out by 3 mm × 3 mm SiPMs, using a ^{22}Na point source located at $x_1 = -20$ mm ± 0.25 mm (green diamonds), $x_2 = 0$ mm ± 0.25 mm (black squares), and $x_3 = 20$ mm ± 0.25 mm (blue circles). The red curves indicate Gaussian fits to the data. The average coincidence resolving time (CRT) equals 101 ps ± 2 ps FWHM, corresponding to 15.1 mm ± 0.3 mm FWHM.

using 3624, 7326, and 3346 coincident events per spectrum, respectively. The FWHM coincidence resolving times (CRTs), determined from Gaussian fits to the data (the red curves in the figure), are 101.8 ps, 99.5 ps, and 103.4 ps for x_1, x_2, and x_3, respectively. The weighted average of these values equals 101 ps ± 2 ps FWHM, corresponding to a TOF positioning resolution of 15.1 mm ± 0.3 mm FWHM.

3.3.3. Pulse height spectra

Figure 3.4 shows the ^{22}Na pulse height spectra measured with both detectors. These were derived by integration of the digitized pulses from the first amplification stages of the preamplifiers. A baseline correction was applied to each pulse before integration. The 511 keV full-energy peaks can be seen to be superimposed on the Compton ridges of the 1275 keV peaks. The latter peaks are relatively small due to the small crystal size.

The observed widths of the 511 keV peaks are ~3.7% FWHM and ~3.2% FWHM for detector 1 and detector 2, respectively. These small widths are partly due to SiPM saturation, as discussed in more detail in section 3.4.3.
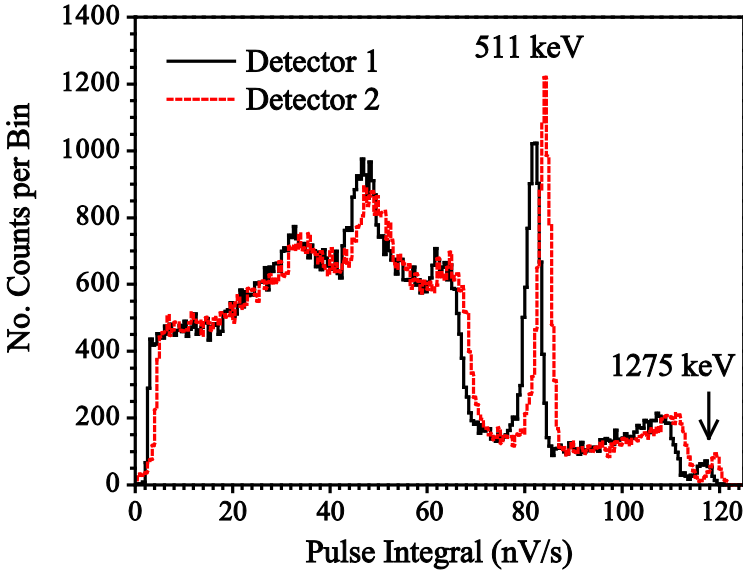
Figure 3.4. Pulse height spectra of the two detectors, measured using a ^{22}Na
source. The observed widths of the 511 keV peaks are ~3.7% FWHM and ~3.2%
FWHM for detector 1 and detector 2, respectively.

Nevertheless, all full-energy peaks are well resolved and can be clearly distinguished from the corresponding Compton ridges.

3.4. Discussion

3.4.1. Timing performance

The above results were achieved using detectors based on 3 mm × 3 mm × 5 mm LaBr$_3$:5%Ce crystals and 3 mm × 3 mm SiPMs. To obtain sufficient system sensitivity, a clinical TOF-PET scanner might, for example, be based on several stacked layers of such detector elements. Alternatively, the detector design might be based on longer crystals. The use of monolithic crystals read out by position-sensitive SiPM arrays may also be considered. While many different detector designs could thus be envisaged, the timing performance is generally expected to deteriorate in larger crystals due to the variation of photon path lengths with the position-of-interaction. Fortunately, it may be possible to at least partly correct for this effect if the position-of-interaction in the crystal is known (Moses and Derenzo 1999, Shibuya *et al.* 2008, Vinke *et al.* 2008, 2010). The results presented here may thus be seen as representing the CRT in principle achievable with LaBr$_3$:5%Ce and 3 mm × 3 mm SiPMs commercially available at the time of writing.

The present work can be compared to results obtained with SiPMs by other authors. Several studies have been performed using LSO:Ce and similar

materials. Some of the best results reported are those from Göttlich *et al.* (2008), who reached a CRT of 460 ps FWHM using two 3 mm × 3 mm × 15 mm lutetium fine silicate (LFS) crystals coupled to the same Hamamatsu SiPMs as the ones used here, those from Burr and Wang (2007), who obtained a CRT of 268 ps FWHM using two 3 mm × 3 mm × 10 mm LYSO:Ce crystals and prototypes of the same SiPMs as used in the present study, and those from Kim *et al.* (2009), who achieved a CRT of 240 ps FWHM using 3 mm × 3 mm × 10 mm LYSO:Ce crystals coupled to the same SiPMs as those used here.

Few studies have so far been performed with LaBr₃:Ce (Schaart *et al.* 2008b), presumably because of the difficulties encountered in using this hygroscopic material. To our knowledge the CRT obtained with LaBr₃:5%Ce in the present work is significantly better than those reported for LSO:Ce, LYSO:Ce, and LFS to date.

It is acknowledged that the performance of a PET scintillator is not only determined by its timing resolution. Compared to LSO:Ce and similar materials, a disadvantage of LaBr₃:Ce is its lower stopping power, giving rise to increased intra- and inter-crystal scattering and requiring thicker detectors to obtain equal detection efficiency. In principle, thicker detectors may give rise to increased parallax errors. However, these can be mitigated by using stacked layers of small detector elements as mentioned above, or by implementing some form of depth-of-interaction (DOI) correction, see e.g. Lewellen (2008) and references therein.

An important advantage of LaBr₃:Ce is its much higher light yield, which is a crucial factor for obtaining high spatial resolution. Moreover, both its superior timing (randoms suppression, TOF) and its excellent energy resolution (scatter rejection) are of great advantage to improve image quality, especially in heavier patients (Daube-Witherspoon *et al.* 2010).

Given the above advantages and disadvantages, it presently is difficult to predict the overall performance of LaBr₃:Ce in comparison to other PET scintillators, especially since the only LaBr₃:Ce-based prototype scanner realized to date (Daube-Witherspoon *et al.* 2010) has not yet been optimized with respect to all of the above factors. In contrast, LSO:Ce and similar materials are used in many commercial systems, most of which have undergone multiple iterations of optimization. Thus, further research into the use of LaBr₃:Ce in TOF-PET is warranted.

3.4.2.   SiPMs vs PMTs

The average 10% – 90% rise time of ~9 ns obtained in this study is relatively large compared to the values typically found with fast PMTs. For example, Kuhn *et al.* (2005) measured a 10% - 90% rise time of ~3 ns for a 4 mm × 4 mm × 30 mm LaBr₃:5%Ce crystal on a Hamamatsu R4998 PMT. In principle, a longer rise time is undesirable as the timing resolution σ_t associated with electronic and sampling noise is equal to the ratio of the noise and the signal slope (Wilmshurst 1985):

$$\sigma_t = \frac{\sigma_v}{\partial v / \partial t} \, , \tag{3.1}$$

where σ_v is the RMS noise voltage and $\partial v / \partial t$ denotes the slope of the pulse leading edge at the point where it crosses the trigger level.

However, the absolute slope $\partial v / \partial t$ is proportional to the photosensor photodetection efficiency. It is not trivial to specify the PDE of the SiPMs used here, since it is a function of bias voltage, temperature, degree of saturation, etc., and varies between individual devices of the same type. However, according to the manufacturer's data sheet[1] it may be as high as ~45% at 380 nm, the wavelength of maximum emission of LaBr$_3$:5%Ce. While it is to be noted that this figure includes contributions from cross-talk and after-pulsing (Du and Retière 2008, Yamamoto et al 2007), it is considerably higher than the quantum efficiency (QE) of, for example, the above-mentioned R4998 PMT, which is estimated to be ~16% at 380 nm from the manufacturer's datasheet[2]. A second advantage of a higher PDE is that a larger number of primary charge carriers per pulse reduces the influence of statistical fluctuations on the timing resolution.

A full analysis of the timing resolution would require additional factors to be taken into account, such as photosensor dark current, transit time spread, etc., but this is left for future publication. Here we merely wish to illustrate that the different characteristics of SiPMs and PMTs make it interesting to compare the timing resolution achieved in this work with those published for PMTs in combination with the same scintillation material.

For example, a CRT of 240 ps FWHM has been measured with two, 4 mm × 4 mm × 30 mm LaBr$_3$:5%Ce crystals coupled to R4998 PMTs (Kuhn *et al.* 2005), while Kyba *et al.* (2008) reported a CRT of 160 ps FWHM for two $\varnothing$13 mm × 13 mm LaBr$_3$:5%Ce crystals coupled to the same PMTs, thereby demonstrating the dependence of CRT on crystal dimensions. A simulation by Kuhn *et al.* (2005) predicts a CRT of ~100 ps FWHM for very small crystals. The dependence of CRT on the time pick-off method was tested by Piemonte *et al.* (2011) by comparing analogue to digital methods. Although it was originally reported that the CRT with digital waveform sampling was superior, further work has since demonstrated that these measurements are sensitive to the assumptions made about the shape of the signal rising edge, and that the timing resolutions obtained with digital and analogue methods are comparable (private communication). Given these results, the present work indicates that SiPM-based scintillation detectors can provide timing resolutions at least as good as those obtained with PMTs.

It is noted that scintillators exist that may provide even better timing resolution than commercial-grade LaBr$_3$:5%Ce. For example, increasing the Ce

---

[1] Hamamatsu Photonics K K, MPPC (Multi-Pixel Photon Counter) S10362 series, S10931 series Cat. No.KAPD1023E03 July 2009 DN http://www.hamamatsu.com

[2] Hamamatsu Photonics K K, 1999 Photomultiplier tube R4998 TPMH1261E02 December 1999 http://www.hamamatsu.com

concentration in LaBr$_3$:Ce to ~30% appears to improve timing resolution significantly (Glodo *et al.* 2005, Kuhn *et al.* 2005). Other materials, such as CeBr$_3$ and LuI$_3$:Ce, are also investigated as candidates for TOF-PET (Shah *et al.* 2004, Shah *et al.* 2005, Glodo *et al.* 2006). Hence, it would be interesting to study the timing performance of SiPMs in combination with LaBr$_3$:Ce(30%) and other promising new materials.

3.4.3.   SiPM saturation

In principle, it might also be possible to further improve the timing resolution by using SiPMs containing fewer but larger microcells, thus improving their fill factor and, therefore, their PDE. However, if the number of microcells would be made too small, this might lead to excessive saturation. Such saturation causes the pulse height spectra of SiPM-based scintillation detectors to increasingly be compressed along the energy axis with increasing gamma energy (Buzhan *et al.* 2001, Stoykov *et al.* 2007). As can be seen from the relative positions of the 511 keV and 1275 keV peaks in figure 4, a significant degree of saturation already occurs in the present experiments. While the excellent energy resolution of LaBr$_3$:Ce already gives rise to a relatively small width of the 511 keV full-energy peaks, this implies that the peak widths observed in Figure 3.4 are additionally reduced by SiPM saturation. From a practical point of view, however, it is important that well-resolved 511 keV full-energy peaks are still obtained. In a clinical PET system, this is crucial for accurate rejection of photons that have undergone Compton scattering in the patient.

It is noted that, in addition to SiPM saturation, the pulse height spectra may in principle also be influenced by electronic non-proportionality (Seifert *et al.* 2008, 2009), this effect is expected to be small in our measurements.

3.5.   Conclusions

The experiments presented here show that SiPM-based scintillation detectors for TOF-PET can provide timing resolutions at least as good as detectors based on conventional PMTs. At the same time, pulse height spectra with well-resolved full-energy peaks can be obtained, which is necessary for accurate rejection of Compton-scattered photons. The use of LaBr$_3$:5%Ce allowed us to achieve a CRT of ~100 ps FWHM for 511 keV annihilation photon pairs, corresponding to a TOF positioning resolution of ~15 mm FWHM. To our knowledge this is the best experimental figure reported for SiPM-based scintillation detectors to date.

It is not unlikely that further optimization of scintillation materials and SiPM technology will lead to even better results in the near future. Given the advantages of SiPMs over PMTs, such as their small size, transparency to 511 keV gamma rays, magnetic field compatibility, etc., we conclude that detectors based on LaBr$_3$:Ce and SiPMs have high potential for use in TOF-PET devices.

Acknowledgements

References

Antich P P, Tsyganov E N, Malakhov N A and Sadygov Z Y 1997 Avalanche photo diode with local negative feedback sensitive to UV, blue and green light *Nucl Instrum Meth A* **389** 491-498

Bizarri G and Dorenbos P 2007 Charge carrier and exciton dynamics in LaBr$_3$:Ce^{3+} scintillators: Experiment and model *Phys Rev B* **75**

Bondarenko G, Buzhan P, Dolgoshein B, Golovin V, Guschin E, Ilyin A, Kaplin V, Karakash A, Klanner R, Pokachalov V, Popova E and Smirnov K 2000 Limited Geiger-mode microcell silicon photodiode: new results *Nucl Instrum Meth A* **442** 187-192

Britvitch I, Johnson I, Renker D, Stoykov A and Lorenz E 2007 Characterisation of Geiger-mode avalanche photodiodes for medical imaging applications *Nucl Instrum Meth A* **571** 308-311

Burr K C and Wang G C 2007 Scintillation detection using 3 mm x 3 mm silicon photomultipliers *IEEE Nuclear Science Symposium and Medical Imaging Conference (2007 NSS/MIC)* (Honolulu, Hawaii) 975-982

Buzhan P, Dolgoshein B, Ilyin A, Kantserov V, Kaplin V, Karakash A, Pleshko A, Popova E, Smirnov S, Volkov Y, Filatov L, Klemin S and Kayumov F 2001 An advanced study of silicon photomultiplier *ICFA Instumentation Bulletin* **32** 28-42

Catana C, Wu Y B, Judenhofer M S, Qi J Y, Pichler B J and Cherry S R 2006 Simultaneous acquisition of multislice PET and MR images: Initial results with a MR-compatible PET scanner *J Nucl Med* **47** 1968-1976

Daube-Witherspoon M E, Surti S, Perkins A, Kyba C C M, Wiener R, Werner M E, Kulp R and Karp J S 2010 The imaging performance of a LaBr$_3$-based PET scanner *Phys Med Biol* **55** 45-64

de Haas J T M and Dorenbos P 2008 Advances in yield calibration of scintillators *IEEE Trans Nucl Sci* **55** 1086-1092

Drozdowski W, Dorenbos P, Bos A J J, de Haas J T M, Kraft S, Maddox E, Owens A, Quarati F G A, Dathy C and Ouspenski V 2007 Effect of proton dose, crystal size, and cerium concentration on scintillation yield and energy resolution of LaBr$_3$:Ce *IEEE Trans Nucl Sci* **54** 736-740

España S, Tapias G, Fraile L M, Herraiz J L, Vicente E, Udias J, Desco M and Vaquero J J 2008 Performance Evaluation of SiPM Detectors for PET Imaging in the Presence of Magnetic Fields *IEEE Nuclear Science*

Symposium and Medical Imaging Conference (2008 NSS/MIC) (Dresden) 2866-2870

Glodo J, Moses W W, Higgins W M, van Loef E V D, Wong P, Derenzo S E, Weber M J and Shah K S 2005 Effects of Ce concentration on scintillation properties of LaBr₃:Ce *IEEE Trans Nucl Sci* **52** 1805-1808

Glodo J, Kuhn A, Higgins W M, van Loef E V D, Karp J S, Moses W W, Derenzo S E and Shah K S 2006 CeBr(3) for Time-of-Flight PET *IEEE Nuclear Science Symposium and Medical Imaging Conference (2006 NSS/MIC)* (San Diego) 1570-1573

Golovin V and Saveliev V 2004 Novel type of avalanche photodetector with Geiger mode operation *Nucl Instrum Meth A* **518** 560-564

Göttlich M, Garutti E, Kozlov V, Schultz-Coulon H C, Tadday A and Terkulov A 2008 Application of Multi-Pixel Photon Counter to Positron Emission Tomography *IEEE Nuclear Science Symposium and Medical Imaging Conference (2008 NSS/MIC)* (Dresden) 2394-2397

Herbert D J, Moehrs S, D'Ascenzo N, Belcari N, Del Guerra A, Morsani F and Saveliev V 2007 The Silicon Photomultiplier for application to high-resolution Positron Emission Tomography *Nucl Instrum Meth A* **573** 84-87

Higgins W M, Glodo J, Van Loef E, Klugerman M, Gupta T, Cirignano L, Wong P and Shah K S 2006 Bridgman growth of LaBr₃:Ce and LaCl₃:Ce crystals for high-resolution gamma-ray spectrometers *J Cryst Growth* **287** 239-242

Judenhofer M S, Wehrl H F, Newport D F, Catana C, Siegel S B, Becker M, Thielscher A, Kneilling M, Lichy M P, Eichner M, Klingel K, Reischl G, Widmaier S, Rocken M, Nutt R E, Machulla H J, Uludag K, Cherry S R, Claussen C D and Pichler B J 2008 Simultaneous PET-MRI: a new approach for functional and morphological imaging *Nat Med* **14** 459-465

Kadrmas D J, Casey M E, Conti M, Jakoby B W, Lois C and Townsend D W 2009 Impact of Time-of-Flight on PET Tumor Detection *J Nucl Med* **50** 1315-1323

Kim C L, Wang G C and Dolinsky S 2009 Multi-Pixel Photon Counters for TOF PET Detector and Its Challenges *IEEE Trans Nucl Sci* **56** 2580-2585

Kolb A, Judenhofer M S, Lorenz E, Renker D and Pichler B J 2008 PET block detector readout approaches using G-APD *IEEE Nuclear Science Symposium and Medical Imaging Conference (2008 NSS/MIC)* (Dresden)

Kuhn A, Surti S, Shah K S and Karp J S 2005 Investigation of LaBr₃ detector timing resolution *IEEE Nuclear Science Symposium and Medical Imaging Conference (2005 NSS/MIC)* (Puerto Rico) 2022-2026

Kuhn A, Surti S, Karp J S, Muehllehner G, Newcomer F M and VanBerg R 2006 Performance assessment of pixelated LaBr₃ detector modules for time-of-flight PET *IEEE Trans Nucl Sci* **53** 1090-1095

Kyba C C A, Glodo J, van Loef E V D, Karp J S and Shah K S 2008 Energy and timing response of six prototype scintillators for TOF-PET *IEEE Trans Nucl Sci* **55** 1404-1408

Lewellen T K 2008 Recent developments in PET detector technology *Phys Med Biol*

53 R287-R317

Llosá G, Belcari N, Bisogni M G, Collazuol G, Del Guerra A, Marcatili S, Barrillon P, de la Taille C, Bondil-Blin S, Dinu N, Melchiorri M, Tarolli A and Piemonte C 2008 Evaluation of the First Silicon Photomultiplier Matrices for a Small Animal PET Scanner *IEEE Nuclear Science Symposium and Medical Imaging Conference (2008 NSS/MIC)* (Dresden) 2849-2855

McElroy D P, Saveliev V, Reznik A and Rowlands J A 2007 Evaluation of silicon photomultipliers: A promising new detector for MR compatible PET *Nucl Instrum Meth A* **571** 106-109

Moses W W and Derenzo S E 1999 Prospects for time-of-flight PET using LSO scintillator *IEEE Trans Nucl Sci* **46** 474-478

Moses W W 2007 Recent advances and future advances in time-of-flight PET *Nucl Instrum Meth A* **580** 919-924

Musienko Y, Auffray E, Lecoq P, Reucroft S, Swain J and Trummer J 2007 Study of multi-pixel Geiger-mode avalanche photodiodes as a read-out for PET *Nucl Instrum Meth A* **571** 362-365

Pestotnik R, Korpar S, Chagani H, Dolenec R, Krizan P and Stanovnik A 2010 Silicon photo-multipliers as photon detectors for PET *Nucl Instrum Meth A* **623** 594-596

Piemonte C, Gola A, Picciotto A, Pro T, Serra N, Tarolli A and Zorzi N 2011 Timing performance of large area SiPMs coupled to LYSO using dark noise compensation methods *IEEE Nuclear Science Symposium and Medical Imaging Conference (2011 NSS/MIC)* (Valencia) 3376-3380

Renker D 2007 New trends on photodetectors *Nucl Instrum Meth A* **571** 1-6

Schaart D R, van Dam H T, Seifert S, Vinke R, Dendooven P, Löhner H and Beekman F J 2008a SiPM-Array Based PET Detectors with Depth-of-Interaction Correction *IEEE Nuclear Science Symposium and Medical Imaging Conference (2008 NSS/MIC)* (Dresden) 2856-2860

Schaart D R, Seifert S, van Dam H T, de Boer M R, Vinke R, Dendooven P, Löhner H and Beckman F J 2008b First Experiments with LaBr$_3$:Ce Crystals Coupled Directly to Silicon Photomultipliers for PET Applications *IEEE Nuclear Science Symposium and Medical Imaging Conference (2008 NSS/MIC)* (Dresden) 3266-3269

Schaart D R, van Dam H T, Seifert S, Vinke R, Dendooven P, Löhner H and Beekman F J 2009 A novel, SiPM-array-based, monolithic scintillator detector for PET *Phys Med Biol* **54** 3501-3512

Seifert S, Schaart D R, van Dam H T, Huizenga J, Vinke R, Dendooven P, Löhner H and Beekman F J 2008 A High Bandwidth Preamplifier for SiPM-Based TOF PET Scintillation Detectors *IEEE Nuclear Science Symposium and Medical Imaging Conference (2008 NSS/MIC)* (Dresden) 891-894

Seifert S, van Dam H T, Huizenga J, Vinke R, Dendooven P, Löhner H and Schaart D R 2009 Simulation of Silicon Photomultiplier Signals *IEEE Trans Nucl Sci* **56** 3726-3733

Shah K S, Glodo J, Klugerman M, Higgins W, Gupta T, Wong P, Moses W W,

Derenzo S E, Weber M J and Dorenbos P 2004 LuI3: Ce - A new scintillator for gamma ray spectroscopy *IEEE Trans Nucl Sci* **51** 2302-2305

Shah K S, Glodo J, Higgins W, van Loef E V D, Moses W W, Derenzo S E and Weber M J 2005 CeBr3 scintillators for gamma-ray spectroscopy *IEEE Trans Nucl Sci* **52** 3157-3159

Shao Y, Cherry S R, Farahani K, Slates R, Silverman R W, Meadors K, Bowery A, Siegel S, Marsden P K and Garlick P B 1997 Development of a PET detector system compatible with MRI/NMR systems *IEEE Trans Nucl Sci* **44** 1167-1171

Shibuya K, Nishikido F, Tsuda T, Kobayashi T, Lam C, Yamaya T, Yoshida E, Inadama N and Murayama H 2008 Timing resolution improvement using DOI information in a four-layer scintillation detector for TOF-PET *Nucl Instrum Meth A* **593** 572-577

Song T Y, Wu H Y, Komarov S, Siegel S B and Tai Y C 2008 Sub-Millimeter Resolution PET Detector Module Using Multi-Pixel Photon Counter Array *IEEE Nuclear Science Symposium and Medical Imaging Conference (2008 NSS/MIC)* (Dresden) 4199-4203

Stoykov A, Musienko Y, Kuznetsov A, Reucroft S and Swain J 2007 On the limited amplitude resolution of multipixel Geiger-mode APDs *J Instrum* **2**

Surti S, Kuhn A, Werner M E, Perkins A E, Kolthammer J and Karp J S 2007 Performance of philips gemini TF PET/CT scanner with special consideration for its time-of-flight imaging capabilities *J Nucl Med* **48** 471-480

Townsend D W 2008 Multimodality imaging of structure and function *Phys Med Biol* **53** R1-R39

van Eijk C W E 2002 Inorganic scintillators in medical imaging *Phys Med Biol* **47** R85-R106

Vinke R, Löhner H, Schaart D R, van Dam H T, Seifert S, Beekman F J and Dendooven P 2008 Optimizing timing resolution for TOF PET detectors based on monolithic scintillation crystals using fast photosensor arrays *IEEE Nuclear Science Symposium and Medical Imaging Conference (2008 NSS/MIC)* (Dresden) 3229-3235

Vinke R, Löhner H, Schaart D R, van Dam H T, Seifert S, Beekman F J and Dendooven P 2010 Time walk correction for TOF-PET detectors based on a monolithic scintillation crystal coupled to a photosensor array *Nucl Instrum Meth A* **621** 595-604

Wilmshurst T H 1985 *Signal Recovery from Noise in Electronic Instrumentation* (Bristol: Hilger)

Yamamoto K, Yamamura K, Sato K, Kamakura S, Ota T, Suzuki H and Ohsuka S 2007 Development of multi-pixel photon counter (MPPC) *IEEE Nuclear Science Symposium and Medical Imaging Conference (2007 NSS/MIC)* (Honolulu, Hawaii) 1511-1515

4

Accurate Measurement of the Rise and Decay Times of Fast Scintillators with Solid State Photon Counters

Abstract—In this work we present a measurement setup for the determination of scintillation pulse shapes of fast scintillators. It is based on a time-correlated single photon counting approach that utilizes the correlation between 511 keV annihilation photons to produce start and stop signals in two separate crystals. The measurement is potentially cost-effective and simple to set up while maintaining an excellent system timing resolution of 125 ps. As a proof-of-concept the scintillation photon arrival time histograms were recorded for two well-known, fast scintillators: LYSO:Ce and LaBr$_3$:5%Ce. The scintillation pulse shapes were modeled as a linear combination of exponentially distributed charge transfer and photon emission processes. Correcting for the system timing resolution, the exponential time constants were extracted from the recorded histograms. A decay time of 43 ns and a rise time of 72 ps were determined for LYSO:Ce thus demonstrating the capability of the system to accurately measure very fast rise times. In the case of LaBr$_3$:5%Ce two processes were observed to contribute to the rising edge of the scintillation pulse. The faster component (270 ps) contributes with 72% to the rising edge of the scintillation pulse while the second, slower component (2.0 ns) contributes with 27%. The decay of the LaBr$_3$:5%Ce scintillation pulse was measured to be 15.4 ns with a small contribution (2%) of a component with a larger time constant (130 ns).

4.1.   Introduction

The temporal distribution of scintillation photons is a matter of interest in fundamental scintillator research as well as in the application of scintillators in γ-photon or particle detectors. Accurate measurement of scintillation pulse shapes may contribute to a better understanding of the physical processes involved in the generation of the scintillation photons (Weber *et al.* 2000, Bizarri and Dorenbos 2007). A precise knowledge of the temporal distribution of scintillation photons is also of importance to predict the measured signals and performance of scintillation detectors (e.g. Hyman 1965, Fishburn and Charbon 2010, Seifert *et al.* 2012b, Seifert *et al.* 2012a) The time constants describing the decay of many scintillators are well established. The available data on the rise times of scintillation pulses, however, is limited.

Because of the very short time scales involved (typically < 1 ns), rise time measurements are usually performed using costly equipment such as fast, pulsed X-ray sources in combination with microchannel phototubes or streak cameras. The aim of the present work is to develop a cost-effective method particularly suited for the determination of scintillator rise times. We propose to employ a time-correlated single photon counting (TCSPC) method making use of the correlation between 511 keV annihilation photons to produce start and stop signals in two separate crystals (Bollinger and Thomas 1961, Moszyński and Bengtson 1977). This method enables independent optimization of the timing resolutions of the start and stop detectors and is independent of the scintillation parameters of the crystal under study such as its light yield, or its time constants. The utilization of solid state photon counters, i.e. a silicon photomultiplier (SiPM) and an actively quenched Geiger-mode avalanche photodiode (GM-APD) to respectively read out the start and stop crystals potentially enables a system timing resolution in the order of ~100 ps FWHM. Here, we present a proof-of-concept and first results for the time constants of LYSO:Ce and LaBr$_3$:5%Ce.

4.2.   Methods

4.2.1.   Time-Correlated Single Photon Counting

TCSPC is a method that is commonly used to determine scintillation pulse shapes (Bollinger and Thomas 1961). In such an experiment the temporal distribution of emission times of scintillation photons is obtained from measurements of a large number K of scintillation events in the crystal under test. For any given scintillation event two time stamps are created. The first time stamp marks the beginning of the scintillation pulse and is therefore referred to as the *start* (signal) in the remainder of this work. The second time stamp, the *stop* (signal), marks the emission time of a single, randomly selected scintillation photon. After recording many pairs of time stamps a histogram of the differences Δ*t* between the measured starts and stops is created. The scintillation pulse shape is then typically extracted by fitting a parameterized

model to the measured histogram data.

The measured time difference histogram may contain various contributions of experimental conditions. In our case these are the time resolution of the system, the contribution of stop signals which are not correlated to a start signal and the so-called *start-stop-rate*. In this section we will develop a model describing the distribution of time differences that incorporates these effects.

4.2.1.1. *Scintillation Photon Emission Time Distribution*

Firstly, we consider the probability density function (pdf) $p_{t_e}(t\,|\,\Theta)$ which describes the probability for any given individual scintillation photon to be emitted at a time t after the interaction of a γ-photon at the time Θ in a (scintillation) crystal under test. Since the emission times of individual scintillation photons can be considered to be statistically independent and identically distributed, $p_{t_e}(t\,|\,\Theta)$ equals the scintillation pulse shape, except for a normalization factor. Most commonly, $p_{t_e}(t\,|\,\Theta)$ is described by a linear combination of exponential functions in the following form (e.g. Koechlin and Raviart 1964, Hyman 1965, Glodo *et al.* 2005, Bizarri and Dorenbos 2007):

$$p_{t_e}(t\,|\,\Theta) = \begin{cases} 0 & \forall t : (t < \Theta) \\ \displaystyle\sum_i P_{ec,i} \frac{1}{\left(\tau_{e,i} - \tau_{tr,i}\right)} \times \left[e^{-\frac{t-\Theta}{\tau_{e,i}}} - e^{-\frac{t-\Theta}{\tau_{tr,i}}} \right] & \forall t : (t \geq \Theta), \end{cases} \tag{4.1}$$

where $\tau_{tr,i}$ and $\tau_{e,i}$ are the time constants associated with a certain energy transfer and emission process which occurs with the probability $P_{ec,i}$. The corresponding cumulative distribution function (cdf) $P_{t_e}(t\,|\,\Theta)$ to $p_{t_e}(t\,|\,\Theta)$ is given by

$$P_{t_e}(t\,|\,\Theta) = \sum_i \frac{P_{ec,i}}{\tau_{e,i} - \tau_{tr,i}} \left(\tau_{e,i} - \tau_{tr,i} - \tau_{e,i} e^{-\frac{t-\Theta}{\tau_{e,i}}} + \tau_{tr,i} e^{-\frac{t-\Theta}{\tau_{tr,i}}} \right). \tag{4.2}$$

As a next step, the finite timing resolution of both, the start and the stop signal will be taken into account. The combined contribution of the two error sources to the measured time difference Δt is often referred to as the *system resolution* or the *impulse response function* (IRF). In our case, the largest contribution to the system resolution is associated with the start detector. As will be shown shortly, the timing response of the start detector is well described by a Gaussian function.

Now, we can express the pdf $p_{sc}(\Delta t)$, which describes the distribution of measured differences between a start signal and a stop signal initiated by a scintillation photon as the convolution of the expression in (4.1) and a Gaussian IRF:

$$p_{sc}(\Delta t) = C \cdot \sum_i \frac{P_{ec,i}}{\tau_{e,i} - \tau_{tr,i}} \times \left[a_{\tau_{e,i}}(\Delta t) - a_{\tau_{tr,i}}(\Delta t) \right], \tag{4.3}$$

with the corresponding cdf $P_{sc}(\Delta t)$:

$$P_{sc}(\Delta t) = C\left[g(\Delta t) + \sum_i \frac{P_{ec}}{\tau_{e,i} - \tau_{tr,i}}\left(\tau_{tr,i}a_{\tau_{tr,i}}(\Delta t) - \tau_{e,i}a_{\tau_{e,i}}(\Delta t)\right)\right]. \tag{4.4}$$

C is a normalization constant which is ≈ 1 for all practical cases. The support functions $a_{\tau_{x,i}}(\Delta t)$ and are $g(\Delta t)$ defined as

$$a_{\tau_{x,i}}(\Delta t) = \frac{e^{-\frac{\Delta t - \bar{t}_{start} - \Theta}{\tau_{x,i}} + \frac{1}{2}\frac{\sigma^2}{\tau_{x,i}^2}}}{2} \times \left[erf\left(\frac{\Delta t - \bar{t}_{start} - \Theta - \frac{\sigma^2}{\tau_{x,i}}}{\sqrt{2}\sigma}\right) + erf\left(\frac{\bar{t}_{start} - \frac{\sigma^2}{\tau_{x,i}}}{\sqrt{2}\sigma}\right)\right] \tag{4.5}$$

and

$$g(\Delta t) = \frac{1}{2}\left[erf\left(\frac{\Delta t - \Theta - \bar{t}_{start}}{\sqrt{2}\sigma}\right) + erf\left(\frac{\bar{t}_{start}}{\sqrt{2}\sigma}\right)\right], \tag{4.6}$$

where $\bar{t}_{start}$ is the average start-time relative to the γ-interaction time Θ, σ denotes the standard deviation of the Gaussian IRF and *erf* denotes the so-called Gauss error function.

4.2.1.2. Temporal Distribution of True Stop Signals

Up until this point individual scintillation photons were studied although in principle multiple stop triggers may be induced per scintillation event. For now, we will consider all these stop signals to be measurable and we will refer to them as *true stop signals* or *true stops*. Here we would like to note that in our realization of the TCSPC technique only the first stop signal is observed. This additional condition will be implemented into the model in section 4.2.1.4.

At this point, we need to consider the particular means by which the start signal is obtained in our setup. As mentioned earlier and as described in more detail in section 4.2.4 and the corresponding Figure 4.1, we utilize the temporal correlation between 511 keV annihilation photons that are emitted by a [22]Na source in order to generate a start trigger for a given scintillation event. A consequence of this technique is that not every start trigger is necessarily associated with a corresponding γ-absorption in the crystal under test. Therefore, one has to regard two mutually exclusive event branches depending on the behavior of the annihilation photon passing the crystal under test:

1) it may interact within the crystal and scintillation photons may be detected following the properties of a inhomogeneous Poisson point process, or

2) it may pass the crystal without interaction and no scintillation photons are created.

To describe these two event branches we assign the coincidence probability P_{co} to branch 1). It follows, that branch 2) occurs with a probability of $(1-P_{co})$.

Our experiment is set up such that the probability for any given scintillation photon to trigger the stop detector is small. That is, the expectation value λ of the number of true stops per scintillation event is small (~ 0.1) compared to the

number of emitted scintillation photons (typically several thousand). Thus we can assume the number of photons per scintillation pulse impinging on the stop sensor to be Poisson distributed. This means that the individual stop signals and hence the corresponding time differences Δt can be described by an inhomogeneous Poisson point process (Snyder 1975, pp. 51-53). As will be seen shortly, it is worthwhile to consider the probability $P_{\text{no sc}}(\Delta t_{\text{ul}})$ that no true stop signal is detected until the time Δt_{ul} has elapsed since a given start signal (with no condition on whether or not a stop signal is created afterwards):

$$P_{\text{no sc}}(\Delta t_{\text{ul}}) = \left(1 - P_{co}\right) + P_{co} \times e^{-\lambda P_{sc}(\Delta t_{\text{ul}})} . \tag{4.7}$$

If one considers Δt_{ul} to be the upper limit $\Delta t_{\text{ul}}^{(n)}$ of the nth bin in the time difference histogram, one can see that $P_{\text{no sc}}(\Delta t_{\text{ul}}^{(n)})$ represents the probability that true stop signals do not contribute to any of the n lowest bins. This, in return, equals the product of the probabilities for all the individual $1 \ldots n$ bins to contain no contribution of a true stop signal. This can be utilized to obtain an expression for the probability $P_{\text{sc bin}}(n)$ that at least one photon of a given scintillation event contributes to the nth histogram bin:

$$P_{\text{sc bin}}\left(n\right) = 1 - \frac{P_{\text{no sc}}\left(\Delta t_{\text{ul}}^{(n)}\right)}{P_{\text{no sc}}\left(\Delta t_{\text{ul}}^{(n-1)}\right)} . \tag{4.8}$$

In case of the first histogram bin $\Delta t_{\text{ul}}^{(n-1)}$ is replaced by the value of its lower limit.

4.2.1.3. *False Stop Rate*

A further phenomenon that affects the measured data is the occurrence of stop signals that are not correlated to a start signal. These uncorrelated stops we will denoted as *false stop signals* or *false stops* and their rate of occurrence as the *false stop rate*. There are several sources that contribute to the false stop rate. The most important ones include the dark count rate of the stop detector (see section 4.2.3), the detection of stray light, "missed" start pulses due to the finite γ-sensitivity of the start detector, and possible auto-luminescence of the crystal under test.

For the purpose of the evaluation of the TCSPC experiment presented in this work it will suffice to assume that false stops are independent and uniformly distributed in time. As a consequence, all the different contributions may be summarized in one effective false stop rate R_{fs}. In analogy to the previous section we define the cdf $P_{\text{no fs}}(\Delta t_{\text{ul}}^{(n)})$ describing the probability that false stops do not contribute to the first n histogram bins:

$$P_{\text{no fs}}\left(\Delta t_{\text{ul}}^{(n)}\right) = e^{-R_{\text{fs}}\Delta t_{\text{ul}}^{(n)}} . \tag{4.9}$$

Furthermore the probability $P_{\text{fs bin}}(n)$ for at least one false stop to occur in the nth bin is defined as

$$P_{\text{fs bin}}\left(n\right) = 1 - \frac{P_{\text{no fs}}\left(\Delta t_{\text{ul}}^{(n)}\right)}{P_{\text{no fs}}\left(\Delta t_{\text{ul}}^{(n-1)}\right)} . \tag{4.10}$$

4.2.1.4.   First Photon Time Distribution

In the previous sections the probabilities for all true and false stop signals to contribute to any of the histogram bins were discussed. In our setup, however, only the first stop signal is recorded as is the case in many TCSPC experiments (Bollinger and Thomas 1961, Moszyński and Bengtson 1977, Moses 1993). The probability $P_{\text{1st}}(n)$ for the first stop signal to fall within the nth bin equals the probability that at least one true or false stop signal occurs in the nth bin and that no signal (true or false) contributed to an earlier bin.

Moreover, one has to keep in mind that only events that fall within a certain measurement window are accepted. Start signals that are not followed by a corresponding stop signal before a certain maximum measurement time Δt_{max} are discarded. In other words, $P_{\text{1st}}(n)$ is conditioned by the requirement that a stop pulse is measured within the measurement window, viz. $\Delta t \le \Delta t_{\text{max}}$. Taking this into account we can combine the results of the previous two sections and derive an expression for the probability $P_{\text{1st}}(n)$:

$$P_{\text{1st}}\left(n\right) = \frac{P_{\text{no fs}}\left(\Delta t_{\text{ul}}^{(n-1)}\right) \times P_{\text{no sc}}\left(\Delta t_{\text{ul}}^{(n-1)}\right) \times \left(P_{\text{fs bin}}\left(n\right) + P_{\text{sc bin}}\left(n\right)\right)}{\left(1 - P_{\text{no fs}}\left(\Delta t_{\text{max}}\right) \times P_{\text{no sc}}\left(\Delta t_{\text{max}}\right)\right)} . \tag{4.11}$$

As in the previous sections for the first bin $\Delta t_{\text{ul}}^{(n-1)}$ is replaced by the corresponding lower bin limit. Furthermore, Δt_{max} is given by the upper limit of the last bin in the time difference histogram. The expected number of entries E_{n} in the nth histogram bin can then be calculated by multiplying $P_{\text{1st}}(n)$ with the total number of measurements N that contribute to the histogram.

4.2.2.   Start Detector

As a start detector we employed a SiPM-based scintillation detector. An LYSO:Ce crystal (Crystal Photonics, Inc.) with dimensions 3 mm × 3 mm × 5 mm was enclosed in a reflective casing made from Spectralon, a PTFE based material with a reflectivity specified to be better than 98% at 420 nm (the main emission wavelength of LYSO:Ce). The SiPM (Hamamatsu MPPC-S10362-33-050C) is coupled to the crystal using a silicone encapsulation gel (Lightspan LS-3252). The SiPM has an active area of 3 mm × 3 mm (thus matching the crystal), divided into 3600 individual self-quenched GM-APDs with a 50 μm pitch. The SiPM signal is amplified in two separate branches of a preamplifier made in-house (Huizenga *et al.* 2011). One branch is optimized for the determination of the energy, whereas the other one is used for the determination of the time stamp.

The timing resolution of the start detector was determined using two identical detectors facing a [22]Na source on opposing sides. The setup is described in detail

Table 4.1. Acqiris DC282 parameters specified at the operating conditions used in this work.

Sample Clock Accuracy	Sample Jitter	Effective No. of Bits	Differential Nonlinearity	Integral Nonlinearity
<2 ppm (<1 ps over 400 ns)	1.2 ps (typ)	5.5	<2 LSB (typ)	± 0.15 mV (typ)

elsewhere (Schaart *et al.* 2010, Seifert *et al.* 2012a). In short, the energy branches were used to determine the two pulse heights of each coincident pulse pair. This was done by feeding these signals into a CAEN N568B multi-channel shaping amplifier (shaping time 100 ns) connected to a CAEN V785 multi-channel, peak-sensitive ADC. Additionally, the energy signals were employed to generate a coincidence trigger for two, synchronized, fast 10 bit sampling ADCs (Acqiris DC282, sampling rate 8 GS/s, see Table 4.1 for additional specifications), sampling the timing signals of the SiPMs. The amplification of the timing signals and the ADC range (50 mV) were chosen such that only the first ~12% of the 511 keV signal amplitude was sampled.

Pulse height spectra were created for both detectors. Only events for which the recorded pulse height for both detectors fell within the full-width-at-tenth-maximum (FWTM) of the 511 keV photo peak were accepted for further analysis. For each accepted coincidence event, time stamps were created from the digitized timing signals. This was done by interpolating each trace with a full cubic spline and determining the intersection of the interpolated data with a fixed threshold of 12 mV relative to the baseline. The baseline was determined for each trace individually as the average signal within 2 ns directly before the onset of the pulse. A more detailed description of this method can be found in (Schaart *et al.* 2010, Seifert *et al.* 2012a).

4.2.3.   Stop Detector

The stop detector employs an ID Quantique id100-20 ULN actively quenched GM-APD with an active area of ⌀ 20 μm. This device has a very low dark count rate (< 1 Hz). It incorporates a trigger circuit producing a TTL pulse when a photon is detected. The device is then kept insensitive for 45 ns.

The single photon timing resolution of the id100-20 was determined using a Coherent Chameleon Ultra II modelocked Ti:Sapphire laser producing 150 fs laser pulses at a rate of 80 MHz. The wavelength of the laser light was set to 850 nm and subsequently frequency-doubled using a Coherent Harmonics second harmonics generation unit resulting in a wavelength of 425 nm. A trigger signal for the laser pulses was provided by a Hamamatsu C1808-03 PIN diode. This laser trigger signal and the id100-20 ULN output are digitized using two synchronized Acqiris DC282 sampling ADCs at 8 GS/s as in the previously described measurements. The time jitter of the digitized laser trigger (including the contribution of the ADCs input noise and sampling noise) is estimated to be <10 ps based on the time jitter between the trigger signals of subsequent laser

pulses.

The laser light was attenuated by neutral density filters such that on average one trigger is observed on the id100-20 ULN for 1300 laser pulses. The timing resolution of the id100-20 ULN is determined as the FWHM of a Gaussian fit to the histogram of the measured time differences between the id100-20 ULN signal and the corresponding laser trigger.

4.2.4.   TCSPC Measurements

The TCSPC measurements were performed for two different scintillation materials: LYSO:Ce (Crystal Phonics) and $LaBr_3$:5%Ce (Saint Gobain). The dimensions of both crystals under test were 3 mm × 3 mm × 5 mm. In both cases one of the 3 mm × 3 mm surfaces was polished and coupled to the sensor using the same Silicone gel as for the start detector. The remaining surfaces were chemically etched in case of LYSO:Ce and mechanically depolished in case of $LaBr_3$:5%Ce. No reflective material was used. The measurement involving the $LaBr_3$:5%Ce crystal was performed under a dry atmosphere to prevent deterioration of this highly hygroscopic material. (Moses 1993). A black screen between the crystal and the stop detector prevents detecting photons that are back-reflected from the reflective enclosure of the start sensor.

To avoid a large correction of a possible bias in the measured time constants it is perferable that the average number of detected photons per scintillation pulse λ is << 1 (Moses 1993). In order to estimate an upper limit on λ we consider the average number of fired microcells that was determined for 3 mm × 3 mm SiPMs (Hamamatsu MPPC-S10362-33-050C) optically coupled to the same crystals but placed in a reflective enclosure (Seifert *et al.* 2012a): 4700 in case of LYSO and 6200 for $LaBr_3$:5%Ce. These numbers are corrected for the effects of cross talk, after pulsing and SiPM saturation (van Dam *et al.* 2010). Thus, in these detectors each 50 μm × 50 μm cell on the average received 1–2 photon related triggers events per scintillation pulse. Considering that the active area of a single SiPM microcell is ~5 times larger than the active area of the id100-20 ULN (ID Quantique SA. 2005, Hamamatsu Photonics K.K. 2009) λ would be in the order of 0.1–0.4 if the internal quantum efficinecy of the photosensors sensors as well as the overall photon collection efficiency were comparable for the start detecotr and the combination of id100-20 and the crystal under test. Yet, no reflective wrapping was used for the crystal at the stop detector side and the internal quantum efficiency of the id100-20 ULN appears to be considerably smaller that of the MPPC-S10362-33-050C in the wavelength range of interest (380 nm–420 nm) (ID Quantique SA. 2005, Hamamatsu Photonics K.K. 2009 , Seifert *et al.* 2012a).

The TCSPC setup is depicted in Figure 4.1. The start and stop detectors are facing a ^{22}Na point source (∅ 0.5 mm) on opposite sides at a distance of ~1 cm from the source. The setup thus utilizes the temporal and directional correlation between two emitted 511 keV annihilation photons. The start detector accepts events above 460 keV only. If such a validated start pulse is followed by a stop pulse within a coincidence window of 400 ns, this stop pulse triggers the two
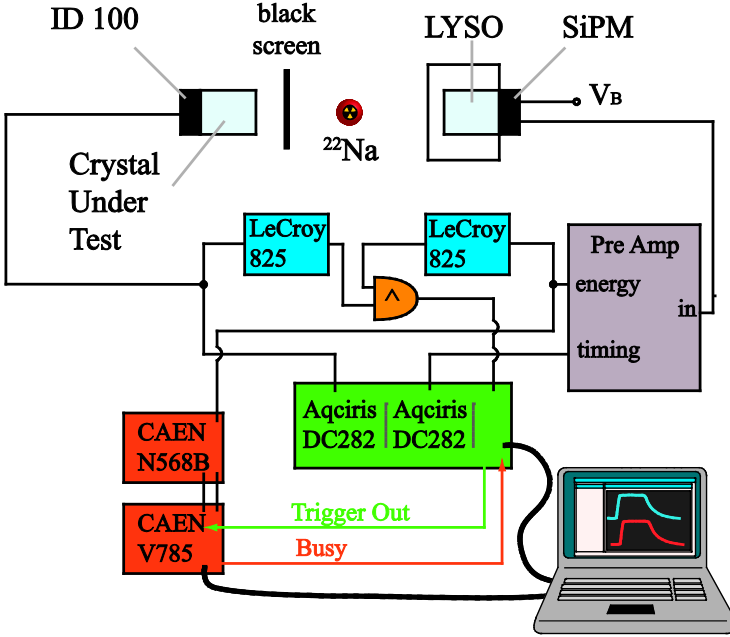
Figure 4.1. Schematic overview of the experimental TCSPC setup. The timing traces of start detector (composed of LYSO:Ce scintillator and SiPM) and stop detector (i.e. crystal-under-test and ID Quantique id100-20) are digitized and time stamps are created offline.

synchronized Acqiris DC282 ADCs; one sampling the start sensor's timing signal, the other sampling the stop sensor's signal output. During all measurements the number of stop pulses was recorded using a NIM counter unit (CEAN N1145). After subtracting the number of valid events the effective false stop rate R_{fs} was estimated by dividing the corrected number of stop pulses by the measurement time.

The time stamps of the two signals are obtained in a post-processing step in the same way as described in section 4.2.2. Thus the sampled signals of both detectors are interpolated with a full cubic spline and time stamps are determined by applying a base line compensated digital leading edge trigger.

A histogram is created for all measured start-stop-differences. This was done using variable bin sizes in order to balance two conflicting requirements on the width of the bins. On one hand the bin width must be small enough to accurately reproduce fast changes within the scintillation signal (namely in the rising edge of the pulse). Conversely, it is convenient for the subsequent fitting procedure if the number of events in the individual bins is well described by a normal distribution. This, however, implies that the number of counts in the individual bins should be large and thus requires large bin widths.

The adjustment of the bin width is facilitated by the fact that expression (4.11)

allows for the choice of arbitrarily spaced bin limits $\Delta t_{\text{ul}}^{(n)}$. For this work the bin widths were chosen to be inversely proportional to the absolute change $|\partial P_{\text{1st}}(n)/\partial n|$ calculated from a first estimate on $P_{\text{1st}}(n)$ that was obtained from an initial fit using a constant bin width. This procedure ensures a small bin width in regions where the expected change of the number of detected stop signals per bin is large. Furthermore, the bin size is subject to two further restrictions:

    1) the maximum bin size is 4 ns and

    2) the size of any bin may not be increased by more than 10% with respect to the previous bin.

The first restriction was introduced to prevent unreasonably large bin sizes prior to the onset of the scintillation pulse (i.e. for $\Delta t < \Theta - \bar{t}_{\text{start}}$). Restriction 2) constrains the bin size in the region where $P_{\text{1st}}(n)$ peaks and $(\partial P_{\text{1st}}(n)/\partial n)^{-1}$ has a pole.

The scintillation pulse shape was then determined by varying the corresponding parameters in the model developed in section 4.2.1 such that the so-called χ^2-statistic is minimized:

$$\chi^2 = \sum_{n=1}^{N} \frac{(M_n - E_n)^2}{E_n},\qquad(4.12)$$

where N is the total number bins and M_n is the measured number of entries in the nth histogram bin. E_n is the expected number of counts in the nth bin for a total of K measured start-stop-differences based on the model developed in section 4.2.1, viz. with $E_n = P_{\text{1st}}(n) \times K$.

The parameter values obtained using the described fitting routine were then used to reevaluate the bin widths according to the procedure described earlier. Subsequently, the fitting was repeated using the updated bin widths.

4.3.   Results and Discussion

4.3.1.   Impulse Response Function

The coincidence timing spectrum of two identical start detectors is plotted together with a Gaussian fit to the data in Figure 4.2. The coincidence resolving time (CRT) is 137 ps FWHM, corresponding to a single-detector timing resolution of 97 ps FWHM. Here it should be noted that this value includes the time spread due to the variation in interaction depth of the γ-photons within the scintillation crystal of the start detector. As this spread is also present in the TCSPC measurements it is justified to include this contribution in the IRF of the system. A further spread can be expected due to the interaction depth of the γ-photons within crystal under test.

The order of magnitude of the contribution of the depth of interaction (DOI) of the γ-photons can roughly be estimated based on the expected difference in the average travel time of direct photons that are emitted from a crystal region close to the sensor with respect to photons emitted from a region far away. It should be noted that for emission from the region closest to the sensor the travel time of the γ-photon through the crystal must be taken into account. The
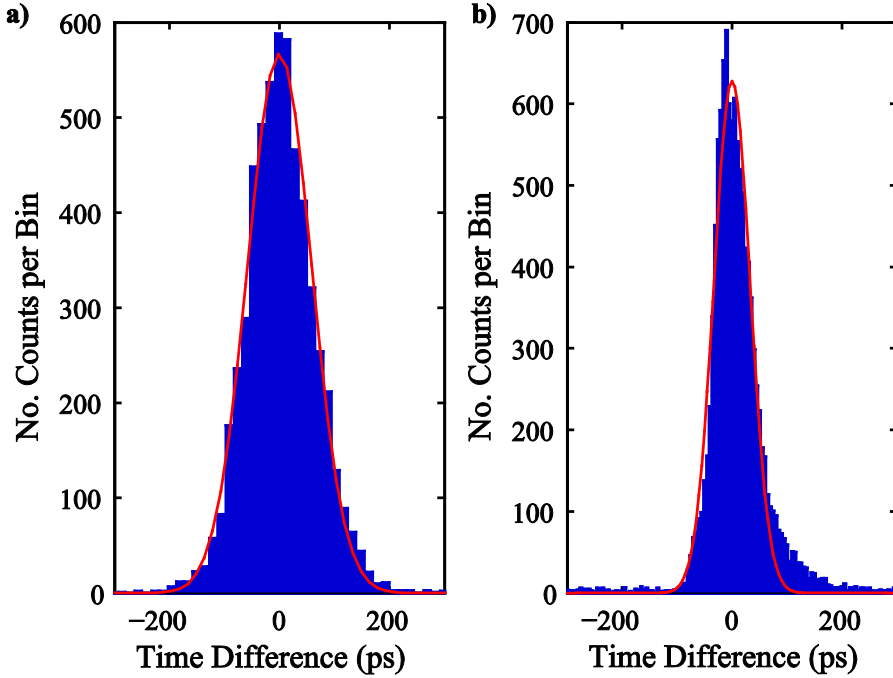
Figure 4.2. a) Timing spectrum for 511 keV annihilation photons measured with two identical (start-) detectors and b) impulse response function of the stop detector irradiated with <1 ps laser pulses. In both plots the measured data are shown (bars) together with Gaussian fits (lines). The FWHM of the fitted functions are 137 ps ± 1 ps and 78 ps ± 3 ps, respectively.

difference in the average travel times for the two extreme cases is then given by

$$\Delta t_{\text{DOI}} = \frac{d}{c}\left[n_{\text{sc}} - n_{\gamma}\right], \tag{4.13}$$

where d is the thickness of the crystal (i.e. 5 mm), c is the speed of light in vacuum and n_{sc} and n_{γ} are the refractive index values for scintillation photons and γ-photons, respectively. Using $n_{\text{sc}} = 1.8$–2.2 (for LYSO and LaBr$_3$:Ce) and $n_{\gamma} = 1$ we estimate the contribution of DOI effects to the timing resolution of a single crystal to be in the order of ~15 ps and thus negligible. 4.2.3

The response of the stop detector irradiated with fs-laser pulses is depicted in figure 2.b. It is apparent that the measured spectrum is slightly asymmetric with a "tail" extending towards longer times. This behavior is has previously been observed for GM-APDs and is generally attributed to the diffusion of charge carriers (Ghioni *et al.* 1988, Cova *et al.* 1989, Lacaita *et al.* 1993). However, in order to maintain the closed form of the expressions (4.3) and (4.4) we represent the measured IRF of the id100-20 ULN with a Gaussian function that is fitted to the measured data. This function is indicated as the solid line in figure 2.b. The

FWHM of this function is 78 ps. The overall IRF of the system then described by the convolution of the two Gaussian functions with a total FWHM of:

$$\sqrt{(97 \text{ ps})^2 + (78 \text{ ps})^2} = 125 \text{ ps (FWHM)} .$$

4.3.2.   Scintillation Pulse Shapes

4.3.2.1.   Fit Procedure

Before discussing the results of the TCSPC measurements it may be instructive to consider some of the details of the data analysis and the fit routine. Of specific interest is the ability of the fit routine to handle a possible bias in the determined time constants if the photon count is too large (i.e. λ is too large). This is important as no information is available on the absolute number of photons that reach the stop detector during a given scintillation pulse. Therefore, it is not possible to discriminate events based on the photon count of the stop detector as is possible if e.g. a PMT or MCP is used instead of the GM-AMD (Moszyński *et al.* 1982).

The formalism introduced in section 2.1 in principle includes the effects of a non-negligible bias on the measured scintillation pulse shape. In this regard, an important matter is the separation of P_{co} (i.e. the probability that a γ-photon interacts with the crystal under test given that a start trigger was detected) and λ (i.e. the average number of detected scintillation photons per scintillation event). It is clear, that the two parameters in are closely related. The main effect of both parameters is their influence on the probability that at least one scintillation photon reaches the stop detector within the measurement time window after a given start signal. This effect is directly visible in the distribution $P_{1st}(n)$ as a change in the ratio between the offset, which is caused by the false stop rate R_{fs}, and the peak that contains the true stop signals. However, while P_{co} only changes this ratio, a change in λ also affects the pulse shape.

Figure 4.3 illustrates the effect of λ on $P_{1st}(n)$. All graphs in Figure 4.3 were plotted using a single set of exponentials and the same model parameters as determined for the LYSO crystal (see Table 4.2) with the exceptions of λ and P_{co}, which were varied such that the ratio between true and false counts remained constant. It can be seen that an increase in λ causes a small, but discernible deviation of the pulse shape from the single exponential decay, which is closely resembled by the plot for $\lambda = 0.002$ (dash-dotted line).

However, even though the fitting procedure in principle can be used to determined λ, this method has to be applied with caution. It heavily relies on the validity of the model. If the applied model is not a good representation of the true scintillation pulse shape then a fit might compensate this mismatch by increasing λ. This means that without supplementary information it is not possible to discern such a model mismatch from the case of a truly large photon count. In this respect λ may be considered as an indicator of how well a model
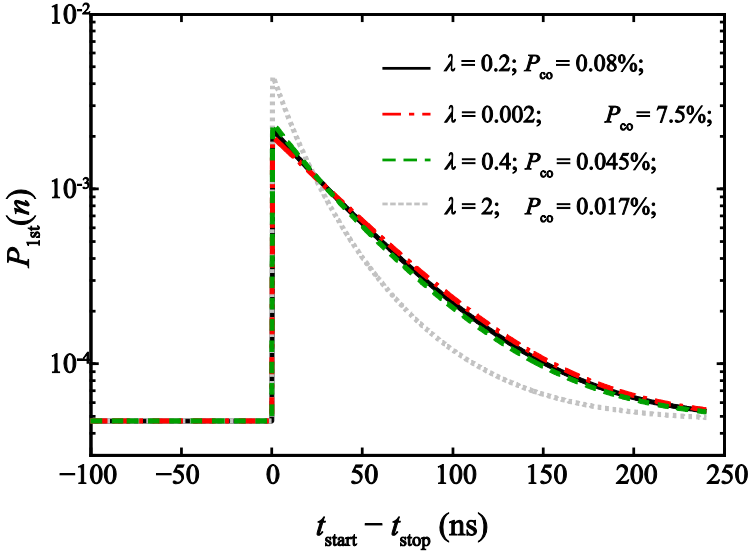
Figure 4.3. $P_{1st}(n)$ for different combinations of P_{co} and λ for which the ratio between true and false counts is preserved. The remaining model parameters were chosen to be the same as for LYSO listed in Table 4.2.

Figure 4.4. a) Time difference histogram measured for LYSO:Ce. b) The same data is shown, but for the rising edge only and on a linear scale. The solid, red lines in both graphs depict the model fit whereas the dashed lines indicate the 95%-confidence interval.

represents the underlying distribution, rather than a physical quantity. In other words, a low λ value ($\lambda \ll 1$) is a necessary, but insufficient, condition for reliable decay time constants.

Lastly we would like to draw attention to the fact that the error bars given for the scintillation pulse parameters in the following sections include the contribution due to the covariance with λ. In other words, the uncertainty on λ is taken into account for the determination of the uncertainties on the different time constants.

4.3.2.2.   LYSO:Ce

The results of the TCSPC measurement on the LYSO:Ce crystal are illustrated in Figure 4.4. The presented data set contains ~200.000 events. The corresponding measured data (dots) as well as the model fit (lines) are shown for the entire range of measured time differences (a) and for the rising edge only (b). In addition, the 95%-prediction intervals for the fitted model are shown in both plots (dashed lines). In order to enhance the clarity of the figure all presented data are normalized to the bin widths.

The fitted parameter values are summarized in Table 4.2. The measured false-stop-rate $R_{fs} = 84$ Hz and the system resolution (125 ps FWHM) were kept constant throughout the fitting procedure. The scintillation decay time constant was determined to be $\tau_e = 43$ ns ± 0.6 ns (where the uncertainty corresponds to the 95%-confidence interval). This value falls well in the range of values from $\tau_e = 40$ ns to $\tau_e = 51$ measured by others for LYSO:Ce (e.g. Pepin *et al.* 2004, Pidol *et al.* 2004, Szupryczynski *et al.* 2004, Qin *et al.* 2005, Nassalski *et al.* 2007, Chewpraditkul *et al.* 2009, Feng *et al.* 2010).

As mentioned above, the data available on the rise times of fast scintillators appears to be scarce even for a well-studied material such as LYSO:Ce. In fact, to the best of our knowledge there are no data available on the rise time of LYSO:Ce scintillators. Nonetheless, two direct measurements of the rising edge of the scintillation pulse of LSO:Ce have been reported by Moses and Derenzo (1999) and Derenzo *et al.* (2000).

Derenzo *et al.* (2000) report on the rise time constants measured for a 3 mm × 3 mm × 30 mm LSO crystal, which was painted black on five sides. They find a dominating fast component ($\tau_{tr,1} = 30$ ps ± 30 ps; with $P_i = 88\%$) that is significantly smaller than the value we obtain for our measurement: $\tau_{tr} = 72$ ps ± 28 ps. As one possible reason for the observed difference one may consider an increased contribution of photons that undergo one or more internal reflections within the crystal before reaching the stop senor. The average number of reflections per photon before reaching the sensor should be small as the etching of the crystal surfaces and the fact that no reflective wrapping was used should prevent extensive light trapping. Nevertheless, this number can be expected to be larger than for the measurements reported by Derenzo *et al.* (2000) where five sides of the crystal were painted black. It should be noted that also the black paint appears to only partially remove the contribution of light transport as

Table 4.2. Fit parameters as determined by the fit routine described section 4.2.4. The error bars indicate 95%-confidence intervals for the parameters.

		LYSO:Ce	LaBr$_3$:5%Ce		
λ		0.17 ± 0.04	0.15 ± 0.14		
P_{co}		$0.9\% \pm 0.2\%$	$0.08\% \pm 0.06\%$		
$\tau_{tr,i}$	(ns)	0.072 ± 0.028	0.270 ± 0.070	2.0 ± 0.9	130 ± 50
$\tau_{e,i}$	(ns)	43.0 ± 0.6	15.4 ± 0.5	15.4 ± 0.5	15.4 ± 0.5
P_i		100%	$72\% \pm 8\%$	$26\% \pm 8\%$	$2\% \pm 1\%$

Derenzo *et al.* (2000) observe a distinct scintillation pulse component with a much longer time constant ($\tau_{tr,2} = 350$ ps ± 70 ps; with $P_2 = 12\%$).

Moses and Derenzo (1999) present a more detailed study on the issue of light transport using the same same setup. They find the 10%-90%-rise-times of two polished 3 mm × 3 mm × 3 mm LSO:Ce crystals ($t_{10-90} = 465$ ps and $t_{10-90} = 484$ ps) to be considerably larger than the 10%-90%-rise-time that is apparent in our measurement: $t_{10-90} = 290$ ps ± 20 ps. This illustrates that the etched surfaces and the optical coupling between the crystal under test and the stop detector indeed reduce the average number of reflections of detected scintillation photons dramatically, thus leading to faster observed scintillation pulse build-up.

4.3.2.3.   LaBr$_3$:5%Ce

The measurement for the LaBr$_3$:5%Ce crystal is depicted in Figure 4.5. Again, the data are presented normalized to the bin widths for better readability. As in the case of LYSO the scintillation time constants, the average number of true-stops per start signal, and the coincidence probability were fitted to the measurement data (see Table 4.2) while the system resolution and the false-stop rate R_{fs} were kept constant. R_{fs} was measured to be 14 Hz which is considerably smaller than in the case of LYSO. This is because in LYSO a large contribution to R_{fs} originates from scintillation photons that are emitted due to the intrinsic activity of lutetium.

The decay of the scintillation pulse is dominated by the emission time constant $\tau_e = 15.4$ ns ± 0.5 ns. This compares well to the value determined by Glodo *et al.* (2005) ($\tau = 15.0$ ns). A further similarity to these measurements is that in contrast to the scintillation pulse shape measured for LYSO a satisfying agreement between model fit and measured data can only be reached using at least two components representing the charge transfer in the crystal. The values we determined for the associated time constants are comparable, yet somewhat smaller than the values measured by Glodo *et al.* (2005): $\tau_{tr,1} = 270$ ps ± 70 ps compared to 370 ps and $\tau_{tr,2} = 2.0$ ns ± 0.9 ns compared to 2.2 ns. However, differences of this magnitude are to be expected as the rising edge of the LaBr$_3$:Ce scintillation is known to be strongly influenced by difficult-to-control crystal growth parameters, such as e.g. the Ce concentration in the material
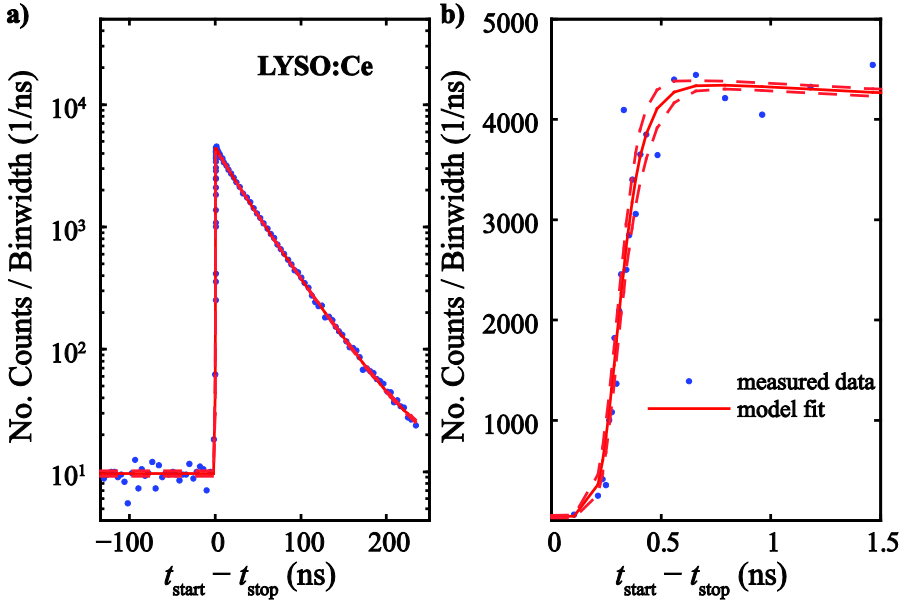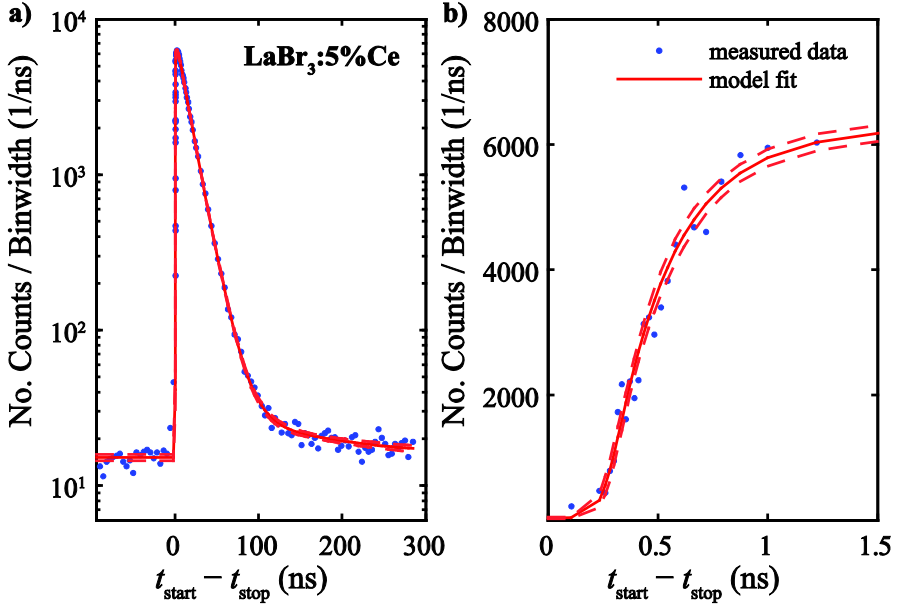
Figure 4.5. a) Time difference histogram measured for LaBr$_3$:5%Ce. b) The same data is shown, but for the rising edge only and on a linear scale. The solid, red lines in both graphs depict the model fit whereas the dashed lines indicate the 95%-confidence interval.

(Glodo *et al.* 2005).

Furthermore, Glodo *et al.* observed a small contribution (P_{ec} = 3%) to the scintillation decay of LaBr$_3$:5%Ce involving a much larger time constant of τ = 55 ns. This component appears to be larger in our measurements ($\tau_{tr,3,}$ =130 ns ± 50 ns). However, there is a strong correlation in the fitting procedure between this time constant $\tau_{tr,3,}$ the average number of true stop pulses λ, and the coincidence probability P_{co} which causes the uncertainty on these parameters to be large. The origin of this component is not entirely clear yet its scale makes it seem unlikely to be associated with the Ce decay. For this reason we chose to associate this time constant with a slow charge transfer rather than an emission process.

4.4.   Conclusion

In this work we discussed a measurement setup for time-correlated single photon counting utilizing solid state photon counters. The overall system timing resolution was 125 ps FWHM. This resolution is worse than the system resolution of 60 ps – 90 ps FWHM obtained by Weber *et al.* (2000) and by Derenzo *et al.* (2000) using a fast pulsed X-ray source. In our case, however, the system resolution is to a large extend determined by the timing resolution of the

start detector (97 ps), which could be improved to ~70 ps by replacing the LYSO:Ce crystal in the start detector by LaBr$_3$:Ce (Schaart *et al.* 2010).

As a proof of concept the rise- and decay constants of LYSO:Ce and LaBr$_3$:5%Ce were measured. The decay time constants compare well to previously published data (e.g. Moses and Derenzo 1999, Pepin *et al.* 2004, Pidol *et al.* 2004, Szupryczynski *et al.* 2004, Glodo *et al.* 2005, Qin *et al.* 2005, Nassalski *et al.* 2007, Chewpraditkul *et al.* 2009, Feng *et al.* 2010). A rise time constant of 72 ps was determined for LYSO:Ce, demonstrating the capability of the system to measure sub-nanosecond pulse shapes. However, this value should be considered as an upper limit on the intrinsic LYSO scintillation pulse rise time as it may contain a significant contribution of the photon transport.

The proposed setup may have some advantages over using a pulsed X-ray source. Firstly, our setup is simple and potentially very cost-effective. Furthermore, the employed method probes the whole volume of the crystal-under-test rather than a thin layer excited by X-rays. This can be important as the scintillation properties might e.g. be non-uniform due to inhomogeneities in the doping concentration. Furthermore, our method allows studying the scintillation pulse shape as a function of crystal dimensions, surface finish, etc., which may e.g. be useful in the development of detectors for TOF-PET.

Acknowledgements:

References

Bizarri G and Dorenbos P 2007 Charge carrier and exciton dynamics in LaBr$_3$:Ce^{3+} scintillators: Experiment and model *Phys Rev B* **75**

Bollinger L and Thomas G E 1961 Measurement of Time Dependence of Scintillation Intensity by a Delayed-Coincidence Method *Rev Sci Instrum* **32** 1044-&

Chewpraditkul W, Swiderski L, Moszynski M, Szczesniak T, Syntfeld-Kazuch A, Wanarak C and Limsuwan P 2009 Scintillation Properties of LuAG:Ce, YAG:Ce and LYSO:Ce Crystals for Gamma-Ray Detection *IEEE Trans. Nucl. Sci.* **56** 3800-3805

Cova S, Lacaita A, Ghioni M, Ripamonti G and Louis T A 1989 20-Ps Timing Resolution with Single-Photon Avalanche-Diodes *Rev Sci Instrum* **60** 1104-1110

Derenzo S E, Weber M J, Moses W W and Dujardin C 2000 Measurements of the intrinsic rise times of common inorganic scintillators *IEEE Trans. Nucl. Sci.* **47** 860-864

Feng H, Jary V, Mihokova E, Ding D, Nikl M, Ren G, Li H, Pan S, Beitlerova A and Kucerkova R 2010 Temperature dependence of luminescence characteristics of Lu 2(1-x)Y2xSiO5: Ce3+ scintillator grown by the Czochralski method *J Appl Phys* **108**

Fishburn M W and Charbon E 2010 System Tradeoffs in Gamma-Ray Detection Utilizing SPAD Arrays and Scintillators *IEEE Trans. Nucl. Sci.* **57** 2549-2557

Ghioni M, Cova S, Lacaita A and Ripamonti G 1988 New silicon epitaxial avalanche diode for single-photon timing at room temperature *Electronics Letters* **24** 1476-1477

Glodo J, Moses W W, Higgins W M, van Loef E V D, Wong P, Derenzo S E, Weber M J and Shah K S 2005 Effects of Ce concentration on scintillation properties of LaBr$_3$:Ce *IEEE Trans. Nucl. Sci.* **52** 1805-1808

Hamamatsu Photonics K.K. 2009 *MPPC S10362-33-050C data sheet* Available: http://sales.hamamatsu.com/en/products/solid-state-division/si-photodiode-series/mppc/part-s10362-33-050c.php

Huizenga J, Seifert S, Schreuder F, Vinke R, Dendooven P, Löhner H, van Dam H T, Beekman F J and Schaart D R 2011 A fast preamplifier concept for SiPM based time-of-flight PET detectors. In: *Proc. sixth Int. Conf. on New Developments in Photodetection* (Lyon: Elsevier)

Hyman L G 1965 Time Resolution of Photomultiplier Systems *Rev Sci Instrum* **36** 193

ID Quantique SA. 2005 *id100-20 data sheet* Available: http://www.idquantique.com/scientific-instrumentation/id100-silicon-apd-single-photon-detector.html

Koechlin Y and Raviart A 1964 Analyse Par Echantillonnage Sur Photons Individuels Des Liquides Fluorescents Dans Le Domaine De La Sub-Nanoseconde *Nucl Instrum Methods* **29** 45-53

Lacaita A, Ghioni M, Cova S and Zappa F 1993 Ultrafast Single-Photon Avalanche-Diodes without Slow Tails in the Pulse Response *IEEE Trans Electron Dev* **40** 2145-2145

Moses W W 1993 A Method to Increase Optical Timing Spectra Measurement Rates Using a Multi-Hit Tdc *Nucl Instrum Meth A* **336** 253-261

Moses W W and Derenzo S E 1999 Prospects for time-of-flight PET using LSO scintillator *IEEE Trans. Nucl. Sci.* **46** 474-478

Moszyński M and Bengtson B 1977 Light-Pulse Shapes from Plastic Scintillators *Nucl Instrum Methods* **142** 417-434

Moszyński M, Vacher J and Odru R 1982 Application of the Hr-400 Microchannel Plate Photomultiplier to Study the Light-Pulse Shape from Fast and Slow Scintillators by Means of the Single Photon Method *Nuclear Instruments & Methods in Physics Research* **204** 141-147

Nassalski A, Kapusta M, Batsch T, Wolski D, Mockel D, Enghardt W and Moszynski M 2007 Comparative study of scintillators for PET/CT detectors *IEEE Trans. Nucl. Sci.* **54** 3-10

Pepin C M, Berard P, Perrot A L, Pepin C, Houde D, Lecomte R, Melcher C L and Dautet H 2004 Properties of LYSO and recent LSO scintillators for phoswich PET detectors *IEEE Trans. Nucl. Sci.* **51** 789-795

Pidol L, Kahn-Harari A, Viana B, Virey E, Ferrand B, Dorenbos P, de Haas J T M and van Eijk C W E 2004 High efficiency of lutetium silicate scintillators, Ce-doped LPS, and LYSO crystals *IEEE Trans. Nucl. Sci.* **51** 1084-1087

Qin L S, Li H Y, Lu S, Ding D Z and Ren G H 2005 Growth and characteristics of LYSO (Lu2(1-x-y)Y2xSiO5 : Ce-y) scintillation crystals *J Cryst Growth* **281** 518-524

Schaart D R, Seifert S, Vinke R, van Dam H T, Dendooven P, Löhner H and Beekman F J 2010 LaBr$_3$:Ce and SiPMs for time-of-flight PET: achieving 100 ps coincidence resolving time *Phys Med Biol* **55** N179-N189

Seifert S, van Dam H T, Vinke R, Dendooven P, Löhner H, Beekman F J and Schaart D R 2012a A Comprehensive Model to Predict the Timing Resolution of SiPM-Based Scintillation Detectors: Theory and Experimental Validation *IEEE Trans. Nucl. Sci.* **59** 190-204

Seifert S, van Dam H T and Schaart D R 2012b The lower bound on the timing resolution of scintillation detectors *Phys Med Biol* **57** 1797-1814

Snyder D L 1975 *Random Point Processes* (New York, London, Sydney, Toronto Wiley-Interscience)

Szupryczynski P, Melcher C L, Spurrier M A, Maskarinec M P, Carey A A, Wojtowicz A J, Drozdowski W, Wisniewski D and Nutt R 2004 Thermoluminescence and scintillation properties of rare earth oxyorthosilicate scintillators *IEEE Trans. Nucl. Sci.* **51** 1103-1110

van Dam H T, Seifert S, Vinke R, Dendooven D, Löhner H, Beekman F J and Schaart D R 2010 A Comprehensive Model of the Response of Silicon Photomultipliers *IEEE Trans. Nucl. Sci.* **57** 2254-2266

Weber M J, Derenzo S E and Moses W W 2000 Measurements of ultrafast scintillation rise times: evidence of energy transfer mechanisms *J Lumin* **87-9** 830-832

5

A Comprehensive Model to Predict the Timing Resolution of SiPM-Based Scintillation Detectors: Theory and Experimental Validation

Abstract - Silicon photomultipliers (SiPMs) are expected to replace photomultiplier tubes (PMTs) in several applications that require scintillation detectors with excellent timing resolution, such as time-of-flight positron emission tomography (TOF-PET). However, the theory about the timing resolution of SiPM-based detectors is not yet fully understood. Here we propose a comprehensive statistical model to predict the timing resolution of SiPM-based scintillation detectors. It incorporates the relevant SiPM-related parameters (viz. the single cell electronic response, the single cell gain, the charge carrier transit time spread, and crosstalk) as well as the scintillation pulse rise and decay times, light yield, and energy resolution. It is shown that the proposed model reduces to the well-established Hyman model for timing with PMTs if the number of primary triggers (photoelectrons in case of a PMT) is Poisson distributed and crosstalk and electronic noise are negligible. The model predictions are validated by measurements of the coincidence resolving times (CRT) for 511 keV photons of two identical detectors as a function of SiPM bias voltage, for two different kinds of scintillators, namely LYSO:Ce and LaBr$_3$:5%Ce. CRTs as low as 138 ps ± 2 ps FWHM for LYSO:Ce and 95 ps ± 3 ps FWHM for LaBr$_3$:5%Ce were obtained, demonstrating the outstanding timing potential of SiPM-based scintillation detectors. These values were found to be in good agreement with the predicted CRTs of 140 ps FWHM and 95 ps FWHM, respectively. Utilizing the proposed model, it can be shown that the CRTs obtained in our experiments are mainly limited by photon statistics while crosstalk, electronic noise and signal bandwidth have relatively little influence.

5.1.   Introduction

Solid state photosensors based on arrays of self-quenched Geiger-mode avalanche photodiodes (GM-APDs, also microcells) are increasingly under consideration as viable alternatives to photomultiplier tubes (PMTs) (Buzhan *et al.* 2003, Otte *et al.* 2005, Dolgoshein *et al.* 2006, Korpar *et al.* 2008, Renker 2009). These so-called silicon photomultipliers (SiPMs) - also referred to as multi-pixel photon counters (MPPCs) or solid state photomultipliers (SSPMs) - exhibit a number of favorable properties such as high gain, low excess noise, insensitivity to magnetic fields, compactness, ruggedness, and cost effectiveness. It has recently been demonstrated that very good timing resolution can be achieved with SiPM-based scintillation detectors (Schaart *et al.* 2010). To further improve detectors and optimize their applications, it is desirable to better understand why such good timing resolution can be achieved and which the limiting factors are.

Research on the theory of the timing uncertainty in scintillation photon counting was pioneered amongst others by Post and Schiff in the early 1950s (Post and Schiff 1950) and continues to date (Fishburn and Charbon 2010). Such models of the photon counting statistics provide valuable insight into the influence of certain parameters on the timing resolution. Nevertheless, it is a misconception that one could draw general conclusions regarding the timing resolution achievable with scintillation detectors from these models, as they apply only to situations in which time stamps can be assigned to individual photons. In reality, the measured quantity in most scintillation detector systems (including PMT- and SiPM-based detectors) is a combination of signals originating from multiple photons.

The way in which the combination of the single photon signals takes place is determined by detector-specific properties such as the single photon response and the signal transit time spread. These parameters may therefore have a large influence on the experimentally determined timing resolution and should be incorporated in any model aimed at predicting absolute values of the timing resolution of scintillation detectors. Several such models have been proposed for PMT-based scintillation (Hyman *et al.* 1964, Hyman 1965, Clinthorne *et al.* 1990, Petrick *et al.* 1991). Arguably the most prominent among these is the theory by Hyman *et al.* (1964), which has found widespread application in scintillation detector research (Bengtson and Moszyński 1970, Glodo *et al.* 2005, Moszyński *et al.* 2006, Szczęśniak *et al.* 2009).

PMT-based models, however, cannot simply be extended to SiPM-based detectors, since SiPMs exhibit several properties that fundamentally distinguish them from PMTs. These include e.g. the highly asymmetric single photon response (exhibiting a fast signal rise time and a relatively slow decay (Haitz 1964, Cova *et al.* 1996)) and the substantial probability for optical crosstalk between the individual microcells of a SiPM.

Several attempts to simulate the timing performance of SiPM based scintillation detectors by means of Monte Carlo methods have been published by

other authors (Henseler *et al.* 2009, Retiere 2009, Liksonov *et al.* 2010). However, a detailed statistical description still seems to be missing.

In this work we propose a comprehensive statistical model of the timing resolution of SiPM-based scintillation detectors that takes into account the characteristics of the scintillation process (i.e. the scintillation pulse shape, the expectation value and variance of the number of emitted photons) as well as all relevant SiPM specific properties such as the photon detection efficiency (PDE), the signal transit time spread, the electronic signal shape, the microcell gain variation, and the electronic noise. To validate the predictions of this model, they are compared to the measured coincidence resolving times (CRTs) of two Hamamatsu MPPC-S10362-33-50C SiPMs optically coupled to 3 mm × 3 mm × 5 mm scintillation crystals of two different types, viz. LYSO:Ce and LaBr$_3$:5%Ce. Furthermore the influence of some key detector properties (namely the scintillator pulse shape, light yield, PDE, crosstalk properties, and the electronic noise contribution) on the CRT achievable with those detectors is investigated.

5.2. Model description

In this section the statistical model for the prediction of the timing resolution of SiPM based scintillating detectors will be derived. Before addressing the details of the modeling, however, a brief description of the basic operating principle of SiPMs is given in section 5.2.1, thereby focusing on those properties that distinguish these sensors from conventional PMTs. Section 5.2.2 then constitutes the most important premises, which are assumed in the development of the model.

Figure 5.1 presents an overview of the various processes considered to contribute to the timing uncertainty. These processes may be classified into three different categories, namely scintillation crystal related contributions, sensor related contributions, and contributions arising from the electronic processing of the signal.

Scintillation crystal related processes, often summarized under the term

Crystal (Emission, Transport)   Sensor (Conversion, Crosstalk, Transport, Summation)   Preamp+ADC (Transport, Amplification, Shaping, Noise)
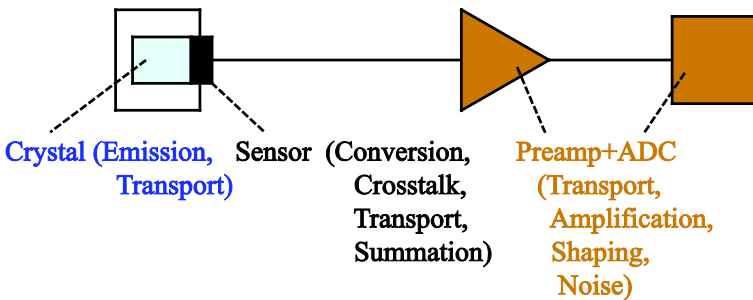
Figure 5.1. Schematic representation of the processes considered to contribute to the timing uncertainty.

photon counting statistics, will be treated in section 5.2.3. Sensor related processes are described in sections 5.2.4 and 5.2.5. The influence of additional shaping of the signal is treated implicitly in the same sections in the form of an effective single cell signal shape. Electronic noise, which is added by the preamplifier and by the ADC, is added to the model in section 5.2.6, where the contributions of counting statistics and (electronic) sensor signal are combined.

5.2.1.   Silicon photomultiplier characteristics and definitions

A SiPM comprises an array of typically $10^2 – 10^5$ parallel-connected microcells, each of which comprises an avalanche photodiode (APD) in series with a quench resistor. The APDs are reverse-biased at a voltage Vbias larger than the APDs' breakdown voltage Vbr and thus operate in Geiger mode (GM).

When a photon is absorbed in one of the GM-APDs, an electron-hole pair may be created. In general, these charge carriers need to migrate a certain distance towards the breakdown region in order to trigger an avalanche. This introduces an average time delay as well as a time spread (the latter is hereafter referred to as charge carrier transit time spread).

The direct triggering of a discharge by a scintillation photon will be denoted as a primary trigger in the remainder of this document. The resulting avalanche is passively quenched by the abovementioned series resistor. The electronic signal measured upon the discharge of a single microcell will be denoted as the single cell signal (SCS).

A phenomenon that may influence the timing performance of SiPMs is optical crosstalk. Such crosstalk is caused by secondary photons emitted upon the recombination of charge carriers in the avalanche, which may trigger additional avalanches in neighboring cells (Lacaita *et al.* 1993, Rech *et al.* 2008). To the best of our knowledge, no studies have yet been carried out regarding the temporal distribution of crosstalk events with respect to the corresponding primary trigger. The following considerations, however, may help to gain a basic understanding of this distribution.

The probability that a secondary photon is emitted at a given point in time is assumed to be proportional to the avalanche current (Lacaita *et al.* 1993, Rech *et al.* 2008). It therefore follows an exponential decay with a time constant determined by the quenching of the avalanche. This time constant is in the order of tens to hundreds of picoseconds for a GM-APD, depending on its equivalent microplasma series resistance R_d and the total cell capacitance C_{tot} (Haitz 1964, Cova *et al.* 1996, Seifert *et al.* 2009).

Furthermore, in analogy with the primary triggers, the triggering of avalanches due to crosstalk is subject to an average transit time and a transit time spread due to photon transport, absorption, and subsequent charge carrier migration. It should be pointed out, however, that the probability distribution of the transit time is not necessarily the same for both crosstalk events and primary triggers, because of the different emission wavelength regions (typically in the near-UV for scintillation photons, mainly in the red to infrared for crosstalk photons) and the different angular distributions of the photons.

The effect of optical saturation of the SiPM (see e.g. Buzhan *et al.* 2001) is considered negligible within the scope of the proposed model. This is justified by the fact that our considerations are limited to a time window of only ~1 ns after the first primary trigger, in which the number of fired cells N_f is still small (viz. $N_f \approx 80$ for LYSO:Ce and $N_f \approx 220$ for LaBr$_3$:5%Ce) compared to the total number of microcells $N_{cells} = 3600$ of the SiPMs employed in our experiments.

Similarly, the probability for one or more dark counts to occur within the ~1 ns time window is very small. Moreover, the influence of dark counts occurring prior to about 2 ns before that measurement interval is largely removed by the baseline correction applied in our measurements (see section 5.3.2). Hence, also the contribution of dark counts to the timing resolution is considered to be negligible in this work. Finally, the narrow time window also excludes any influence of afterpulses, since the associated time constants are much larger than the ~1 ns time window.

5.2.2. Model assumptions

The incorporation of all of the aforementioned processes into a statistical timing model can be simplified drastically under the following assumptions:

A1. The arrival times of the individual scintillation photons are statistically independent and identically distributed (i.i.d.);

A2. The corresponding primary triggers are i.i.d.;

A3. The amplitudes of all single cell signals (SCSs) are i.i.d.;

A4. SCSs are additive;

A5. The temporal distributions of crosstalk events with respect to a primary trigger are i.i.d..

Here, it must be emphasized that assumptions A2, A3, and A4 need to hold only within the limitation of the small time window of ~1 ns after the first primary trigger, where optical saturation is negligible.

5.2.3. Temporal distribution of primary triggers

The probability density function (pdf) describing the distribution of the emission times tem of scintillation photons following the absorption of a γ-photon at $t_0 = 0$ will be denoted as $pt_e(t)$. For many scintillator materials it is sufficient to describe $pt_e(t)$ as the convolution of two exponential functions representing the energy transfer to the luminescence centers and their radiative decay, respectively (Koechlin and Raviart 1964, Hyman 1965). In some cases, however, multiple event chains (i.e. energy transfer followed by radiative decay) leading to the emission of scintillation photons need to be taken into account (Glodo *et al.* 2005, Bizarri and Dorenbos 2007). In such cases the shape of the scintillation pulse can be described as a linear combination of the time profiles corresponding to the individual chains:

$$
p_{t_e}(t\mid\Theta) = \begin{cases} 0 & \forall t:(t<\Theta) \\[2ex] \displaystyle\sum_i P_{ec,i}\frac{1}{(\tau_{d,i}-\tau_{r,i})}\times\left[e^{-\frac{t-\Theta}{\tau_{d,i}}}-e^{-\frac{t-\Theta}{\tau_{r,i}}}\right] & \forall t:(t\geq\Theta) \end{cases}, \tag{5.1}
$$

where $P_{ec,i}$, $\tau_{r,i}$, and $\tau_{d,i}$ are the probability that a given event chain occurs, the rise time constant, and the decay time constant associated with the ith competing event chain, respectively.

Any scintillation photon can trigger an avalanche in a microcell after some time interval t_{trans} following the time of emission t_e (see Figure 5.2). There are two major contributions to t_{trans}. One contribution is the photon transit time, i.e. the time difference between the emission of a scintillation photon and its absorption in a microcell. The second contribution is the charge carrier transit time. The combined influence of these transport processes can be described by the convolution of the pdfs describing the individual transport processes. Due to the small dimensions of the scintillation crystals employed in this work, however, this pdf is considered to be dominated by the detector transit time spread and therefore modeled as a truncated Gaussian (Hyman *et al.* 1964) with an average transit time $\overline{t}_{trans}$ and a transit time spread σ_{trans}:

$$
p_{t_{trans}}(t) = \begin{cases} 0 & \forall t:(t<0) \\[2ex] \displaystyle\frac{c}{\sigma_{trans}\sqrt{2\pi}}e^{-\frac{(t-\overline{t}_{trans})^2}{2\sigma_{trans}^2}} & \forall t:(t\geq 0) \end{cases}, \tag{5.2}
$$

where the normalization constant c is given by

$$
c = \frac{2}{1+erf\left(\dfrac{\overline{t}_{trans}}{\sigma_{trans}\sqrt{2}}\right)}, \tag{5.3}
$$

with *erf* being the Gauss error function. Here, it should be noted that the absolute value of $\overline{t}_{trans}$ has no significance for our model, since a constant delay could be added without influencing the timing resolution. In this work a value of $\overline{t}_{trans}=4\times\sigma_{trans}$ is used (Hyman *et al.* 1964).

In what follows we will use the condition D that a given scintillation photon will be detected by the SiPM. In other words, D implies that a primary trigger is created. Commonly, the expected fraction of scintillation photons that satisfies D is referred to as the detector PDE η. It is noted that this definition of η includes all processes that might cause losses during the photon transport and therefore depends on the detector geometry as well as on the optical coupling material and the reflective enclosure of the scintillation detector (van Dam *et al.* 2010).

Under the condition D, the pdf $pt_{pt}(t\mid D)$ describing the probability for a primary trigger to occur at time t_{pt} can be obtained. Since the trigger time t_{pt} is simply the sum of t_e and t_{trans}, $pt_{pt}(t\mid D)$ is given by the convolution of $pt_e(t)$ and

$pt_{\text{trans}}(t)$ resulting in

$$p_{t_{\text{pt}}}\left(t\,|\,\text{D}\right) = \int_0^t p_{t_{\text{e}}}\left(t - \tilde{t}\right) \times p_{t_{\text{trans}}}\left(\tilde{t}\right) d\tilde{t} \,. \tag{5.4}$$

5.2.4. SiPM response

5.2.4.1. Single cell signal

The single cell signal $v_{\text{scs}}(t,a)$ is modeled as the product of the (single cell) signal amplitude a and shape function $f(t)$ that is normalized to the peak value and describes the signal as a function of the time t elapsed since the cell was triggered:

$$v_{\text{scs}}(t,a) = a \times f(t) \,. \tag{5.5}$$

It should be noted that $f(t)$ describes the signal shape at the 'point-of-measurement', i.e. after shaping by subsequent circuitry (here composed of a low-pass filter, formed by the sensor capacitance and the preamplifier input impedance, and the finite bandwidth of the subsequent amplification stages and the ADCs). This definition is applicable, since the assumptions introduced in section 5.2.2 imply that the order in which the individual processes are incorporated within the model can be chosen freely and that the summation of the individual SCSs and the shaping can be interchanged. Also, this definition is convenient, since it allows for a direct measurement of $f(t)$.

We will assume that $f(t)$ is the same for all fired cells and not subject to statistical fluctuations. This assumption is plausible, since the signals contain a large number of electrons (typically $\sim 10^5 - 10^6$) and all SCS are shaped by the same shaping circuitry. The amplitude a, however, is assumed to be Gaussian distributed around a mean $\bar{a}$ with standard variation σ_{a}:

$$p(a) = \frac{1}{\sigma_{\text{a}}\sqrt{2\pi}} e^{-\frac{(a-\bar{a})^2}{2\sigma_{\text{a}}^2}} \,. \tag{5.6}$$

The pdf $pv_{\text{scs}}(v\,|\,t, t_{\text{pt}})$ describing the probability for a SCS to assume a value v at a given time t as a response to a single trigger event at the time t_{pt} is then given by

$$p_{v_{\text{scs}}}\left(v\,|\,t, t_{\text{pt}}\right) = \begin{cases} h(v\,|\,t, t_{\text{pt}}) & \forall t : \left(t \geq t_{\text{pt}}\right) \\ \delta(v) & \forall t : \left(t < t_{\text{pt}}\right) \end{cases}, \tag{5.7}$$

where $\delta(v)$ is the Dirac delta function while the function $h(v\,|\,t, t_{\text{pt}})$ is defined as follows:

$$h\left(v\,|\,t, t_{\text{pt}}\right) = \frac{1}{f(t - t_{\text{pt}})\sigma_{\text{a}}\sqrt{2\pi}} e^{-\frac{\left(v - f(t - t_{\text{pt}})\bar{a}\right)^2}{2f(t - t_{\text{pt}})^2\sigma_{\text{a}}^2}} \,. \tag{5.8}$$
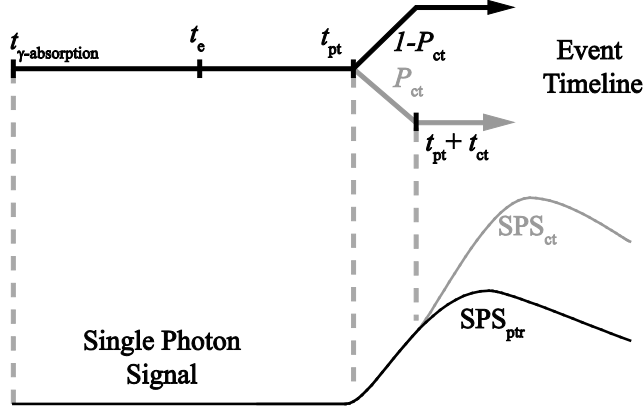
Figure 5.2. Schematic representation of the branching event cascade for a given single photon signal (SPS) indicating the event timeline and the resulting SPS with (gray) and without (black) a possible crosstalk event. Note that the depicted time line and the SPS are not to scale.

5.2.4.2.   Crosstalk

In the case that exactly one crosstalk trigger occurs at a given time t_{ct} after a primary trigger at t_{pt} (see Figure 5.2), the pdf $pv_{cts}(v \,|\, t, t_{pt}, t_{ct})$ describing the probability distribution of the combined signal v including the crosstalk signal is given by

$$p_{v_{cts}}\left(v \,|\, t, t_{pt}, t_{ct}\right) = \begin{cases} p_{v_{scs}}\left(v \,|\, t, t_{pt}\right) & \forall t : \left(t < t_{ct} + t_{pt}\right) \\ q\left(v \,|\, t, t_{pt}, t_{ct}\right) & \forall t : \left(t \geq t_{ct} + t_{pt}\right) \end{cases}. \tag{5.9}$$

As one can see from this definition, at a given time t, $pv_{cts}(v \,|\, t, t_{pt}, t_{ct})$ equals the definition for $pv_{scs}(v \,|\, t, t_{pt})$ in the trivial cases that the primary trigger has not occurred yet (i.e. the signal is zero) and if the crosstalk event is triggered at a time later than t. In the case that both trigger events occur before t and thus contribute to the signal, $pv_{cts}(v \,|\, t, t_{pt}, t_{ct})$ equals the function $q(v \,|\, t, t_{pt}, t_{ct})$, which is the convolution of $h(v \,|\, t, t_{pt})$ and $h(v \,|\, t, t_{pt} + t_{ct})$:

$$q\left(v \,|\, t, t_{pt}, t_{ct}\right) = \frac{e^{-\frac{\left(v - \left(f(t - t_{pt}) + f(t - t_{pt} - t_{ct})\right)\bar{a}\right)^2}{2\left(f(t - t_{pt})^2 + f(t - t_{pt} - t_{ct})^2\right)\sigma_a^2}}}{\sqrt{\left(f(t - t_{pt})^2 + f(t - t_{pt} - t_{ct})^2\right)}\sigma_a \sqrt{2\pi}}. \tag{5.10}$$

We define P_{ct} as the probability for a single crosstalk event to occur after one single cell has been fired. In this paper only single crosstalk events will be taken into account, thus assuming that the probabilities for one cell to trigger crosstalk events in more than one other cell and for a crosstalk event to trigger another crosstalk event are negligible (van Dam *et al.* 2010). For the devices employed

in this work the sum of the neglected probabilities is estimated from the ratio of the peak areas shown in Figure 5.5 to be in the order of $2\% - 4\%$ compared to $P_{ct} \approx 10\% - 20\%$.

With the inclusion of single crosstalk events, the pdf $pv_{pts}(v \,|\, t, t_{pt})$ of the signal v at a given time t due to a given primary trigger occurring at the time t_{pt} is given by

$$p_{v_{pts}}\left(v\,|\,t,t_{pt}\right) = \left(1 - P_{ct}\right) \times p_{v_{scs}}\left(v\,|\,t,t_{pt}\right) + P_{ct} \times p_{v_{cts}}\left(v\,|\,t,t_{pt}\right)$$

$$= p_{v_{scs}}\left(v\,|\,t,t_{pt}\right) \times$$

$$\left(1 - P_{ct} + P_{ct} \times \int\limits_{t-t_{pt}}^{\infty} p_{t_{ct}}(\tilde{t}\,|\,t_{pt},C)d\tilde{t}\right) \tag{5.11}$$

$$+ P_{ct} \times \int\limits_{0}^{t-t_{pt}} p_{t_{ct}}(\tilde{t}\,|\,t_{pt},C) \times q\left(v\,|\,t,t_{pt},\tilde{t}\right)d\tilde{t} \;,$$

where $pt_{ct}(t_{ct} \,|\, t_{pt}, C)$ is the pdf describing the probability that the crosstalk trigger occurs after a time interval t_{ct} following t_{pt}, given the condition C that a crosstalk event will follow the primary trigger.

One contribution to the temporal distribution $pt_{ct}(t_{ct} \,|\, t_{pt}, C)$ of crosstalk events with respect to the primary trigger is the emission probability of photons during the avalanche process. It is considered to follow an exponential decay with a time constant corresponding to $C_{tot} \times R_d$. A further contribution to $pt_{ct}(t_{ct} \,|\, t_{pt}, C)$ arises from the combined transit time spread of crosstalk photons and the corresponding charge carriers. Since the expectation value and the shape of this combined distribution are unknown, we will in first instance consider the absorption of crosstalk photons as well as the subsequent triggering of discharges to occur instantaneously, so $pt_{ct}(t_{ct} \,|\, t_{pt}, C)$ is given by

$$p_{t_{ct}}\left(t\,|\,t_{pt},C\right) = \begin{cases} 0 & \forall t:(t < t_{pt}) \\ \dfrac{1}{C_{tot} \times R_d}\, e^{-\frac{t}{C_{tot}R_d}} & \forall t:(t \geq t_{pt}) \end{cases}. \tag{5.12}$$

This approximation is used if not mentioned otherwise. In cases where we study the possible influence of a finite distribution, the exponential emission probability (5.12) is convoluted with a bi-exponential function with equal rise and fall times ($\tau_r = \tau_d = \tau_{ct}$), where we would like to make note of the fact that by no means we propose this function to carry any physical significance other than that it fulfills the properties of normalization, exhibits the mentioned finite rise and fall times, and does not extend below t_0.

5.2.5.   Single photon signal expectation value and variance

One can now define the single photon signal (SPS) as the electronic signal originating from a detected scintillation photon. Here we would like to underline two distinct differences with the definition of the SCS. First, the SCS is defined

for a single fired cell, whereas the SPS includes the possibility of crosstalk. Second, the SCS is defined relative to t_{pt} and therefore is a sensor inherent property, while the SPS is defined relative to the time of absorption of the γ-photon t_0 and thus includes the influences of the scintillation process and the charge carrier transit time.

The chain of events contributing to the SPS is depicted in Figure 5.2. The pdf $pv_{sps}(v \mid t, D)$ associated with the probability for the SPS to assume a value v at a given time t is determined by the probability that the photon triggers an avalanche at time t_{pt}, as described by $pt_{pt}(t_{pt} \mid D)$ in (5.4), and the probability that this leads to a signal amplitude v at t, as given by $pv_{pts}(v \mid t, t_{pt})$ in (5.11):

$$p_{v_{sps}}\left(v \mid t, D\right) = \int_0^\infty p_{t_{pt}}\left(t_{pt}\right) \times p_{v_{sps}}\left(v \mid t, t_{pt}\right) dt_{pt} \ . \tag{5.13}$$

It can be shown that the expectation value $E[v_{sps} \mid t, D]$ of the SPS at a given time t then equals

$$E\left[v_{sps} \mid t, D\right] = \overline{a} \int_0^t p_{t_{pt}}\left(t_{pt} \mid D\right) \times f\left(t - t_{pt}\right) t_{pt}$$

$$+ P_{ct} \overline{a} \int_0^t p_{t_{pt}}\left(t_{pt} \mid D\right) \times \int_0^{t - t_{pt}} p_{t_{ct}}\left(\tilde{t} \mid t_{pt}, C\right) \tag{5.14}$$

$$\times f\left(t - \tilde{t} - t_{pt}\right) \cdot d\tilde{t} \ dt_{pt}.$$

That is, $E[v_{sps} \mid t\, D]$ equals the sum of the expectation value of the signal originating from a primary trigger and the average signal due to crosstalk following a primary trigger. Furthermore, the variance of the SPS is given by

$$\text{var}\left[v_{sps} \mid t, D\right] = E\left[v_{sps}^2 \mid t, D\right] - E\left[v_{sps} \mid t, D\right]^2 . \tag{5.15}$$

where $E[v^2_{sps} \mid t, D]$ is given by

$$E\left[v_{\text{sps}}^2 \mid t, \text{D}\right] = \bar{a}^2 r_{\text{SiPM}}^2 \int_0^t p_{t_{\text{pt}}}\left(t_{\text{pt}} \mid \text{D}\right) \times f\left(t - t_{\text{pt}}\right)^2 dt_{\text{pt}}$$

$$+ \left(\begin{array}{c} \bar{a}^2 r_{\text{SiPM}}^2 P_{\text{ct}} \int_0^t p_{t_{\text{pt}}}\left(t_{\text{pt}} \mid \text{D}\right) \times \\[2ex] \int_0^{t-t_{\text{pt}}} p_{t_{\text{pt}}}\left(t_{\text{pt}} \mid \text{D}\right) \times f\left(t - t_{\text{pt}} - \tilde{t}\right) d\tilde{t} \; dt_{\text{pt}} \end{array} \right) \tag{5.16}$$

$$+ \left(\begin{array}{c} 2\bar{a}^2 P_{\text{ct}} \int_0^t p_{\text{pt}}\left(t_{\text{pt}} \mid \text{D}\right) \times f\left(t - t_{\text{pt}}\right) \times \\[2ex] \int_0^{t-t_{\text{pt}}} p_{t_{\text{ct}}}\left(t \mid \text{C}\right) \times f\left(t - t_{\text{pt}} - \tilde{t}\right) d\tilde{t} \; dt_{\text{pt}} \end{array} \right),$$

with the factor r_{SiPM} defined as

$$r_{\text{SiPM}} = \sqrt{1 + \frac{\sigma_a^2}{\bar{a}^2}} . \tag{5.17}$$

5.2.6.   SiPM signal expectation value and variance

The total SiPM signal V_Σ at a given time t caused by a given number N_{pt} of primary triggers is the sum of the N_{pt} distinct single photon signals $v_{\text{sps},n}$, where n is an integer between 1 and N_{pt}, as long as assumptions A1 – A5 hold. Consequently, the expectation value $E[V_\Sigma \mid t, N_{\text{pt}}]$ of the total signal V_Σ is given by the sum of the expectation values of the N_{pt} single photon signals, as follows from the assumption of statistical independence:

$$E\left[V_\Sigma \mid t, N_{\text{pt}}\right] = \sum_{n=1}^{N_{\text{pt}}} E\left[v_{\text{sps},n} \mid t, \text{D}\right] = N_{\text{pt}} \times E\left[v_{\text{sps}} \mid t, \text{D}\right]. \tag{5.18}$$

The same applies to the variance varΣ(V | t, Nsc) of the summed signal:

$$\text{var}\left[V_\Sigma \mid t, N_{\text{pt}}\right] = \sum_{n=1}^{N_{\text{pt}}} \text{var}\left[v_{\text{sps},n} \mid t, \text{D}\right] = N_{\text{pt}} \times \text{var}\left[v_{\text{sps}} \mid t, \text{D}\right]. \tag{5.19}$$

As a next step, also the variance of N_{pt} is taken into account. For mono-energetic γ-radiation the standard deviation of the number of primary triggers σpt is commonly expressed in terms of the statistical variation of N_{pt} (assuming Poisson statistics) and the so called intrinsic energy resolution R_{int} of the scintillation material (Dorenbos *et al.* 1995, Nassalski *et al.* 2007a):

$$\sigma_{\text{pt}} = \bar{N}_{\text{pt}} \sqrt{\left(\frac{R_{\text{int}}^2}{2.35^2} + \frac{1}{\bar{N}_{\text{pt}}}\right)}, \tag{5.20}$$

where $\bar{N}_{\text{pt}}$ is the mean of N_{pt}.

It is acknowledged that a significant portion of photons may escape the crystal after undergoing a Compton interaction, thus depositing only a part of their energy in the crystal. However, this is not problematic if the energy deposited in the crystal is measured with a resolution that is sufficiently high to allow for the discrimination of Compton scattered events as is the case in the experiments shown in this paper (see section 5.3.2).

The signal expectation value $E[V_\Sigma \,|\, t]$ and variance $\mathrm{var}[V_\Sigma \,|\, t]$ of the SiPM-scintillator system in response to mono-energetic γ-photons are then given by

$$E\left[V_\Sigma \,|\, t\right] = \bar{N}_{\mathrm{pt}} \times E\left[v_{\mathrm{sps}} \,|\, t\right] \text{ and} \tag{5.21}$$

$$\mathrm{var}\left[V_\Sigma \,|\, t\right] = \bar{N}_{\mathrm{pt}} \times \mathrm{var}\left[v_{\mathrm{sps}} \,|\, t\right] + \sigma_{\mathrm{pt}}^2 \times E\left[v_{\mathrm{sps}} \,|\, t\right]^2. \tag{5.22}$$

Finally, measurement noise needs to be included in the timing model. Measurement noise is considered here as the standard deviation σ_{el} of the (measured) electronic signal for a given, constant sensor signal (e.g. a zero signal). This definition includes electronic noise, pick-up of interference, and ADC quantization noise. As long as the measurement noise is statistically independent of the signal itself (which is fulfilled in most cases), the total variance of the measured electronic scintillation signal $\mathrm{var}_{\mathrm{tot}}[V_\Sigma \,|\, t]$ simply equals the sum of $\mathrm{var}[V_\Sigma \,|\, t]$ and σ_{el}.

5.2.7. Timing uncertainty

We can now define the time t_{th} at which the signal crosses a certain threshold level. The standard deviation σ_{t} of t_{th} can be obtained by evaluating (21) and (22) at the time $\bar{t}_{\mathrm{th}}$ where $E[V_\Sigma \,|\, \mathrm{t}]$ crosses V_{th} (i.e. $E\left[V_\Sigma \,|\, \bar{t}_{\mathrm{th}}\right] = V_{\mathrm{th}}$). In first-order approximation σ_{t} is then given by

$$\sigma_{\mathrm{t}} \approx \frac{\sqrt{\mathrm{var}_{\mathrm{tot}}\left[V_\Sigma \,|\, \bar{t}_{\mathrm{th}}\right]}}{\dfrac{\partial}{\partial \bar{t}_{\mathrm{th}}} E\left[V_\Sigma \,|\, \bar{t}_{\mathrm{th}}\right]} = \frac{\sqrt{\dfrac{E\left[v_{\mathrm{sps}}^2 \,|\, \bar{t}_{\mathrm{th}}, \mathrm{D}\right]}{\bar{N}_{\mathrm{pt}}} + \dfrac{R_{\mathrm{int}}^2}{2.35^2} \times E\left[v_{\mathrm{sps}} \,|\, \bar{t}_{\mathrm{th}}\right]^2 + \dfrac{\sigma_{\mathrm{el}}^2}{\bar{N}_{\mathrm{pt}}^2}}}{\dfrac{\partial}{\partial \bar{t}_{\mathrm{th}}} E\left[v_{\mathrm{sps}} \,|\, \bar{t}_{\mathrm{th}}\right]}. \tag{5.23}$$

Here it might be interesting to highlight the special case of a purely Poisson distributed $\bar{N}_{\mathrm{pt}}$ ($R_{\mathrm{int}} = 0$), negligible crosstalk contribution ($P_{\mathrm{ct}} = 0$), and negligible electronic noise ($\sigma_{\mathrm{el}} = 0$). Then, (5.23) can be reduced to

$$\sigma_{\mathrm{t}} = \frac{1}{\sqrt{\bar{N}_{\mathrm{pt}}}} \times \frac{r_{\mathrm{SiPM}} \sqrt{\displaystyle\int_0^{\bar{t}_{\mathrm{th}}} P_{t_{\mathrm{pt}}}\left(t_{\mathrm{pt}} \,|\, \mathrm{D}\right) \times f\left(\bar{t}_{\mathrm{th}} - t_{\mathrm{pt}}\right)^2 dt_{\mathrm{pt}}}}{\dfrac{\partial}{\partial \bar{t}_{\mathrm{th}}} \displaystyle\int_0^{\bar{t}_{\mathrm{th}}} P_{t_{\mathrm{pt}}}\left(t_{\mathrm{pt}} \,|\, \mathrm{D}\right) \times f(\bar{t}_{\mathrm{th}} - t_{\mathrm{pt}}) dt_{\mathrm{pt}}}. \tag{5.24}$$

This form is equivalent to the expression for the so-called straight response in the model for timing with PMT based detectors presented by Hyman et al. (Hyman *et al.* 1964). In (5.24) the factor r_{SiPM} can be seen as the SiPM equivalent of the PMT gain dispersion under the assumption of a Poisson

distribution of photoelectrons with mean value $\overline{N}_{pt}$. The equivalence of the two timing models in this special case is noteworthy particularly so as they have been derived via conceptually very different approaches.

Finally, the standard deviation in the difference between the time stamps obtained from two independent but identical detectors in a coincidence experiment then equals $\sigma_{t,co} = \sqrt{2} \times \sigma_t$. In the common case of a Gaussian time difference distribution, the FWHM coincidence resolving time (CRT) is then given by $CRT = 2.35 \times \sqrt{2} \times \sigma_t$.

5.3. Experimental methods

In all measurements the SiPM signals were amplified using preamplifiers made in-house, comprising two separate amplification branches. One branch has a bandwidth of 66 MHz and is optimized for the determination of the scintillation pulse energy. The second branch has a bandwidth of 2 GHz and is used for fast timing. The amplifier is described in detail by Huizenga *et al.* (2011). For each detector, the output of the fast timing branch (hereafter referred to as *timing signal*) was sampled by one of two synchronized 10-bit sampling ADCs (Acqiris DC282, sampling rate 8 GS/s, clock jitter $\leq$ 1.2 ps). Unless mentioned otherwise, data analysis was performed offline on the sampled timing signals.

All measurements were performed at a stable ambient temperature (23°C $\pm$ 1°C) without further temperature stabilization of the sensor or electronics. In order to account for possible temperature changes in between different measurements, which may result in changes of V_{br} and/or possible drifts in V_{bias} a correction was applied to those measured parameter values that depend on the voltage-over-breakdown $V_{ob} = |V_{bias} - V_{br}|$ (i.e., the parameters $\overline{N}_{pt}$ and Pct). This correction was based on the average single cell amplitude $\overline{a}$, which was determined for each measurement as described in section 5.3.1.3.

5.3.1. Model Input parameters

For several model input parameters it was necessary to perform dedicated measurements. The details of those measurements are discussed in the following. The values of all input parameters, including those that were obtained directly from literature, will be presented in section 5.4.1.

5.3.1.1. Scintillation pulse shape

The scintillation pulse time constants for LYSO:Ce and LaBr$_3$:5%Ce were determined in a time correlated single photon counting experiment as described in (Seifert *et al.* 2010).

5.3.1.2. Average number of primary triggers

In order to minimize the influence of saturation, the average number of primary triggers $\overline{N}_{pt}$ was determined using low energy γ-photons (27.3 keV from a ^{125}I source) with the method discussed in detail in (van Dam *et al.* 2010).

In short, this method makes use of a comprehensive analytical model predicting the effective number of fired cells (i.e. the signal charge divided by the charge of a single cell signal) in response to a given scintillation pulse. The model includes the effects of crosstalk, afterpulses and saturation. The product of detector PDE η and light yield Y for a given detector is determined using ($\eta \times Y$) as a fit parameter and fitting the model predictions to the experimental data.

It should be noted that the values are free from contributions of crosstalk and afterpulses, which otherwise would be as high as 30% (Du and Retiere 2008, Retiere *et al.* 2009, van Dam *et al.* 2010). These values were then used to estimate $\bar{N}_{pt}$ for 511 keV γ-photons, taking into account the light yield non-proportionality of the scintillators (0.96 for LaBr$_3$:5%Ce (Owens *et al.* 2007) and 0.70 in the case of LYSO:Ce (Pidol *et al.* 2004, Kapusta *et al.* 2005).

The measurements were performed using the same bias voltages as in the validation measurements described in section 5.3.2. As touched upon earlier, however, V_{ob} might be subject to long term thermal drifts. Therefore, V_{ob} was determined for each of these measurements and a linear correction for changes in V_{ob} was applied to the measured values of $\bar{N}_{pt}$.

5.3.1.3.   Single cell signals

In order to determine the signal shape function $f(t)$, the SiPMs (MPPC-S10362-33-050C) were illuminated with a Hamamatsu PLP-04 laser (wavelength 633 nm, average pulse duration 50 ps, repetition rate 10 kHz). The laser light was attenuated with neutral density filters so that only a few cells (~30) were fired. The signal of the timing branch of the preamplifiers was recorded with an Acqiris DC282 digitizer (10 bit at 8 GS/s) for 2000 laser pulses. These traces were normalized and then averaged. A cubic spline interpolation was performed in order to obtain a continuous function $f(t)$.

In order to determine the average single cell amplitude $\bar{a}$ as well as the amplitude standard variation σ_a, amplitude histograms of dark pulses were measured for different SiPM bias voltages. This was done by first finding and isolating dark pulses that did not overlap within a time window of 20 ns. For each of these pulses the amplitude was determined by means of a least square fit of the normalized average single cell signal $f(t)$, using the amplitude, an offset value, and the pulse-starting-time as fit parameters. The fitted amplitude values were subsequently histogrammed. From these histograms the average single cell amplitude $\bar{a}$ was determined as the average distance between the first three neighboring peaks in the dark pulse amplitude distribution. Based on this value, V_{ob} was determined for each measurement.

The relative amplitude standard variation σ_a, which in principle does not depend on V_{ob}, was extracted from the width of the first peak occurring in the dark pulse spectrum measured at $V_{ob} = 1.54$ V. This voltage was chosen as the best compromise between the peak-height to noise ratio (which improves with increasing bias voltage) and the contribution of afterpulses and overlapping dark counts.

5.3.1.4.   *Optical crosstalk probability*

The probability P_{ct} for a single crosstalk event to occur given that there was a primary trigger was determined with the method employed by Du and Retiere (2008) and Retiere *et al.* (2009) at the same bias voltages as used in the measurements described in section 5.3.2.

5.3.1.5.   *Electronic noise*

The electronic noise was determined for each measurement from the baseline of the digitized traces. It was measured as the standard deviation σ_{el} of the difference between the recorded signal and a baseline value. This baseline value was determined for each measurement point as the signal average in the time window between 1 ns and 2 ns prior to the measurement point, so as to match the procedure described in section 5.3.2.

5.3.2.   Validation measurements

In order to validate the model predictions, the coincidence resolving time of two identical SiPM-based scintillation detectors facing a ^{22}Na point source from opposite sides was determined. Figure 5.3 shows a schematic representation of the measurement setup. Each detector comprised a 3 mm × 3 mm × 5 mm crystal of either LYSO:Ce (Crystal Photonics, Inc) or LaBr$_3$:Ce5% (Saint Gobain, Brillance 380). All crystals had one polished surface, whereas the remaining five sides were chemically etched in the of case LYSO:Ce and depolished in the case of LaBr$_3$:5%Ce. The SiPMs (Hamamatsu MPPC-S10362-
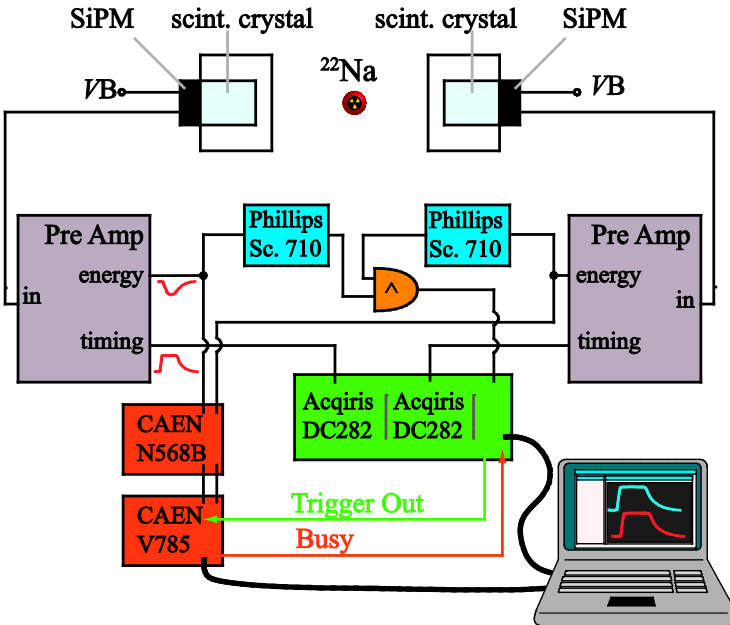
Figure 5.3. Schematic overview of the experimental setup.

33-050C) were coupled directly to the polished crystal surfaces using a Silicone encapsulation gel (Lightspan LS-3252). The crystals were enclosed in Spectralon®, a PTFE based material with a reflectivity specified better than 98% at 420 nm (the main emission wavelength of LYSO:Ce).

The gain of the preamplifier timing channels and the ADC settings were chosen such that the ADC range (set to 50 mV for LYSO:Ce and to 100 mV for LaBr$_3$:5%Ce) corresponded to about 10% – 15% of the full pulse height. The drawback that the timing signal clipped after exceeding the maximum of the ADC range (making a second channel for energy determination necessary) was outweighed by the improvement in signal-to-noise-ratio, as the ADC noise appeared to be the largest noise source in our setup.

The energy deposited in the scintillator was determined from the signals of the slower preamplifier branches. These energy signals were fed into leading edge discriminators (Phillips Scientific 710) set to accept events above 410 keV. The discriminator outputs were used to create a coincidence trigger for the ADCs sampling the timing signals of the SiPMs. In addition, the energy signals were shaped (CAEN N568B shaping amplifier) and the peak values were digitized (CAEN V785) and stored. In a post-processing step a refined energy selection was applied using an energy window on the full-width-at-tenth-maximum (FWTM) of the 511 keV photopeak.

For each accepted event a time stamp was created from the digitized timing signals. This was done by interpolating each trace with a full cubic spline and determining the intersection of the interpolated data with a fixed threshold relative to the baseline. The baseline was determined for each trace individually as the average signal within 2 ns directly before the onset of the pulse. This procedure was repeated for each measurement at several different threshold levels ranging from 1.5 mV to 30 mV, corresponding to about ~1 to ~20 times the maximum single cell signal amplitude. The CRT was determined as the FWHM of Gaussian fits to the measured time difference spectra.

5.4. Results

In section 5.4.1, we first present the values of the model input parameters determined for the SiPM-based scintillation detectors described in section 5.3.2. Subsequently, the model is validated by comparison to measurements (section 5.4.2). Finally, we utilize the validated model to study the dependence of the CRT on several SiPM and scintillator parameters (section 5.4.3).

5.4.1. Model Input parameters

5.4.1.1. *Scintillator properties*

The time constants and the corresponding P_{ec} that define the scintillation pulse shapes for LYSO:Ce and LaBr$_3$:5%Ce are summarized in Table 5.1. A single event chain (see section 5.2.3) was found to be sufficient to describe the scintillation pulse of LYSO:Ce. The pulse shape of LaBr$_3$:5%Ce has been

Table 5.1. Model input parameters associated with the scintillators

	$\tau_{r,i}$ / $P_{ec,i}$ (ns)	τ_d (ns)	R_{int} (FWHM at 511keV)
LYSO	0.09 / 1	43.8 ± 0.8	9.0 % [1]
LaBr$_3$:5%Ce	0.37 / 0.8 2.2 / 0.2	15	3.5 % [1]

[1] (Nassalski *et al.* 2007b)

investigated by Glodo *et al.* (2005) as a function of the Ce-concentration. They found that at least two energy transfer processes have to be taken into account in order to adequately describe the rising edge of the scintillation pulse. We observed the same in our measurements and the values for $\tau_{r,1}$ and $\tau_{r,2}$ as well as the probabilities of their occurrence are very similar to the values reported in (Glodo *et al.* 2005). However, in our samples we did not find a significant second component in the decay process. Therefore, two event chains were modeled with $\tau_{d,1} = \tau_{d,2} = \tau_d$ and with $\tau_{r,1}$ and $\tau_{r,2}$, as listed in Table 5.1.

5.4.1.2. *Average number of primary triggers*

The values determined for the average number of primary triggers $\bar{N}_{pt}$ per 511 keV scintillation event are listed in Table 5.2 and Table 5.3 for LYSO:Ce and LaBr$_3$:5%Ce, respectively. The major advantage of the method used to determine these values (see section 5.3.1.2) is that it directly gives a measure for $\bar{N}_{pt}$ and no further assumptions regarding the photon collection efficiency have to be made. A drawback of the method is that it does not allow for a direct estimation of the uncertainty in the measurement. However, presumably the

Table 5.2. Model input paremeters associated with the SiPMs for the measurements wtih LYSO:Ce

V_{ob}	**(V)**	1.14	1.35	1.54	2.12
$\bar{N}_{pt}$		3300	3600	3900	4700 [1]
η		0.25 [2]	0.27 [2]	0.29 [2]	0.35 [2]
$\bar{a}$	**(mV)**	1.31 ± 0.07	1.55 ± 0.06	1.77 ± 0.06	2.44 ± 0.09
σ_a / $\bar{a}$		0.12	0.12	0.12	0.12
R_d	**(kΩ)**	1	1	1	1
C_{tot}	**(fF)**	90	90	90	90
σ_{el}	**(mV)**	0.31 ± 0.04	0.31 ± 0.04	0.32 ± 0.04	0.36 ± 0.04
P_{ct}		0.10 ± 0.01	0.12 ± 0.01	0.14 ± 0.01	0.24 ± 0.02
σ_{trans}	**(ps)**	139 [3]	131 [3]	124 [3]	120 [3]

[1] value obtained by linear extrapolation (see text)

[2] calculated from $\bar{N}_{pt}$ using the absolute light yield reported by de Haas and Dorenbos (2008) (26000 photons/MeV)

[3] Ronzhin *et al.* (2010)

Table 5.3. Model input paremeters associated with the SiPMs for the measurements wtih LaBr₃:5%Ce

V_{ob}	**(V)**	1.22	1.37	1.54	2.06
$\bar{N}_{pt}$		4900	5200	5500	6200 [1]
η		0.136 [2]	0.144 [2]	0.150 [2]	0.173 [2]
$\bar{a}$	**(mV)**	1.59 ± 0.07	1.78 ± 0.07	2.00 ± 0.06	2.69 ± 0.09
$\sigma_a / \bar{a}$		0.12	0.12	0.12	0.12
R_d	**(kΩ)**	1	1	1	1
C_{tot}	**(fF)**	90	90	90	90
σ_{el}	**(mV)**	0.30 ± 0.04	0.31 ± 0.04	0.30 ± 0.04	0.40 ± 0.04
P_{ct}		0.11 ± 0.01	0.14 ± 0.01	0.15 ± 0.01	0.23 ± 0.02
σ_{trans}	**(ps)**	132 [3]	127 [3]	124 [3]	120 [3]

[1] value obtained by linear extrapolation (see text)

[2] calculated from $\bar{N}_{pt}$ using the absolute light yield reported by de Haas and Dorenbos (2008) (70000 photons/MeV)

[3] Ronzhin *et al.* (2010)

largest contribution to this uncertainty is the measurement error in the determination of the charge gain per fired cell, which is in the order of 5%. Other contributions arise from the determination of the crosstalk probability and the afterpulse properties (i.e. the afterpulse time constants and the average number of afterpulses per primary trigger).

At the highest bias voltage the relative contributions of crosstalk and afterpulsing become very large. Unfortunately, the determination of the afterpulse properties becomes problematic at higher bias voltages due to the drastically increasing dark count rate (Retiere *et al.* 2009, van Dam *et al.* 2010), causing the error bars on $\bar{N}_{pt}$ to become unreasonably large. We therefore opted for a linear extrapolation of the values obtained at lower V_{ob}. A simple linear extrapolation method was chosen based on the data published by Eckert *et al.* (2010), which suggest that a linear function describes the V_{ob}-dependency of the PDE reasonably well within the voltage range applied in our measurements ($V_{ob} = 1.14$ V to $V_{ob} = 2.12$ V).

For illustration, the corresponding value of the detector PDE, η, calculated from $\bar{N}_{pt}$ is also shown in Table 5.2 and Table 5.3. Here, literature values for the scintillator light yield were employed (de Haas and Dorenbos 2008). The lower PDE obtained for LaBr₃:5%Ce compared to LYSO:Ce is caused by the difference in the SiPM spectral sensitivity at the main emission wavelength of the materials: 380 nm for LaBr₃:5%Ce and 420 nm for LYSO:Ce, respectively.

The values for the intrinsic energy resolution R_{int} (FWHM at 511 keV) for the scintillation materials used in this work were taken from literature (Dorenbos *et al.* 1995) (Nassalski et al. 2007b) and are listed in Table 5.1.
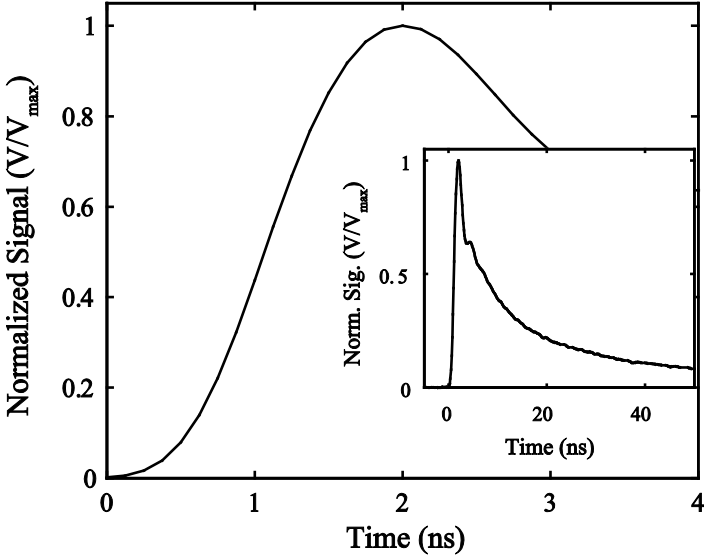
Figure 5.4. Initial part of the average MPPC-S10362-33-050C single cell signal shape f(t) measured as the normalized electronic response to a fast laser pulse. The full signal shape is shown in the inset.

5.4.1.3.   Single cell signal properties

Figure 5.4 shows the initial part of the single cell signal shape function $f(t)$, determined as described in section 5.3.1.3.The inset shows the full pulse shape. It can be seen that the single cell signal decay time is much longer than its rise time, a feature characteristic for SiPMs.

Figure 5.5 shows some examples of dark pulse amplitude histograms determined at different bias voltages. The histograms show well-separated peaks for 1, 2, and 3 simultaneously fired cells. These data were employed to determine the average single cell amplitude $\bar{a}$. Table 5.2 and Table 5.3 show the values for $\bar{a}$ as well as σ_a that were determined at the different V_{ob} used in the validation measurements employing for LYSO:Ce and LaBr$_3$:5%Ce, respectively.

5.4.1.4.   Optical crosstalk

The measured probabilities P_{ct} for a single crosstalk event to occur given that there was a primary trigger are shown in Table 5.2 and Table 5.3. As mentioned in section 5.2.4.2, one contribution to the temporal distribution crosstalk events with respect to the primary trigger is considered to follow an exponential decay with a time constant corresponding to $C_{tot} \times R_d$. Whereas C_{tot} is readily determined from a measurement of the single cell gain of the SiPM (see section 5.3.1.3) and (Cova *et al.* 1996)), we are currently not aware of any method to
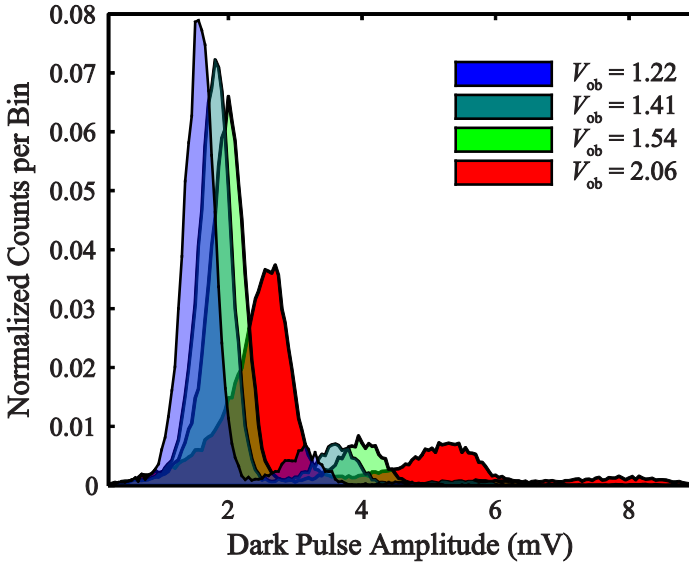
Figure 5.5. Dark pulse amplitude histograms for different values of the voltage-over-breakdown V_{ob} as obtained for the validation measurements with LaBr$_3$:5%Ce.

measure R_d accurately for SiPMs. Therefore, if not mentioned otherwise, a typical value of $R_d = 1$ kΩ is assumed (Cova *et al.* 1996, Seifert *et al.* 2009). The influence of choosing different values for R_d will be discussed in section 5.4.3.2.

5.4.1.5.   Electronic noise

The values for the electronic noise contribution σel for each value of V_{ob} as determined according to the method described in section 5.3.1.5 are listed in Table 5.2 and Table 5.3.

5.4.1.6.   Effective transit time spread

Because of the small size of the scintillation crystals, the charge carrier transit time spread is expected to be the dominant factor in the effective transit time spread σ_{trans}. The values for σ_{trans} listed in Table 5.2 and Table 5.3 are taken from literature (Ronzhin *et al.* 2010). These values were measured for Hamamatsu MPPCs with the same microcell pitch as the SiPMs used in our validation measurements (50 μm) but with a sensor area of 1 mm × 1 mm.

Here it should be noted that also values of σ_{trans} for the MPPC-S10362-33-050C (with 3 mm × 3 mm active area) have been measured by Ronzhin *et al.* (2010). They found these values to be considerably larger than σ_{trans} measured for the 1 mm × 1 mm device (i.e. 220 ps – 330 ps compared to the values listed in Table 5.2 and Table 5.3). Nevertheless, the transit time spread is expected to

be similar for the two types of MPPCs as the microcell structure is the same for both devices and consequently there is no difference in the transit time spread of individual cells. Furthermore, the dimensions of the larger SiPMs are too small for a significant contribution of the propagation delay difference between microcells at different locations within the same device. However, the nine-times larger capacitance of these SiPMs with a larger active area has a significant deteriorative effect on the slope to noise ratio resulting in a relatively increased influence of the electronic noise on the determination of σtrans. Therefore, the smaller devices with the smaller terminal capacitance are in principle better suited for single photon timing experiments needed to determine σtrans.

5.4.2.   Comparison of model and measurement

A comparison between the model predictions and the measurements is shown in Figure 5.6 and Figure 5.7. The graphs depict the coincidence resolving time as a function of the trigger threshold level at four different voltages-over-breakdown V_{ob} for LaBr$_3$:5%Ce and LYSO:Ce, respectively. To facilitate comparison of the presented data, all threshold levels are given in terms of equivalent single cell signal amplitudes, i.e. $V_{th}/\bar{a}$. The error bars on the
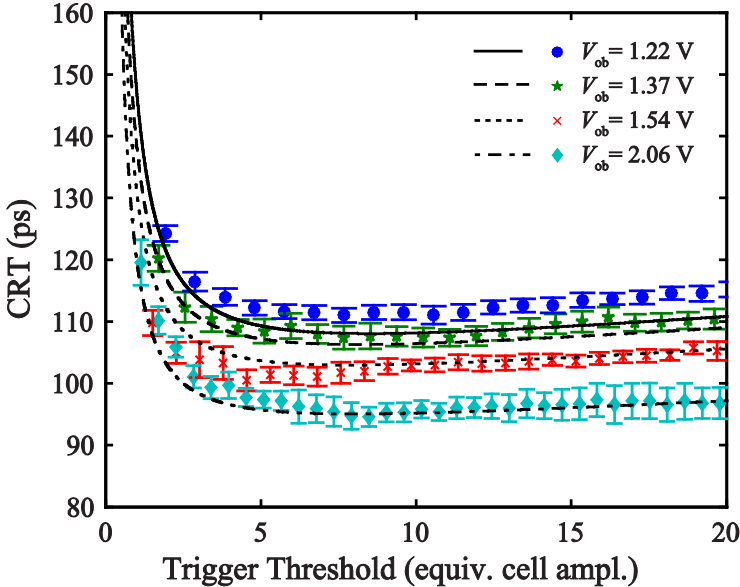
Figure 5.6. Comparison between the predicted CRT (lines) and the measured one (symbols) as a function of the trigger threshold for LaBr$_3$:5%Ce measured at V_{ob} = 1.22 V (circles and solid line), at V_{ob} = 1.37 V (stars and dashed line), at V_{ob} = 1.54 V (crosses and dotted line), and at V_{ob} = 2.06 V (diamonds and dash-dotted line).
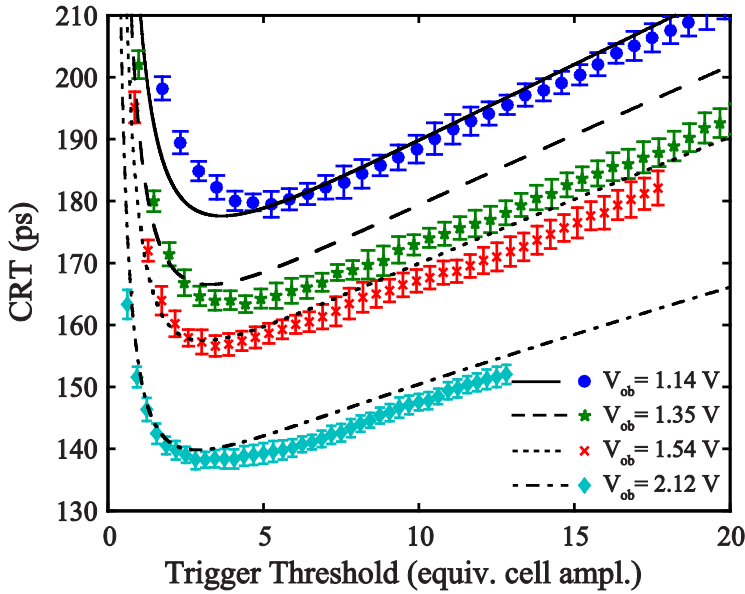
Figure 5.7. Comparison between the predicted CRT (lines) and the measured one (symbols) as a function of the trigger threshold for LYSO:Ce measured at $V_{ob} = 1.14$ V (circles and solid line), at $V_{ob} = 1.35$ V (stars and dashed line) at $V_{ob} = 1.54$ V (crosses and dotted line), and at $V_{ob} = 2.12$ V (diamonds and dash-dotted line).

measured data correspond to the 95% confidence intervals on the widths of the Gaussian distributions that were fitted to the timing spectra. It can be seen that the CRT depends strongly on the value of the leading edge threshold applied. The lowest CRTs (95 ps $\pm$ 3 ps FWHM for LaBr$_3$:5%Ce and 138 ps $\pm$ 2 ps FWHM for LYSO:Ce) are obtained at the highest bias voltages (equivalent to $V_{ob} = 2.06$ V and $V_{ob} = 2.12$ V, respectively) and at relatively low threshold levels (equivalent to 8 and 3 SCS amplitudes, respectively).

In the case of LaBr$_3$:5%Ce the model slightly underestimates the measured values at the lower bias voltages. For LYSO:Ce, on the other hand, the model predictions are somewhat too large at higher bias voltages. These differences between the measurements and model predictions are small but not negligible. However, due to the large number of model input parameters it cannot be said with certainty which of the associated uncertainties contribute most significantly to the overall uncertainty in the predicted timing resolution. The matter is further complicated by the fact that some of the input parameters are literature values and not all details of their measurement are known. In particular the parameter $\overline{N}_{pt}$ may be associated with relatively large uncertainties, for multiple reasons such as the uncertainties in the corrections for crosstalk and afterpulsing and the assumed nonlinearity of the light yield (see section 5.3.1.2). Also the values of

σ_{trans}, which do not contain any contribution of photon transit within the crystal (section 5.4.1.6), should be considered with care.

Nevertheless, it can be said that the model predictions are mostly in agreement with the measurements. This holds for the shape of the curves, the trend as V_{ob} is varied, and the absolute values. This is especially satisfactory in light of the facts that all model input parameters were either measured or taken from literature and that no fits or parameter adjustments were applied anywhere.

5.4.3. Dependence of CRT on SiPM and scintillator properties

In the following, the dependence of the detector timing resolution on several SiPM- and scintillator-specific properties is investigated. To this end the value of CRT_{min}, defined as the minimum calculated CRT in the range of threshold levels between 3 and 10 equivalent cell amplitudes, is studied as a function of several model input parameters. Only one parameter is varied at a time, while the remaining ones are kept constant at the values employed to calculate the CRTs at $V_{ob} = 1.54$ V for both detectors.

5.4.3.1. Influence of $\bar{N}_{pt}$ and scintillator time constants

The summed number of primary triggers that have occurred until a given point in time is mainly determined by: $\bar{N}_{pt}$, $\tau_{r,1}$, $\tau_{r,2}$, and τ_d. The initial primary trigger rate is proportional to $\bar{N}_{pt}$ as well as to $1/\tau_d$ as long as τ_d can be considered large with respect to $\tau_{r,1}$ (and $\tau_{r,2}$). Obviously, the initial rate also increases with the inverse of the fastest rise time constant $1/\tau_{r,1}$, yet this increase is not strictly linear.

Figure 5.8 shows CRT_{min} against the relative parameter value of $\bar{N}_{pt}$, $\tau_{r,1}$, $\tau_{r,2}$, and τ_d for LaBr$_3$:5%. As expected, the graphs corresponding to the relative change in $\bar{N}_{pt}$, and in $1/\tau_d$ overlap almost entirely. Only at large $1/\tau_d$ a small deviation can be seen due to the fact that τ_d then approaches $\tau_{r,1}$ and/or $\tau_{r,2}$. The minimum calculated CRT is proportional to the inverse square root of the varied parameter, as is known to be the case when counting statistics are the dominating factor contributing to the timing resolution (Post and Schiff 1950, Hyman *et al.* 1964, Fishburn and Charbon 2010). The variations in CRT_{min} with $\tau_{r,1}$ and/or $\tau_{r,2}$ are considerably smaller than the variation with the other two parameters. Similar trends are observed for LYSO:Ce, however, the corresponding graphs are omitted here for brevity.

5.4.3.2. Influence of crosstalk

As discussed in sections 5.2.1 and 5.2.4.2 the distribution of crosstalk events with respect to the corresponding primary trigger is determined by three parameters: P_{ct}, τ_{ct}, and the product of R_d and C_{tot}. Figure 5.9 illustrates the influence of these parameters on the predicted CRT_{min} for LaBr$_3$:5%. It can be seen that large variations in either of these parameters ($\pm 100\%$) lead to only small changes in the observed CTR_{min} ($\pm \sim 3$ ps).
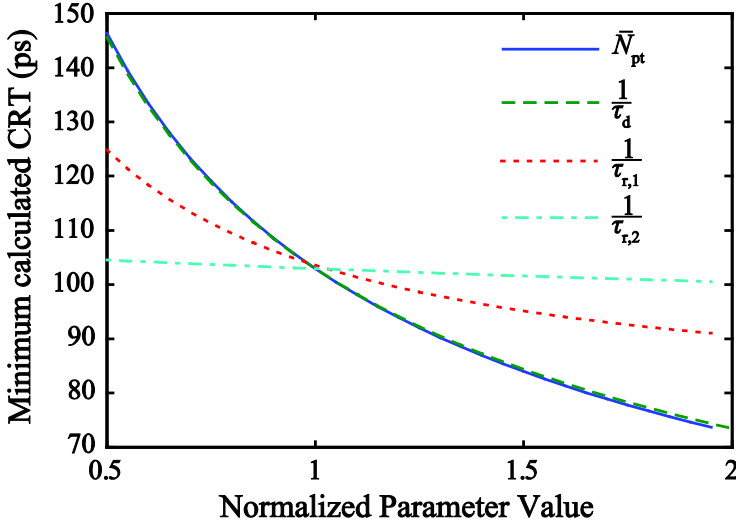
Figure 5.8. Minimum calculated CRT for LaBr$_3$:5%Ce as a function of the relative difference in $\bar{N}_{pt}$ (solid line), $1/\tau_d$ (dashed line), $1/\tau_{r,1}$ (dotted line), and $1/\tau_{r,2}$ (dashed-doted line) with the remaining parameters kept constant at the values employed to calculate the CRTs at $V_{ob} = 1.54$ V. The curves for $\bar{N}_{pt}$ and $1/\tau_d$ mostly overlap.
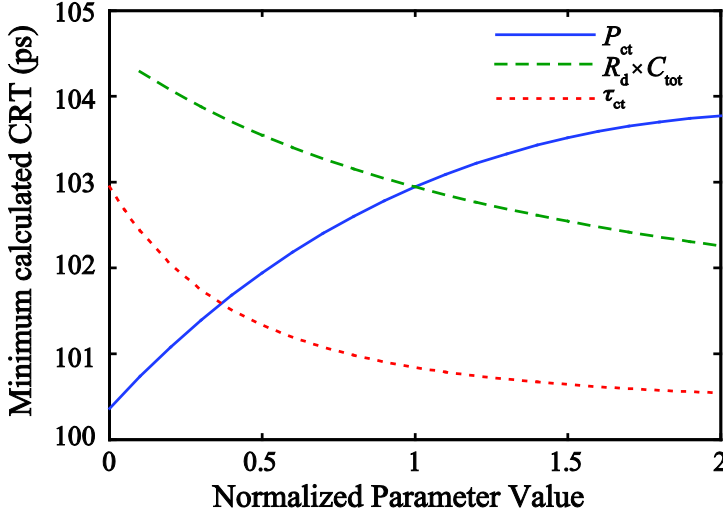
Figure 5.9. Calculated minimum CRT for LaBr$_3$:5%Ce as a function of P_{ct} (solid line), $C_{tot} \times R_d$, (dashed line) and τ_{ct} (dotted line). P_{ct} and $C_{tot} \times R_d$ are normalized to the values listed in Table 5.2 for $V_{ob} = 1.54$ V. The parameter τ_{ct} is normalized to 150 ps (although it is 0 in all other calculations). The remaining parameters were kept constant at the values employed to calculate the CRTs at $V_{ob} = 1.54$ V.

A second interesting fact is that CRT_{min} is getting smaller as the time constant τ_{ct} increases. This may be somewhat counterintuitive, since with increasing τ_{ct} also the spread of the distribution crosstalk event increases and a larger spread in time should be associated with a larger contribution to the timing uncertainty. At this point, it is important to recall that the trigger threshold of optimum timing is at low values and therefore the threshold crossing occurs relatively soon after the first cell is fired. An increase of τ_{ct}, however, also means that the average delay between the corresponding primary trigger and the crosstalk event increases. This, in return reduces the average number of crosstalk events occurring before the time of threshold crossing and thus the overall contribution of crosstalk to the timing uncertainty.

A similar effect can be observed when the value for $R_d \times C_{tot}$ is increased, effectively increasing the time constant of the exponential decay in $pt_{ct}(t \mid t_{pt}, C)$. As one may expect, CTR_{min} decreases with decreasing P_{ct} since reducing the amount of crosstalk effectively reduces the signal variance.

Similar conclusions can be obtained when the same graphs are plotted for LYSO:Ce, however for reasons of brevity these are not shown here.

5.5.   Discussion

5.5.1.   CRT dependence on the trigger threshold level

Among the noteworthy observations in this study are the values of the (normalized) trigger threshold $V_{th,opt}$ at which the CRT assumes a minimum. When comparing Figure 5.6 and Figure 5.7, one can see that in all cases $V_{th,opt}$ is larger for LaBr$_3$:5%Ce ($V_{th,opt} \approx 10$ equivalent cell amplitudes) than for LYSO:Ce ($V_{th,opt} \approx 3$ equivalent cell amplitudes). This is a direct consequence of the difference in photon statistics between the two systems. A similar influence of the scintillator properties on the optimum trigger point has been shown by Hyman (1965) for the so-called integral response of PMT signals (without the addition of electronic noise).

The mechanism underlying this phenomenon is the fact that, in contrast to what is sometimes assumed, it is generally not the first detected photon (or the first primary trigger) that provides the optimum timing resolution in a realistic scintillation detector (i.e. with a finite scintillator rise time and some form of transit time spread). This was also demonstrated by Fishburn and Charbon (2010). Applying these authors' model of the counting statistics in scintillation detectors to our experimental conditions, one can calculate the expected spread of the trigger time of a fired cell of a given order within the sequence of all scintillation related trigger events (i.e. the 1st, 2nd, 3rd, ... single cell trigger). This is illustrated in Figure 5.10 for both crystal types and the highest V_{ob} used in the respective experiments.

It should be noted, that the horizontal axis in Figure 5.6 and Figure 5.7 cannot directly be related to the one in Figure 5.10. Due to the finite rise time of the SCSs one can find an infinite number of permutations of trigger times for any number of single cell triggers that lead to the same analog sum. In other words, a
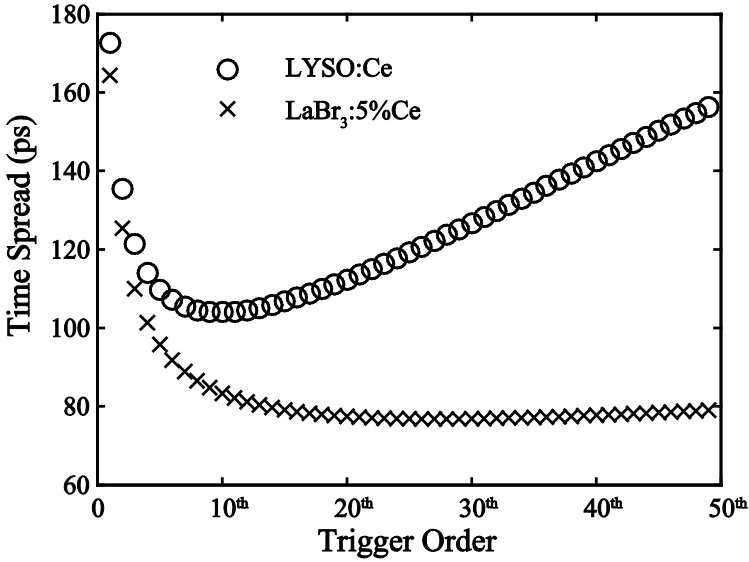
Figure 5.10. Expected arrival time spread (FWHM) for individual photons calculated following (Fishburn and Charbon 2010) employing the same scintillator properties as used in this work for LaBr₃:5%Ce (crosses) and LYSO:Ce (circles). The necessary detector properties (σ_{trans} and η) were set to match the ones measured at the highest respective V_{ob}.

given threshold value does not have a unique number of fired cells prior to the time of threshold crossing.

Nevertheless, the comparison between the single photon trigger time spread depicted in Figure 5.10 and the graphs in Figure 5.6 and Figure 5.7 yields a striking similarity, illustrating how the basic shape of the graphs in Figure 5.6 and Figure 5.7 is determined by single-photon counting statistics. E.g. the primary trigger that carries the smallest time variance can be estimated to be the 25th to 28th trigger in case of LaBr₃:5%Ce, in contrast to the 6th to 8th trigger in case of LYSO:Ce, depending on V_{ob}.

5.5.2.   Influence of electronic noise

The fact that, due to the counting statistics involved, "earlier" primary triggers and, therefore, lower threshold values are more favorable in the case of LYSO:Ce also has implications for the influence of electronic noise on the minimum obtainable CRT. This is because the slope of the rising edge of the signal is smaller at lower signal values. As a consequence the relative contribution of electronic noise is smaller for the LaBr₃:5%Ce detectors than for the LYSO:Ce detectors. This can be demonstrated by removing the contribution of the electronic noise from the model predictions completely, resulting in improvements of the minimum CRT of 1 ps – 2 ps in the case of LaBr₃:5%Ce

and 7 ps – 13 ps in the case of LYSO:Ce (depending on V_{ob}).

It is in fact remarkable that the contribution of electronic noise is only about ~8% at most. The significance of this becomes clear, if we impose a bandwidth limitation in the form of a digital RC-low-pass-filter on the SCS shape $f(t)$. For example the predicted CRT in the case of LYSO:Ce degrades only by about 10% when a RC-filter with a cutoff frequency of 200 MHz is assumed. The impact on the CRT is even less in the case of LaBr$_3$:5%Ce (about 2%), as expected from the previous discussion. It might therefore seem that the demands on the preamplifier bandwidth are not very severe. This is only the case, however, as long as counting statistics favor "late" triggers. In a detector with considerable lower photon collection efficiency, for example, earlier primary triggers will be associated with the lowest variance (Fishburn and Charbon 2010). In such a detector, lower threshold levels would be required, which in return also increases the demand on amplifier bandwidth and noise.

5.5.3. Influence of amplitude walk

A further interesting result is obtained when the variation in the number of primary triggers σ_{pt}, i.e. the corresponding term in (5.22), is set to zero. This allows for an estimate on the improvement in the CRT if an ideal correction for amplitude walk could be achieved. Doing so results in surprisingly small differences compared to the cases where σpt is taken into account. For LaBr$_3$:5%Ce, CRT$_{min}$ reduces by 1% and for LYSO:Ce it is 2% lower. Apparently, the low trigger thresholds that are applied minimize amplitude walk, explaining why it is possible to achieve such good timing resolutions with a simple leading edge trigger.

5.5.4. Model limitations

In the derivation of the timing model (section 5.2) two significant approximations were made. First, only single crosstalk events were taken into account, based on the notion that only a few percent of the primary triggers give rise to more than one crosstalk event (see section 5.2.4.2). Given that the influence of crosstalk on the timing uncertainty appears to be small in any case (see section 5.4.3.2), this approximation seems justified. Furthermore a more detailed knowledge of the temporal distribution of crosstalk events would be desirable if more accurate predictions of the influence of crosstalk on the CRT are required. However, a detailed investigation of the crosstalk phenomenon is considered beyond the scope of this paper.

The second approximation is that the dark count rate has not been included in the timing model. The best CRTs (95 ps ± 3 ps FWHM for LaBr$_3$:5%Ce and 138 ps ± 2 ps FWHM for LYSO:Ce) were obtained at relatively high overvoltages (V_{ob} = 2.1 V), at which the dark count rate is in the hundreds of megacounts per second. This, however, has very little influence as the baseline correction applied in these measurements largely removes any contribution from dark counts that occur earlier than about 2 ns before the scintillation pulse. Furthermore, at such overvoltages the probability for a dark count to occur

within these 2 ns and the time of threshold crossing (in total ~3 ns) is still relatively small (in the order of 0.5%). Only at very high overvoltages ($V_{ob} \geq 2.5$ V), the assumption of a negligible influence of the dark count rate may no longer hold and dark counts may have to be included in the modeling.

It can be concluded that the applied approximations are justified and that the proposed model accurately predicts the CRT measured with the SiPM-based scintillation detectors investigated in this work.

The considerations in this paper are limited to small crystal sizes, resulting in a negligible influence of the photon transit time spread. This, however, is not a requirement imposed by the model. Formally, the incorporation of photon transit time spread is relatively simple. As long as the assumptions of statistical independence hold, all one needs to do is to change the corresponding distribution function $pt_{trans}(t)$ in (5.2) accordingly. This is feasible, since no conditions are imposed on the nature of this distribution. It is assumed to be Gaussian in our considerations, yet in principle it may be replaced by any function that fulfills the requirements on a pdf.

In practice, however, it may not be trivial to acquire an accurate description of $pt_{trans}(t)$. It includes two major contributions. One is the spread in the average arrival time of the scintillation photons due to the variation of the position of interaction (DOI) of the γ-photons in the crystal (Moses and Derenzo 1999, Shibuya *et al.* 2008, Vinke *et al.* 2010). The second contribution arises from the variation in the optical path lengths and, therefore, the transit times of individual scintillation photons within the crystal (Moses and Derenzo 1999, Choong 2009). Especially the determination of the last contribution is challenging since it is difficult to measure accurately, while simulations are very sensitive to the definition of the optical properties of the scintillation crystal, the reflective enclosure, and the interfaces between them, all of which are difficult to determine accurately (van der Laan *et al.* 2010).

5.6.   Conclusion

We have developed a comprehensive statistical model to predict the timing resolution of scintillation detectors based on silicon photomultipliers. It incorporates the relevant scintillator properties (i.e. the scintillation pulse shape and the light yield) as well as the SiPM electronic response, crosstalk and transit time spread. It was shown that the proposed model reduces to the well-established Hyman model for timing with PMTs (Hyman *et al.* 1964) under the assumptions of a Poisson distributed number of primary triggers (photoelectrons in case of a PMT), negligible crosstalk probabilities, and negligible electronic noise.

To validate the model and to illustrate how the proposed model can be used to better understand which factors dominate the timing resolution of a SiPM-based scintillation detector, all necessary model input parameters were determined for two sets of detectors employing Hamamatsu MPPC-S10362-33C sensors optically coupled to small LYSO:Ce crystals or LaBr$_3$:5%Ce, respectively. The

predicted coincidence resolving times as a function of the threshold level of a leading edge trigger are in good agreement to measured data for these detectors. Specifically, CRTs as low as 138 ps ± 2 ps FWHM for LYSO:Ce and 95 ps ± 3 ps FWHM for LaBr$_3$:5%Ce were obtained, demonstrating the outstanding timing potential of SiPM-based scintillation detectors.

The proposed model could be used to obtain valuable information regarding the major contributions to these CRT values. For our detectors, it was shown that the CRT is mainly limited by photon counting statistics (as determined by the average number of primary triggers, the scintillation pulse shape and the effective transit time spread). The spread in the total number of detected photons, the SiPM dark current, crosstalk, electronic noise, and amplifier bandwidth all appear to have much less influence on the CRT. Consequently, further improvement of the CRT of our detectors can essentially only be achieved by increasing the primary trigger rate, viz. by increasing the detector PDE, increasing the scintillator light yield, and/or reducing the scintillator rise and decay times.

Acknowledgements

Appendix

List of symbols and abbreviations

a .... static single cell amplitude
CRT .... coincidence resolving time (FWHM)
C .... condition that a cross-talk event occurs
C_{tot} .... total microcell capacitance
D .... condition that a scintillation photon is detected by the SiPM at some point in time
$f(t)$ .... normalized signal shape function
N_{cells} .... total number of microcells comprising a SiPM
N_f .... number of fired microcells (including crosstalk and afterpulses)
N_{pt} .... number of primary triggers
P_{ct} .... probability for exactly one crosstalk event to occur
$P_{ec,I}$ .... probability of the ith event chain, leading to the emission of a scintillation photon
R_d .... micro plasma series resistance
R_{int} .... intrinsic energy resolution of the scintillation material (FWHM)
σ_a .... single cell amplitude standard deviation
SCS .... single cell signal (excluding possible crosstalk)
σ_{el} .... electronic noise (standard deviation)

SPS .... single photon signal; SiPM response to a single detected photon including crosstalk

σ_{pt} .... standard deviation of the number of primary triggers

σ_t .... single detector standard deviation of the time stamp determined by means of leading edge triggering

$\sigma_{t,co}$ .... standard deviation of the difference between time stamps of two detectors determined by means of leading edge triggering

σ_{trans} .... effective transit time spread (standard deviation)

t_{ct} .... crosstalk event trigger time relative to the corresponding primary trigger time

$\tau_{d,i}$ .... exponential decay time constant associated with the ith event chain

t_e .... emission time of a scintillation photon relative to the γ-interaction time

t_{pt} .... primary trigger time (relative to the γ interaction time); sum of tem and ttrans

$\tau_{r,i}$ .... exponential rise time constant associated with the ith event chain

t_{th} .... time of threshold crossing

t_{trans} .... effective transit time - delay between tem and the registration of an associated electronic signal

$v_{scs}(t,a)$ .... single cell signal value at the time t after a trigger occurred

v .... measured signal value as a response to a single primary trigger

V .... signal value summed for all fired cells

V_{th} .... leading edge trigger value

List of probability density functions

$p_{cts}(v \mid t, t_{pt}, t_{ct})$ .... pdf for the signal at a given t, for a given t_{pt}, and including a crosstalk event at the time t_{ct}

$p_{em}(t_{em})$ .... pdf for the emission times of scintillation photons

$p_{pt}(t_{pt} \mid D)$ .... pdf for the primary trigger times given condition D

$p_{trans}(t_{trans})$ .... pdf for the effective transit times

$p_{scs}(v \mid t, t_{pt})$ .... pdf for the single cell signal value at a given time t and a given primary trigger time t_{pt}

$p_{ct}(t_{ct} \mid t_{pt}, C)$ .... pdf for the crosstalk induced trigger time for a given t_{tp} and given that condition C is fulfilled

$pv_{sps}(v \mid t, D)$ .... pdf for the SPS value at a given time t and given that condition D is fulfilled

List of expectation values and variances

$E_{sps}(v \mid t, D)$ .... expectation value of the single cell signal at a given time

	t and given that condition D is fulfilled (including one possible crosstalk event per primary trigger)
$E_\Sigma(V \mid t)$	expectation value of the SiPM signal at a given time *t* in response to a scintillation pulse
$E_\Sigma(V \mid t, N_{pt})$	expectation value for the SiPM signal at a given time *t* in response to N_{pt} primary triggers
$var_{sps}(v \mid t, D)$	variance of the single photon signal at a given time t and given that condition D is fulfilled (including one possible crosstalk event per primary trigger)
$var_\Sigma(V \mid t)$	variance of the SiPM signal at a given time *t* in response to a scintillation pulse
$var_\Sigma(V \mid t, N_{sc})$	variance of the SiPM signal at a given time *t* in response to N_{pt} primary triggers
$var_{tot}(V \mid t)$	total variance of the measured electronic scintillation signal *V* at a given time *t*

References

Bengtson B and Moszyński M 1970 Timing Properties of Scintillation Counters *Nucl Instrum Methods* **81** 109-&

Bizarri G and Dorenbos P 2007 Charge carrier and exciton dynamics in LaBr$_3$:Ce^{3+} scintillators: Experiment and model *Phys Rev B* **75**

Buzhan P, Dolgoshein B, Ilyin A, Kantserov V, Kaplin V, Karakash A, Pleshko A, Popova E, Smirnov S, Volkov Y, Filatov L, Klemin S and Kayumov F 2001 An advanced study of silicon photomultiplier *ICFA Instumentation Bulletin* **32** 28-42

Buzhan P, Dolgoshein B, Filatov L, Ilyin A, Kantzerov V, Kaplin V, Karakash A, Kayumov F, Klemin S, Popova E and Smirnov S 2003 Silicon photomultiplier and its possible applications *Nucl Instrum Meth A* **504** 48-52

Choong W S 2009 The timing resolution of scintillation-detector systems: Monte Carlo analysis *Phys Med Biol* **54** 6495-6513

Clinthorne N H, Petrick N A, Rogers W L and Hero A O 1990 A Fundamental Limit on Timing Performance with Scintillation Detectors *IEEE Trans Nucl Sci* **37** 658-663

Cova S, Ghioni M, Lacaita A, Samori C and Zappa F 1996 Avalanche photodiodes and quenching circuits for single-photon detection *Appl Optics* **35** 1956-1976

de Haas J T M and Dorenbos P 2008 Advances in yield calibration of scintillators *IEEE Trans Nucl Sci* **55** 1086-1092

Dolgoshein B, Balagura V, Buzhan P, Danilov M, Filatov L, Garutti E, Groll M, Ilyin A, Kantserov V, Kaplin V, Karakash A, Kayumov F, Klemin S, Korbel V, Meyer H, Mizuk R, Morgunov V, Novikov E, Pakhlov P, Popova E, Rusinov V, Sefkow F, Tarkovsky E and Tikhomirov I 2006 Status report on silicon photomultiplier development and its applications *Nucl Instrum Meth A* **563** 368-376

Dorenbos P, deHaas J T M and vanEijk C W E 1995 Non-proportionality in the scintillation response and the energy resolution obtainable with scintillation crystals *IEEE Trans Nucl Sci* **42** 2190-2202

Du Y and Retiere F 2008 After-pulsing and cross-talk in multi-pixel photon counters *Nucl Instrum Meth A* **596** 396-401

Eckert P, Schultz-Coulon H C, Shen W, Stamen R and Tadday A 2010 Characterisation studies of silicon photomultipliers *Nucl Instrum Meth A* **620** 217-226

Fishburn M W and Charbon E 2010 System Tradeoffs in Gamma-Ray Detection Utilizing SPAD Arrays and Scintillators *IEEE Trans Nucl Sci* **57** 2549-2557

Glodo J, Moses W W, Higgins W M, van Loef E V D, Wong P, Derenzo S E, Weber M J and Shah K S 2005 Effects of Ce concentration on scintillation properties of LaBr3 : Ce *IEEE Trans Nucl Sci* **52** 1805-1808

Haitz R H 1964 Model for Electrical Behavior of Microplasma *J Appl Phys* **35** 1370-&

Henseler D, Grazioso R, Zhang N and Schmand M 2009 SiPM Performance in PET Applications: An Experimental and Theoretical Analysis *IEEE Nuclear Science Symposium and Medical Imaging Conference (2009 NSS/MIC)* 1941-1948

Huizenga J, Seifert S, Schreuder F, Vinke R, Dendooven P, Löhner H, van Dam H T, Beekman F J and Schaart D R 2011 A fast preamplifier concept for SiPM based time-of-flight PET detectors. In: *Proc. sixth Int. Conf. on New Developments in Photodetection* (Lyon: Elsevier)

Hyman L G, Schluter R A and Schwarcz R M 1964 Study of High Speed Photomultiplier Systems *Rev Sci Instrum* **35** 393-&

Hyman L G 1965 Time Resolution of Photomultiplier Systems *Rev Sci Instrum* **36** 193

Kapusta M, Szupryczynski P, Melcher C L, Moszyński M, Balcerzyk M, Carey A A, Czamacki W, Spurrier M A and Syntfeld A 2005 Non-proportionality and thermoluminescence of LSO : Ce *IEEE Trans Nucl Sci* **52** 1098-1104

Koechlin Y and Raviart A 1964 Analyse Par Echantillonnage Sur Photons Individuels Des Liquides Fluorescents Dans Le Domaine De La Sub-Nanoseconde *Nucl Instrum Methods* **29** 45-53

Korpar S, Dolenec R, Hara K, Iijima T, Krizan P, Mazuka Y, Pestotnik R, Stanovnik A and Yamaoka M 2008 Measurement of Cherenkov photons with silicon photomultipliers *Nucl Instrum Meth A* **594** 13-17

Lacaita A L, Zappa F, Bigliardi S and Manfredi M 1993 On the Bremsstrahlung

Origin of Hot-Carrier-Induced Photons in Silicon Devices *IEEE Trans Electron Dev* **40** 577-582

Liksonov D, Barbier B and Chavanelle J 2010 Development of a simulation tool to predict the behavior of a SiPM detector coupled to a scintillation crystal *Nuclear Science Symposium Conference Record (NSS/MIC), 2010 IEEE* 1747-1751

Moses W W and Derenzo S E 1999 Prospects for time-of-flight PET using LSO scintillator *IEEE Trans Nucl Sci* **46** 474-478

Moszyński M, Kapusta M, Nassalski A, Szczęśniak T, Wolski D, Eriksson L and Melcher C L 2006 New prospects for time-of-flight PET with LSO scintillators *IEEE Trans Nucl Sci* **53** 2484-2488

Nassalski A, Kapusta M, Batsch T, Wolski D, Mockel D, Enghardt W and Moszynski M 2007a Comparative study of scintillators for PET/CT detectors *IEEE Trans Nucl Sci* **54** 3-10

Nassalski A, Moszynski M, Szczęśniak T, Wolski D and Batsch T 2007b The road to the common PET/CT detector *IEEE Trans Nucl Sci* **54** 1459-1463

Otte A N, Barral J, Dolgoshein B, Hose J, Klemin S, Lorenz E, Mirzoyan R, Popova E and Teshima M 2005 A test of silicon photomultipliers as readout for PET *Nucl Instrum Meth A* **545** 705-715

Owens A, Bos A J J, Brandenburg S, Dorenbos P, Drozdowski W, Ostendorf R W, Quarati F, Webb A and Welter E 2007 The hard X-ray response of Ce-doped lanthanum halide scintillators *Nucl Instrum Meth A* **574** 158-162

Petrick N, Clinthorne N H, Rogers W L and Hero A O 1991 1st Photoelectron Timing Error Evaluation of a New Scintillation Detector Model *IEEE Trans Nucl Sci* **38** 174-177

Pidol L, Kahn-Harari A, Viana B, Virey E, Ferrand B, Dorenbos P, de Haas J T M and van Eijk C W E 2004 High efficiency of lutetium silicate scintillators, Ce-doped LPS, and LYSO crystals *IEEE Trans Nucl Sci* **51** 1084-1087

Post R F and Schiff L I 1950 Statistical Limitations on the Resolving Time of a Scintillation Counter *Phys Rev* **80** 1113-1113

Rech I, Ingargiola A, Spinelli R, Labanca I, Marangoni S, Ghioni M and Cova S 2008 Optical crosstalk in single photon avalanche diode arrays: a new complete model *Opt Express* **16** 8381-8394

Renker D 2009 New developments on photosensors for particle physics *Nucl Instrum Meth A* **598** 207-212

Retiere F, Du Y, Foreman S, Kitching P, Kostin A, Lindner T, Low M, Masliah P, Moult I, Oser S, Tanaka H and Vacheret A 2009 Characterization of Multi Pixel Photon Counters for T2K Near Detector *Nucl Instrum Meth A* **610** 378-380

Retiere F 2009 MPPC Response Simulation and High Speed Readout Optimization *IEEE Nuclear Science Symposium and Medical Imaging Conference (2009 NSS/MIC)* (Orlando, Florida) 2197-2200

Ronzhin A, Albrow M, Byrum K, Demarteau M, Los S, May E, Ramberg E, Va'vra J and Zatserklyaniy A 2010 Tests of timing properties of silicon

photomultipliers *Nucl Instrum Meth A* **616** 38-44

Schaart D R, Seifert S, Vinke R, van Dam H T, Dendooven P, Löhner H and Beekman F J 2010 LaBr$_3$:Ce and SiPMs for time-of-flight PET: achieving 100 ps coincidence resolving time *Phys Med Biol* **55** N179-N189

Seifert S, van Dam H T, Huizenga J, Vinke R, Dendooven P, Löhner H and Schaart D R 2009 Simulation of Silicon Photomultiplier Signals *IEEE Trans Nucl Sci* **56** 3726-3733

Seifert S, Steenbergen J H L, van Dam H T, Vinke R, Dendooven P, Löhner H, Beekman F J, Dorenbos P, van der Kolk E and Schaart D R 2010 Accurate measurements of the rise and decay times of fast scintillators with solid state photon counters *IEEE Nuclear Science Symposium and Medical Imaging Conference (2010 NSS/MIC)* 1736-1739

Shibuya K, Nishikido F, Tsuda T, Kobayashi T, Lam C, Yamaya T, Yoshida E, Inadama N and Murayama H 2008 Timing resolution improvement using DOI information in a four-layer scintillation detector for TOF-PET *Nucl Instrum Meth A* **593** 572-577

Szczęśniak T, Moszyński M, Świderski Ł, Nassalski A, Lavoute P and Kapusta M 2009 Fast Photomultipliers for TOF PET *IEEE Trans Nucl Sci* **56** 173-181

van Dam H T, Seifert S, Vinke R, Dendooven D, Löhner H, Beekman F J and Schaart D R 2010 A Comprehensive Model of the Response of Silicon Photomultipliers *IEEE Trans Nucl Sci* **57** 2254-2266

van der Laan D J, Schaart D R, Maas M C, Beekman F J, Bruyndonckx P and van Eijk C W E 2010 Optical simulation of monolithic scintillator detectors using GATE/GEANT4 *Phys Med Biol* **55** 1659-1675

Vinke R, Löhner H, Schaart D R, van Dam H T, Seifert S, Beekman F J and Dendooven P 2010 Time walk correction for TOF-PET detectors based on a monolithic scintillation crystal coupled to a photosensor array *Nucl Instrum Meth A* **621** 595-604

6

The Lower Bound on the Timing Resolution of Scintillation Detectors

Abstract - The timing performance of scintillation detectors is ultimately limited by photon counting statistics. In fact, photon counting statistics form a dominant contribution to the overall timing resolution of many state-of-the-art detectors. A common approach to investigate this contribution is to calculate the variance in the registration times of individual scintillation photons within the photosensor. However, in general the single-photon variance is not equal to the intrinsic limit on the timing resolution, since in principle one can make use of the timing information carried by all photons detected. In this work the Cramér-Rao lower bound on the timing resolution of a scintillation detector, based on the information contained in the full set of registered photons, is calculated. The results appear to be in good agreement with trends observed in literature. Furthermore, it is shown that the time stamp obtained from any single scintillation photon never yields the optimum timing resolution for realistic scintillation detectors. Yet, it appears that the intrinsic timing resolution limit can be approached closely by making use of the time stamps from a relatively small number of photons emitted during the initial part of the scintillation pulse.

6.1.   Introduction

The timing resolution of scintillation detectors is a matter of importance in a variety of applications. One of the most demanding applications might be time-of-flight positron emission tomography (TOF PET). It is well established that improvements in the timing resolution of TOF PET scanners directly relate to better signal-to-noise ratio and image quality (e.g. Budinger 1983, Moses 2003, Lois *et al.* 2010, Conti 2011) Consequently, detectors for TOF PET require excellent timing resolution. At the same time, other detector parameters (such as the γ-detection efficiency, spatial resolution, and energy resolution) should not be deteriorated.

One contribution to the timing performance originates in the statistical fluctuations of the registration times of individual scintillation photons. These so-called photon counting statistics are of particular interest since they put an ultimate limit on the timing resolution that can be achieved with a given scintillation detector. In many state-of-the-art detectors, in which other factors such as the readout electronics and data analysis algorithms have been optimized, photon counting statistics form a dominant contribution to the overall timing resolution. A thorough understanding of this intrinsic performance limitation can therefore be a valuable tool in the evaluation and further improvement of the timing resolution of scintillation detectors. Consequently, photon counting statistics have been the subject matter of a number of previous theoretical works, such as the investigations by Post and Schiff (1950), Lynch (1975), or Fishburn and Charbon (2010).

An advantage of restricting theoretical considerations to the contribution of photon counting statistics only is that the results obtained are usually applicable to a wide range of detectors. This approach can thus be seen as complementary to efforts aimed at modeling the timing performance of a specific scintillation detector as closely as possible, typically taking into account a large number of detector properties (e.g. Hyman *et al.* 1964, Hyman 1965, Bengtson and Moszyński 1970, Clinthorne *et al.* 1990, Petrick *et al.* 1991, Seifert *et al.* 2012). Focusing on the contribution of photon counting statistics drastically reduces the complexity of the modeling as well as the number of required input parameters.

Moreover, the subject of photon counting statistics is of high interest in light of recent technological developments in the field of digital photosensors that preserve the quantized nature of the light signal even for fast scintillation pulses. One such type of sensor is the so-called digital silicon photomultiplier (dSiPM) (Degenhardt *et al.* 2009). In this device many small (typically < 100 µm × 100 µm) sensors with single-photon sensitivity (so-called microcells) share a common time-to-digital converter (TDC), such that a time stamp is assigned only to the first detected photon of a scintillation pulse. A second example of a digital solid-state sensor results from the integration of large numbers of single-photon avalanche diodes (SPADs), each read out by a dedicated TDC, into so-called SPAD TDC arrays (Gersbach *et al.* 2009, Richardson *et al.* 2009).

A well-established strategy when addressing the contribution of photon

counting statistics to the overall timing resolution of scintillation detectors is to calculate the variance in the registration times of single photons (Post and Schiff 1950, Lynch 1975, Fishburn and Charbon 2010). Even though this approach has led to important insights into the matter of scintillation pulse timing, it does have the shortcoming of assuming that only one single photon determines the timing uncertainty. In general, the single-photon variance is not equal to the intrinsic limit on the timing resolution of scintillation detectors, since in principle one can make use of the information carried by all photons detected.

Moreover, in most scintillation detectors the timing information is in fact derived from multiple photons. This is due to the finite temporal response of the analog light sensors that are still being applied in most scintillation detectors. For example, the anode current of a photomultiplier tube (PMT) at a given point in time is generally considered to be the sum of several single-photoelectron signals. Therefore, the time stamp derived from a PMT signal can be viewed as being determined by a weighted average of the arrival times of a number of single-photoelectron signals at the anode, the weights being determined by the shape of the single-photoelectron signal (Hyman *et al.* 1964, Hyman 1965, Bengtson and Moszyński 1970). Similar arguments can be made for other photosensors such as multi-channel plates (MCPs) and (analog) silicon photomultipliers (SiPMs) (Seifert *et al.* 2012).

In this work we will show that the lower limit on the timing resolution of a scintillation detector can be calculated using a relatively simple formalism. To this end the Fisher information regarding the γ interaction time carried by all detected scintillation photons is calculated. This information can then be used to calculate the Cramér-Rao lower bound on the variance of any unbiased estimator for the γ interaction time, which can be interpreted as the intrinsic timing resolution that is achievable with a given scintillation detector.

The Cramér-Rao formalism provides a versatile tool which we explored previously to calculate the intrinsic limit on the spatial resolution of γ-detectors based on monolithic scintillation crystals (van der Laan *et al.* 2006). Here it is utilized to investigate the lower bound on the timing resolution for three detector concepts: 1) the "ideal" photosensor, in which individual time stamps are generated for all detected photons (as in e.g. SPAD TDC arrays); 2) a photosensor that provides a time stamp for the nth detected photon only (e.g. the first one in the case of the dSiPM); and 3) a photosensor that generates individual time stamps for the first n detected photons. In view of the recent developments in digital photon counters discussed before, the third concept might potentially provide an optimum between the SPAD TDC array, in which the large area occupied by the TDCs severely compromises the photon detection efficiency (PDE), and the dSiPM, where the fact that a time stamp is produced for one photon only may lead to sub-optimal timing performance.

6.2. Methods

In this section the model for the lower bound on the timing resolution of

scintillation detectors will be derived. Specifically, in 6.2.1 the statistical properties of times stamps assigned to each scintillation photon are discussed. Section 6.2.2 considers the implications of ordering the set of acquired time stamps. The distribution functions derived in 6.2.1 and 6.2.2 are then applied in 6.2.3 to calculate the so-called Fisher information on the γ-photon interaction time contained in certain subsets of time stamps. Lastly, the Fisher information is utilized in 6.2.4 to calculate the Cramér-Rao lower bound on the expected variance of an estimator on the γ-photon interaction time.

6.2.1.   Time stamp distribution

Let us first assume that a total of N photons are detected following the absorption of a γ-photon at a time Θ. In general the emission times te of these photons can be considered to be statistically independent and identically distributed (i.i.d.) according to the probability density function (pdf) $pt_e(t\,|\,\Theta)$. For many scintillation materials it is sufficient to describe $pt_e(t\,|\,\Theta)$ as the convolution of two exponential functions representing the energy transfer and the radiative decay, respectively (Koechlin and Raviart 1964, Hyman 1965). In some cases, however, a number of different cascades of processes contribute to the scintillation (e.g. different energy transfer mechanisms populating the luminescence centers) and, consequently, all of these need to be taken into account (Glodo *et al.* 2005, Bizarri and Dorenbos 2007). If each of these cascades occurs with a probability $P_{ec,i}$ the shape of the scintillation pulse can be characterized by a linear combination of the time profiles corresponding to the individual cascades:

$$p_{t_e}\left(t\,|\,\Theta\right)=\begin{cases} 0 & \forall t:(t<\Theta)\\ \displaystyle\sum_i P_{ec,i}\frac{1}{\left(\tau_{d,i}-\tau_{r,i}\right)}\times\left[e^{-\frac{t-\Theta}{\tau_{d,i}}}-e^{-\frac{t-\Theta}{\tau_{r,i}}}\right] & \forall t:(t\geq\Theta). \end{cases} \tag{6.1}$$

The corresponding cumulative distribution function (cdf) is

$$P_{t_e}\left(t\,|\,\Theta\right)=\int_{-\infty}^{t}p_{t_e}\left(\hat{t}\,|\,\Theta\right)d\hat{t}=\int_{\Theta}^{t}p_{t_e}\left(\hat{t}\,|\,\Theta\right)d\hat{t}$$

$$=\sum_i\frac{P_{ec,i}}{\tau_{d,i}-\tau_{r,i}}\left(\tau_{d,i}-\tau_{r,i}-\tau_{d,i}e^{-\frac{t-\Theta}{\tau_{d,i}}}+\tau_{r,i}e^{-\frac{t-\Theta}{\tau_{r,i}}}\right). \tag{6.2}$$

Now, we consider an ideal photon counter which was defined as a photosensor which is able to record time stamps for all photons as they are detected. Let $T_N=\{t_1, t_2, \dots t_n, \dots t_N\,|\,\Theta\}$ be the set of these time stamps. At this point it must be emphasized that no explicit order is assumed in T_N. The indexing merely indicates the fact that the elements in T_N represent discrete time stamps. Furthermore, the photon detection and the assignment of time stamps are considered to be ideal in the sense that the i.i.d. property is preserved. This explicitly does neither imply that detection and/or time stamping are

instantaneous, nor does it mean that they are noise-free. In fact, in most relevant cases photon transport has to be taken into account as well as sensor inherent processes that add to the absolute transit times and the spread in T_N. However, the assumption that T_N is i.i.d. allows us to treat these effects in the form of a single effective transit time t_{trans} between the actual emission time te of a given individual scintillation photon and its corresponding time stamp t. It is implied that also the t_{trans} for all scintillation photon signals are i.i.d.. The corresponding pdf will be denoted as $pt_{trans}(t)$. The pdf $pt_n(t \mid \Theta)$ for the individual time stamps in T_N then is given by

$$p_{t_n}\left(t \mid \Theta\right) = \int_{-\infty}^{\infty} p_{t_e}\left(t - \tilde{t} \mid \Theta\right) \times p_{t_{trans}}\left(\tilde{t}\right) d\tilde{t}$$
$$= \int_{0}^{t-\Theta} p_{t_e}\left(t - \tilde{t} \mid \Theta\right) \times p_{t_{trans}}\left(\tilde{t}\right) d\tilde{t} \ . \tag{6.3}$$

The corresponding cdf is

$$P_{t_n}\left(t \mid \Theta\right) = \int_{-\infty}^{t} p_{t_n}\left(\hat{t} \mid \Theta\right) d\hat{t}$$
$$= \int_{0}^{t-\Theta} P_{t_e}\left(t - \tilde{t} \mid \Theta\right) \times p_{t_{trans}}\left(\tilde{t}\right) d\tilde{t} \ . \tag{6.4}$$

The distribution of effective transit times depends on a number of detector parameters such as the size and aspect ratio of the scintillation crystal, its surface finish, reflective wrapping, probabilities for self-absorption and re-emission of scintillation photons, and the photosensor signal transit time distribution (Moses and Derenzo 1999, Choong 2009, Lecoq *et al.* 2010, Vinke *et al.* 2010). However, for small scintillation crystals $pt_{trans}(t)$ is dominated by the transit time spread of the photosensor, which in most cases can be described adequately by a Gaussian function with an average transit time and a standard deviation of σ_{trans}. For simplicity, the analysis that follows will be limited to this case. Furthermore, the function $pt_{trans}(t)$ is truncated at $t = 0$ so as to not allow for negative transit times (i.e. $pt_{trans}(t) = 0$ for all t < 0).

It is emphasized that the formalism presented does not require $pt_{trans}(t)$ to follow a Gaussian distribution and that $pt_{trans}(t)$ may be replaced with any pdf that describes the combined effects of photon transport and signal transport. However, as the timing resolution achievable with detector in which photon transport is negligible still forms a lower bound on the timing resolution of a detector where this is not the case, we will model $pt_{trans}(t)$ with a Gaussian function describing the photosensor transit time spread only. Equations (6.3) and (6.4) can then be expressed as

$$p_{t_n}\left(t \mid \Theta\right) = C \cdot \sum_i \frac{P_{ec,i}}{\tau_{d,i} - \tau_{r,i}} \times \left[a_{\tau_{d,i}}\left(t \mid \Theta\right) - a_{\tau_{r,i}}\left(t \mid \Theta\right)\right]. \tag{6.5}$$

$$P_{t_n}\left(t\mid\Theta\right)=C\left[g\left(t\mid\Theta\right)+\sum_i P_{ec}\left(\frac{\tau_{r,i}}{\tau_{d,i}-\tau_{r,i}}a_{\tau_{r,i}}\left(t\mid\Theta\right)-\frac{\tau_{d,i}}{\tau_{d,i}-\tau_{r,i}}a_{\tau_{d,i}}\left(t\mid\Theta\right)\right)\right],\quad(6.6)$$

with the support functions $a\tau_{x,i}(t\mid\Theta)$, $g(t\mid\Theta)$ in being defined as

$$a_{\tau_{x,i}}\left(\Delta t\mid\Theta\right)=\frac{e^{-\frac{t-\bar{t}_{trans}-\Theta}{\tau_{x,i}}+\frac{\sigma_{trans}^2}{2\tau_{x,i}^2}}}{2}$$

$$\times\left[erf\left(\frac{t-\bar{t}_{trans}-\Theta-\frac{\sigma_{trans}^2}{\tau_{x,i}}}{\sqrt{2}\sigma_{trans}}\right)+erf\left(\frac{t_{trans}-\frac{\sigma_{trans}^2}{\tau_{x,i}}}{\sqrt{2}\sigma_{trans}}\right)\right]\qquad(6.7)$$

and

$$g(t\mid\Theta)=\frac{1}{2}\left[erf\left(\frac{t-\Theta-\bar{t}_{trans}}{\sqrt{2}\sigma_{trans}}\right)+erf\left(\frac{\bar{t}_{trans}}{\sqrt{2}\sigma_{trans}}\right)\right].\qquad(6.8)$$

The normalization constant C accounts for the truncation of $pt_{trans}(t)$. It can be derived from the requirement

$$1\doteq\lim_{t\to\infty}P_{t_n}\left(t\mid\Theta\right)=C\frac{1}{2}\left[1+erf\left(\frac{\bar{t}_{trans}}{\sqrt{2}\sigma_{trans}}\right)\right].\qquad(6.9)$$

It follows that

$$C=\frac{2}{1+erf\left(\frac{\bar{t}_{trans}}{\sqrt{2}\sigma_{trans}}\right)}\approx1\quad(\text{for }\bar{t}_{trans}\gg\sigma_{trans}).\qquad(6.10)$$

6.2.2. Order Statistics

So far, no specific order has been assumed in the set of recorded time stamps T_N. By sorting the elements in T_N in ascending order, however, we can create the ordered set $T_{(N)}=\{t_{(1)}\leq t_{(2)}\leq\ldots\leq t_{(N)}\}$. In this work, brackets are used to indicate an ordered set, in which each element $t_{(n)}$ is referred to as the nth order statistic. At this point, we will also define the ordered subset $T_{(1\ldots n)}$ for future reference. $T_{(1\ldots n)}$ is composed of the n smallest elements in T_N. Evidently, the elements in $T_{(N)}$ and in $T_{(1\ldots n)}$ are neither independent, due to the inequality condition, nor are they identically distributed. The pdf $f_{(n)\mid N}(t\mid\Theta)$ for the nth order statistic can be shown to be given by (David 1989)

$$f_{(n)\mid N}\left(t\mid\Theta\right)=\binom{N}{n}\times n\times P_{t_n}^{n-1}\left(t\mid\Theta\right)\times\left[1-P_{t_n}\left(t\mid\Theta\right)\right]^{N-n}\times p_{t_n}\left(t\mid\Theta\right).\qquad(6.11)$$

The probability for the nth order statistic, viz. for the nth smallest time stamp t(n), to be smaller than t is given by the cdf $F_{(n)\mid N}(t\mid\Theta)$ (David 1989):

$$F_{(n)|N}\left(t\mid\Theta\right)=\sum_{k=n}^{N}\binom{N}{k}P_{t_{\rm n}}^{k}\left(t\mid\Theta\right)\left[1-P_{t_{\rm n}}\left(t\mid\Theta\right)\right]^{N-k}. \tag{6.12}$$

6.2.3. Fischer information

The Fisher information $I(\Theta)$ regarding the parameter Θ is defined as (DeGroot 1986)

$$I(\Theta)\overset{\rm def}{=}\int_{-\infty}^{\infty}\left[\frac{\partial}{\partial\Theta}\ln p_{t_{\rm n}}\left(t\mid\Theta\right)\right]^{2}p_{t_{\rm n}}\left(t\mid\Theta\right)dt. \tag{6.13}$$

The Fisher information of independent samples is additive. Since the (unordered) set T_N is i.i.d., it follows that the information in the complete set, $I_N(\Theta)$, is given by

$$\begin{aligned}I_{N}(\Theta)&=N\cdot\int_{-\infty}^{\infty}\left[\frac{\partial}{\partial\Theta}\ln p_{t_{\rm n}}\left(t\mid\Theta\right)\right]^{2}p_{t_{\rm n}}\left(t\mid\Theta\right)dt\\[6pt]&=N\cdot\int_{-\infty}^{\infty}\left[\frac{\partial}{\partial\Theta}p_{t_{\rm n}}\left(t\mid\Theta\right)\right]^{2}\frac{1}{p_{t_{\rm n}}\left(t\mid\Theta\right)}dt.\end{aligned} \tag{6.14}$$

Secondly we will consider an estimator which utilizes only one time stamp, namely the nth order statistic. With the definition of the $n^{\rm th}$ order statistic's pdf (6.11) the corresponding Fisher information is given by:

$$I_{(n)|N}(\Theta)=\int_{-\infty}^{\infty}\left[\frac{\partial}{\partial\Theta}\ln f_{(n)|N}\left(t\mid\Theta\right)\right]^{2}f_{(n)|N}\left(t\mid\Theta\right)dt. \tag{6.15}$$

Thirdly, we will consider the case where Θ is estimated on basis of the ordered subset $T_{(1\ldots n)}$. The order statistics are not i.i.d. and a formal definition of the Fisher information $I_{(1\ldots n)|N}(\Theta)$ requires the calculation of the joint pdf for the first n order statistics. In consequence an n-multiple integral would need to be evaluated which in most cases is not trivial. However, it has been shown by Park (1996, 2003) that this problem can be reduced to a double integral of the form

$$I_{(1\ldots n)|N}(\Theta)=N\cdot\int_{-\infty}^{\infty}\left(\frac{\partial}{\partial\Theta}\ln h\!\left(t\mid\Theta\right)\right)^{2}\Pr\left\{t_{(n-1)}>t\mid\Theta,N\right\}p_{t_{\rm n}}\left(t\mid\Theta\right)dt, \tag{6.16}$$

where $h(t\mid\Theta)$ is given by

$$h\!\left(t\mid\Theta\right)=\frac{p_{t_{\rm n}}\left(t\mid\Theta\right)}{1-P_{t_{\rm n}}\left(t\mid\Theta\right)} \tag{6.17}$$

and $\Pr\{t_{(n-1)}>t\mid\Theta,N\}$ is defined as

$$\Pr\left\{t_{(n-1)}>t\mid\Theta,N\right\}=1-F_{(n-1)|N}\left(t\mid\Theta\right). \tag{6.18}$$

6.2.4. Lower bound on the γ-interaction time estimate

Now, let Ξ_X be an unbiased estimator for Θ based on a (sub)set of choice X (here $X=T_N$, $X=t_{(n)}$, or $X=T_{(1\ldots n)}$). Then its expected variance $\mathrm{var}(\Xi_X\mid\Theta)$

satisfies the Cramér-Rao inequality (DeGroot 1986):

$$\text{var}\left(\Xi_X \mid \Theta\right) \geq \frac{1}{I_X(\Theta)}, \tag{6.19}$$

where $I_X(\Theta)$ is the Fisher information in the (sub)set X as defined in (6.14), (6.15), or (6.16), respectively. The inverse of $I_X(\Theta)$ is also called the Cramér-Rao lower bound.

In a timing experiment one is interested in the estimate of the γ-interaction time Θ of a given scintillation event and the inequality described in (6.19) constitutes the intrinsic timing resolution limit for any given scintillation detector that matches the input parameters used in the calculation of I_N. The lower bound on the timing resolution Δt_{LB} is thus calculated in terms of a standard deviation, viz. as the square root of the inverse of $I_X(\Theta)$.

It should be noted that the validity of (6.19) does not depend on the specific details of the estimator, which means that also detectors that do not preserve the information on individual scintillation photons are bound by Δt_{LB}. For example, in a timing experiment involving conventional analog light sensors the estimator is represented by the electronic response of the sensor and subsequent (pre)amplifiers and the way in which the time stamp is generated from the electronic signal (e.g. leading edge discrimination or constant fraction discrimination).

6.3.   Results and Discussion

In the following section the intrinsic limit on the timing resolution is exemplified for several scintillation detectors used in practice and the results are compared with literature data for the timing resolution measured with these detectors. In section 6.3.1.2 the influence of the most important model input parameters on the intrinsic timing resolution limit will be investigated. In section 6.3.2 the lower limit on the timing resolution that can be achieved utilizing an ordered subset of time stamps is discussed. Finally, some limitations of the proposed model are discussed in section 6.3.3.

6.3.1.   Intrinsic timing resolution

6.3.1.1.   *Comparison with measured data.*

In order to illustrate the formalism and the meaning of the calculated lower bound Δt_{LB} is compared to the measured timing resolution Δt_{meas} (single-detector standard deviation) reported in literature for several different scintillation detectors. This comparison is summarized in Table 6.1, Table 6.2, and Table 6.3 and illustrated in Figure 6.1. In Table 6.1 the scintillation crystals and the γ-sources utilized in the experiments by the various authors are listed. The corresponding scintillation pulse parameters, i.e. the time constants $\tau_{r,i}$ and $\tau_{d,i}$ are summarized in Table 6.2. Table 6.3 holds the photosensor type, the corresponding transit time spread, the timing resolution of the reference detector
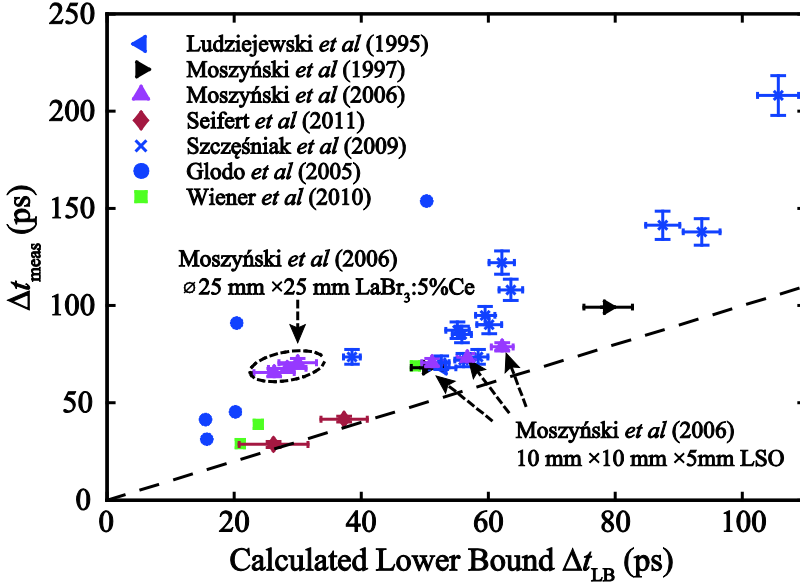
Figure 6.1. Measured timing resolution Δt_{meas} (in terms of the standard deviation of a single detector) as a function of the calculated intrinsic timing resolution limit Δt_{LB} for the corresponding scintillation detector under the assumption that the contribution of photon transport is negligible (see text, Table 6.1, Table 6.2, and Table 6.3). The dashed line indicates the expected timing resolution that could be achieved with an efficient, unbiased estimator under the same conditions.

and the comparison between Δt_{meas} and Δt_{LB}.

Whenever possible Δt_{LB} was calculated using the scintillator and detector properties published in the corresponding references (see Table 6.1 and Table 6.2). In some cases, however, not all scintillator properties were given by the authors. In those instances the missing input parameters were taken from literature data measured for the same material as specified in Table 6.1. Furthermore, in all cases Δt_{LB} was calculated under the approximation that the contribution of the transport of optical photons to the effective transit time distribution $pt_{\mathrm{trans}}(t)$ is negligible (see also 6.2.1). Thus, it is assumed that $pt_{\mathrm{trans}}(t)$ can be described by a Gaussian function with a width σ_{trans} that is determined by the transit time spread of the photosensor only.

For all examples given in Table 6.1 to Table 6.3 the measured timing resolution Δt_{meas} is given in terms of the standard deviation for a single detector. The contribution of the reference detectors (see Table 6.3) was subtracted quadratically, if necessary. In cases where the authors specify the timing resolution as a full-width-at-half-maximum (FWHM) of the recorded timing spectrum we estimate the measured standard deviation Δt_{meas} assuming a

Gaussian shaped timing spectrum (i.e. $\Delta t_{\text{meas}} = \text{FWHM} / 2.35$).

Furthermore, the uncertainties on the predicted lower bounds $u(\Delta t_{\text{LB}})$ are given for those cases where error estimates on the measured parameters were provided by the authors. To this end the contribution of the standard uncertainty $u(x)$ on an individual parameter x to Δt_{LB} is estimated as the difference in Δt_{LB} computed at $x + u(x)$ and at $x - u(x)$ (denoted as $\Delta t_{\text{LB}}|_{x+u(x)}$ and $\Delta t_{\text{LB}}|_{x-u(x)}$, respectively)), while keeping all other parameters fixed. Subsequently, these individual contributions are treated as standard uncertainties and $u(\Delta t_{\text{LB}})$ is estimated as

$$u(\Delta t_{\text{LB}}) = \sqrt{\sum_{i} \left(\frac{\Delta t_{\text{LB}}|_{x_i+u(x_i)} - \Delta t_{\text{LB}}|_{x_i+u(x_i)}}{2} \right)^2}. \qquad (6.20)$$

It is noted, that this formalism assumes independence of the individual $u(x)$. In reality this assumption may not always hold, especially in the case of the scintillation pulse time constants which are usually determined by fitting routines that may e.g. compensate changes in one of multiple τ_d by adjusting the remaining time constants accordingly. Neglecting this negative covariance introduces a bias on the estimated uncertainty towards larger values. The error bars given in Table 6.3 and Figure 6.1 can thus be interpreted as conservative error estimates.

In Figure 6.1 Δt_{meas} is plotted against Δt_{LB}. Additionally, the expected timing resolution of an efficient, unbiased estimator (i.e. $\Delta t_{\text{meas}} = \Delta t_{\text{LB}}$) is indicated as the dashed line in the same figure. It can be seen in Figure 6.1 and Table 6.3, that all measurements of the timing resolution are larger than Δt_{LB}, as expected. The factors causing the differences between the calculated lower bound and the experimental data can be categorized into three classes: 1) errors in the input parameters used to calculate Δt_{LB}; 2) contributions to the measured timing resolution that are not included in the presented formalism (e.g. photon transport, electronic noise, space charge effects in a PMT); 3) the estimator applied in the experiments may not be an efficient one.

Here, a fundamental difference between class 1 and the remaining two contributions should be considered. The measurement errors in the input parameters may influence the difference between Δt_{meas} and Δt_{LB} in any direction, whereas contributions 2 and 3 can only lead to an increase in this difference. Therefore, the latter two contributions do not alter the fact that the calculated Δt_{LB} constitutes a lower limit on the best possible timing resolution achievable with the corresponding scintillation detector.

This observation is relevant as the approximation made in this work that the photon transport is negligible may not be fulfilled for all measurements presented in the corresponding tables and Figure 6.1. For example, in the case of Moszyński *et al.* (2006) (see annotations to the up-pointing triangles in Figure 6.1) it can be observed that the measurements with the 25 mm high LaBr$_3$:5%Ce crystal are systematically further away from the corresponding calculated Δt_{LB} than the measurements employing a LYSO crystal of only 5 mm height. This

indicates that at least in the case of the measurement with the 25 mm high LaBr$_3$:5%Ce crystal photon transport has a significant influence on the timing resolution. The same comparison also yields a measure of the magnitude of the contribution of photon transport to the timing resolution.

Table 6.1. Properties of the scintillation crystals and the γ-sources employed in the measurements for which the measured timing resolution is compared to the predicted lower bound.

	Reference	Scintillator	Crystal size (mm)	γ-source (mean energy)
1	Ludziejewski *et al.* (1995)	LSO:Ce	$14.5 \times 4 \times 5$	^{60}Co (1253 keV)
2	Moszyński *et al.* (1997)	LuAP:0.105mol%Ce	$\sim\varnothing 7 \times \sim 1$	^{60}Co (1253 keV)
3		LuAP:0.105mol%Ce	$\sim\varnothing 7 \times \sim 1$	^{22}Na (511 keV)
4-6	Moszyński *et al.* (2006)	LaBr3:5%Ce	$\varnothing 25 \times 25$	^{22}Na (511 keV)
7-9		LSO:Ce	$10 \times 10 \times 5$	^{22}Na (511 keV)
10	Seifert *et al.* (2012)	LYSO:Ce	$3 \times 3 \times 5$	^{22}Na (511 keV)
11		LaBr$_3$:5%Ce	$3 \times 3 \times 5$	^{22}Na (511 keV)
12-24	Szczęśniak *et al.* (2009)	LSO:Ce	$10 \times 10 \times 5$	^{22}Na (511 keV)
25	Glodo *et al.* (2005)	LaBr$_3$:0.5%Ce	~ 1 cm^3 [1]	^{22}Na (511 keV)
26		LaBr$_3$:5%Ce	~ 1 cm^3 [1]	^{22}Na (511 keV)
27		LaBr$_3$:10%Ce	~ 1 cm^3 [1]	^{22}Na (511 keV)
28		LaBr$_3$:20%Ce	~ 1 cm^3 [1]	^{22}Na (511 keV)
29		LaBr$_3$:30%Ce	~ 1 cm^3 [1]	^{22}Na (511 keV)
30	Wiener *et al.* (2010)	LYSO:Ce	$4 \times 4 \times 5$	^{22}Na (511 keV)
31		LaBr$_3$:5%Ce	$4 \times 4 \times 5$	^{22}Na (511 keV)
32		LaBr$_3$:30%	$4 \times 4 \times 5$	^{22}Na (511 keV)

[1] Glodo J 2011 *private communication*

Table 6.2. Scintillation pulse properties used in the comparison of the predicted lower bound on the timing resolution with measured values. Values in brackets were not given in the original reference and are therefore taken from other references, as indicated.

	N	$\tau_{r,i}$ (ps)	$\tau_{d,i}$ (ns)	$P_{ec,i}$ (%)
1	5260 ± 375	(see data set 10)	46.6 ± 1.4	1
2	3460 ± 250	600 / 600	16.8 ± 1 / 79 ± 5	90 ± 3 / 10 ± 3
3	1410 ± 102	600 / 600	16.8 ± 1 / 79 ± 5	90 ± 3 / 10 ± 3
4	8200 ± 300	(see data set 11)	(see data set 11)	(see data set 11)
5	8700 ± 300	(see data set 11)	(see data set 11)	(see data set 11)
6	9000 ± 300	(see data set 11)	(see data set 11)	(see data set 11)
7	3500 ± 100	(see data set 10)	42 ± 0.5	1
8	3930 ± 100	(see data set 10)	42 ± 0.5	1
9	4140 ± 100	(see data set 10)	42 ± 0.5	1
10	4700 ± 700 [1]	89 ± 13 [1]	43 ± 0.3 [1]	1
11	6200 ± 900 [1]	280 ± 40 / 2000 ± 450 / 15400 ± 300 [2]	15.4 ± 0.3 / 15.4 ± 0.3 / 130 ± 30 [2]	71 ± 8 / 27 ± 8 / 2 ± 1 [2]
12	3100 ± 100	(see data set 10)	42 ± 0.5	1
13	3100 ± 100	(see data set 10)	42 ± 0.5	1
14	2600 ± 100	(see data set 10)	42 ± 0.5	1
15	3300 ± 100	(see data set 10)	42 ± 0.5	1
16	2700 ± 100	(see data set 10)	42 ± 0.5	1
17	2500 ± 100	(see data set 10)	42 ± 0.5	1
18	2900 ± 100	(see data set 10)	42 ± 0.5	1
19	3200 ± 100	(see data set 10)	42 ± 0.5	1
20	4100 ± 100	(see data set 10)	42 ± 0.5	1
21	3200 ± 100	(see data set 10)	42 ± 0.5	1
22	3600 ± 100	(see data set 10)	42 ± 0.5	1
23	3300 ± 100	(see data set 10)	42 ± 0.5	1
24	2800 ± 100	(see data set 10)	42 ± 0.5	1

[1] Measured according to method described by van Dam *et al.* (2010); error bars denote a standard uncertainty estimated under the assumption of a uniform distribution in between extreme values.

[2] Determined by time correlated single photon counting. Details are given in Chapter 4. The error bars denote the standard uncertainty of the fitted parameters

Table 6.2. (Continued).

	N	$\tau_{r,i}$ (ps)	$\tau_{d,i}$ (ns)	$P_{ec,i}$ (%)
25	8530 [3]	2000 / 15000 / 15000	15.2 / 19 / 55	28 / 56 / 0.16
26	8790 [4]	380 / 2200 / 2200	15 / 15 / 55	70 / 27 / 3
27	8260 [3]	500 / 500 / 500	16.5 / 4.5 / 55	89 / 5 / 6
28	8090 [3]	160 / 150 / 160	17.5 / 4.5 / 55	89 / 5 / 6
29	8170 [3]	200 / 200 / 200	18 / 2.5 / 55	91 /4 / 5
30	(1800) [5]	(see data set 10)	(see data set 10)	1
31	(5600) [6]	(see data set 11)	(see data set 11)	(see data set 11)
32	(4600) [5]	(see data set 29)	(see data set 29)	(see data set 29)

[3]   Calculated using the relative light yield given by Glodo *et al.* (2005) in '*table I*' and the value for LaBr$_3$:5%Ce.

[4]   Calculated using the estimate of 17400 photoelectrons / MeV (*section IV* in Glodo *et al.* (2005)), at γ-photon energy 511 keV.

[5]   Calculated using the relative light yield listed by Wiener *et al.* (2010) in '*table II'*.

[6]   Wiener R 2011 *private communication.*

Table 6.3. Comparison between Δt$_{meas}$ and the calculated lower bound Δt$_{LB}$. Δt$_{LB}$ was calculated transit time spread σ$_{trans}$, the scintillation pulse properties given in Table 6.2. The timing resolution and the lower bound both are given in terms of the standard deviation for a single detector.

	Photosensor	σ_{trans} (ps)	Δt_{ref} (ps)	Δt_{meas} (ps)	Δt_{LB} (ps)
1	Photonis XP2020Q	(273 ± 5) [1]	34	68	53 ± 5
2	Photonis XP2020Q	(273 ± 5) [1]	34	68	50 ± 5
3	Photonis XP2020Q	(273 ± 5) [1]	54	99	78 ± 8
4	Photonis XP20Y0/DA	280 ± 13	54.5 ± 2	70 ± 2	29 ± 2
5	Photonis XP20D0	260 ± 13	54.5 ± 2	68 ± 2	28 ± 2
6	Photonis XP20D0	220 ± 13	54.5 ± 2	65 ± 2	26 ± 2
7	Photonis XP20Y0/DA	280 ± 13	54.5 ± 2	78 ± 2	62 ± 4
8	Photonis XP20D0	260 ± 13	54.5 ± 2	73 ± 2	56 ± 4
9	Photonis XP20D0	220 ± 13	54.5 ± 2	71 ± 2	51 ± 4

[1]   According to Moszyński (1993).

Table 6.3 (Continued).

	Photosensor	σ_{trans} (ps)	Δt_{ref} (ps)	Δt_{meas} (ps)	Δt_{LB} (ps)
10	MPPC-S10362-33-50C	120 ± 20 [2]	42 ± 2 [3]	42 ± 2	37 ± 8
11		120 ± 20 [2]	29 ± 2 [3]	29 ± 2	26 ± 5
12	Photonis XP2882	664 ± 34	54.5 ± 2	208 ± 11	106 ± 7
13	Photonis XP32X1	221 ± 13	54.5 ± 2	122 ± 6	62 ± 5
14	Photonis XP31X2	192 ± 9	54.5 ± 2	108 ± 6	63 ± 4
15	Photonis XP3060	187 ± 9	54.5 ± 2	85 ± 4	55 ± 4
16	Photonis XP3060	145 ± 9	54.5 ± 2	87 ± 4	57 ± 5
17	Photonis XP1020	167 ± 9	54.5 ± 2	90 ± 5	60 ± 5
18	Photonis XP20G0	421 ± 21	54.5 ± 2	141 ± 7	87 ± 6
19	Photonis XP2020	209 ± 9	54.5 ± 2	94 ± 5	59 ± 4
20	Photonis XP20D0	209 ± 9	54.5 ± 2	70 ± 4	52 ± 3
21	Photonis XP20D0	200 ± 9	54.5 ± 2	73 ± 4	58 ± 4
22	Photonis XP20D0	209 ± 9	54.5 ± 2	72 ± 4	56 ± 6
23	Photonis XP1485	553 ± 30	54.5 ± 2	138 ± 7	94 ± 6
24	Hamamatsu R5320	60 ± 3	54.5 ± 2	74 ± 4	38 ± 5
25	Hamamatsu H5321	68	64	154	50
26	Hamamatsu H5321	68	64	91	20
27	Hamamatsu H5321	68	64	45	20
28	Hamamatsu H5321	68	64	41	16
29	Hamamatsu H5321	68	64	31	16
30	Hamamatsu R4998	68	63	69	48
31	Hamamatsu R4998	68	63	39	24
32	Hamamatsu R4998	68	63	29	21

[2] Values measured by Ronzhin *et al.* (2010) for MPPCs with 1 mm × 1 mm active area are employed. Error bars denote a standard uncertainty estimated under the assumption of a uniform distribution in between extreme values.

[3] CRTs measured for two identical detectors; Δt_{ref} and Δt_{meas} determined by division by $\sqrt{2}$.

In the following section the influences of the different model parameters on the calculated lower bound are investigated. One consequence of the assumption of independent and identically distributed time stamps is that I_N is proportional to N (see (6.14)). This also means that the lower limit on the variance is inversely proportional to N. This relation has already been indicated by a number of different models predicting the timing resolution of scintillation detectors (Post and Schiff 1950, Hyman *et al.* 1964, Fishburn and Charbon 2010). Yet, here it is shown that the same also holds for the lower bound and is independent of the actual shape of the distribution of the time stamps.

Furthermore, this property allows us to use the normalized lower bound $\Delta t_{\text{LB,norm}} = \Delta t_{\text{LB}} \times \sqrt{N}$ in the following considerations. In order to investigate the influence of the remaining parameters on the calculated lower bound, we assume a scintillation pulse with single exponential rise and decay constants (i.e. the parameter i assumes a single value in (6.1)) and we calculate $\Delta t_{\text{LB,norm}}$ as a function of the different input parameters.

In Figure 6.2 $\Delta t_{\text{LB,norm}}$ is plotted as a function of the square root of τ_r for several different values of σ_{trans} calculated for $\tau_d = 40$ ns. It can be seen that $\Delta t_{\text{LB,norm}}$ linearly depends on $\sqrt{\tau_r}$, as long as τ_r is sufficiently larger than σ_{trans} (i.e. $\tau_r > \sim 4 \times \sigma_{\text{trans}}$). For values of τ_r smaller than $\sim\sigma_{\text{trans}} / 4$, the rising edge is almost entirely dominated by the contribution of the Gaussian (noise) term and, therefore, decreasing τ_r does not further reduce the calculated lower bound. Furthermore, it can be shown that $\Delta t_{\text{LB,norm}}$ also depends linearly on $\sqrt{\tau_d}$ (as long as $\tau_d > \sim 4 \times \sigma_{\text{trans}}$ holds). This is expected since τ_d and τ_r are essentially interchangeable in (6.1). That is, one may write

$$\frac{1}{(\tau_d - \tau_r)} \times \left[e^{-\frac{t-\Theta}{\tau_d}} - e^{-\frac{t-\Theta}{\tau_r}} \right] = \frac{1}{(\tau_r - \tau_{\text{dl}})} \times \left[e^{-\frac{t-\Theta}{\tau_r}} - e^{-\frac{t-\Theta}{\tau_d}} \right]. \tag{6.21}$$

In Figure 6.3 a similar plot is presented for $\Delta t_{\text{LB,norm}}$ as a function of $\sqrt{\sigma_{\text{trans}}}$ calculated at different values of τ_r. In line with the discussion above, the different graphs in Figure 6.3 converge as σ_{trans} increases to values larger than $\sim 4 \times \tau_r$. In this regime, where σ_{trans} is the dominating contribution to $\Delta t_{\text{LB,norm}}$, a linear relation between $\Delta t_{\text{LB,norm}}$ and $\sqrt{\sigma_{\text{trans}}}$ is apparent. However, in contrast to the behavior observed when τ_r was changed, $\Delta t_{\text{LB,norm}}$ keeps improving as σtrans is reduced, even when σtrans is much smaller than τr. This can be explained qualitatively if one considers that the largest contribution to the information integral in (6.14) originates from the part of $pt_n(t \mid \Theta)$ with the largest (relative) slope. For a noiseless scintillation pulse as described by (6.1) this is at the pulse onset. The convolution with the Gaussian noise term in (6.3) reduces the slope in this region regardless of the value of τ_r.

Lastly, it should also be noted that the proposed formalism is scalable in time, which means that if all time constants (including σ_{trans}) are multiplied by a given constant, the calculated lower bound $\Delta t_{\text{LB,norm}}$ is changed by the same factor.
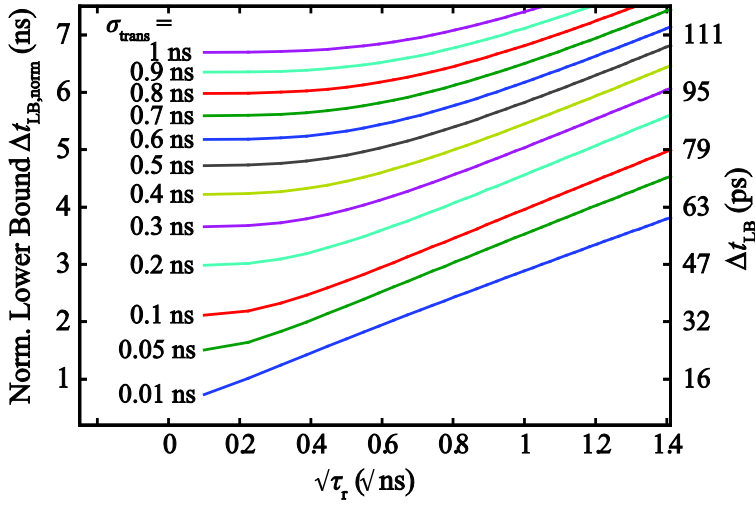
Figure 6.2. Normalized lower bound on the timing resolution $\Delta t_{LB,norm}$ as a function of the square root of the rise time constant τ_r of a single-process scintillation pulse for different values of the transit time spread σ_{trans}. The values were calculated at a constant decay time of 40 ns. The axis on the right indicates the expected lower bound for N = 4000.

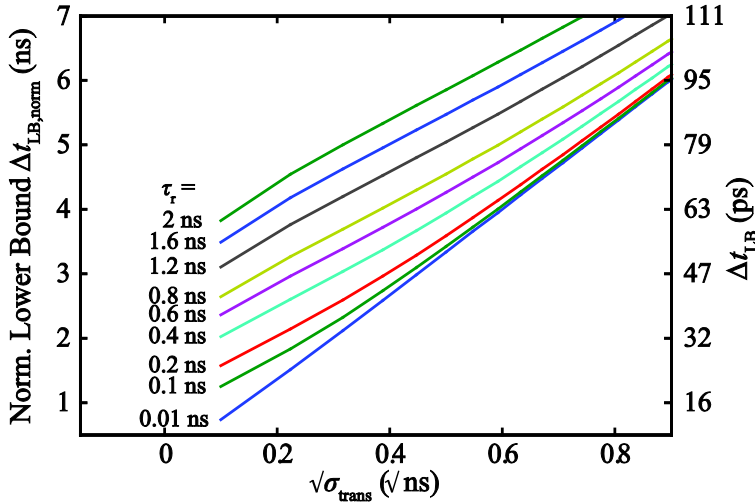Figure 6.3. Normalized lower bound on the timing resolution $\Delta t_{LB,norm}$ as a function of the square root of the transit time spread σ_{trans} for different values of the rise time of a single-process scintillation pulse. The values were calculated at a constant decay time of 40 ns. The axis on the right indicates the expected lower bound for N = 4000.

6.3.2. Fisher information and lower bound in the first n order statistics

The consequences of using reduced sets of time stamps for the estimation of the γ-interaction time are illustrated in Figure 6.4.a) and Figure 6.4.b) for two exemplary scintillation detectors. The detector parameters are taken from measurements by Seifert *et al.* (2012) (see also Table 6.2 and Table 6.3). They match measured values for scintillation detectors employing Hamamatsu MPPC-S10362-33-50C light sensors optically coupled to two different scintillation crystals: LYSO:Ce (Figure 6.4.a) and LaBr3:5%Ce (Figure 6.4.a). The crosses in these figures depict the expected lower bound on the timing resolution for the situation where only a single time stamp, viz. the nth order statistic, is utilized in the estimation of the γ-interaction time, as a function of n. The circles represent Δt_{LB} for the case of an estimator based on a subset of the smallest n time stamps obtained for a given scintillation pulse as a function of n. In addition, the intrinsic timing resolution limit for these detectors is shown as a solid line.

At first we will focus on the lower bound on the timing resolution that can be achieved with an exemplary detector that provides a single (i.e. the nth) time stamp, which is represented by the crosses in Figure 6.4.a) and Figure 6.4.b). This approach is very similar (and in some cases equivalent) to models proposed by other authors calculating the variance of (given) single-photon time stamps (Post and Schiff 1950, Fishburn and Charbon 2010). A noteworthy observation is that in general it is not the first order statistic (or the first detected photon) that is associated with the smallest standard deviation. This is in agreement with the model presented by Fishburn and Charbon (2010).

A second important feature is that for both the LaBr$_3$:5%Ce- and the LYSO:Ce-based detector the smallest lower bound that can be achieved with a single time stamp is significantly larger than the intrinsic limit imposed by the detector properties. This is generally the case for realistic scintillation detectors. This is pointed out as simplified models describing detectors with an infinitely fast scintillation pulse rise time and zero effective transit time spread suggest otherwise. The practical implication of this is that a scintillation detector designed for optimum timing should preferably make use of multiple time stamps.

The difference between the standard deviation of the optimum single-photon time stamp and the intrinsic limit of the scintillation detector appears to be about 10% – 20% for the detectors investigated here. However, the implementation of the capability to record time stamps for all detected photons may be technologically challenging and/or degrade other, crucial detector parameters (e.g. the PDE). Nevertheless, as time stamps of larger order (i.e. 'late photons') appear to carry only little additional information regarding the γ-interaction time, it is sufficient to record a relatively small number of time stamps. As can be seen in Figure 6.4.a) and Figure 6.4.b), the lower bound on the timing resolution that can be achieved using the set of the smallest n time stamps (circles) rapidly approaches the theoretical minimum as the set size is increased.
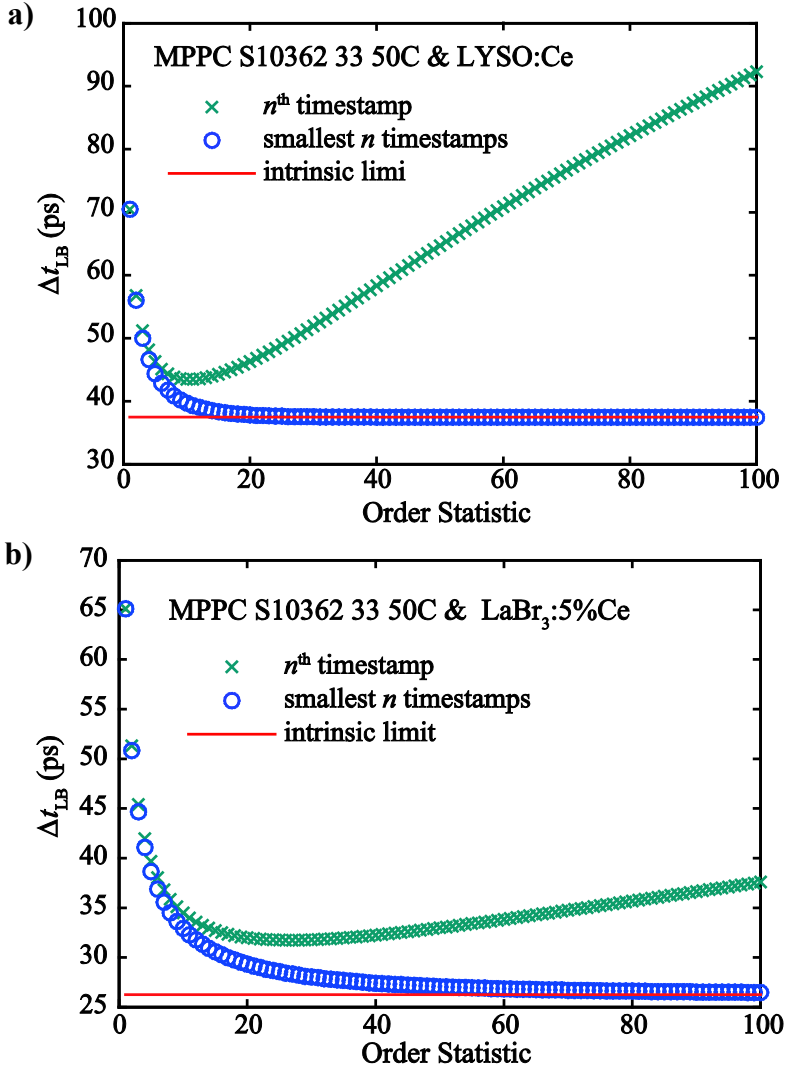
Figure 6.4. Lower bound on the timing resolution Δt_{LB} that can be obtained with estimators based on a single time stamp (crosses) and estimators based on the first n time stamps (circles), as a function of the order statistic n. The graphs were calculated for an exemplary scintillation detector utilizing LYSO:Ce (a) and LaBr$_3$:5%Ce (b), respectively. The input parameters were chosen according to data sets 10 and 11 in Table 6.2 and Table 6.3. The solid line indicates the intrinsic limit on the timing resolution that could be achieved if all time stamps were used.

Here it should be noted that the number of time stamps needed to reach the intrinsic resolution limit within a certain tolerance might even be made smaller than suggested in these figures, by optimizing the spacing in n (e.g. utilizing every second time stamp between 1 and *n*). Such an optimization, however, is considered beyond the scope of the present paper.

6.3.3.   Model limitations

An essential requirement on the set of photon registration times T_N that was introduced in section 6.2.1 is that all of the acquired N time stamps are i.i.d.. Even though this condition might be fulfilled for some scintillation detectors it is certainly not met in general. In particular for solid-state photosensors based on Geiger-mode avalanche diodes (i.e. SPAD-TDC arrays and SiPMs), optical saturation may reduce the detection probability for "late" photons, thereby violating the independence condition. In this particular case, however, one can make use of the fast convergence of the lower bound calculated for the first *n* detected photons shown in section 6.3.2. The fact that Δt_{LB} calculated for the set of the *n* smallest time stamps approaches the intrinsic timing resolution limit within 5% for values of *n* in the order of 10 to 100 in most realistic detectors means that saturation is negligible for the detection of the photons that are most relevant for timing (given that the correct estimator is applied).

Furthermore, in this work all calculations were performed for a given, fixed total number of detected photons N, whereas in practice N is a random variable associated with a certain spread. For many cases of practical relevance, however, the contribution due to the spread in N is small. It can be shown that, under the assumption that N is accurately known for each scintillation event, the calculated lower bound increases by ~ 0.1% for a Gaussian distribution of N with a FWHM of 20% (see Appendix). The influence of the variation of N on the measured timing resolution of realistic detectors can be considerably larger since N itself is subject to measurement uncertainties and since the same means to determine a time stamp (i.e. the estimator for the γ-interaction time) is usually employed for all N. Nevertheless, this influence can be as small as 1 % to 2 % as shown e.g. in (Seifert *et al.* 2012).

Lastly, it is pointed out that the general conclusions regarding the lower bound on the timing resolution are valid even if the spread in N is not negligible. Nevertheless, in such cases the application of the calculated intrinsic timing resolution as a performance measure might be compromised.

6.4.   Conclusion

Photon counting statistics form an important and, in fact, often dominant, contributor to the overall timing performance of a scintillation detector. In this paper we propose a formalism that allows one to calculate the lower bound on the timing resolution based on the Fisher information carried by all photons detected per scintillation pulse. We have shown that, without adding complexity, this quantity is better suited as a measure of the intrinsic timing resolution limit

of scintillation detectors than the single-photon standard deviation. The proposed formalism is generally applicable since it is independent on the photosensor response (with the exception of its contribution to the effective transit time spread) or the details of how the time stamps are obtained in a given experiment.

For two detectors based on LYSO:Ce and LaBr$_3$:Ce studied in detail in this work, the intrinsic timing resolution limit appeared to be about ~10% to ~20% lower than the single-photon standard deviation. However, we also showed that the use of a relatively small number of photon time stamps in principle is sufficient to estimate the γ-interaction time with an uncertainty close to the intrinsic limit.

These findings may have practical implications for the development of future photon-counting light sensors for fast scintillation detectors. That is, time stamps should preferably be generated for multiple photons in order to obtain the best possible timing performance. This, however, increases the technological complexity of the sensor. Moreover, it might reduce the PDE of the device, which would at least partly cancel the benefit of multiple time stamps.

For accurate timing applications a compromise between the concepts of two types of currently available photon-counting light sensor might therefore be desirable. The dSiPM on one hand offers a relatively high PDE, yet in these devices all microcells share a common TDC so one is limited to single-photon timing. SPAD-TDC arrays, on the other hand, have the capability to create time stamps for all detected photons, but at the cost of reduced photodetection efficiency. An optimum configuration might potentially be achieved by sharing multiple TDCs between all microcells such that time stamps can be determined for a limited number of detected photons of a certain statistical order.

Acknowledgements

Appendix

In order to estimate the contribution of a finite energy resolution to the calculated lower bound we will consider a detector that is capable of applying an efficient, unbiased estimator for the γ-interaction time Θ for all values of N, that is to say that the expected variance of each estimate Ξ of the gamma interaction time at a given N is equal to the corresponding lower bound:

$$\mathrm{var}\left(\Xi \mid \Theta, N\right) = \frac{1}{N \times I\left(\Theta\right)} . \tag{6.22}$$

The total variance including variations of N is given by

$$\text{var}\left(\Xi \mid \Theta\right) = \text{E}\left[\text{var}\left(\Xi \mid \Theta, N\right)\right] + \text{var}\left(\text{E}\left[\Xi \mid \Theta, N\right]\right). \tag{6.23}$$

The condition that the estimator is unbiased implies that the expectation value $\text{E}[\Xi \mid \Theta, N]$ is the same for all N, i.e. $\text{var}(\text{E}[\Xi \mid \Theta, N]) = 0$ and one obtains the following expression for the total variance $\text{var}(\Xi \mid \Theta)$:

$$\text{var}\left(\Xi \mid \Theta\right) = \frac{1}{I\left(\Theta\right)} \times \sum_{N=1}^{\infty} \frac{P\left(N\right)}{N}, \tag{6.24}$$

where P(N) is the probability to detect exactly N photons. The relative difference Δ_{rel} between the square root of the expression (6.24) and the lower bound on the timing resolution Δt_{LB} calculated fixed number of detected photons that correspond to the mean $\overline{N}$ of the distribution P(N) is given by

$$\Delta_{\text{rel}} = \sqrt{\overline{N} \times \sum_{N=1}^{\infty} \frac{P\left(N\right)}{N} - 1}. \tag{6.25}$$

References

Bengtson B and Moszyński M 1970 Timing Properties of Scintillation Counters *Nucl Instrum Methods* **81** 109-&

Bizarri G and Dorenbos P 2007 Charge carrier and exciton dynamics in $LaBr_3:Ce^{3+}$ scintillators: Experiment and model *Phys Rev B* **75**

Budinger T F 1983 Time-of-Flight Positron Emission Tomography - Status Relative to Conventional Pet *J Nucl Med* **24** 73-76

Choong W S 2009 The timing resolution of scintillation-detector systems: Monte Carlo analysis *Phys Med Biol* **54** 6495-6513

Clinthorne N H, Petrick N A, Rogers W L and Hero A O 1990 A Fundamental Limit on Timing Performance with Scintillation Detectors *IEEE Trans Nucl Sci* **37** 658-663

Conti M 2011 Focus on time-of-flight PET: the benefits of improved time resolution *Eur J Nucl Med Mol I* **38** 1147-1157

David H A 1989 *Order Statistics* (New York, London, Sydney, Toronto: John Wiley & Son, Inc)

Degenhardt C, Prescher G, Frach T, Thon A, de Gruyter R, Schmitz A and Ballizany R 2009 The Digital Silicon Photomultiplier - A Novel Sensor for the Detection of Scintillation Light *IEEE Nuclear Science Symposium and Medical Imaging Conference (2009 NSS/MIC)* (Orlando, Florida) 2383-2386

DeGroot M H 1986 *Probability and Statistics*: Addison-Wesley Publishing Company, Inc)

Fishburn M W and Charbon E 2010 System Tradeoffs in Gamma-Ray Detection

Utilizing SPAD Arrays and Scintillators *IEEE Trans Nucl Sci* **57** 2549-2557

Gersbach M, Maruyama Y, Labonne E, Richardson J, Walker R, Grant L, Henderson R, Borghetti F, Stoppa D and Charbon E 2009 A Parallel 32x32 Time-To-Digital Converter Array Fabricated in a 130 nm Imaging CMOS Technology *Proc Eur Solid-State* 197-200

Glodo J, Moses W W, Higgins W M, van Loef E V D, Wong P, Derenzo S E, Weber M J and Shah K S 2005 Effects of Ce concentration on scintillation properties of LaBr3 : Ce *IEEE Trans Nucl Sci* **52** 1805-1808

Hyman L G, Schluter R A and Schwarcz R M 1964 Study of High Speed Photomultiplier Systems *Rev Sci Instrum* **35** 393-&

Hyman L G 1965 Time Resolution of Photomultiplier Systems *Rev Sci Instrum* **36** 193

Koechlin Y and Raviart A 1964 Analyse Par Echantillonnage Sur Photons Individuels Des Liquides Fluorescents Dans Le Domaine De La Sub-Nanoseconde *Nucl Instrum Methods* **29** 45-53

Lecoq P, Auffray E, Brunner S, Jarron P, Knapitsch A, Meyer T and Powolny F 2010 Factors Influencing Time Resolution of Scintillators and Ways to Improve Them *IEEE Trans Nucl Sci* **57** 2411-2416

Lois C, Jakoby B W, Long M J, Hubner K F, Barker D W, Casey M E, Conti M, Panin V Y, Kadrmas D J and Townsend D W 2010 An Assessment of the Impact of Incorporating Time-of-Flight Information into Clinical PET/CT Imaging *J Nucl Med* **51** 237-245

Ludziejewski T, Moszyńska K, Moszyński M, Wolski D, Klamra W, Norlin L O, Devitsin E and Kozlov V 1995 Advantages and Limitations of Lso Scintillator in Nuclear-Physics Experiments *IEEE Trans Nucl Sci* **42** 328-336

Lynch F J 1975 Basic Limitation of Scintillation-Counters in Time Measurements *IEEE Trans Nucl Sci* **Ns22** 58-64

Moses W W and Derenzo S E 1999 Prospects for time-of-flight PET using LSO scintillator *IEEE Trans Nucl Sci* **46** 474-478

Moses W W 2003 Time of flight in PET revisited *IEEE Trans Nucl Sci* **50** 1325-1330

Moszyński M 1993 Prospects for New Fast Photomultipliers *Nucl Instrum Meth A* **337** 154-164

Moszyński M, Wolski D, Ludziejewski T, Kapusta M, Lempicki A, Brecher C, Wisniewski D and Wojtowicz A J 1997 Properties of the new LuAP:Ce scintillator *Nucl Instrum Meth A* **385** 123-131

Moszyński M, Gierlik M, Kapusta M, Nassalski A, Szczęśniak T, Fontaine C and Lavoute P 2006 New Photonis XP20D0 photomultiplier for fast timing in nuclear medicine *Nucl Instrum Meth A* **567** 31-35

Park S 2003 On the asymptotic Fisher information in order statistics *Metrika* **57** 71-80

Park S G 1996 Fisher information in order statistics *J Am Stat Assoc* **91** 385-390

Petrick N, Clinthorne N H, Rogers W L and Hero A O 1991 1st Photoelectron Timing Error Evaluation of a New Scintillation Detector Model *IEEE Trans Nucl Sci* **38** 174-177

Post R F and Schiff L I 1950 Statistical Limitations on the Resolving Time of a Scintillation Counter *Phys Rev* **80** 1113-1113

Richardson J, Walker R, Grant L, Stoppa D, Borghetti F, Charbon E, Gersbach M and Henderson R K 2009 A 32x32 50ps Resolution 10 bit Time to Digital Converter Array in 130nm CMOS for Time Correlated Imaging *Ieee Cust Integr Cir* 77-80

Ronzhin A, Albrow M, Byrum K, Demarteau M, Los S, May E, Ramberg E, Va'vra J and Zatserklyaniy A 2010 Tests of timing properties of silicon photomultipliers *Nucl Instrum Meth A* **616** 38-44

Seifert S, van Dam H T, Vinke R, Dendooven P, Löhner H, Beekman F J and Schaart D R 2012 A Comprehensive Model to Predict the Timing Resolution of SiPM-Based Scintillation Detectors: Theory and Experimental Validation *IEEE Trans Nucl Sci* **59** 190-204

Szczęśniak T, Moszyński M, Świderski Ł, Nassalski A, Syntfeld-Kazuch A, Dehaine A G and Kapusta M 2009 A Comparative Study of Fast Photomultipliers for Timing Experiments and TOF PET *IEEE Trans Nucl Sci* **56** 1017-1023

van Dam H T, Seifert S, Vinke R, Dendooven D, Löhner H, Beekman F J and Schaart D R 2010 A Comprehensive Model of the Response of Silicon Photomultipliers *IEEE Trans Nucl Sci* **57** 2254-2266

van der Laan D J, Maas M C, Schaart D R, Bruyndonckx P, Leonard S and van Eijk C W E 2006 Using Cramer-Rao theory combined with Monte Carlo simulations for the optimization of monolithic scintillator PET detectors *IEEE Trans Nucl Sci* **53** 1063-1070

Vinke R, Löhner H, Schaart D R, van Dam H T, Seifert S, Beekman F J and Dendooven P 2010 Time walk correction for TOF-PET detectors based on a monolithic scintillation crystal coupled to a photosensor array *Nucl Instrum Meth A* **621** 595-604

Wiener R I, Kaul M, Surti S and Karp J S 2010 Signal analysis for improved timing resolution with scintillation detectors for TOF PET imaging *Nuclear Science Symposium Conference Record (NSS/MIC), 2010 IEEE* 1991-1995

7

A novel, SiPM-array-based, Monolithic Scintillator Detector for PET

Abstract - Silicon photomultipliers (SiPMs) are of great interest to positron emission tomography (PET), as they enable new detector geometries for e.g. depth-of-interaction (DOI) determination, are MR-compatible, and offer faster response and higher gain than other solid-state photosensors such as avalanche photodiodes (APDs). Here we present a novel detector design with DOI correction, in which a position-sensitive SiPM array is used to read out a monolithic scintillator. Initial characterization of a prototype detector consisting of a 4 × 4 SiPM array coupled to either the front or back surface of a 13.2 mm × 13.2 mm × 10 mm LYSO:Ce^{3+} crystal shows that front-side readout (FSR) results in significantly better performance than conventional back-side readout (BSR). Spatial resolutions < 1.6 mm FWHM were measured at the detector center in response to a ~0.54 mm FWHM diameter test beam. Hardly any resolution losses were observed at angles of incidence of up to 45º, demonstrating excellent DOI correction. About ~14% FWHM energy resolution was obtained. The timing resolution, measured in coincidence with a BaF_2 detector, equals 960 ps FWHM.

7.1.   Introduction

Positron emission tomography (PET) enables imaging of biological processes and is increasingly being used in the clinic as well as in biomedical research (Phelps 2000, Gambhir 2002, Rohren *et al.* 2004, Nestle *et al.* 2009). PET has proven its value in the diagnosing, staging, and restaging of cancer. It furthermore plays a growing role in e.g. radiotherapy treatment planning, in radionuclide- and chemo-therapy monitoring, and in other fields such as neurology and cardiology.

PET instrumentation is continuously being improved, driven by the need for better image quality and shorter scanning times. At the detector level, this requires higher spatial resolution - including correction for depth-of-interaction (DOI) errors, higher sensitivity, improved count-rate performance, and better energy resolution (Lewellen 2008). In addition, clinical PET will benefit from further improvement of time-of-flight (TOF) performance (Muehllehner and Karp 2006, Moses 2007), as TOF-PET with ~600 ps coincidence resolving time (CRT) has already demonstrated significant improvement in image quality, especially in heavier patients (Surti *et al.* 2007).

It is furthermore desirable to integrate complementary imaging modalities (Cherry 2004, Townsend 2008). For example, the combination of the functional and anatomical imaging capabilities of PET and X-ray CT, respectively, into hybrid PET/CT systems has had tremendous impact within the field of oncology (Beyer *et al.* 2000, Czernin *et al.* 2007, Israel and Kuten 2007). At present, various groups are working on the more difficult challenge of combining PET and MRI (Shao *et al.* 1997, Catana *et al.* 2006, Judenhofer *et al.* 2008, Townsend 2008). Potential advantages of PET/MRI include the far better soft-tissue contrast of MRI compared to CT and the elimination of the CT dose, which tends to be responsible for most of the overall dose received by the patient during a PET/CT scan. True PET/MRI integration, however, requires PET detectors that are very compact, do not distort the operation of the MRI system, and are insensitive to magnetic fields.

The ideal PET detector would perform optimally with respect to each of the above criteria and be affordable at the same time. Scintillation detectors based on solid-state photosensors are very promising in this respect. In contrast with conventional photomultiplier tubes (PMTs), such sensors can be made MR-compatible. Furthermore, their small size enables novel detector geometries that allow DOI determination as well as a high detector packing fraction to maximize PET system sensitivity. The importance of sensitivity should not be underestimated as the reconstructed resolution of clinical PET images is often limited by the number of acquired counts rather than by the system resolution (Muehllehner and Karp 2006). Furthermore, combating the inherent physical limits on PET spatial resolution by compensating for positron range and non-collinearity in the image reconstruction process requires sufficient statistical quality of the acquired data (Cherry 2004).

Whereas solid-state photosensors such as PIN diodes and avalanche

photodiodes (APDs) have been explored by many authors, a particularly interesting new class of devices are silicon photomultipliers (SiPMs) (Antich *et al.* 1997, Bondarenko *et al.* 2000, Golovin and Saveliev 2004, Britvitch *et al.* 2007, Herbert *et al.* 2007, McElroy *et al.* 2007, Musienko *et al.* 2007, Renker 2007). These can be fabricated using CMOS technology, offering the possibility of low cost when made in large quantities. They have gains in the order of ~10^6 and are very fast, which is crucial for TOF-PET. In fact, CRTs of 237 ps FWHM and 240 ps FWHM have recently been demonstrated using 3 mm × 3 mm SiPMs coupled to small crystals of , respectively, $LaBr_3:Ce^{3+}$ (Schaart *et al.* 2008b) and $LYSO:Ce^{3+}$ (Kim *et al.* 2009). As of very recently, SiPMs can be manufactured into compact arrays that can be used as position-sensitive light sensors in PET detectors (España *et al.* 2008, Llosá *et al.* 2008, Schaart *et al.* 2008a, Kolb *et al.* 2010).

The aim of this paper is to present an initial characterization of the first SiPM-array based PET detector following the monolithic scintillator concept explored using APD arrays by Maas *et al.* (2006, 2009). This monolithic approach has previously been shown to allow not only high resolution and excellent DOI correction, but also very high system sensitivity (van der Laan *et al.* 2007). Two readout geometries are compared in this work: front-side readout (FSR) and conventional back-side readout (BSR).

7.2.   Materials and Methods

7.2.1.   Detector

The detector prototype is based on a 13.2 mm × 13.2 mm × 10 mm monolithic $LYSO:Ce^{3+}$ scintillator with optically polished surfaces (Crystal Photonics). The 13.2 mm × 13.2 mm crystal surfaces match the sensitive area of the SiPM array, which is optically coupled to the crystal using Sylgard 527 dielectric gel. All other faces of the crystal are covered with a highly reflective PTFE-based material (Spectralon). The SiPM array (SensL SPMArray 3035G16) is a 4 × 4 array of SiPM pixels mounted onto a 550 μm thick white float glass substrate using flip chip technology, see the inset in Figure 7.1. The 16 silicon dies are mounted at a pitch of 3.3 mm. Each pixel has an active area of 2.85 mm × 2.85 mm, made up of 3640 Geiger-mode avalanche photodiodes (microcells). The SiPM array was operated at the manufacturer-specified bias voltage of 29.3 V, exceeding the breakdown voltage by 2.0 V and corresponding to a gain of ~10^6.

The blue squares in Figure 7.1 show the photo-detection efficiency (PDE) in air of the 2.85 mm × 2.85 mm active area of a single SiPM pixel at 2 V above breakdown (SensL, private communication). It is emphasized that these values are free of any contributions from after-pulsing or crosstalk[8]. The solid black

---

[8]   SensL Technical Note *SPM Photon Detection Efficiency: Rev 1.4*, December 2007 http://www.sensl.com/pdfs/SPM_Tech_App_Notes/TN_PDE.pdf
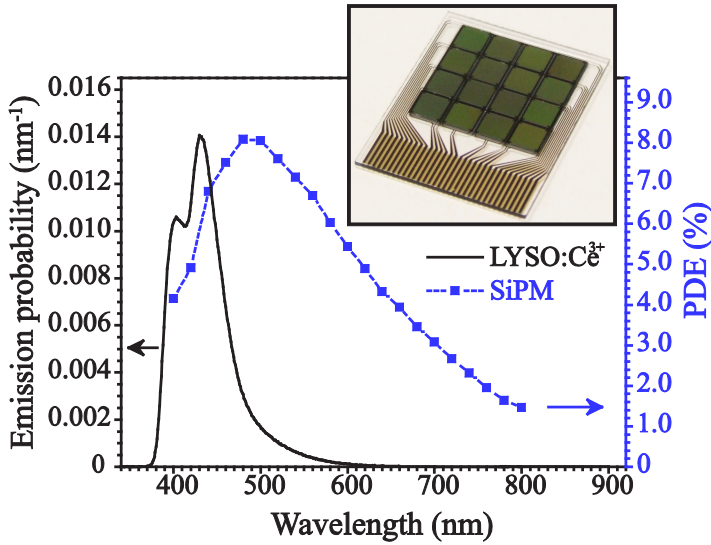
Figure 7.1. Photo-detection efficiency of the 2.85 mm × 2.85 mm active area of a single SiPM pixel of a SensL SPMArray 3035G16 at 2 V above the breakdown voltage (blue squares, right-hand y-axis), in comparison to the emission probability per nm per scintillation photon of a 3 mm × 3 mm × 3 mm LYSO:Ce^{3+} crystal (solid black line, left-hand y-axis). The inset shows the essential parts of the SiPM array: 4 × 4 SiPM pixels mounted onto a glass substrate with readout tracks. Photograph courtesy SensL, Ireland.

line in Figure 7.1 shows the emission spectrum of a 3 mm × 3 mm × 3 mm LYSO:Ce^{3+} crystal (Crystal Photonics), measured as described by de Haas and Dorenbos (2008). The effective PDE of the SiPM active area, weighted by the normalized LYSO:Ce^{3+} emission spectrum, equals ~5.9%. As the fractional active area of the array equals ~75%, the effective PDE of the entire array in air is estimated to be ~4.4%.

7.2.2. Position estimation

Rather than the interaction point of the annihilation photon, its entry point on the crystal front surface is estimated, using the statistical algorithm described by Maas *et al.* (2009). For convenience we briefly summarize the method here. As indicated in Figure 7.2, reference data are first collected by irradiating the detector with 511 keV photons at a series of known positions (x_i, y_j) and angles of incidence θ_k on the crystal front surface. At each position and angle the light distributions of n_{ref} reference events are recorded. The entry point of an unknown annihilation photon is subsequently estimated by calculating the sum-of-squared-differences of its light distribution with those of all events in the reference set recorded at the θ_k closest to the angle of incidence θ of the unknown event. In a PET scanner, θ can be estimated from the positions of the
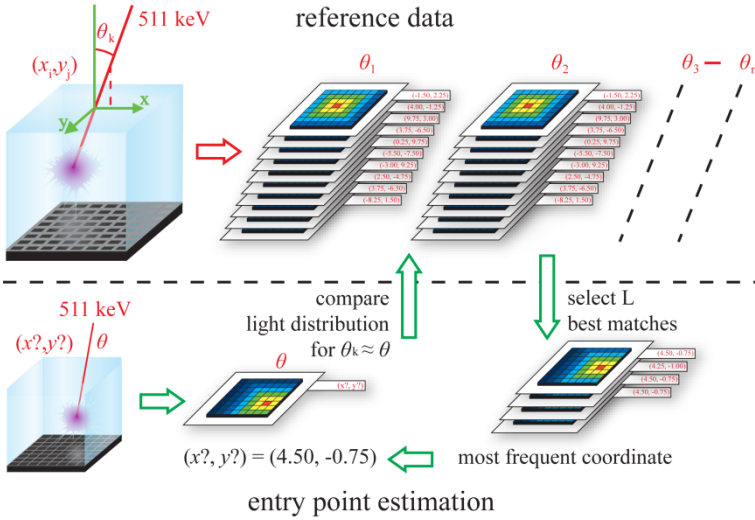
154

Figure 7.2. Schematic representation of the nearest-neighbour algorithm used to estimate the entry point (x,y) of the annihilation photon on the front surface of the crystal from the scintillation light distribution measured by the position-sensitive SiPM array. See text for details.

two detectors triggering in coincidence (Maas *et al.* 2009). A subset of the reference data consisting of the *L* closest matches ('*nearest neighbors*') is selected, and the most frequently occurring entry point within this subset is assigned to the unknown event.

7.2.3.   Measurements

Measurements were performed using the setup described by (Maas *et al.* 2009). Briefly, the detector is contained in a temperature-controlled box and can be irradiated at different positions and angles of incidence with a < 1 mm diameter test beam of annihilation photons, defined by placing the detector close to a 0.5 mm diameter ^{22}Na source and operating it in coincidence with a collimated BGO detector placed on the opposite side of the source. The SiPM signals were preamplified using a 16-channel readout board designed to minimize nonlinearity due to SiPM impedance variations. The design and characteristics of these preamplifiers have been described by (Seifert *et al.* 2008). The preamplified SiPM pulses were shaped and their pulse heights digitized using the multichannel data acquisition system described by Maas *et al.* (2009). In parallel, a trigger signal was generated by adding the 16 SiPM signals by means of a fast summing amplifier on the preamplifier board.

Spatial resolution measurements were performed by recording reference events at a rectangular, equidistant grid of reference beam positions (x_i, y_j), having a pitch of 0.25 mm and covering the entire front surface of the crystal. At non-perpendicular incidence, the same reference grid was used and the lateral crystal surface turned towards the beam was included in the measurement. The
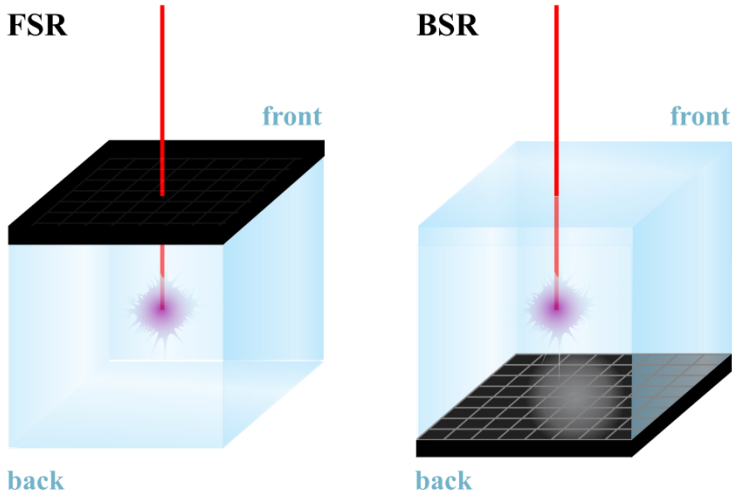
Figure 7.3. Schematic representation of the readout geometries investigated. Left: front-side readout (FSR) geometry. Right: back-side readout (BSR).

reference events were also used as test events, using the leave-one-out method described by Maas *et al.* (2009). All measurements were conducted at ~24°C.

Pulse height spectra were derived by correcting the digitized pulse heights of all detector channels for offsets, adding the 16 corrected pulse heights of each event, and normalizing the result such that the center of the full-energy peak corresponded to 511 keV.

The detector timing resolution was determined by placing the detector in coincidence with a BaF_2 crystal on a XP2020Q PMT connected to an Ortec 579 fast filter amplifier (FFA) and an Ortec 935 constant fraction discriminator (CFD). The SiPM sum signal was fed into a second, identical FFA and a LeCroy WavePro 7300 oscilloscope was used to measure the time difference between the CFD logic pulse and the moment at which the second FFA output signal crossed a fixed threshold corresponding to ~10 keV. Only full-energy events were accepted.

7.3.   Results

Measurements were performed in two different readout geometries: *front-side readout* (FSR), in which the SiPM array is placed on the crystal surface facing the radiation source, and conventional *back-side readout* (BSR), see Figure 7.3. It is emphasized that FSR is possible without significantly disturbing the annihilation photon beam since the SiPM array is very thin and consists of low-Z materials only. Specifically, a Monte Carlo simulation of the detector using GATE (Jan *et al.* 2004), showed that the probability of a 511 keV photon undergoing at least one Compton or Raleigh interaction in the SiPM array before

being detected (i.e., before undergoing at least one Compton and/or photoelectric interaction in the crystal), equals ~3%.

7.3.1.   Spatial resolution

The detector spatial response (i.e., the two-dimensional histogram of the differences between the true and estimated annihilation photon entry points) can in principle be derived at each point of the measurement grid. However, the number of events n_{ref} recorded at each point is limited, resulting in considerable statistical fluctuations if the histogram is determined for one such point only. As the spatial response appears to be approximately constant over the central area of the detector, the results obtained within the central 3.25 mm × 3.25 mm were combined into a single error histogram.

Figure 7.4 shows the corresponding result obtained in FSR geometry. The full-width-at-half-maximum (FWHM) and the full-width-at-tenth-maximum (FWTM) are shown in Table 7.1. It is noted that these result still contain the influence of the ~0.54 mm FWHM diameter test beam. Furthermore, they were obtained at a low energy threshold of ~50 keV applied to the sum of the 16 SiPM signals.

Interestingly, increasing the energy threshold to ~400 keV hardly appears to improve these results (< 1%). On first sight one might expect that low-energy

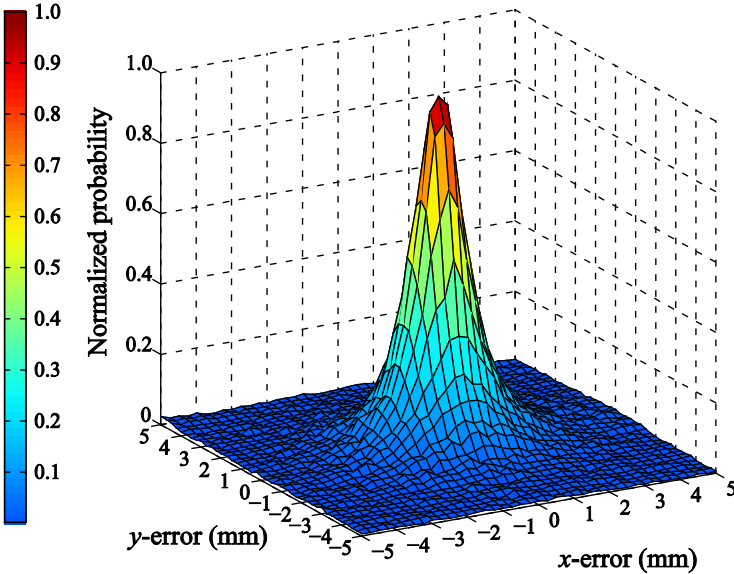*Figure 7.4. Detector spatial response to a ~0.54 mm FWHM diameter test beam, measured in FSR geometry at the detector center and at normal incidence using n_{ref} = 1000 and L = 750.*

Table 7.1. FWHM and FWTM of the spatial response at the detector center at normal incidence. Results were obtained in FSR geometry and are not corrected for the ~0.54 mm FWHM diameter test beam.

Direction	FWHM (mm)	FWTM (mm)
x	1.58	4.06
y	1.56	4.23

events would be positioned less accurately due to the lower amount of scintillation light emitted. However, in most of these events the scintillation light will be emitted from a single (Compton) interaction location. In contrast, many of the events in the full-energy peak appear to involve multiple interactions within the crystal (see section 7.3.4). Events in which the scintillation light is emitted from multiple interaction locations may be more difficult to position than single-interaction events. Apparently, the resulting average positioning accuracy is similar for events in the full-energy peak, most of which involve multiple interactions, and events in the Compton ridge, most of which involve a single interaction, so that the detector spatial resolution becomes almost independent of the energy threshold.

Similar to what was found in APD-based monolithic detectors by Maas *et al.* (2009), the spatial resolution shows some degradation near the detector edges. For example, the solid black line in Figure 7.5 shows the FWHM of the detector spatial response in the x-direction as a function of *x*. At each *x*, all results obtained between *x* - 0.5 mm and *x* + 0.5 mm (i.e., over the entire length of the crystal in the *y*-direction) were combined into a 2D error histogram in order to minimize statistical fluctuations. At about ~3 mm from the crystal edge, the FWHM starts to increase, until it reaches a maximum at ~2 mm from the edge. At smaller distances the FWHM decreases again, as the error histograms are being truncated on one side by the crystal edge.

The dashed blue line in Figure 7.5 shows the FWHM of the detector spatial response in the *y*-direction as a function of *x*, derived from the same error histograms used to obtain the solid black curve. Interestingly, no significant dependence of the FWHM in the *y*-direction on *x* is observed. Conversely, the FWHM in the *y*-direction was found to depend on *y*, whereas the FWHM in the *x*-direction did not. Hence, the FWHM in a given direction (*x* or *y*) is only affected by a crystal edge perpendicular to that direction, in agreement with what was found by Maas *et al.* (2009).

7.3.2.   FSR versus BSR

In a further series of measurements the resolutions obtained in different readout geometries and at different angles of incidence were compared. In these measurements, the [22]Na point source had to be placed at a larger distance from the detector box to allow it to rotate. This resulted in a larger, but constant, test beam diameter of ~0.64 mm FWHM.

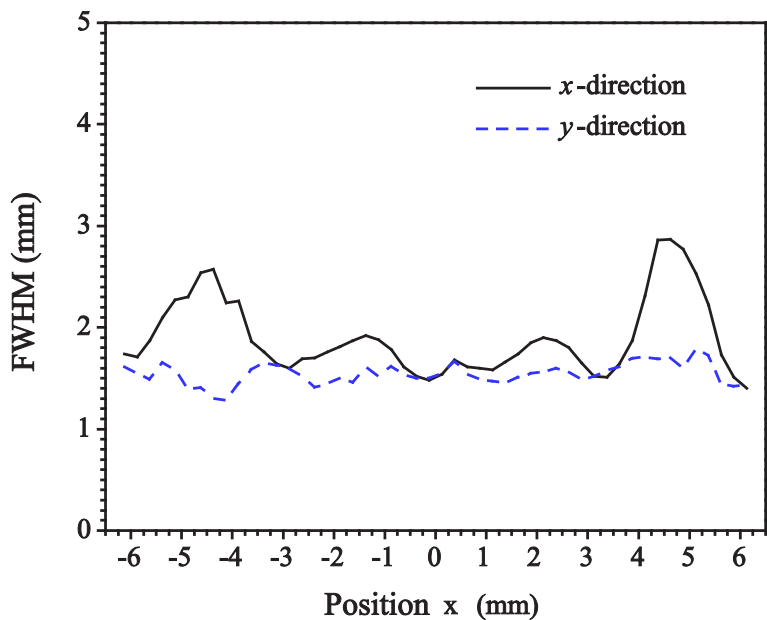The results were analyzed by combining the data obtained over the entire

Figure 7.5. FWHM of the detector spatial response in the x-direction (solid black curve) and in the y-direction (dashed blue curve), as a function of x. Data were measured in FSR geometry at perpendicular incidence, using a ~0.54 mm FWHM diameter test beam and with $n_{ref} = 1000$ and $L = 750$.

crystal surface into a single error histogram, which we will denote as the '*average detector spatial response*.' It is noted that these results cannot be compared directly to those obtained at the detector center (i.e., Table 7.1 and Figure 7.4), both because of the larger beam diameter and because of the larger FWHM values observed near the detector edges (see Figure 7.5).

   The FSR and BSR results are compared in Table 7.2. FSR appears to perform considerably better than BSR. We therefore focus on FSR in the remainder of this work.

Table 7.2. Comparison of front- and back-side readout. Values represent the FWHM and FWTM in the x-direction of the detector spatial response at normal incidence, averaged over the entire detector surface, not corrected for the ~0.64 mm FWHM diameter test beam.

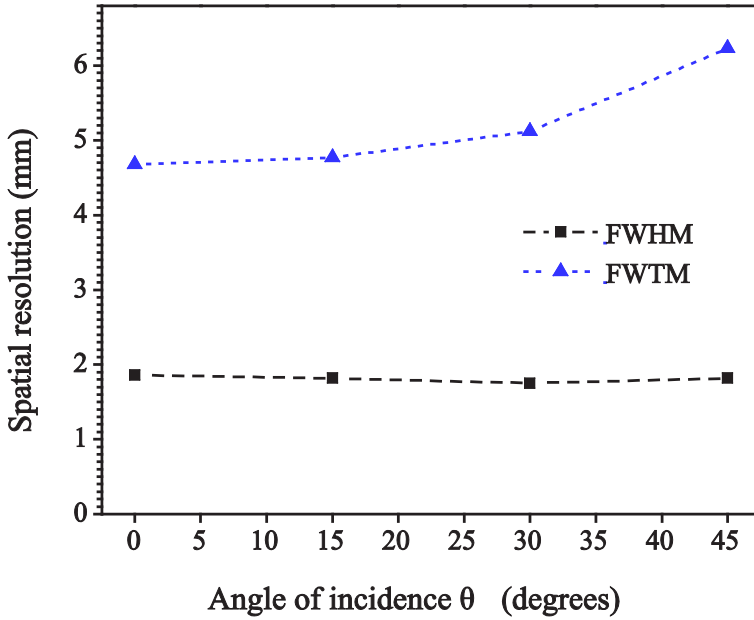| Readout geometry	FWHM (mm)	FWTM (mm)
ront surface readout (FSR)	1.86	4.68
Back surface readout (BSR)	2.21	5.33

Figure 7.6. FWHM and FWTM of the average detector spatial response in the x-direction, measured as a function of the angle of incidence θ using a ~0.64 mm FWHM diameter test beam. Data were obtained in FSR geometry with n_{ref} = 250 and L = 1000.

7.3.3.   DOI correction

Estimating the annihilation photon entry point has the advantage that DOI errors are, in principle, eliminated (Maas *et al.* 2009). This intrinsic DOI correction was tested by irradiating the detector at different angles of incidence θ and deriving the average spatial response projected onto a plane perpendicular to the test beam. In this way, the results correlate directly to the uncertainty in the position of the line-of-response (LOR) in a PET scanner.

Figure 7.6 shows the FWHM and FWTM of the average detector response as a function of θ, determined in FSR geometry using the same test beam diameter as in Table 7.2. Hardly any spatial resolution losses are observed for angles of incidence of up to 45°. Only the FWTM increases slightly with increasing angle of incidence.
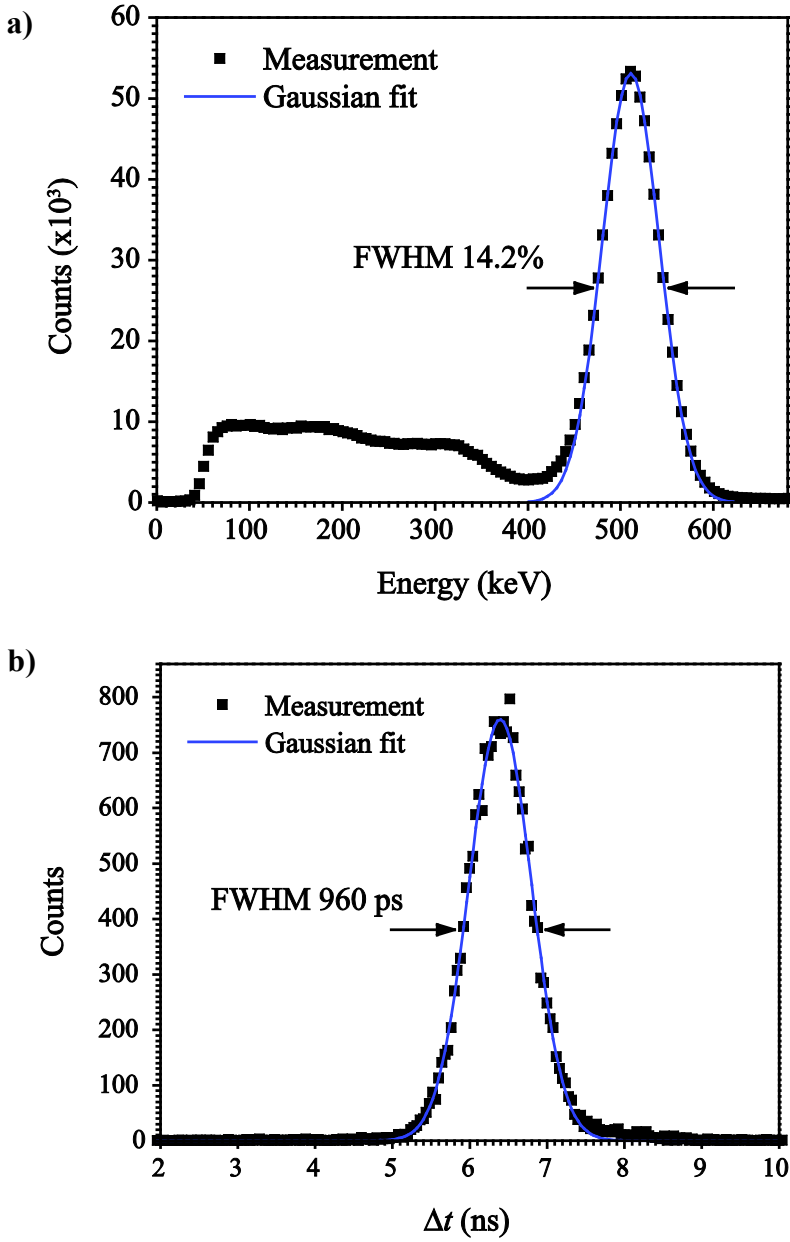
Figure 7.7. Pulse height spectrum (a) measured by irradiating the entire detector with 511 keV photons. Timing spectrum (b) measured in coincidence with a BaF$_2$ detector. Both spectra were measured in FSR geometry. Black squares represent measured data, while solid blue lines indicate Gaussian fits.

7.3.4.   Energy and timing resolution

The black squares in Figure 7.7.a show a typical pulse height spectrum measured with 511 keV photons. As explained in section 7.2.3, the entire detector surface was uniformly irradiated. The full-energy peak contains ~60% of the total number of counts recorded, while the probability of photoelectric interaction of 511 keV photons in LYSO:Ce^{3+} equals about ~30% of the total probability of interaction. This is attributed to the relatively large size of the crystal: a significant fraction of the detected annihilation photons undergo Compton scattering before being absorbed completely. A Gaussian fit to the full-energy peak is indicated by the solid blue line. The corresponding energy resolution equals 14.2% FWHM at 511 keV.

Figure 7.7.b shows the timing spectrum of the detector, measured in coincidence with a BaF$_2$ crystal. The timing resolution equals 960 ps FWHM. As the contribution of the BaF$_2$ crystal is considered negligible, the CRT of two of the SiPM-based detectors in coincidence is expected to be $0.96 \times \sqrt{2} \approx 1.4$ ns FWHM.

7.4.   Discussion and conclusion

A novel, SiPM-array based, high-resolution, monolithic scintillator PET detector with DOI correction has been developed. As the SiPM array is very thin and composed of low-Z materials only, it can be placed on the front surface of the crystal without significantly disturbing the annihilation photon beam. Such FSR geometry appears to provide better performance than conventional BSR, confirming earlier findings obtained with APD-based monolithic PET detectors (Maas *et al.* 2006). The superior performance of FSR is attributed to the fact that ~60% of the annihilation photons are absorbed in the front half of the crystal. Events occurring closer to the SiPM array result in more sharply peaked light distributions that vary more strongly with the position of interaction. Consequently, these events can be positioned more accurately, as has been discussed by van der Laan *et al.* (2006). These results illustrate the potential of SiPMs for the development of novel detector designs aiming at, for example, compactness, DOI determination, and MR-compatibility.

In FSR geometry, spatial resolutions < 1.6 mm FWHM were measured at the detector center in response to a ~0.54 mm FWHM diameter test beam. Slightly larger FWHM values were found near the detector edges, very similar to what was found in APD-based monolithic detectors by Maas *et al.* (2009). Fully characterizing the dependence of the detector spatial response as a function of the position and angle of incidence would allow these effects to be compensated for during iterative image reconstruction, a topic that warrants further research. Hardly any resolution losses were observed at angles of incidence of up to 45º, demonstrating excellent DOI correction. About ~14% FWHM energy resolution was obtained. The single detector timing resolution is estimated to be 960 ps FWHM, translating into a CRT of ~1.4 ns for two detectors in coincidence.

The present results may be compared to those obtained recently by other

authors using SiPM arrays. Kolb *et al.* (2010) could resolve a 12×12 array of 1.5 mm $\times$ 1.5 mm $\times$ 10 mm LYSO:Ce^{3+} pixels using a 3×3 array, made in-house using 3 mm $\times$ 3 mm SiPMs and dedicated light guides. They achieved a single detector timing resolution of 950 ps FWHM and ~22% FWHM energy resolution. España *et al.* (2008) nicely resolved a 4×4 array of 1.5 mm $\times$ 1.5 mm $\times$ 12 mm LYSO:Ce^{3+} pixels using a 6 mm $\times$ 6 mm active area, monolithic 2×2 SiPM array. They obtained energy resolutions between 11% and 22% FWHM for single crystals at different locations on the array, but provided no information on timing resolution yet. Llosá *et al.* (2008) reported ~15% FWHM energy resolution and a CRT of ~3.3 ns FWHM using 4 mm $\times$ 4 mm $\times$ 5 mm monolithic LYSO:Ce^{3+} crystals coupled to a SiPM array consisting of 4×4 pixels of 1 mm $\times$ 1 mm size in a common substrate, in preparation of spatial resolution measurements.

   While very similar timing resolutions were obtained with all approaches, the energy resolution tends to be better for monolithic crystals. All detectors appear to achieve good spatial resolution, although it is to be noted that the position information obtained with pixelated crystals is discrete (crystal identification), whereas our approach yields (pseudo-) continuous coordinates. An advantage of monolithic scintillators is that the reduction of inter-crystal dead space results in higher system sensitivity (van der Laan *et al.* 2007). Another important advantage of the present approach is the excellent DOI correction.

   The spatial resolution obtained in this work is slightly worse than that achieved with APD-based monolithic detectors by Maas *et al.* (2009). This is mainly attributed to the relatively low PDE of the active area of the present SiPM arrays, viz. ~6%, compared to 25%-30% for PMTs and up to ~75% for APDs. However, the spatial resolution obtained with APDs is inherently limited by their relatively large excess noise factor and dark current, as analyzed quantitatively by Maas *et al.* (2008). Due to the relatively low gain of APDs, preamplifier noise is another limiting factor. Thus, further improvement of the SiPM photo-detection efficiency might eventually result in better spatial resolution than can be obtained with APDs.

   Although the timing resolution obtained with SiPM arrays is considerably better than that of APD-based monolithic PET detectors (Maas *et al.* 2009), it is still insufficient for TOF-PET (Muehllehner and Karp 2006). In fact, obtaining the best possible timing resolution has not been emphasized upon in this work, as the present quality of the SiPM arrays used was not expected to allow CRTs significantly smaller than 1 ns. Nevertheless, CRTs $\leq$ 240 ps have recently been demonstrated with small LYSO:Ce^{3+} and LaBr$_3$:Ce^{3+} crystals coupled to 3 mm $\times$ 3 mm SiPMs having higher PDE and lower dark current (Schaart *et al.* 2008b, Kim *et al.* 2009), demonstrating that TOF determination with SiPM-based scintillation detectors is in principle feasible.

   We conclude that SiPMs are a very promising new class of light sensors for use in PET scintillation detectors and that further improvement of these devices may lead to detectors with unsurpassed overall performance.

Acknowledgements

References

Antich P P, Tsyganov E N, Malakhov N A and Sadygov Z Y 1997 Avalanche photo diode with local negative feedback sensitive to UV, blue and green light *Nucl Instrum Meth A* **389** 491-498

Beyer T, Townsend D W, Brun T, Kinahan P E, Charron M, Roddy R, Jerin J, Young J, Byars L and Nutt R 2000 A combined PET/CT scanner for clinical oncology *J Nucl Med* **41** 1369-1379

Bondarenko G, Buzhan P, Dolgoshein B, Golovin V, Guschin E, Ilyin A, Kaplin V, Karakash A, Klanner R, Pokachalov V, Popova E and Smirnov K 2000 Limited Geiger-mode microcell silicon photodiode: new results *Nucl Instrum Meth A* **442** 187-192

Britvitch I, Johnson I, Renker D, Stoykov A and Lorenz E 2007 Characterisation of Geiger-mode avalanche photodiodes for medical imaging applications *Nucl Instrum Meth A* **571** 308-311

Catana C, Wu Y B, Judenhofer M S, Qi J Y, Pichler B J and Cherry S R 2006 Simultaneous acquisition of multislice PET and MR images: Initial results with a MR-compatible PET scanner *J Nucl Med* **47** 1968-1976

Cherry S R 2004 In vivo molecular and genomic imaging: new challenges for imaging physics *Phys Med Biol* **49** R13-R48

Czernin J, Allen-Auerbach M and Schelbert H R 2007 Improvements in cancer staging with PET/CT: Literature-based evidence as of September 2006 *J Nucl Med* **48** 78s-88s

de Haas J T M and Dorenbos P 2008 Advances in yield calibration of scintillators *IEEE Trans Nucl Sci* **55** 1086-1092

España S, Tapias G, Fraile L M, Herraiz J L, Vicente E, Udias J, Desco M and Vaquero J J 2008 Performance Evaluation of SiPM Detectors for PET Imaging in the Presence of Magnetic Fields *IEEE Nuclear Science Symposium and Medical Imaging Conference (2008 NSS/MIC)* (Dresden) 2866-2870

Gambhir S S 2002 Molecular imaging of cancer with positron emission tomography *Nat Rev Cancer* **2** 683-693

Golovin V and Saveliev V 2004 Novel type of avalanche photodetector with Geiger mode operation *Nucl Instrum Meth A* **518** 560-564

Herbert D J, Moehrs S, D'Ascenzo N, Belcari N, Del Guerra A, Morsani F and

Saveliev V 2007 The Silicon Photomultiplier for application to high-resolution Positron Emission Tomography *Nucl Instrum Meth A* **573** 84-87

Israel O and Kuten A 2007 Early detection of cancer recurrence: F-18-FDG PET/CT can make a difference in diagnosis and patient care *J Nucl Med* **48** 28s-35s

Jan S, Santin G, Strul D, Staelens S, Assie K, Autret D, Avner S, Barbier R, Bardies M, Bloomfield P M, Brasse D, Breton V, Bruyndonckx P, Buvat I, Chatziioannou A F, Choi Y, Chung Y H, Comtat C, Donnarieix D, Ferrer L, Glick S J, Groiselle C J, Guez D, Honore P F, Kerhoas-Cavata S, Kirov A S, Kohli V, Koole M, Krieguer M, van der Laan D J, Lamare F, Largeron G, Lartizien C, Lazaro D, Maas M C, Maigne L, Mayet F, Melot F, Merheb C, Pennacchio E, Perez J, Pietrzyk U, Rannou F R, Rey M, Schaart D R, Schmidtlein C R, Simon L, Song T Y, Vieira J M, Visvikis D, de Walle R V, Wieers E and Morel C 2004 GATE: a simulation toolkit for PET and SPECT *Phys Med Biol* **49** 4543-4561

Judenhofer M S, Wehrl H F, Newport D F, Catana C, Siegel S B, Becker M, Thielscher A, Kneilling M, Lichy M P, Eichner M, Klingel K, Reischl G, Widmaier S, Rocken M, Nutt R E, Machulla H J, Uludag K, Cherry S R, Claussen C D and Pichler B J 2008 Simultaneous PET-MRI: a new approach for functional and morphological imaging *Nat Med* **14** 459-465

Kim C L, Wang G C and Dolinsky S 2009 Multi-Pixel Photon Counters for TOF PET Detector and Its Challenges *IEEE Trans Nucl Sci* **56** 2580-2585

Kolb A, Lorenz E, Judenhofer M S, Renker D, Lankes K and Pichler B J 2010 Evaluation of Geiger-mode APDs for PET block detector designs *Phys Med Biol* **55** 1815-1832

Lewellen T K 2008 Recent developments in PET detector technology *Phys Med Biol* **53** R287-R317

Llosá G, Belcari N, Bisogni M G, Collazuol G, Del Guerra A, Marcatili S, Barrillon P, de la Taille C, Bondil-Blin S, Dinu N, Melchiorri M, Tarolli A and Piemonte C 2008 Evaluation of the First Silicon Photomultiplier Matrices for a Small Animal PET Scanner *IEEE Nuclear Science Symposium and Medical Imaging Conference (2008 NSS/MIC)* (Dresden) 2849-2855

Maas M C, van der Laan D J, Schaart D R, Huizenga J, Brouwer J C, Bruyndonckx P, Leonard S, Lemaitre C and van Eijk C W E 2006 Experimental characterization of monolithic-crystal small animal PET detectors read out by APD arrays *IEEE Trans Nucl Sci* **53** 1071-1077

Maas M C, Schaart D R, van der Laan D J, van Dam H T, Huizenga J, Brouwer J C, Bruyndonckx P, Lemaitre C and van Eijk C W E 2008 Signal to noise ratio of APD-based monolithic scintillator detectors for high resolution PET *IEEE Trans Nucl Sci* **55** 842-852

Maas M C, Schaart D R, van der Laan D J, Bruyndonckx P, Lemaitre C, Beekman F J and van Eijk C W E 2009 Monolithic scintillator PET detectors with intrinsic depth-of-interaction correction *Phys Med Biol* **54** 1893-1908

McElroy D P, Saveliev V, Reznik A and Rowlands J A 2007 Evaluation of silicon photomultipliers: A promising new detector for MR compatible PET *Nucl*

Instrum Meth A **571** 106-109

Moses W W 2007 Recent advances and future advances in time-of-flight PET *Nucl Instrum Meth A* **580** 919-924

Muehllehner G and Karp J S 2006 Positron emission tomography *Phys Med Biol* **51** R117-R137

Musienko Y, Auffray E, Lecoq P, Reucroft S, Swain J and Trummer J 2007 Study of multi-pixel Geiger-mode avalanche photodiodes as a read-out for PET *Nucl Instrum Meth A* **571** 362-365

Nestle U, Weber W, Hentschel M and Grosu A L 2009 Biological imaging in radiation therapy: role of positron emission tomography *Phys Med Biol* **54** R1-R25

Phelps M E 2000 Positron emission tomography provides molecular imaging of biological processes *P Natl Acad Sci USA* **97** 9226-9233

Renker D 2007 New trends on photodetectors *Nucl Instrum Meth A* **571** 1-6

Rohren E M, Turkington T G and Coleman R E 2004 Clinical applications of PET in oncology *Radiology* **231** 305-332

Schaart D R, van Dam H T, Seifert S, Vinke R, Dendooven P, Löhner H and Beekman F J 2008a SiPM-Array Based PET Detectors with Depth-of-Interaction Correction *IEEE Nuclear Science Symposium and Medical Imaging Conference (2008 NSS/MIC)* (Dresden) 2856-2860

Schaart D R, Seifert S, van Dam H T, de Boer M R, Vinke R, Dendooven P, Löhner H and Beckman F J 2008b First Experiments with LaBr(3):Ce Crystals Coupled Directly to Silicon Photomultipliers for PET Applications *IEEE Nuclear Science Symposium and Medical Imaging Conference (2008 NSS/MIC)* (Dresden) 3266-3269

Seifert S, Schaart D R, van Dam H T, Huizenga J, Vinke R, Dendooven P, Löhner H and Beekman F J 2008 A High Bandwidth Preamplifier for SiPM-Based TOF PET Scintillation Detectors *IEEE Nuclear Science Symposium and Medical Imaging Conference (2008 NSS/MIC)* (Dresden) 891-894

Shao Y, Cherry S R, Farahani K, Slates R, Silverman R W, Meadors K, Bowery A, Siegel S, Marsden P K and Garlick P B 1997 Development of a PET detector system compatible with MRI/NMR systems *IEEE Trans Nucl Sci* **44** 1167-1171

Surti S, Kuhn A, Werner M E, Perkins A E, Kolthammer J and Karp J S 2007 Performance of philips gemini TF PET/CT scanner with special consideration for its time-of-flight imaging capabilities *J Nucl Med* **48** 471-480

Townsend D W 2008 Multimodality imaging of structure and function *Phys Med Biol* **53** R1-R39

van der Laan D J, Maas M C, Schaart D R, Bruyndonckx P, Leonard S and van Eijk C W E 2006 Using Cramer-Rao theory combined with Monte Carlo simulations for the optimization of monolithic scintillator PET detectors *IEEE Trans Nucl Sci* **53** 1063-1070

van der Laan D J, Maas M C, de Jong H W A M, Schaart D R, Bruyndonckx P,

Lemaitre C and van Eijk C W E 2007 Simulated performance of a small-animal PET scanner based on monolithic scintillation detectors *Nucl Instrum Meth A* **571** 227-230

8

Monolithic LaBr$_3$:Ce Crystals on Silicon Photomultiplier Arrays for Time-of-Flight Positron Emission Tomography

Abstract - Positron emission tomography (PET) detectors based on monolithic scintillation crystals exhibit good spatial and energy resolution, intrinsically provide depth-of-interaction information, have high γ-photon capture efficiency, and may reduce the manufacturing costs compared to pixelated crystal arrays. Here, we present the characterization of a detector consisting of an 18.0 mm × 16.2 mm × 10.0 mm monolithic LaBr$_3$:5%Ce scintillator directly coupled to a 4 × 4 array of silicon photomultipliers (SiPMs). An energy resolution of 6.4% FWHM was obtained. The point-spread-function (PSF) was determined for different regions of the detector. The full-width-at-half-maximum (FWHM) of the PSF was measured to be < 1.5 mm at the center of the detector and < 1.7 mm averaged over the entire crystal. Both values are not corrected for the ~0.6 mm FWHM test beam diameter. Furthermore, the influence of edge effects was investigated. We found that near the edges of the detector the spatial resolution degrades to 2.2 mm (FWHM) and a bias is the position estimates up to 1.5 mm was observed. Moreover, the coincidence resolving time (CRT) for two identical detectors in coincidence was measured to be as small as ~198 ps FWHM.

8.1.   Introduction

The use of monolithic scintillators on multi-channel light sensors is a promising detector concept for application in time-of-flight (TOF) positron emission tomography (PET). Monolithic scintillator detectors exhibit a number of favorable properties such as the intrinsically available depth-of-interaction (DIO) information, good spatial resolution, excellent energy resolution, high γ-photon capture efficiency, and relatively simple detector assembly (Bruyndonckx *et al.* 2004, 2006, Maas *et al.* 2006, and 2007, van der Laan *et al.* 2007, van Dam *et al.* 2011a, b). This detector concept is all the more interesting as recent progress in solid-state photosensor technology has made arrays of so-called silicon photomultipliers (SiPMs) commercially available. SiPMs (also referred to as multi-pixel photon counters (MPPCs) or solid state photomultipliers (SSPMs)) offer high gain, fast response, insensitivity to magnetic fields, compactness, ruggedness, and potential cost effectiveness.

Recently, applying one of the first available arrays of SiPMs (SensL SPMarray 3035G16) to a 13.2 mm ×13.2 mm ×10.0 mm monolithic LYSO:Ce^{3+} scintillator yielded very promising results (Schaart *et al.* 2009). A spatial resolution as good as 1.58 mm full-width-at-half-maximum (FWHM) and an energy resolution of 14.2% at 511 keV were measured. Yet, the (single detector) timing resolution of this detector was moderate with 960 ps FWHM. In principle, however, SiPM based scintillation detectors are capable of much better timing performance as e.g. shown by Kim *et al.* (2009) and Wang (2010). One reason for the suboptimal timing resolution in our earlier measurement was the performance of the preamplifiers. In order to overcome this issue a new amplifier concept was developed (Huizenga *et al.* 2011). Using these improved readout electronics we could recently demonstrate for individual SiPMs (Hamamatsu MPPC-S10362-33-50C) optically coupled to 3 mm × 3 mm × 5 mm LaBr$_3$:5%Ce scintillators that SiPMs can even outperform the timing performance of conventional photomultiplier tubes (PMTs) (Schaart *et al.* 2010, Seifert *et al.* 2012).

In this work, an improved monolithic scintillator detector is characterized. In this detector a 16-channel version of our improved preamplifier is utilized to read out the signals of a 4 × 4 SiPM array which is directly optically coupled to a matching, monolithic, LaBr$_3$:5%Ce scintillator. This scintillator material was chosen for its higher light yield (de Haas and Dorenbos 2008), better energy resolution (Nassalski *et al.* 2007) and better timing performance (Seifert *et al.* 2012) compared to LYSO:Ce.

8.2.   Methods

8.2.1.   Detector

The detector is based on a bare 18.0 mm × 16.2 mm × 10.0 mm monolithic LaBr$_3$:5%Ce scintillator (Saint-Gobain) with one 18.0 mm × 16.2 mm surface optically polished and the remaining five surfaces mechanically depolished. The
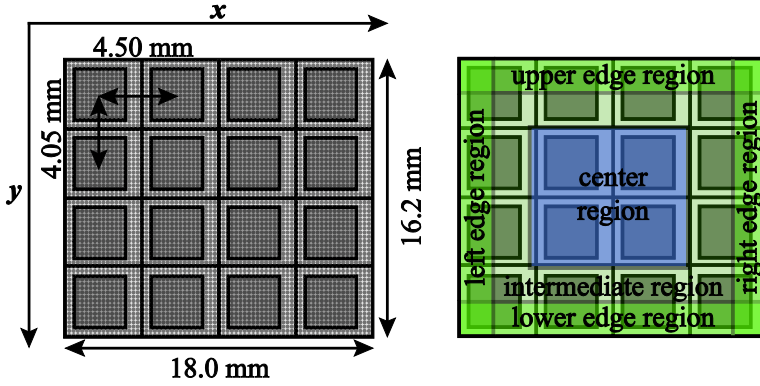
Figure 8.1. In-scale representation of the SiPM sensor array indicating the active area of the SiPMs, as well as the γ-photon irradiation gr grid (dots in the left panel). The panel on the right depicts the selected regions of interest used in the analysis of the data.

polished crystal surface matches the dimensions of the SiPM array and is optically coupled to it using LS-3252 encapsulation gel from Nusil. All other faces of the crystal are covered with a highly reflective PTFE-based material (Spectralon). The SiPM array (Hamamatsu MPPC S11064–050P) consists of 4 × 4 SiPM pixels (see Figure 8.1) mounted at a pitch of 4.50 mm in one direction (hereafter referred to as the *x*-direction) and 4.05 mm in the other direction (the y-direction). Each pixel has an active area of 3 mm × 3 mm, made up of 3600 Geiger-mode avalanche photodiodes (microcells).

Because of the high degree of hygroscopicity of the $LaBr_3$:5%Ce crystal, the detector is contained in a moisture-tight enclosure. This detector enclosure is directly connected to a second casing which provides electronic shielding for the preamplifiers. The temperature inside the shielding box is regulated actively. This is done by a feedback loop where the temperature is measured as close to the SiPM as possible while regulating the cooling power of a Peltier element which is used to cool the air that is constantly flushed through the shielding-box. In this way the measured temperature inside the shielding-box was kept at 15.00 ºC ± 0.03 ºC during the measurements. Additionally, the temperature of the moisture-tight enclosure was monitored on the outside to be 17.13 ºC ± 0.13 ºC. In both cases the temperature uncertainties are given as $2 \times \sigma_T$ where σ_T is the standard deviation in the measurement data. The temperature as well as the temperature fluctuations of the SiPM array is expected to be in between the values measured at the two locations.

8.2.2.   Preamplifier

The preamplifier for the 4 × 4 SiPM array is based on a preamplifier concept that was developed to specifically suit the requirements of SiPMs. In this concept the amplifier input stage features a common-base transimpedance
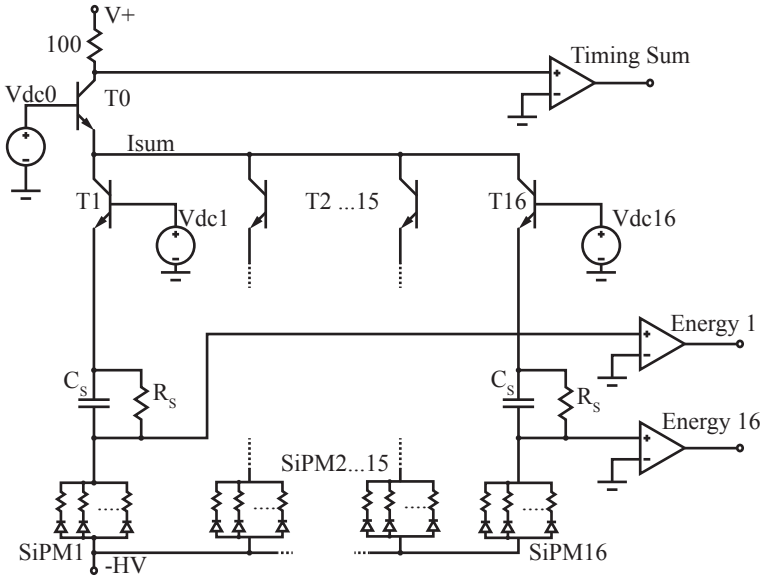
Figure 8.2. Simplified schematic layout of the 16 channel amplifier.

amplifier which presents a very low input impedance to the SiPM at high frequencies. A single-channel version of this preamplifier has been shown to enable excellent timing performance when used in combination with individual SiPMs (MPPC-S10362-33-50C) and small scintillation crystals (Seifert *et al.* 2011).

The details of the single channel amplifier are described elsewhere (Huizenga *et al.* 2011). In short, the main feature of this amplifier is a transistor in common-base configuration at the amplifier input of each channel. By applying a constant voltage to the transistor base this transistor configuration is acting as voltage source, i.e. the voltage at the transistor emitter is kept constant while a low impedance is presented to the SiPMs. The signal current at the emitter of the transistor is also present at the collector which in turn presents a high impedance to subsequent circuitry, thus essentially isolating the large SiPM capacitance from subsequent electronics.

The concept of the single-channel design enables relatively easy adaption towards a multichannel amplifier. In this work the design shown in Figure 8.2 was implemented to read out the 16-channel SiPM array. Each detector element has its own input transistor (T1 – T16), similar to the single channel version. The individual energy signals are obtained by inserting a filter network (comprised by R_s and C_s) in between each SiPM and the input of the corresponding transistor.

In order to obtain a combined timing signal from all detector elements the signal currents are summed by connecting all collectors to the input of a secondary common-base amplifier (T0) which keeps this node (Isum) at a

constant voltage. In order to minimize transit time differences between the channels the trace length of each collector to the summing node must be kept equal. The transit time on the printed circuit board is more than 50 ps/cm. It can therefore contribute significantly to timing errors.

The sum of the signal currents is present at the collector of this transistor. In analogy to the input stage of each channel, this second common-base amplifier isolates the parasitic capacitances of the 16 collectors and the inherent parasitic layout capacitances of the board traces from the subsequent resistor (100 Ω), which is used to convert the summed current signal to a voltage. Keeping the capacitance at this point low is of utmost importance for the bandwidth of the amplifier because the resistor and the capacitances form a low-pass filter for the signal.

A practical feature of this design is the ability to fine-tune the individual SiPM detector bias voltages. The total bias voltage across the detector is the sum of the -HV voltage and the emitter voltage of the input transistor. This emitter voltage can be controlled via the base voltage for each channel separately (Vdc1 ... Vdc16). In this way the SiPM array can be operated using a single bias supply only.

8.2.3.   Measurements

All measurements were performed at two bias voltages corresponding to $V_{ob} = 1.2$ V and $V_{ob} = 2.0$ V above the average breakdown voltage of the SiPMs in the array. The lower V_{ob} corresponds to the recommended bias voltage given by the manufacturer, while $V_{ob} = 2.0$ V appeared to be optimal in terms of the timing resolution. Spatial resolution measurements were performed using the setup described by Maas *et al.* (2009). The detector is irradiated with a beam of 511 keV annihilation photons in the so-called *front-side readout* (FSR) geometry, i.e. the photosensor is coupled to the surface of the scintillation crystal facing the beam, which we define as the front surface (see Figure 8.3). The beam is defined by placing the detector close to a 0.5 mm diameter [22]Na source and operating it in coincidence with a collimated LaBr$_3$:5%Ce detector (Saint-Gobain 25S25) placed on the opposite side of the source. The collimators' bore diameter is 5 mm, the distance between source and collimator is 815 mm, and the distance between the source and the closest surface of the LaBr$_3$:5%Ce crystal is 27.3 mm.

A geometric estimate of the beam diameter thus results in ~0.69 mm at the crystal surface closest to the source diverging up to ~0.77 mm at the crystal surface furthest away. A more detailed analysis of the beam size by means of a Monte Carlo simulation that takes into account the finite positron range and acolinearity results in a beam-profile with a FWHM of 0.57 mm and 0.64 mm at planes corresponding to the crystal surfaces closest and furthest away from the [22]Na source, respectively (Maas *et al.* 2010).
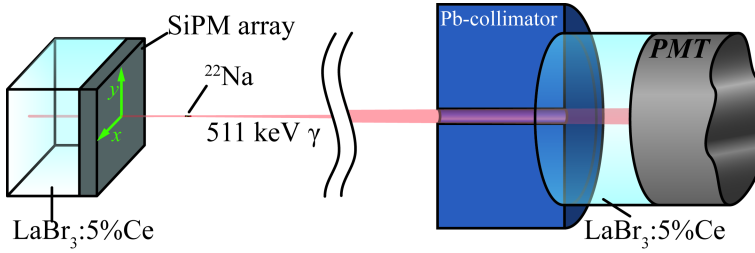
Figure 8.3. Illustration of the measurement geometry showing a monolithic scintillator detector irradiated in front-side readout (FSR) geometry at a given position $v = (x,y)$ by a perpendicularly incident beam of γ-photons. This beam is defined by electronic collimation accepting only coincidence events between the detector-under-test and a reference detector with a Pb-collimator.

    The detector is mounted on a translation stage that allows moving the detector in the plane perpendicular to the annihilation photon beam (i.e. the *x-y*-plane). Reference events were recorded at an equidistant, 71×65 grid of reference beam positions (x_i, y_j), covering the entire front surface of the crystal at a pitch of 0.25 mm (as indicated by the dots in Figure 8.1). At each grid position 300 events were acquired.

    Pulse height spectra were derived by correcting the digitized pulse heights of all detector channels for offsets and gain differences and then adding the 16 corrected pulse heights of each event. The spectra were normalized such that the center of the full-energy peak corresponded to 511 keV. No corrections for nonlinearity of the SiPMs signal were applied, assuming that the influence of saturation is negligible as will be justified in section 8.3.1.

    The energy resolution was determined as the FWHM of a Gaussian fit to the 511 keV full-energy-peak including a constant offset. In order to exclude the broadening due the x-ray escape peak, only data above 495 keV were considered for the fit. Under absence of so-called transfer noise and a negligible noise contribution of readout electronics the energy resolution of a scintillation detector is commonly expressed in terms of the so-called intrinsic energy resolution R_{int} of the scintillation material and the statistical variation of the number of detected photons N under the assumption of Poisson statistics (Dorenbos *et al.* 1995, Moszyński *et al.* 1998):

$$\frac{\Delta E_{FWHM}}{\bar{E}} = \sqrt{\left(R_{int}^2 + 2.35^2 \frac{ENF}{\bar{N}} \right)}, \tag{8.1}$$

where *ENF* is often referred to as the excess noise factor. It represents the broadening of the signal variance due to the dispersion associated with the multiplication process(es) in the photosensor. Without this dispersion the statistical contribution to the signal variance follows Poison statistics, i.e. $ENF = 1$.

    The detector timing resolution was determined by irradiating an area of

~4 mm diameter with 511 keV annihilation photons from a ^{22}Na point source and measuring the coincidence resolving time (CRT) against a reference detector. The irradiated area was located in the center of the detector if not mentioned otherwise. The reference detector consists of a 3 mm × 3 mm × 5 mm LaBr$_3$:5%Ce crystal mounted on a 3 mm × 3 mm SiPM (MPPC-S10362-33-50C). The single-detector timing resolution of this reference detector was previously measured to be 65 ps FWHM (Seifert *et al.* 2011). The fast summed signal of the monolithic LaBr$_3$:5%Ce detector and the timing signal of the reference detector were sampled by two synchronized 10-bit sampling ADCs (Acqiris DC282, sampling rate 8 GS/s). Simultaneously, the signals of the energy channels were shaped (CAENN568B; 100 ns shaping time) and the peak values were digitized (CEAN V785) and stored together with the timing traces for off-line analysis.

Only full-energy events, i.e. events within the full-width-at-tenth-maximum, FWTM, of the 511 keV peak, were selected for further processing of the timing data. This selection corresponds to an energy window of 481 keV – 541 keV for the measurement with $V_{ob} = 1.2$ V and of 475 keV – 547 keV for the data recorded at $V_{ob} = 2.0$ V, respectively. For all valid events a cubic spline interpolation was performed on the sampled traces and time stamps were determined as the point where the interpolated trace crosses a certain threshold value. This threshold value was optimized separately for each measurement. A more detailed description of the method is given elsewhere (Schaart *et al.* 2010, Seifert *et al.* 2011).

8.2.4. Position estimation

The complete set of 1,384,500 measured events served both as reference data for the position estimation and as test data for the determination of the spatial resolution, using the leave-one-out method described by Maas *et al.* (2009). The position of interaction of a given test event was determined by an improved form of the so called *k*-nearest neighbor (*k*-NN) method described by van Dam *et al.* (2011a). First all light patterns were normalized such that the sum of all 16 SiPM signals equaled unity. The unknown annihilation photon interaction position $\mathbf{v} = (x,y)$ of the unclassified event was subsequently estimated by calculating the Euclidean distances, i.e. the square root of the sum-of-squared-differences, of the measured light distribution to those of all events in the reference set. A subset of the reference data consisting of the *k* (here $k = 400$) closest matches (*nearest neighbors*) was selected and a histogram of their (x,y) irradiation coordinates was created. This 2D irradiation position histogram is smoothed with a moving average filter of 5 × 5 bins. Thus, each new bin value is based on the average of 25 bin values of the original histogram. Near the edges of the histogram the number of bins for averaging was decreased at the side of the edge. The coordinate corresponding to the maximum value of the smoothed histogram was assigned to the unclassified event.

A 2D-error histogram was created from the differences between all estimated coordinates and their respective 'true' irradiation points. By proper

normalization one may obtain the so-called point-spread function (PSF) for the detector. The PSF was interpolated with a 2D cubic spline and the FWHM and the FWTM of the interpolated PSF were determined as measures for the detector spatial resolution along the x-direction and y-direction, respectively.

The above procedure was repeated using only the errors corresponding to irradiation positions from specific regions of interest. One region, hereafter referred to as *center region*, is demarcated by a 9.25 mm × 8.25 mm rectangle around the 4 pixels in the center of the sensor. Furthermore, four *edge regions* were defined which include all irradiation points recorded within 2 mm of either edge of the sensor. These regions will be denoted as *upper*, *lower*, *left*, and *right edge region* according to their position relative to the center region. Lastly, all remaining data points are summarized in the *intermediate region*. All regions are depicted in Figure 8.1.

In order to evaluate a possible bias in the position estimation a bias vector $\mathbf{b}(\mathbf{v})$ was calculated at each reference beam position $\mathbf{v} = (x_i, y_j)$. The individual vector elements of $\mathbf{b}(\mathbf{v})$ are hereby defined as the mean difference between the reference beam position $\mathbf{v}$ and the corresponding estimates on the x-y-coordinates ($\hat{x}(\mathbf{v})$ and $\hat{y}(\mathbf{v})$):

$$
\mathbf{b}(\mathbf{v}) = \begin{bmatrix} \dfrac{\sum\limits_{m=1}^{M}\left(\hat{x}_m(\mathbf{v}) - x_i\right)}{M} \\[2em] \dfrac{\sum\limits_{m=1}^{M}\left(\hat{y}_m(\mathbf{v}) - y_j\right)}{M} \end{bmatrix}, \tag{8.2}
$$

where $\hat{x}_m(\mathbf{v})$ and $\hat{y}_m(\mathbf{v})$ are the estimated x-y-coordinates of the mth data point recorded at $\mathbf{v}$. M is the number of reference events recorded per position (viz. $M = 300$).

One possible issue with the calculation of $\mathbf{b}(\mathbf{v})$ is the contribution of random events. As random events are not correlated to the beam position they cause a background which is distributed within the bounds of the crystal dimensions. It is easy to see that if (8.2) is evaluated for a uniform distribution the resulting bias vector increases towards the edges of this distribution. This means, that including random events in the bias estimation leads to an overestimation of the bias vector towards the detector edges. In order to reduce this effect only those terms were taken into account in the corresponding sums in (8.2) for which $\hat{x}_m(\mathbf{v}) - x_i$ and $\hat{y}_m(\mathbf{v}) - y_j$ are smaller than 4 mm (which corresponds to approximately the FWTM of the PSF, see section 8.3.2.

8.3. Results and discussion

8.3.1. Energy spectra

Figure 8.4 shows the pulse height spectrum containing all data measured over the entire surface of the detector for $V_{\text{ob}} = 1.2$ V (squares) and $V_{\text{ob}} = 2.0$ V
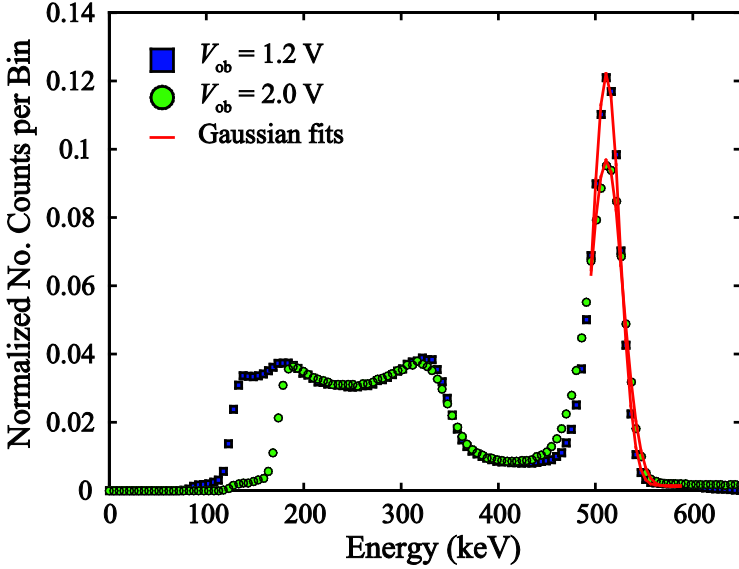
Figure 8.4. Energy spectra recorded with 511 keV γ-photons normalized to the integral of the photopeak region (410 keV – 560 keV). The spectra recorded at $V_{ob} = 1.2$ V (squares) and at $V_{ob} = 2.0$ V (circles) are depicted together with the corresponding Gaussian fits through the corresponding full energy peaks (lines).

(circles). Both spectra were normalized to the integral value of the photopeak region between 410 keV and 560 keV. For illustration the fitted function used to estimate the energy resolution for the measurement at $V_{ob} = 1.2$ V is depicted by the red curve in Figure 8.4. The FHWM of the fitted function equals 6.4% in the case of $V_{ob} = 1.2$ V and 7.8% in the case of $V_{ob} = 2.0$ V. This observed difference can be attributed to the increasing probabilities for crosstalk and afterpulses to occur as V_{ob} is increased (Du and Retiere 2008), which increases the observed excess noise of the SiPMs.

We estimate the photon detection efficiency (PDE) of the detector to be 7% at $V_{ob} = 1.2$ V and 9% at $V_{ob} = 2.0$ V, by multiplying the fill factor (49%) of the array and the measured PDE of the 3 mm × 3 mm × 5 mm LaBr$_3$:5%Ce crystal coupled to a single 3 mm × 3 mm MPPC-S10362-33-050C (Seifert *et al.* 2011), which is identical to a single pixel in the MPPC-S11064-050P array. This means that on average ~2250 and ~3100 microcells are fired, respectively, in response to a 511 keV γ photon. Using these values in (8.1) one can estimate the *ENF* for the MPPC array. This results in *ENF* = 1.2 at $V_{ob} = 1.2$ V and *ENF* = 2.7 at $V_{ob} = 2.0$ V. This increase in the observed excess noise is in agreement with the values given by (Szczęśniak *et al.* 2010) for the upper limit of the excess noise for the MPPC-S10362-33-050C.

The influence of optical SiPM saturation is considered to be negligible. The
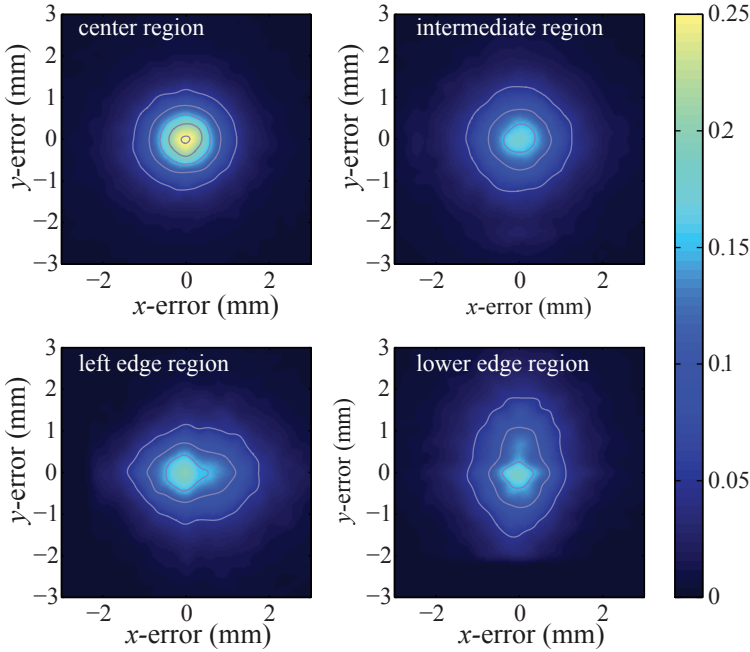
Figure 8.5. Point spread functions averaged for all irradiation positions within different regions as defined in Figure 8.1: center region (top left), the intermediate region (top right), the left edge region (lower left), and the lower edge region (lower right).

total number of fired cells might be up to ~50% larger than the number of cells that are triggered by scintillation photons (2250 – 3100) due to crosstalk and afterpulsing. Yet, the number of microcells in the whole of the array equals 16 × 3600 = 57600, which is an order of magnitude larger, still. This assessment may be confirmed by comparing the two pulse height spectra presented in Figure 8.4, which reveal no significant change in the relative positions of the 511 keV photo-peak and Compton edge.

8.3.2. Position Estimation

8.3.2.1. Spatial resolution

The point spread function obtained in the center region; the intermediate region, the left edge region, and the lower edge region (as defined in Figure 8.1 and section 8.2.4) are depicted in Figure 8.5. The plots for the right edge region and the upper edge region are omitted as they are essentially mirror images of the left edge region and the lower edge region, respectively. In addition, the spatial resolutions in terms of the FWHM and the FWTM of the PSF in the x- and y-direction that were determined for the measurements at the two different V_{ob}, are summarized in Table 8.1 for all defined regions. It is noteworthy, that

Table 8.1. spatial resolution values for the entire detector and the two regions of interest (see text and Figure 8.1)

V_{ob}	Region	x-direction		y-direction	
		FWHM	FWTM	FWHM	FWTM
1.2 V	entire detector	1.64 mm	4.03 mm	1.54 mm	3.97 mm
	center	1.43 mm	3.30 mm	1.36 mm	3.08 mm
	intermediate	1.76 mm	4.12 mm	1.66 mm	4.52 mm
	upper edge	1.64 mm	3.94 mm	2.12 mm	4.64 mm
	lower edge	1.60 mm	3.95 mm	2.16 mm	4.94 mm
	left edge	2.15 mm	4.95 mm	1.43 mm	3.87 mm
	right edge	2.02 mm	4.43 mm	1.48 mm	3.79 mm
2.0 V	entire detector	1.63 mm	4.11 mm	1.59 mm	3.92 mm
	center	1.44 mm	3.32 mm	1.39 mm	3.14 mm
	intermediate	1.72 mm	4.54 mm	1.66 mm	4.55 mm
	upper edge	1.60 mm	3.90 mm	2.30 mm	4.91 mm
	lower edge	1.60 mm	3.82 mm	2.19 mm	5.09 mm
	left edge	2.11 mm	4.86 mm	1.43 mm	3.74 mm
	right edge	1.96 mm	4.80 mm	1.57 mm	3.79 mm

the spatial resolution that was obtained at $V_{ob} = 2.0$ V does not seem to be worse compared to the values obtained at $V_{ob} = 1.2$. One might expect a degradation of the spatial resolution due to the large increase in the excess noise at the higher bias voltage (van der Laan *et al* 2007). Yet, in the present detector this degradation is partially compensated for by the increase in the photon detection efficiency and the corresponding increase in the number of detected photons.

The spatial resolution in the center region of the detector (~1.4 mm FWHM) is excellent for application in clinical PET. It is can be noted that the resolution in the *y*-direction appears to be slightly better than the resolution in the *x*-direction. This probably is a result of the difference in the pixel pitch for the two directions (see Figure 8.1), which may be explained best by considering the underlying mechanisms of the position estimation routine.

As described in section 8.2.4, the estimation of a given interaction position is based on the resulting light distribution on the photosensor. The probability for a given event at $\mathbf{v} = (x, y)$ to be misclassified by a certain distance $\Delta \mathbf{v}$ depends on the similarity between the measured light distribution and the light distributions recorded at $\mathbf{v} + \Delta \mathbf{v}$. In other words, the spatial resolution, i.e. the ability to distinguish two neighboring interaction positions, depends on the change in the measured light distribution with a certain change in the interaction position (van der Laan *et al* 2007). It should be noted that this limitation of the spatial resolution by the gradient in the light distribution with respect to the interaction position is a general principle and independent on the exact means of the

position estimation.

Now, let us consider a scintillation event at $\mathbf{v} = (x, y)$ somewhere in the center of the detector. The intensity of direct scintillation light (i.e. light which was not reflected or scattered prior to its detection) decreases monotonically with increasing distance from $\mathbf{v}$. In consequence, the intensity measured by the two sensor pixels that are direct neighbors to the pixel closest to $\mathbf{v}$ observe less direct light than the two neighbors in the y-direction, due to the ~30% larger inactive area between neighboring pixels in the x-direction. As a result, the absolute change of the light distribution with a certain change of $\mathbf{v}$ in x-direction is smaller than if the same change is applied in the y-direction.

The reduction of the change in the measured light distribution with a given change in $\mathbf{v}$ also leads to the degradation of the spatial resolution in the intermediate and edge regions of the detector that can be observed in Figure 8.5 and Table 8.1. The light distributions become more and more similar for neighboring interaction positions towards the edges of the detector due to the reflection of scintillation light at the sides of the crystal. Therefore the resolution worsens significantly (up to 2.2 mm FWHM) in the direction perpendicular to the closest edge. It is interesting to note that the resolution parallel to the edges does not change significantly compared to the values determined for the entire detector even for interactions close to the edge.

The degradation in the spatial resolution discussed in the previous paragraph is mitigated by a second edge-effect, which is that only coordinates within the bounds of the detector can be assigned. This truncation of the PSF at the edges of the detector is visible in the corresponding graphs in Figure 8.5 in the form of a distinct asymmetry of the average PSFs in the edge regions with respect to the axis parallel to the closest edge.

8.3.2.2. *Positioning bias*

The calculated bias vector $\mathbf{b}(\mathbf{v})$ as a function of the reference beam position $\mathbf{v}$ is illustrated in Figure 8.6. In order to keep this figure legible the average of $\mathbf{b}(\mathbf{v})$ over intervals of 3×3 irradiation positions (i.e. 0.75 mm × 0.75 mm) is displayed. Furthermore the length of $\mathbf{b}(\mathbf{v})$ - calculated as the Euclidian norm of $\mathbf{b}(\mathbf{v})$ - is show in the same figure. The detector center exhibits a bias of negligible magnitude (<0.1 mm). In the intermediate region the bias vector $\mathbf{b}(\mathbf{v})$ has a magnitude in the order of ~0.5 mm and is pointed away from the detector center. The edge regions exhibit the strongest bias (up to 1.5 mm), yet in contrast to the intermediate region $\mathbf{b}(\mathbf{v})$ it is directed towards the center of the detector. This behavior is a consequence of the two competing edge effects that were discussed in the previous section.

The increasing similarity between light distributions of neighboring interaction positions with decreasing distance to the crystal edge means that for a given interaction at $\mathbf{v}$ with a corresponding light distribution it is more likely to find matching light distributions at coordinates closer towards the detector edge than to find matching light distributions at coordinates closer to the detector
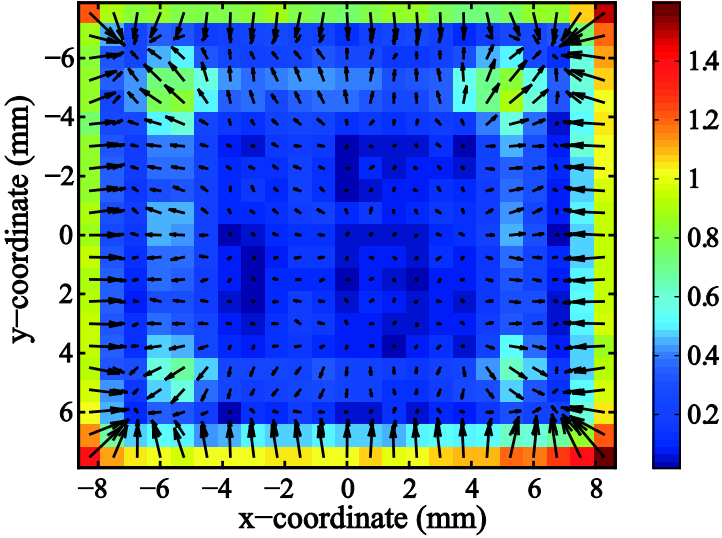
Figure 8.6. Bias vector b(v) averaged over 3 × 3 irradiation positions (0.75 mm × 0.75 mm) as a function of the (average) reference beam position v. The color scale indicates the length of b(v).

center. The position estimation relies on the selection of a number of best matching light distributions (see section 8.2.4) which is a probabilistic process. As a result, the position estimation for events within a certain range of a crystal edge (in our case ~4 mm) is biased toward the crystal edge as observed in the intermediate region.

The same reasoning can be applied when considering the influence of the PSF cut-off at the detector edges. This truncation of the sample space for the selection of best matching light distributions reduces the number of matching light distributions with coordinates closer towards the edge than the true interaction position **v**. Additionally, the maximum distance for a misclassification is bound on one side by the distance between **v** and the edge of the detector. The combination of the biased sample space and the asymmetric probability distribution of misclassifications results in the bias towards the detector center that is evident for events close to the detector edge.

It is interesting to note the different ranges for the two competing edge effects. The effect of increasing light distribution similarity has a range of ~4 mm. As argued in the text above, this effect is closely related to the layout of the photosensor and it is therefore not surprising that its range is similar to the pixel pitch. The influence of the truncation of possible coordinates, on the other hand, is directly linked to the misclassification of events. Its range is therefore determined by the average range of coordinates from which matching distributions are drawn in the positioning routine, which roughly corresponds to the spatial resolution in our measurement (i.e. ~2 mm in the edge regions).

This distinction has consequences for the formation of strategies aimed at minimizing the influence of edge effects on the accuracy and the bias of the γ-interaction position estimation in monolithic scintillation detectors. The influence of light distribution similarity might e.g. be minimized by intelligent photosensor design with smaller pixels towards the edges of the crystal. It is expected that such a design would not only reduce the bias in the intermediate region but also lead to an improvement of the spatial resolution. This, in return, would also reduce the bias due to the coordinate-cut-off. Beyond this, however, we see no further obvious design solution to reduce the contribution of the coordinate-cut-off.

In principle one could correct for the remaining bias in the position reconstruction by reversing the vectors shown in Figure 8.6 and using this data as a transformation map. A different approach would be to re-bin data obtained for uniform irradiation of the detector in such a way that the number of counts per bin is equal for all bins and to apply a transformation to the bin edges in order to obtain a uniform grid. Alternatively, a more crude solution could be to choose the bin size large enough so that the bias introduced by the coordinate-cut-off appears is contained within one bin, thus avoiding the need for additional bias-correction entirely.

8.3.3. Timing resolution

In Figure 8.7 the coincidence spectra that were obtained at the different V_{ob} are compared. The spectra are plotted together with their corresponding Gaussian fits (red curves). The FWHM of those fits is used as a measure of the timing resolution. Quadratically subtracting the timing resolution of the reference detector (65 ps FWHM) and multiplying with $\sqrt{2}$ yields the predicted CRT between two identical detectors operated at the same voltage-over-breakdown: CRT = 239 ps FWHM and CRT = 198 ps FWHM for $V_{ob} = 1.2$ V and $V_{ob} = 2.0$ V, respectively. Thus a significant improvement is observed at the larger V_{ob}.

This is the reversed trend as the one that was observed for the energy. The reason for this lays in the fundamental difference between the observed excess noise for SiPM-based scintillation detectors and for detectors based on proportional photosensors such as photomultiplier tubes (PMTs) and avalanche photodiodes (APDs). The *ENF* is commonly defined in terms of the relative deterioration of the observed energy resolution of a scintillation detector (see equation (8.1)). This deterioration is associated with the multiplication noise for individual photoelectrons/electron-hole-pairs in the case of PMTs and APDs. In contrast, the *ENF* of SiPMs, which are based on a large number of Geiger-mode single-photon counters, is largely dominated by crosstalk and afterpulsing.

The latter two effects occur with a certain time delay after the firing of the original microcell by a scintillation photon. As the time stamps for scintillation events are created at very early parts of the scintillation pulse, it can be argued that the influence of afterpulses on the CRT is negligible and that the contribution of crosstalk is small (Seifert *et al.* 2011). The fact that these two
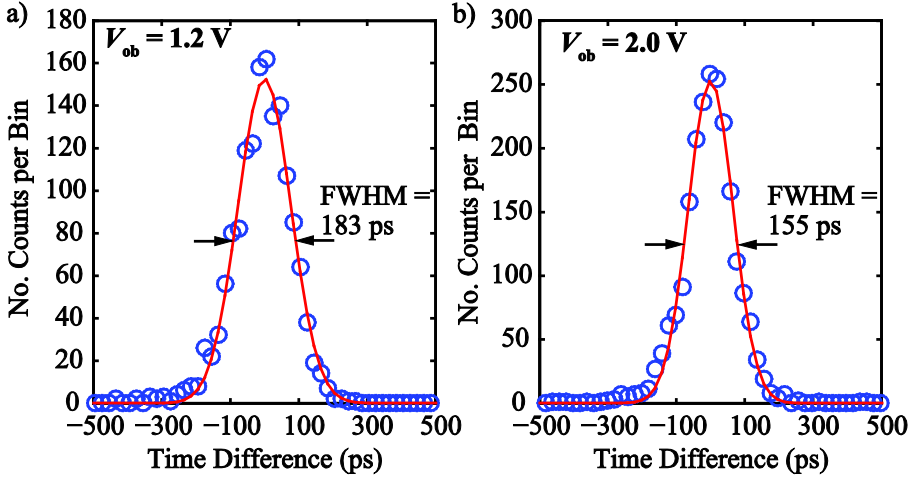
Figure 8.7. Time difference spectra measured at the center of the monolithic 18.0 mm × 16.2 mm × 10.0 mm LaBr₃:5%Ce crystal in coincidence with a 3 mm × 3 mm × 5 mm LaBr₃:5%Ce reference detector (single-detector timing resolution 65 ps FWHM). The spectra were measured at V_{ob} = 1.2 V (a) and V_{ob} = 2.0 V (b).

major contributions to the *ENF* of SiPM-based scintillation detectors have only little influence on the timing resolution means that *ENFs* determined from pulse-height spectra cannot be applied in the same way to timing performance as for detectors based on PMTs or APDs.

In order to investigate a possible dependence of the timing resolution on the interaction position, timing spectra were measured at a number of different detector positions such that the centers of the irradiated areas were located at various distances (Δx, Δy) from the detector center: (Δx = 0 mm, Δy = 0 mm); (Δx = 4 mm, Δy = 0 mm); (Δx = 4 mm, Δy = 4 mm); and (Δx = 8 mm, Δy = 0 mm). These measurements were performed at an intermediate bias voltage V_{ob} = 1.6 V. The FWHM determined for the recorded timing spectra are summarized in table 2. The changes of the FWHM with respect to the center of the detector are within 4% – 6% and do not exhibit a clear trend. It thus would

Table 8.2. Width (FWHM) of the timing spectra measured irradiating different areas of the detector.

Distance to detector center		FWHM
Δx	Δy	
0 mm	0 mm	174 ps
4 mm	0 mm	168 ps
4 mm	4 mm	164 ps
8 mm	0 mm	167 ps

appear that the timing resolution is uniform throughout the detector.

8.4.   Conclusions

Our experiments show that monolithic LaBr$_3$:5%Ce-based PET detectors equipped with currently available SiPM arrays and dedicated readout electronics may offer a combination of very good spatial and energy resolution as well as excellent timing performance. No appreciable effect of SiPM saturation was observed in the energy spectra because of the large number of available microcells in the detector array (57,600). This can be an added advantage of monolithic scintillation crystals compared to e.g. one-to-one coupling of small scintillation crystals where an increase of the linear range of the detector often has to be balanced with the resulting decrease of the SiPM fill-factor.

As expected, increasing the applied bias voltage above the nominal value increases the observed excess noise and, thus, worsens the energy resolution of the detector from 6.4% FWHM to 7.8% FWHM. In contrast, the measured spatial resolution of about ~1.6 mm FWHM was affected only marginally by the increase in V_{ob} despite the increase of the *ENF*. This is attributed to the increase in the PDE of the SiPMs, which largely compensates for the degrading effect of the larger *ENF*.

Considering that timing resolution of state of the art TOF PET systems is in the order of 375 ps – 600 ps (Surti *et al.* 2007, Daube-Witherspoon *et al.* 2010, Lois *et al.* 2010) the CRT that was measured for our detector is certainly encouraging. Moreover, the timing resolution significantly improved at the higher V_{ob} (from CRT = 239 ps FWHM to CRT = 198 ps FWHM). This illustrates that the concept of the excess noise factor must be applied with caution to SiPMs, because the energy resolution and the timing performance are affected very differently by afterpulsing and crosstalk. As an energy resolution of 7.8% FWHM is still respectable for a PET detector it might thus be favorable to operate the detector at comparatively large V_{ob} for optimum overall performance in a TOF PET system. Furthermore, improvements on the image quality due to a better energy resolution or a better spatial resolution are limited by statistical noise and, in the case of spatial resolution, the physical limits of the positron range and acollinearity of the annihilation photons. In contrast, there is not such limitation on the benefits of the timing resolution of a TOF PET system (e.g. Moses 2007, Conti 2011).

Nonetheless, the detector presented in this work is a prototype and a number of practical issues need to be addressed before the presented detector concept can be taken to a full system level. For example the front-side readout of scintillators might be challenging from a system engineering point of view. One particular issue in this respect might be the possible need for temperature control of the SiPMs to avoid gain fluctuations. An elegant solution to this problem has been demonstrated by Yamamoto *et al.* (2011) in the form of temperature-dependent V_{ob}-control of the SiPMs. Other crucial issues are the detector calibration and the processing of the data. Some interesting concepts have been

introduced in order to address these challenges such as e.g. the application of neural networks for the position estimation by Bruyndonckx *et al.* (2007), or the suggestion of a much faster line-source-calibration by van Dam *et al.* (2011a). Nevertheless, these works are first steps and considerable effort will be required to refine and combine these concepts and test them in practice. Furthermore, the application of monolithic scintillators might require novel image recostruction algorithms in order to bring out the full potential of these detectors.

Still, the results presented in this work indicate that it may well be worth the effort to tackle these remaining obstacles. The combination of an energy resolution <10%, a spatial resolution <2 mm and a timing resolution <200 ps highlights the unique potential of monolithic scintillators for application in TOF PET. In addition, γ-radiation detectors utilizing monolithic scintillators will hugely benefit from recent developments in the field of pixelated solid state photosensors. For example, the dead space in between the individual pixels is practically eliminated in the next generation of 4×4 SiPM arrays from Hamamatsu (MPPC S11828-3344M), thus improving the overall photon detection efficiency by almost 50% [9]. A further example is the emergence of the so-called digital SiPM (Degenhardt *et al.* 2009) which facilitates nearly noise-free measurements of the light intensities on the individual pixels as well as accurate time stamping for individual pixels

Acknowledgements

References

Bruyndonckx P, Leonard S, Tavernier S, Lemaitre C, Devroede O, Wu Y B and Krieguer M 2004 Neural network-based position estimators for PET detectors using monolithic LSO blocks *IEEE Trans Nucl Sci* **51** 2520-2525

Bruyndonckx P, Lemaitre C, Leonard S, Schaart D R, van der Laan D J, Maas M C, Bevroede O, Wu Y B, Krieguer M and Tavernier S 2006 Initial characterization of a nonpixelated scintillator detector in a PET prototype demonstrator *IEEE Trans Nucl Sci* **53** 2543-2548

Bruyndonckx P, Lemaitre C, Schaart D, Maas M, van der Laan D J, Krieguer M, Devroede O and Tavernier S 2007 Investigation of an in situ position calibration method for continuous crystal-based PET detectors *Nucl Instrum Meth A* **571** 304-307

---

[9] Hamamatsu Photonics K.K. Solid State Division 2011
sales.hamamatsu.com/info/eul/MPPC/PDF/S11828-3344M_eng.pdf

Conti M 2011 Focus on time-of-flight PET: the benefits of improved time resolution *Eur J Nucl Med Mol I* **38** 1147-1157

Daube-Witherspoon M E, Surti S, Perkins A, Kyba C C M, Wiener R, Werner M E, Kulp R and Karp J S 2010 The imaging performance of a LaBr(3)-based PET scanner *Phys Med Biol* **55** 45-64

de Haas J T M and Dorenbos P 2008 Advances in yield calibration of scintillators *IEEE Trans Nucl Sci* **55** 1086-1092

Degenhardt C, Prescher G, Frach T, Thon A, de Gruyter R, Schmitz A and Ballizany R 2009 The Digital Silicon Photomultiplier - A Novel Sensor for the Detection of Scintillation Light *IEEE Nuclear Science Symposium and Medical Imaging Conference (2009 NSS/MIC)* (Orlando, Florida) 2383-2386

Dorenbos P, deHaas J T M and vanEijk C W E 1995 Non-proportionality in the scintillation response and the energy resolution obtainable with scintillation crystals *IEEE Trans Nucl Sci* **42** 2190-2202

Du Y and Retiere F 2008 After-pulsing and cross-talk in multi-pixel photon counters *Nucl Instrum Meth A* **596** 396-401

Huizenga J, Seifert S, Schreuder F, Vinke R, Dendooven P, Löhner H, van Dam H T, Beekman F J and Schaart D R 2011 A fast preamplifier concept for SiPM based time-of-flight PET detectors. In: *Proc. sixth Int. Conf. on New Developments in Photodetection* (Lyon: Elsevier)

Kim C L, Wang G C and Dolinsky S 2009 Multi-Pixel Photon Counters for TOF PET Detector and Its Challenges *IEEE Trans Nucl Sci* **56** 2580-2585

Lois C, Jakoby B W, Long M J, Hubner K F, Barker D W, Casey M E, Conti M, Panin V Y, Kadrmas D J and Townsend D W 2010 An Assessment of the Impact of Incorporating Time-of-Flight Information into Clinical PET/CT Imaging *J Nucl Med* **51** 237-245

Maas M C, van der Laan D J, Schaart D R, Huizenga J, Brouwer J C, Bruyndonckx P, Leonard S, Lemaitre C and van Eijk C W E 2006 Experimental characterization of monolithic-crystal small animal PET detectors read out by APD arrays *IEEE Trans Nucl Sci* **53** 1071-1077

Maas M C, Schaart D R, van der Laan D J, Bruyndonckx P, Lemaitre C, Beekman F J and van Eijk C W E 2009 Monolithic scintillator PET detectors with intrinsic depth-of-interaction correction *Phys Med Biol* **54** 1893-1908

Maas M C, van der Laan D J, van Eijk C W E, Schaart D R, Beekman F J, Bruyndonckx P and Lemaitre C 2010 Model of the point spread function of monolithic scintillator PET detectors for perpendicular incidence *Med Phys* **37** 1904-1913

Moses W W 2007 Recent advances and future advances in time-of-flight PET *Nucl Instrum Meth A* **580** 919-924

Moszyński M, Kapusta M, Wolski D, Szawłowski M and Klamra W 1998 Energy resolution of scintillation detectors readout with large area avalanche photodiodes and photomultipliers *IEEE Trans Nucl Sci* **45** 472-477

Nassalski A, Moszynski M, Szczęśniak T, Wolski D and Batsch T 2007 The road to

the common PET/CT detector *IEEE Trans Nucl Sci* **54** 1459-1463

Schaart D R, van Dam H T, Seifert S, Vinke R, Dendooven P, Löhner H and Beekman F J 2009 A novel, SiPM-array-based, monolithic scintillator detector for PET *Phys Med Biol* **54** 3501-3512

Schaart D R, Seifert S, Vinke R, van Dam H T, Dendooven P, Löhner H and Beekman F J 2010 LaBr(3):Ce and SiPMs for time-of-flight PET: achieving 100 ps coincidence resolving time *Phys Med Biol* **55** N179-N189

Seifert S, van Dam H T, Vinke R, Dendooven P, Löhner H, Beekman F J and Schaart D R 2011 A Comprehensive Model to Predict the Timing Resolution of SiPM-Based Scintillation Detectors: Theory and Experimental Validation *submitted to IEEE Trans Nucl Sci*

Seifert S, van Dam H T, Vinke R, Dendooven P, Löhner H, Beekman F J and Schaart D R 2012 A Comprehensive Model to Predict the Timing Resolution of SiPM-Based Scintillation Detectors: Theory and Experimental Validation *IEEE Trans Nucl Sci* **59** 190-204

Surti S, Kuhn A, Werner M E, Perkins A E, Kolthammer J and Karp J S 2007 Performance of philips gemini TF PET/CT scanner with special consideration for its time-of-flight imaging capabilities *J Nucl Med* **48** 471-480

Szczęśniak T, Moszyński M, Grodzicka M, Wolski D, Świderski Ł, Szawłowski M and Kapusta M 2010 Time resolution of scintillation detectors based on SiPM in comparison to photomultipliers *Nuclear Science Symposium Conference Record (NSS/MIC), 2010 IEEE* 1728-1735

van Dam H T, Seifert S, Vinke R, Dendooven P, Löhner H, Beekman F J and Schaart D R 2011a Improved Nearest Neighbor Methods for Gamma Photon Interaction Position Determination in Monolithic Scintillator PET Detectors *IEEE Trans Nucl Sci* **58** 2139-2147

van Dam H T, Seifert S, Vinke R, Dendooven P, Löhner H, Beekman F J and Schaart D R 2011b A practical method for depth of interaction determination in monolithic scintillator PET detectors *Phys Med Biol* **56** 4135-4145

van der Laan D J, Maas M C, de Jong H W A M, Schaart D R, Bruyndonckx P, Lemaitre C and van Eijk C W E 2007 Simulated performance of a small-animal PET scanner based on monolithic scintillation detectors *Nucl Instrum Meth A* **571** 227-230

Wang G C 2010 Timing Optimization of Solid-State Photomultiplier Based PET Detectors *IEEE Trans Nucl Sci* **57** 25-30

Yamamoto S, Satomi J, Watabe T, Watabe H, Kanai Y, Imaizumi M, Shimosegawa E and Hatazawa J 2011 A temperature-dependent gain control system for improving the stability of Si-PM-based PET systems *Phys Med Biol* **56** 2873-2882

9 Concluding Remarks and Discussion

9.1. Silicon Photomultipliers for TOF PET

The performance of SiPMs and the timing resolutions that can be achieved with scintillation detectors employing these devices crucially depend on the properties of the preamplifier and the applied readout strategy. To make the best possible use of SiPMs a good understanding of the signal generation in SiPMs and their electronic properties is essential. These aspects differ significantly from other light sensors such as conventional photomultiplier tubes (PMTs).

PMTs present a small capacitance and high resistance to subsequent circuitry and in most instances it is sufficient to treat these devices as ideal current sources. This allows for a large degree of freedom in the design and the optimization of preamplifiers. The requirements on the readout of SiPMs are much less relaxed due to their large terminal capacitance and their changing output impedance upon the breakdown of a number of microcells. In particular a low input impedance of the preamplifier circuitry is essential to maintain the beneficial timing properties of SiPMs (see also chapter 2, Seifert *et al.* 2009, Huizenga *et al.* 2011).

A further element that has to be optimized for accurate timing with SiPM based scintillation detectors is the trigger scheme. The findings presented in chapter 5 indicate that a simple leading edge trigger performs remarkably well. Nevertheless, it should be noted that a careful optimization of the trigger threshold is required. This is especially important in the case of LYSO for which the timing resolution degrades rapidly as the trigger threshold is moved away from its optimum value.

In general, the optimum value for the trigger level is at low signal levels (in the order of a few equivalent fired cells). This emphasizes the need for (relatively) high bandwidth, low noise preamplifiers with low input impedance. Additionally, it is vital that measures are taken to suppress baseline fluctuations due to dark-counts, e.g. by baseline subtraction or high pass filtering (see chapter 3 and chapter 4 in this work, Gola *et al.* 2011, Piemonte *et al.* 2011). Dark count induced base line fluctuations effectively increase the electronic noise. This, in turn, may degrade the timing resolution either directly, i.e. by decreasing the accuracy of the trigger time stamp, or indirectly by limiting the usable range of values for the trigger threshold. This aspect is important as other performance parameter of SiPMs (e.g. the internal quantum efficiency) improve with increasing voltage-over-breakdown (V_{ob}) while increasing V_{ob} also

increases the dark-count rate. The application of a baseline correction facilitates the use of large V_{ob}, which in turn improves the overall timing performance. In this context it should be noted that all experiments presented here were performed at ~20°C. Cooling of the sensors reduces dark-count rate at a given V_{ob} and hence further increases the usable V_{ob}-range (Gola *et al.* 2011, Piemonte *et al.* 2011).

Even though SiPMs might appear to be more challenging to apply than conventional PMTs, the research conducted in the scope of this thesis clearly shows that SiPMs can be a viable alternative to PMTs in applications where accurate timing is essential. The timing resolution that was achieved using small scintillation crystals (CRT = 95 ps FWHM and CRT = 138 ps FWHM for LaBr$_3$:5%Ce and LYSO, respectively) demonstrates that SiPMs based scintillation detectors can even outperform classical PMTs in terms of timing resolution (see chapter 3 and chapter 5). It can be concluded that at this point all aspects that are required to effectively use SiPMs in TOF PET are in principle known.

Nevertheless, some engineering challenges remain before this technology can be successfully taken to a system level. For example, up until this point it is not clear if the approach to digitize the signal traces at an early stage and to determine time stamps in a post processing step is a prerequisite to maintain the outstanding timing characteristics of SiPM based scintillation detectors. The early signal digitization with a sampling ADC for each channel may be difficult to implement in a power- and cost-effective manner. On the other hand, recently multi-channel, low noise, high-speed sampling ADCs have become available (Friederich *et al.* 2010, Ritt *et al.* 2010, Ronzhin *et al.* 2012), which may facilitate an aggressive digitization approach.

Furthermore, one should consider the constant progress that can be observed in the development of SiPMs. Of special interest are the increasing capabilities of manufactures to integrate individual SiPMs into pixel-arrays. The arrays that were used in this work (SensL SPMArray 3035G16 and Hamamatsu MPPC S11064-050P) were assembled from individual silicon dies which leads to a substantial insensitive area in-between the individual pixels. Recently, SiPM arrays fabricated onto monolithic pieces of silicon have become available (Hamamatsu MPPC S11828-3344M)[10]. The much smaller insensitive inter-pixel area increases the overall photon detection efficiency and/or facilitates much smaller pixel sizes, which may be beneficial for timing resolution and spatial resolution (see also chapter 8).

A further interesting development is the recent introduction of a fully digital version of the SiPM (Degenhardt *et al.* 2009, Frach *et al.* 2009). In these devices the concept of early digitization is taken to the extreme and digital signals are produced at a single cell level. A time stamp can be created for the first cell fired in a device by on-chip TDCs while a build-in counter determines the number of

---

[10] Hamamatsu Photonics K.K. Solid State Division 2011
sales.hamamatsu.com/info/eul/MPPC/PDF/S11828-3344M_eng.pdf

fired cells for a given scintillation event. This approach is virtually insensitive to electronic noise and thus cuts out the difficulties associated with preamplification and signal transmission. However, this comes at the cost of flexibility, e.g. in the determination of the time stamp (Frach *et al.* 2009). On the other hand, for scintillators with a fast intrinsic rise time (such as LYSO) a trigger scheme utilizing one of the earliest fired cells can still yield excellent timing resolution (see chapter 6, Degenhardt *et al.* 2009).

9.2. LaBr$_3$:Ce in TOF PET

The high light yield of LaBr$_3$:Ce (~70 photons / keV) in combination with its fast decay time (15 ns) has stirred some excitement concerning the application of this material in TOF PET. The results that were obtained for the test detectors presented in this work confirm that an outstanding timing performance can be achieved with scintillation detectors utilizing this material. In particular the CRT measured for a pair of small LaBr$_3$:5%Ce crystals coupled to matching SiPMs of just below 100 ps (FWHM) is remarkable as it was unprecedented at the time (Seifert *et al.* 2009, Schaart *et al.* 2010). Meanwhile, these findings have been confirmed by Wiener *et al.* (2010) with small LaBr$_3$:Ce crystals on conventional PMTs.

Still, when compared to the timing resolution that was obtained with LYSO:Ce (CRT = 138 ps FWHM) the improvement is not as large as one might expect based on established timing models considering the ~2 times higher light yield and 2.5 times faster decay time. This holds even after the different emission spectra of the materials (wavelength of maximum intensity is at 380 nm for LaBr$_3$:5%Ce and 420 nm for LYSO:Ce) and the resulting poorer PDE for the LaBr$_3$:Ce based detectors are taken into account. The smaller–than–expected benefit of LaBr$_3$:5%Ce is owed to the considerably slower rise time of the LaBr$_3$:5%Ce scintillation compared to L(Y)SO:Ce (chapter 4, Glodo *et al.* 2005). The degrading effect of the slower rise time was quantified using advanced timing models (chapter 5 and chapter 6).

It should be noted, that increasing the Ce concentration in LaBr$_3$:Ce can decrease the scintillation pulse rise time considerably thus further improving the (Glodo *et al.* 2005, Wiener *et al.* 2010). Yet the benefit of a higher Ce concentration may be lessened by an increase of the probability for self-absorption (van Dam *et al.* 2012). Self-absorption (and subsequent reemission) induces a delay of scintillation photons which is the more severe the larger the average path length of the scintillation photons prior to detection. This is especially troublesome as in principle thicker crystals are required to obtain the same γ-detection efficiency as an L(Y)SO crystal due to the lower density and effective atomic number of LaBr$_3$. Moreover, thicker crystals are disadvantageous for the energy resolution, the spatial resolution, and the timing resolution even without the contribution of self-absorption.

What is more is that recently it was shown that co-doping LSO with Ca can reduce the decay time of the scintillation pulse by as much as 25% (Spurrier *et*

al. 2008). Recent results obtained with 3 mm × 3 mm × 5 mm crystals of LSO:Ce,Ca confirm the improved timing capabilities of this material. When coupled to analog SiPMs (Hamamatsu MPPC–S10362–33–50C), a CRT of 125 ps was obtained, while a CRT of 120 ps was measured in combination with a prototype digital SiPM (Philips Digital Photon Counter) (van der Lei *et al.* 2011).

It thus appears that the difference in timing performance of LaBr$_3$:Ce and L(Y)SO:Ce (and related materials) is in the order of 20 % – 40 % at best and it should be considered carefully, if the improvement of the timing resolution justifies the implementation of LaBr$_3$:Ce in PET systems. LaBr$_3$:Ce is highly hygroscopic, which is a disadvantage that is not shared by L(Y)SO:Ce. The hygrosopicity makes LaBr$_3$:Ce much more challenging to handle and raises questions about the long term stability of the detectors.

9.3.   Monolithic scintillators

The application of monolithic scintillators rather than pixelated crystal blocks in PET detectors has received renewed attention in the last years (Takacs *et al.* 2000, Bruyndonckx *et al.* 2004, LeBlanc and Thompson 2004, Lerche *et al.* 2005, 2006, Maas *et al.* 2006, and 2007, van der Laan *et al.* 2007, van Dam *et al.* 2011a, b). To a large part this is owned to the availability of multi-channel APDs, which facilitate a (potentially) cost effective implementation of this concept. By now, it is well established that monolithic scintillator detectors offer an intriguing combination of favorable properties such as the intrinsically available depth-of-interaction (DIO) information, good spatial resolution, excellent energy resolution, high γ-photon capture efficiency, and relatively simple detector assembly. However, due to the poor timing performance of conventional APDs most of the previously proposed detector concepts focus on preclinical applications.

Nevertheless, the light transport in monolithic scintillators is in principle faster and more efficient compared to pixelated block detectors where the photon transport is hampered by the large number of reflections that scintillation photons need to undergo before reaching the photosensor (Moses and Derenzo 1999). Consequently, the application of monolithic scintillators appears to be appealing for TOF PET if they are combined with fast light sensors. This notion is confirmed by the results presented in chapter 7 and chapter 8 in this work.

The characterization of a detector prototype comprising the first available SiPM array (SensL SPMArray 3035G16) and a 13.2 mm × 13.2 mm × 10 mm LYSO:Ce crystal (presented in chapter 7) confirmed the intrinsically good energy resolution ($\Delta E/E$ = 14%) and spatial resolution (R_s < 1.6 mm). Furthermore, the capability of the detector to correct for DIO effects was shown. Yet the timing performance of this detector was still moderate (CRT = 1.4 ns FWHM) due to the low PDE and comparatively slow electronic response of the SiPMs in conjunction with a suboptimal preamplifier configuration.

Meanwhile, SiPM arrays with improved characteristics have become available. The array that was used in our second detector prototype (Hamamatsu MPPC S11064–050P) exhibits a higher PDE and much improved timing characteristics. In addition, the spectral sensitivity of this device better matches

Table 9.1. Overview of prototype PET detectors based on SiPMs. In most detectors LYSO:Ce crystals were used, except for the one in Seifert et al. (LaBr$_3$:Ce) and the ones in Song et al., Yamamoto et al., and Yamaya et al. (LGSO). ΔE/E denotes the FWHM energy resolution and R$_S$ denotes the FWHM spatial resolution (with courtesy of van Dam 2012).

Reference	No. of crystals	Crystals Size (mm^3)	No. of SiPM pixels	Pixel size (mm^2)	ΔE/E (%)	CRT (ps)	R$_S$ (mm)
Llosá *et al.* (2010)	1	12×12×5	8×8	1.5×1.4	16	8500	0.9
Schaart *et al.* (2009)	1	13×13×10	4×4	3×3	14	1400	1.9
Seifert *et al.* (2012)	1	16×18×10	4×4	3×3	6.4	200	1.6
van der Lei *et al.* (2011)	1	24×24×10	6×6	4×4	11	<350	1.0
Degenhardt *et al.* (2011)	8×8	4×4×22	8×8	4×4	10	290	–
Delfino *et al.* (2010)	12×12	1×1×10	2×(4×4)	3×3	20	–	–
España *et al.* (2008), (2010)	4×4	1.5×1.5×12	2×2	3×3	11–22	–	–
Hong *et al.* (2011)	4×4	3×3×20	4×4	3×3	19	1600	–
Kato *et al.* (2011)	4×4	3×3×10	4×4	3×3	14	–	–
Kim *et al.* (2011)	4×4	3×3×25	4×4	3×3	9	310	–
Kolb *et al.* (2010)	12×12	1.5×1.5×10	3×3	3×3	14	1400	–
Solf *et al.* (2009)	4×4	4×4×22	8×8	4×4	15	680	–
Song *et al.* (2010)	10×10	0.8×0.8×3	4×4	3×3	20	1700	–
Yamamoto *et al.* (2011)	15×15	0.7×0.7×6	4×4	3×3	15	–	–
Yamaya *et al.* (2011)	12×12×12	1×1×1	6×(4×4)	3×3	11	–	–

the emission spectrum of L(Y)SO:Ce and enables the use of LaBr$_3$:5%Ce, which was not feasible with the SPMArray. A significantly enhanced performance could be observed for a detector combining the MPPC array with a 18.0 mm × 16.2 mm × 10.0 mm sized, monolithic LaBr$_3$:5%Ce scintillator, and with improved read out electronics (chapter 8). This detector offers a spatial resolution of R_s = ~1.6 mm, an energy resolution of $\Delta E/E$ = 7.8%, and a CRT of 200 ps (FWHM). These values are certainly encouraging as they constitute significant improvements over current state of the art TOF PET detectors (see chapter 1) as well as other SiPM based prototype detectors (Table 9.1).

Before a full PET system utilizing monolithic scintillator detectors can be realized, however, a number of practical issues need to be addressed. The most crucial matters are the detector calibration and the processing of the data. Some interesting solutions have been proposed in order to address these challenges such as e.g. the application of neural networks for the position estimation by Bruyndonckx *et al.* (2007), or the suggestion of a much faster line-source-calibration by van Dam *et al.* (2011a). Nevertheless, these works are first steps and considerable effort will be required to refine and combine these concepts and test them in the environment of full PET rings.

Still, the comparison in Table 9.1 highlights the unique potential of monolithic scintillators for application in TOF PET. It can be constituted that it will be worth the effort to tackle the remaining obstacles. More so, as γ-radiation detectors utilizing monolithic scintillators will hugely benefit from the previously mentioned, recent developments in the field of multi-channel solid state photosensors. E.g. the use of SiPM arrays with practically no dead space in between the individual pixels (i.e. Hamamatsu MPPC S11828-3344M) would improve the effective detector PDE of our otherwise comparable second detector prototype by almost 50%. Furthermore, arrays of digital SiPMs (Degenhardt *et al.* 2009) facilitate nearly noise-free measurements of the light intensities on the individual pixels as well as accurate time stamping for individual pixels. First measurements with these devices coupled to 24 mm × 24 mm × 10 mm LSO:Ce,Ca yielded outstanding spatial resolution (1 mm) and a timing resolution of <350 ps (see Table 9.1, van der Lei *et al.* 2011).

9.4.   The prospects and Limitations of TOF PET

It has been shown by Conti *et al.* (2011) that reducing the number of image counts in by a factor of 2.5 for a TOF PET system with a CRT of 200 ps does not lead to any apparent loss of image quality when compared to state of the art TOF-PET system with a CRT of 500 ps. This constitutes a large benefit in clinical practice as this in principle allows working with much reduced amounts of activity without compromising the diagnostic value of a clinical PET scan. Considering the results which could already be achieved in the scope of this work and recent developments in photosensor technology and scintillation materials it certainly appears feasible to realize a TOF PET system with a CRT of 200 ps.
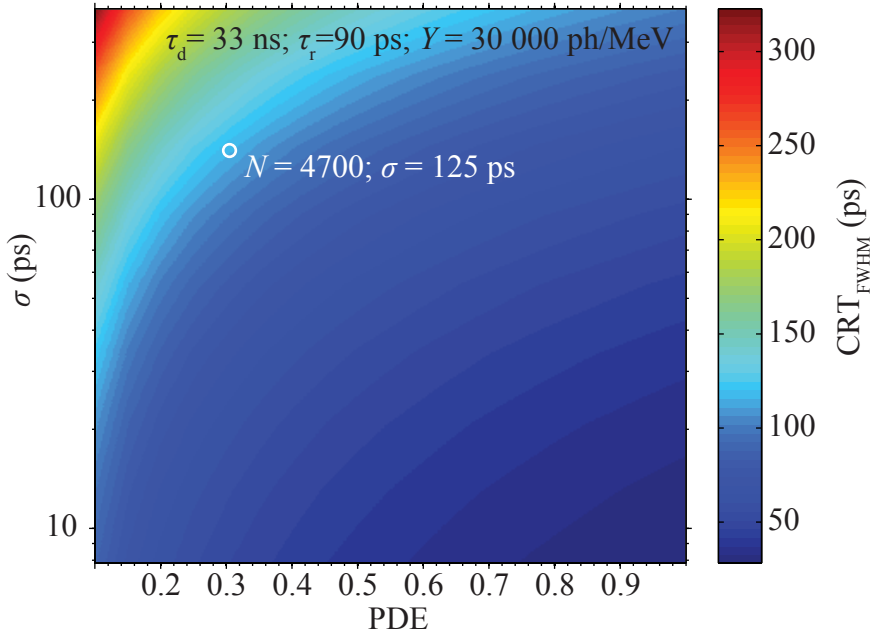
Figure 9.1. Coincidence resolving time (CRT) achievable with LSO:Ce,Ca as a function of detector PDE and effective transit time spread (σ).

Further improvements might be realized by relatively small changes to the read out of the detectors. For our detector prototype only the summed signal of all 16 photosensor channels was utilized to determine a times stamp for a given scintillation event. Yet it might be beneficial to determine a time stamp based on information from individual channels. In this context it might further improve the timing resolution if this information is combined with the estimate on the 3d γ-interaction position (Vinke *et al.* 2010). If these methods can be exploited to their full potential it might be possible to achieve a CRT of ~150 ps. It would appear that TOF PET detectors with a significantly better CRT are not to be expected with currently available technology.

Still, in principle it is possible to reach a timing resolution that is considerably better than 150 ps (see chapter 3 and 5). Using the model introduced in chapter 6 it can been shown that even CRTs well below 100 ps could be achieved with currently available scintillators and slightly improved photodetectors. This is exemplified in Figure 9.1 for LSO:Ce,Ca (decay time τ_d = 33 ns, rise time τ_r = 90 ps, and light yield Y = 30000 ph/MeV). This figure illustrates that a prerequisite for a CRT below 100 ps is a small effective transit time spread (σ < 100 ps). Currently, the only means to keeping σ small enough is to utilize small scintillation crystals (~5 mm thickness) in order to minimize the transit time spread for the scintillation photons. As this reduces the sensitivity of the

individual detector elements several such detector elements might have to be stacked in order to maintain an acceptable system sensitivity. Similar detector concepts have been proposed by others (e.g. McCallum *et al.* 2005, Llosa *et al.* 2008) as a means to improve the detector spatial resolution and obtain DOI information. Currently, such a detector design might not be economic as the required number of detector channels increases with each detector layer. However, the prospect of a CRT of < 100 ps might well justify the technologically challenging implementation of this concept.

References

Bruyndonckx P, Leonard S, Tavernier S, Lemaitre C, Devroede O, Wu Y B and Krieguer M 2004 Neural network-based position estimators for PET detectors using monolithic LSO blocks *IEEE Trans Nucl Sci* **51** 2520-2525

Bruyndonckx P, Lemaitre C, Leonard S, Schaart D R, van der Laan D J, Maas M C, Bevroede O, Wu Y B, Krieguer M and Tavernier S 2006 Initial characterization of a nonpixelated scintillator detector in a PET prototype demonstrator *IEEE Trans Nucl Sci* **53** 2543-2548

Bruyndonckx P, Lemaitre C, Schaart D, Maas M, van der Laan D J, Krieguer M, Devroede O and Tavernier S 2007 Investigation of an in situ position calibration method for continuous crystal-based PET detectors *Nucl Instrum Meth A* **571** 304-307

Conti M, Eriksson L and Westerwoudt V 2011 Estimating image quality for future generations of TOF PET scanners *Nuclear Science Symposium and Medical Imaging Conference (NSS/MIC), 2011 IEEE* 2407-2414

Degenhardt C, Prescher G, Frach T, Thon A, de Gruyter R, Schmitz A and Ballizany R 2009 The Digital Silicon Photomultiplier - A Novel Sensor for the Detection of Scintillation Light *IEEE Nuclear Science Symposium and Medical Imaging Conference (2009 NSS/MIC)* (Orlando, Florida) 2383-2386

Degenhardt C, Thon A, Zwaans B, Schultze R, Muehlens R and de Gruyter R 2011 Highly Integrated Arrays of Digital SiPMs with easy Readout Interface *presented at IEEE Nuclear Science Symposium and Medical Imaging Conference (2011 NSS/MIC)* (Valencia)

Delfino E P, Majewski S, Raylman R R and Stolin A 2010 Towards 1mm PET resolution using DOI modules based on dual-sided SiPM readout *Nuclear Science Symposium Conference Record (NSS/MIC), 2010 IEEE* 3442-3449

España S, Tapias G, Fraile L M, Herraiz J L, Vicente E, Udias J, Desco M and Vaquero J J 2008 Performance Evaluation of SiPM Detectors for PET Imaging in the Presence of Magnetic Fields *IEEE Nuclear Science Symposium and Medical Imaging Conference (2008 NSS/MIC)* (Dresden) 2866-2870

España S, Fraile L M, Herraiz J L, Udias J M, Desco M and Vaquero J J 2010

Performance evaluation of SiPM photodetectors for PET imaging in the presence of magnetic fields *Nucl Instrum Meth A* **613** 308-316

Frach T, Prescher G, Degenhardt C, de Gruyter R, Schmitz A and Ballizany R 2009 The Digital Silicon Photomultiplier - Principle of Operation and Intrinsic Detector Performance *IEEE Nuclear Science Symposium and Medical Imaging Conference (2009 NSS/MIC)* (Orlando, Florida) 1959-1965

Friederich H, Davatz G, Hartmann U, Howard A, Meyer H, Murer D, Ritt S and Schlumpf N 2010 A scalable DAQ system based on the DRS4 waveform digitizing chip *Real Time Conference (RT), 2010 17th IEEE-NPSS* 1-5

Glodo J, Moses W W, Higgins W M, van Loef E V D, Wong P, Derenzo S E, Weber M J and Shah K S 2005 Effects of Ce concentration on scintillation properties of LaBr3 : Ce *IEEE Trans Nucl Sci* **52** 1805-1808

Gola A, Piemonte C and Tarolli A 2011 Analog Circuit for Timing Measurements with Large Area SiPMs Coupled to LYSO Crystals *IEEE Nuclear Science Symposium and Medical Imaging Conference (2011 NSS/MIC)* (Valencia) 3376-3380

Hong K J, Choi Y, Kang J, Hu W, Jung J H, Min B J, Chung Y H and Jackson C 2011 Performance evaluation of a PET detector consisting of an LYSO array coupled to a 4x4 array of large-size GAPD for MR compatible imaging *J Instrum* **6**

Huizenga J, Seifert S, Schreuder F, van Dam H T, Dendooven P, Löhner H, Vinke R and Schaart D R 2011 A fast preamplifier concept for SiPM-based time-of-flight PET detectors *Nuclear Instruments and Methods in Physics Research Section A: Accelerators, Spectrometers, Detectors and Associated Equipment* in press

Kato T, Kataoka J, Nakamori T, Miura T, Matsuda H, Sato K, Ishikawa Y, Yamamura K, Kawabata N, Ikeda H, Sato G and Kamada K 2011 Development of a large-area monolithic 4 x 4 MPPC array for a future PET scanner employing pixelized Ce:LYSO and Pr:LuAG crystals *Nucl Instrum Meth A* **638** 83-91

Kim C L, McDaniel D L and Ganin A 2011 Time-of-Flight PET Detector Based on Multi-Pixel Photon Counter and Its Challenges *IEEE Trans Nucl Sci* **58** 3-8

Kolb A, Lorenz E, Judenhofer M S, Renker D, Lankes K and Pichler B J 2010 Evaluation of Geiger-mode APDs for PET block detector designs *Phys Med Biol* **55** 1815-1832

LeBlanc J W and Thompson R A 2004 A novel PET detector block with three-dimensional hit position encoding *IEEE Trans Nucl Sci* **51** 746-751

Lerche C W, Benlloch J M, Sanchez F, Pavon N, Escat B, Gimenez E N, Fernandez M, Torres I, Gimenez M, Sebastia A and Martinez J 2005 Depth of gamma-ray interaction within continuous crystals from the width of its scintillation light-distribution *IEEE Trans Nucl Sci* **52** 560-572

Llosa G, Battiston R, Belcari N, Boscardin M, Collazuol G, Corsi F, Dalla Betta G F, Del Guerra A, Dinu N, Levi G, Marcatili S, Moehrs S, Marzocca C, Piemonte C and Pozza A 2008 Novel Silicon Photomultipliers for PET

Applications *Nuclear Science, IEEE Transactions on* **55** 877-881

Llosá G, Barrio J, Lacasta C, Bisogni M G, Del Guerra A, Marcatili S, Barrillon P, Bondil-Blin S, de la Taille C and Piemonte C 2010 Characterization of a PET detector head based on continuous LYSO crystals and monolithic, 64-pixel silicon photomultiplier matrices *Phys Med Biol* **55** 7299-7315

Maas M C, van der Laan D J, Schaart D R, Huizenga J, Brouwer J C, Bruyndonckx P, Leonard S, Lemaitre C and van Eijk C W E 2006 Experimental characterization of monolithic-crystal small animal PET detectors read out by APD arrays *IEEE Trans Nucl Sci* **53** 1071-1077

McCallum S, Clowes P and Welch A 2005 A four-layer attenuation compensated PET detector based on APD arrays without discrete crystal elements *Phys Med Biol* **50** 4187-4207

Moses W W and Derenzo S E 1999 Prospects for time-of-flight PET using LSO scintillator *IEEE Trans Nucl Sci* **46** 474-478

Piemonte C, Gola A, Picciotto A, Pro T, Serra N, Tarolli A and Zorzi N 2011 Timing performance of large area SiPMs coupled to LYSO using dark noise compensation methods *IEEE Nuclear Science Symposium and Medical Imaging Conference (2011 NSS/MIC)* (Valencia) 3376-3380

Ritt S, Dinapoli R and Hartmann U 2010 Application of the DRS chip for fast waveform digitizing *Nuclear Instruments and Methods in Physics Research Section A: Accelerators, Spectrometers, Detectors and Associated Equipment* **623** 486-488

Ronzhin A, Albrow M G, Los S, Ramberg E, Guo Y, Kim H, Zatserklyaniy A, Mazzillo M, Carbone B, Condorelli G, Fallica P, Piana A, Sanfilippo D, Valvo G and Ritt S 2012 Waveform digitization for high resolution timing detectors with silicon photomultipliers *Nuclear Instruments and Methods in Physics Research Section A: Accelerators, Spectrometers, Detectors and Associated Equipment* **668** 94-97

Schaart D R, van Dam H T, Seifert S, Vinke R, Dendooven P, Löhner H and Beekman F J 2009 A novel, SiPM-array-based, monolithic scintillator detector for PET *Phys Med Biol* **54** 3501-3512

Schaart D R, Seifert S, Vinke R, van Dam H T, Dendooven P, Löhner H and Beekman F J 2010 LaBr(3):Ce and SiPMs for time-of-flight PET: achieving 100 ps coincidence resolving time *Phys Med Biol* **55** N179-N189

Seifert S, Vinke R, van Dam H T, Löhner H, Dendooven P, Beekman F J and Schaart D R 2009 Ultra Precise Timing with SiPM-Based TOF PET Scintillation Detectors *IEEE Nuclear Science Symposium and Medical Imaging Conference (2009 NSS/MIC)* (Orlando, Florida) 2329-2333

Seifert S, van Dam H T, Vinke R, Dendooven P, Löhner H, Beekman F J and Schaart D R 2011 A Comprehensive Model to Predict the Timing Resolution of SiPM-Based Scintillation Detectors: Theory and Experimental Validation *submitted to IEEE Trans Nucl Sci*

Seifert S, van Dam H T, Huizenga J, Vinke R, Dendooven P, Löhner H and Schaart D R 2012 Monolithic LaBr_3:Ce crystals on silicon photomultiplier arrays

for time-of-flight positron emission tomography *Phys Med Biol* **57** 2219–2233

Solf T, Schulz V, Weissler B, Thon A, Fischer P, Ritzert M, Mlotok V, Piemonte C and Zorzi N 2009 Solid-State Detector Stack for ToF-PET/MR *2009 Ieee Nuclear Science Symposium Conference Record, Vols 1-5* 2798-2799

Song T Y, Wu H Y, Komarov S, Siegel S B and Tai Y C 2010 A sub-millimeter resolution PET detector module using a multi-pixel photon counter array *Phys Med Biol* **55** 2573-2587

Spurrier M A, Szupryczynski P, Yang K, Carey A A and Melcher C L 2008 Effects of Ca2+ co-doping on the scintillation properties of LSO : Ce *IEEE Trans Nucl Sci* **55** 1178-1182

Takacs G J, Rosenfeld A B, Lerch M L F, Lindsay S W, Taylor G N, Meikle S R, Eberl S and Perevertailo V L 2000 Design and simulation of continuous scintillator with pixellated photodetector *Nuclear Science Symposium Conference Record, 2000 IEEE* 20/20-20/24 vol.23

van Dam H T, Seifert S, Vinke R, Dendooven P, Löhner H, Beekman F J and Schaart D R 2011a Improved Nearest Neighbor Methods for Gamma Photon Interaction Position Determination in Monolithic Scintillator PET Detectors *IEEE Trans Nucl Sci* **58** 2139-2147

van Dam H T, Seifert S, Vinke R, Dendooven P, Löhner H, Beekman F J and Schaart D R 2011b A practical method for depth of interaction determination in monolithic scintillator PET detectors *Phys Med Biol* **56** 4135-4145

van Dam H T, Seifert S, Drozdowski W, Dorenbos P and Schaart D R 2012 Optical absorption length, scattering length, and refractive index of LaBr$_3$:Ce *submitted to IEEE Transactions on Nuclear Science*

van Dam H T 2012 *Monolithic scintillatios and SiPMs in time-of-flight PET detectors* PhD Thesis (Delft, The Netherlands: Delft University of Technology)

van der Laan D J, Maas M C, de Jong H W A M, Schaart D R, Bruyndonckx P, Lemaitre C and van Eijk C W E 2007 Simulated performance of a small-animal PET scanner based on monolithic scintillation detectors *Nucl Instrum Meth A* **571** 227-230

van der Lei G J, van Dam H T, Seifert S and Schaart D R 2011 First performance measurements of monolithic scintilators coupled to digital SiPM arrays for TOF-PET *presented at IEEE Nuclear Science Symposium and Medical Imaging Conference (2011 NSS/MIC)* (Valencia)

Vinke R, Löhner H, Schaart D R, van Dam H T, Seifert S, Beekman F J and Dendooven P 2010 Time walk correction for TOF-PET detectors based on a monolithic scintillation crystal coupled to a photosensor array *Nucl Instrum Meth A* **621** 595-604

Wiener R I, Kaul M, Surti S and Karp J S 2010 Signal analysis for improved timing resolution with scintillation detectors for TOF PET imaging *Nuclear Science Symposium Conference Record (NSS/MIC), 2010 IEEE* 1991-1995

Yamamoto S, Watabe H and Hatazawa J 2011 Performance comparison of Si-PM-
        based block detectors with different pixel sizes for an ultrahigh-resolution
        small-animal PET system *Phys Med Biol* **56** N227-N236
Yamaya T, Mitsuhashi T, Matsumoto T, Inadama N, Nishikido F, Yoshida E,
        Murayama H, Kawai H, Suga M and Watanabe M 2011 A SiPM-based
        isotropic-3D PET detector X'tal cube with a three-dimensional array of 1
        mm(3) crystals *Phys Med Biol* **56** 6793-6807

Summary

Positron emission tomography (PET) is a nuclear medical imaging modality. Its aim is to visualize the 3-dimensional distribution of a radiopharmaceutical (also called the tracer) within a patient (clinical PET) or test-animal (in case of preclinical investigations). The information that can be obtained from the reconstructed distribution depends on the specifics of the tracer. In general it is linked to a certain physiological processes. The most common clinical application of PET makes use of (^{18}F-)FDG: a ^{18}F-labeled, glucose-like molecule that targets the glucose metabolism. Consequently, an FDG PET scan visualizes the glucose uptake of different tissue types, has proven to be a very valuable tool in the diagnosis, staging, and monitoring of carcinoma and metastasis.

In PET the tracer molecules are labeled with position emitting isotopes. Positrons annihilate close to their point of emission with electrons that are abundant in the surrounding tissue. As this takes place, a pair of 511 keV γ-photons is emitted on (almost) antiparallel trajectories. The detection of both photons belonging to one such annihilation pair allows localizing their point of origin to a so-called line-of-response (LOR), which is defined between the two points of detection.

The decision if two detected γ-photons originate from the same annihilation event is based on the difference in their detection times, i.e. two γ-photons are classified as an annihilation pair if they are detected within a small time window. Depending on the count rate within the individual detector elements and the width of the coincidence acceptance window two uncorrelated γ-detections might be misclassified as annihilation pair. These events are referred to as *random* events or *randoms*.

Detecting a large number of annihilation photon pairs facilitates the 3d reconstruction of the PET-tracer distribution. The practical, clinical value of a reconstructed PET image crucially depends on how accurately the original tracer distribution can be reconstructed from the acquired PET data. This accuracy is fundamentally limited by the number of detected (true) annihilation photon pairs, the ratio between true, random and scattered events, as well as the accuracy with which each γ-photon can be localized in space and time.

All these limiting factors are largely determined by properties of the employed scintillator detectors: namely the spatial resolution, their timing resolution, their energy resolution, their γ-capture efficiency, and their depth of interaction (DOI) resolution. Consequently, an improvement of the detector

performance in these key areas will lead to improved image quality, allow for shorter scan times per patient, and/or permit to work with reduced tracer activity. It is the aim of this work to investigate as to how far the performance of detectors for application in PET can be improved by using new materials and innovative detector design. In this, a particular emphasis will be on the timing performance of the detectors as it has been shown that utilizing so called time-of-flight information can lead to a drastic reduction of statistical noise in the reconstructed image which is often the dominating noise source in clinical PET.

A key component in every scintillator detector is the photosensor that is applied to detect the scintillation light. A novel type of photosensor that has received growing interest as a replacement for conventional photomultiplier tubes (PMTs) in TOF-PET detectors are so-called silicon photomultipliers (SiPMs). SiPMs are solid state light sensors that offer comparable gain and timing response with respect to PMTs but offer some distinct advantages. SiPMs are insensitive to magnetic fields and can be produced to be nonmagnetic, which allows for integration in magnetic resonance imaging (MRI) devices. Furthermore, SiPMs are essentially transparent for 511 keV γ-photons, they are compact and rugged and can be in integrated relatively easily into pixel-arrays, which allows for novel detector designs.

In order to make the best use of the potential offered by of SiPMs it is important that subsequent front end electronics are optimized to meet the specific demands of these sensors. Such an optimization requires a detailed understanding of the properties of SiPMs as well as the generated electronic signals. Important insights in these matters can be gained from equivalent circuit models such as the one presented in chapter 2. In this chapter it is demonstrated how such a model can be applied to simulate the combined electronic response of the SiPM and subsequent front end electronics. These simulations constitute an invaluable tool for the development of suitable preamplifiers, they help to understand the signal generation and signal transport within SiPMs, and can predict unexpected effects such as the electronic signal nonlinearity.

A further potential improvement of the TOF-PET detector performance can be achieved by replacing the scintillation material. A particular interesting candidate in this respect is the recently discovered $LaBr_3$:Ce due to its high light yield (~70 photons / keV), its fast decay time (15 ns) and its good intrinsic energy resolution (< 3% at 511 keV). Especially the conjunction of high light yield and fast decay make $LaBr_3$:Ce highly interesting for application in fields where accurate timing is essential. The outstanding timing capabilities of $LaBr_3$:Ce in combination with SiPMs and an optimized readout architecture are demonstrated in chapter 3. The measurements described there yield an exceptional coincidence resolving time (CRT) of 100 ps (FWHM) for two detectors utilizing $LaBr_3$:5%Ce crystals with a size of 3 mm × 3 mm × 5 mm.

Still, the measurements presented in chapter 4 show, that the favorable timing properties of $LaBr_3$:Ce are somewhat diminished by a much slower rise time of the scintillation pulse when compared to e.g. LYSO (280 ps up to 2 ns compared

to 90 ps for LYSO). A slower buildup of the scintillation signal increases the statistical variation of the arrival times of individual scintillation photons at the photosensor. In consequence, the time stamp that can be obtained in combination with a specific photo detector degrades. This is shown and quantified by means of a comprehensive model that predicts the timing resolution of SiPM based scintillation detectors (chapter 5). The model predictions and the corresponding validation measurements show that the CRT that can be obtained with LYSO-SiPM-detectors (CRT = 138 ps FWHM) is nearly as good as for the LaBr$_3$:5%Ce based detectors. The presented data and model predictions also reveal the importance of the careful optimization of the applied trigger scheme as an ill conditioned trigger can easily degrade the timing performance by more than 50 %.

Further insight in the mechanism behind the surprisingly similar timing performance of LaBr$_3$:5%Ce and LYSO is given by means of a rigorous statistical description of the photon detection process in chapter 6. As the generation/emission, transport, and detection of scintillation photons are independent statistical processes it is possible to calculate the lower limit on the timing resolution in a relatively simple formalism based on the timing information carried by each individual photon. The calculation of the so-called Cramér-Rao lower bound on the timing resolution associated with the detectors that were used in the above mentioned experiments shows that the observed CRTs of both types of detectors is almost entirely governed by the statistical properties of the photon detection indicating that little to no improvement can be expected from further optimization of readout electronics or time stamp generation.

Lastly, the concept of monolithic scintillator detectors read out by pixelated sensor arrays is explored. Utilizing monolithic crystals instead of pixelated blocks offers several advantages such as a good special resolution while maintaining a good energy resolution, intrinsic DOI-information, ease of assembly, and faster light transport. In chapter 7 and chapter 8 two detector prototypes based on this concept are characterized. In both cases the detectors employ 10 mm thick monolithic scintillation crystals with footprints matching 4 × 4 SiPM arrays (13.2 mm × 13.2 mm and 18.0 mm × 16.2 mm, respectively). The detector described in chapter 7 is based on the first available SiPM array (SensL SPMArray 3035G16) and an LYSO:Ce scintillator. This detector exhibits a good energy resolution ($\Delta E/E$ = 14%) and spatial resolution (R_s < 1.6 mm in the detector center). Furthermore, the capability of the detector to correct for DIO effects was shown. Yet, the due to the low PDE and comparatively slow electronic response of the SiPMs the CRT measured for this detector was moderate (CRT = 1.4 ns FWHM). The second detector prototype, which is characterized in chapter 8, utilizes an SiPM array with much improved PDE and timing properties (Hamamatsu MPPC S11064–050P). The spectral sensitivity of this sensor array furthermore allowed for the use of LaBr$_3$:5%Ce. The applied changes in the detector materials and read out architecture

amounted to a dramatic improvement of the timing resolution to CRT = 200 ps (FWHM) and energy resolution (7.8 %) and a slight improvement of the spatial resolution (R_s < 1.5 mm in the center of the detector).

The results presented in this work clearly show that monolithic scintillator detectors combined with SiPM readout can outperform conventional PMT-pixelated-block detectors in terms of spatial resolution, energy, and timing resolution. Nevertheless, the integration of monolithic scintillator detectors in TOF-PET and TOF-PET/MR systems requires further research and some important matters such as shortening the time consuming system calibration or the optimization of data handling and data processing still have to be addressed.

Samenvatting

Positronemissietomografie (PET) is een nucleaire medische beeldvormingstechniek die erop is gericht is de 3-dimensionale verdeling van een radioactief farmaceuticum, de zogenoemde *tracer,* binnen een patiënt (klinische PET) of een proefdier (in het geval van preklinische onderzoeken) te visualiseren. De soort informatie die uit een gereconstrueerde tracerverdeling kan worden verkregen is afhankelijk van de specifieke tracerkenmerken. In het algemeen is deze informatie aan bepaalde fysiologische processen gekoppeld. De belangrijkste klinische toepassing van PET maakt gebruik van (^{18}F-) FDG: een ^{18}F-gelabeld, glucoseachtige molecule die zich op het glucosemetabolisme richt. Op deze manier visualiseert een FDG-PET-scan de glucoseopname van verschillende weefseltypen. Dit heeft zich als een zeer waardevol hulpmiddel bewezen bij de diagnose, classificatie en het monitoren van carcinoma en metastasen.

PET-tracermoleculen worden met positronenemitterende isotopen gemarkeerd. Positronen annihileren vlak bij het punt van emissie met elektronen die overvloedig aanwezig zijn in het omliggende weefsel. Volgend op iedere positron-elektron-annihilatie wordt een 511 keV γ-fotonenpaar uitgezonden op in (bijna) antiparallelle richtingen. Door detectie van beide fotonen die tot een dergelijk annihilatiepaar behoren, wordt een zogenaamde *line-of-response* (LOR) gedefinieerd als de verbindende lijn tussen de twee punten van detectie. Vervolgens kan het gerelateerde positronemissiepunt worden ingeperkt tot locaties vlak bij de LOR.

De beslissing of twee gedetecteerde γ-fotonen tot dezelfde annihilatiegebeurtenis behoren, is gebaseerd op het verschil tussen hun detectietijden. Dat wil zeggen dat twee γ-fotonen als annihilatiepaar worden geclassificeerd als hun detectietijden binnen een beperkt tijdvenster vallen. Afhankelijk van de telsnelheid in de aparte individuele detectorelementen en de lengte van het coïncidentievenster, kunnen twee γ-fotonen ook ten onrechte als annihilatiepaar worden geclassificeerd. In zulke gevallen is er sprake van *random events* of *randoms* in tegenstelling tot *true events* voor echte annihilatiefotonenparen.

Het detecteren van een groot aantal annihilatiefotonenparen maakt een driedimensionale reconstructie van de PET-tracerdistributie mogelijk. De praktische, klinische waarde van een gereconstrueerd PET beeld is sterk afhankelijk van hoe nauwkeurig de oorspronkelijke tracerdistributie gereconstrueerd kan worden op basis van de gemeten PET-data. Deze

nauwkeurigheid is wezenlijk beperkt door het absolute aantal gedetecteerde (echte) annihilatieparen, de verhouding tussen *trues* en *randoms* en de nauwkeurigheid waarmee elk γ-foton in ruimte en tijd gelokaliseerd kan worden.

Al deze beperkende factoren worden grotendeels bepaald door de eigenschappen van de gebruikte scintillatiedetectoren: namelijk de plaats-, tijds- en energieresolutie; de efficiëntie waarmee γ-fotonen gedetecteerd kunnen worden en de diepte-van-interactie (*depth-of-interaction,* DOI) resolutie. Derhalve zal een verbetering van de detectorprestaties op deze belangrijke gebieden tot een verbeterde beeldkwaliteit leiden, zodat met een kortere meettijd per patiënt en/of met verminderde traceractiviteit gewerkt kan worden.

Het doel van dit proefschrift is, te onderzoeken in hoeverre de prestaties van detectoren voor toepassing in PET verbeterd kunnen worden door het gebruik van nieuwe materialen en geavanceerd detectordesign. Hierbij wordt in het bijzonder nadruk gelegd op een mogelijke verbetering van de tijdresolutie, omdat het gebruik van zogenaamde *time-of-flight* (TOF) informatie kan leiden tot een drastische vermindering van de statistische ruis in het gereconstrueerde beeld. Statistische ruis fluctuaties zijn vaak de dominante ruisbron in de klinische toepassing van PET.

Een sleutelelement in elke scintillatiedetector is de lichtsensor die wordt toegepast om het scintillatielicht te detecteren. Er is momenteel groeiende belangstelling voor een nieuw soort lichtsensor als vervanging van conventionele photomultiplier tubes (PMTs) in TOF-PET-detectoren: de zogenaamde silicon photomultipliers (SiPMs). SiPMs zijn halfgeleider lichtsensoren die een met PMTs vergelijkbare tijdsrespons en een vergelijkbare gevoeligheid voor scintillatiefotonen bieden, maar bovendien een aantal duidelijke voordelen tonen. SiPMs zijn ongevoelig voor magnetische velden en zijn zelf niet-magnetisch, waardoor integratie in magnetic resonance imaging (MRI) apparaten mogelijk is. Bovendien zijn SiPMs hoofdzakelijk vrijwel transparant voor 511 keV γ-fotonen; ze zijn compact en robuust; en ze kunnen relatief gemakkelijk in compacte pixel-arrays geïntegreerd worden, waardoor nieuwe detectorontwerpen mogelijk worden.

Om optimaal gebruik te kunnen maken van de mogelijkheden die SiPMs bieden, is het van belang dat ook de front-end elektronica geoptimaliseerd is om aan de specifieke eisen van deze sensoren te voldoen. Een dergelijke optimalisering vereist een gedetailleerd begrip van de eigenschappen van SiPMs en de gegenereerde elektronische signalen. Belangrijke inzichten in deze materie kunnen worden verkregen uit equivalentcircuitmodellen zoals die in hoofdstuk 2. In dat hoofdstuk wordt gedemonstreerd hoe een dergelijk model kan worden toegepast om de gecombineerde elektronische reactie van een SiPM en de navolgende er op aangesloten elektronica te simuleren. Deze simulaties vormen een waardevol instrument voor de ontwikkeling van geschikte voorversterkers, ze geven inzicht in de signaalgeneratie en het signaaltransport binnen de SiPMs, en ze kunnen helpen onverwachte effecten te voorspellen, zoals de niet-lineariteit van het elektronische signaal niet-lineariteit.

Verdere verbetering van de TOF-PET-detectorprestatie kan worden bereikt door vervanging van het scintillatiemateriaal. Een bijzonder interessante kandidaat in dit verband is de het recent ontdekte LaBr$_3$:Ce. LaBr$_3$:Ce toont een bijzonder hoge lichtopbrengst (~ 70 fotonen / keV), een uiterst snelle scintillatie-afvaltijd (15 ns) en de goede intrinsieke energieresolutie (<3% bij 511 keV). Vooral de combinatie van hoge lichtopbrengst en snelle afvaltijd maakt LaBr$_3$:Ce zeer interessant voor toepassing in gebieden waar nauwkeurige tijdmetingen van belang zijn. De uitstekende timingprestatie van detectoren, waarin LaBr$_3$:Ce kristallen (3 mm × 3 mm × 5 mm) met SiPM lichtsensoren gecombineerd zijn, wordt in hoofdstuk 3 aangetoond. De metingen die in dit hoofdstuk worden beschreven leveren een ongeëvenaarde tijdresolutie (*coincidence resolving time*, CRT) van 100 ps (FWHM) voor twee detectoren in coïncidentie.

Desondanks tonen de metingen in hoofdstuk 4, dat de gunstige timingeigenschappen van LaBr$_3$:Ce enigszins worden verminderd door een veel tragere stijgtijd van de scintillatiepuls in vergelijking met bijvoorbeeld LYSO:Ce; 280 ps tot 2 ns voor LaBr$_3$:Ce tegenover <90 ps voor LYSO. Een langzamere opbouw van het scintillatiesignaal vergroot de statistische variatie in de aankomsttijden van individuele scintillatiefotonen bij de lichtsensor. Als deze fotonen met een bepaalde lichtsensor worden gemeten, is het gevolg van grotere aankomsttijdvariaties dat de bepaling van het moment waarop de scintillatiepuls is ontstaan, onnauwkeuriger wordt. Dit wordt in hoofdstuk 5 inzichtelijk gemaakt en gekwantificeerd. In dit hoofdstuk wordt een uitgebreid model geïntroduceerd dat de timingresolutie van SiPM-gebaseerde scintillatiedetectoren voorspelt.

Uit de modelvoorspellingen en de bijbehorende validatiemetingen blijkt dat de CRT die met LYSO-SiPM-detectoren kan worden bereikt (138 ps FWHM) bijna even zo goed is als de met LaBr$_3$:5%Ce-gebaseerde detectoren gemeten CRT. Verder blijkt uit de gepresenteerde metingen en modelvoorspellingen hoe groot het belang is van een zorgvuldige optimalisatie van het toegepaste triggerschema is. Een slecht geconditioneerde trigger kan de timingprestaties met meer dan 50% verminderen.

Een dieper inzicht in het mechanisme achter de verrassend soortgelijke timingprestaties van LaBr$_3$:5%Ce en LYSO wordt in hoofdstuk 6 gegeven door middel van een strikt statistische beschrijving van het fotonendetectieproces. Omdat ladingsdragergeneratie, (scintillatie)fotonenemissie, fotonentransport en fotonendetectie statistisch onafhankelijke processen zijn, is het mogelijk om de ondergrens van de tijdsresolutie met een relatief eenvoudig formalisme te berekenen. Dit gebeurt op basis van de tijdsinformatie die door elk foton wordt gedragen word. Uit de berekening van de zogenaamde Cramér-Rao ondergrens blijkt dat de tijdsresolutie van de detectoren, die in de bovengenoemde experimenten worden gebruikt, vrijwel uitsluitend door de statistische eigenschappen van de fotondetectie is bepaald is. Dat betekent onder meer, dat weinig tot geen verbetering verwacht kan worden van verdere optimalisatie van

uitleeselektronica of triggerschema.

Ten slotte wordt het concept van de monolithische scintillatoren, uitgelezen door een sensorpixelmatrix, onderzocht. Het gebruik van monolithische kristallen biedt een aantal voordelen, waaronder een goede plaatsresolutie met behoud van een goede energieresolutie, de intrinsiek aanwezige DOI-informatie, het montagegemak en de het efficiënte lichttransport. In hoofdstuk 7 en hoofdstuk 8 worden twee op dit concept gebaseerde detectorprototypes gekenmerkt. In beide detectoren worden monolithische scintillatiekristallen met een dikte van 10 mm verwerkt. De overige kristaldimensies komen met de dimensies van de gebruikte 4 × 4 SiPM-matrices overeen (13,2 mm × 13,2 mm respectievelijk 18,0 mm × 16,2 mm). De in hoofdstuk 7 beschreven detector is gebaseerd op de eerste commercieel beschikbare 4 × 4 SiPM-array (SensL SPMArray 3035G16) en een LYSO:Ce-scintillator. Deze detector toont een goede energieresolutie ($\Delta E / E = 14\%$) en een excellente plaatsresolutie (R <1,6 mm FWHM in het detectormidden). Bovendien word het vermogen van de detector om DOI-effecten te corrigeren gedemonstreerd. Desondanks heeft deze detector een lage fotonendetectie-efficiencie (*photon detection efficiency,* PDE) en een relatief trage elektronische reactie van de SiPMs. Daardoor is de gemeten CRT voor deze detector matig (CRT = 1,4 ns FWHM).

Het tweede detectorprototype, dat gekenmerkt wordt in hoofdstuk 8, maakt gebruik van een SiPM-array met verbeterd PDE en sterk verbeterde timing eigenschappen (Hamamatsu mppc MPPC S11064-050P). De spectrale gevoeligheid van deze sensor maakt bovendien het gebruik van LaBr$_3$:5%Ce mogelijk. De wijzigingen in de detectormaterialen en verregaande verbeteringen in de uitleesarchitectuur gaf een drastische verbetering van de tijdsresolutie (CRT = 200 ps, FWHM), een verbeterde energieresolutie (7,8%) en een licht verbeterde plaatsresolutie (R_s <1,5 mm in het midden van de detector).

Op basis van de in dit proefschrift besproken resultaten kan worden geconcludeerd dat monolithische-scintillator-detectoren met SiPM uitlezing een unieke combinatie van eigenschappen tentoonstellen, die deze detectoren veelbelovend maken voor toekomstige TOF-PET en TOF-PET/MRI systemen maken. Desondanks vereist de implementatie van monolithische-scintillator-detectoren TOF PET-systemen wel nog veel onderzoek en betere oplossingen op belangrijke gebieden. Zo moet bijvoorbeeld het langdurige systeemkalibratieproces worden verkort. Bovenal moeten geprimeerde goede oplossingen worden gevonden voor zowel het transport als ook de verwerking van de enorme datastroom, die van door monolithische-scintillator-detectoren wordt gegenereerd, worden gevonden.

Acknowledgements

It is with great pleasure that I express my gratitude to the many people who have directly or indirectly contributed to this thesis. Yet, I fear that the following list may not be complete and I therefore begin these acknowledgements by apologizing to those whose contribution I might have forgotten to include. Please be assured that my negligence is in no way related to how much I valued your input.

First of all, I gratefully acknowledge my promotor Freek Beekman for his support, for his positive attitude, for the insightful discussions, and the helpful comments. Secondly, I would like to thank my supervisor Dennis Schaart. Dennis, I am very thankful for the tremendous amount of time and effort that you invested in me and in my work. However, even more than your direct involvement in this thesis I appreciated your style of guidance and mentorship. I found the many, many opportunities to discuss scientific problems on the level of equals invaluable for my personal growth and the development of this thesis. Not only did these discussions provide direct feedback to results but often they also inspired new research questions to work on. Most of all I am grateful for the seemingly unshakable trust that you displayed in me and I cannot begin to express how much I appreciated the freedom that I experienced to investigate the things that I found interesting, even if it meant getting sidetracked on occasion.

The person who possibly suffered the most for his contribution to this thesis is Herman van Dam. Herman. Please accept my sincere apologies along with my gratitude for the innumerable times that I interrupted your work because I had something "interesting" to discuss or a problem that I felt I needed to share. I sometimes wonder how you got anything else done. Thank you for providing a suitably critical second opinion on all of my works. Thank you for spotting the obvious and the hidden mistakes in some of them and for making me feel more confident about those where you could not find any faults. Thank you for the many fruitful, interesting and stimulating discussions. In short, thank you for having been a great colleague.

As this work was part of a larger collaboration I had the pleasure of meeting a number of talented and knowledgeable scientists who have inspired me either in discussion or though their work. I much appreciated the collaboration with the members of the SciSiLiA consortium: Ruud Vinke, Peter Dendoven, and Herbert Löhner from KVI Groningen and Andreas Thon from Philips Research (Europe–Aachen). Furthermore, I highly valued the inspiring and fruitful

conversations with Mark Korevaar and Matthew Fishburn.

Special thanks also go to Marnix Maas and Jan van der Laan who laid the groundwork for the research presented in this thesis. Thank you for the time you took to answer my many questions for and your help when I was still new to the field of PET-detectors. Above all, however, I appreciated the friendly atmosphere you helped create which made me feel welcome and at home in the RD&M. The same holds for all other former and present members and visitors of this group with whom I had the pleasure of working with over the past five years: Adrie, Alastair, Alice, Brendan, Andreas, Candice, Christina, Danang, David, Enrica, Edith, Erik, Francesco, Frans, Greg, Gustavo, Leo, Lorette, Ivan, Jacob, José, Jan, Johan, Marlies, Michiel, Mikhail, Melvin, Pieter, Pjotr, Rob, Romée, Samuel, Victor, and Xander. Thank you all for making my time here so enjoyable, for discussions and engaging conversations, for shared coffee, cake, and beer.

While working on this thesis I received outstanding support in many respects from the excellent staff members at the Delft University of Technology. In particular I am indebted to Jan Huizenga for sharing his vast experience and knowledge in analog electronics. I thank Martijn de Boer for the support in the lab and with the design, construction, and maintenance of various experiential setups. I thank the staff of DEMO and in particular William van Goozen and Jeroen Koning for constantly proving to me how great it is to work with people how really know their trade. José Buurman and Thea Miedema I thank for their administrative support. Thank you all. It was a great pleasure working with you.

Of all the people who were instrumental in the development of this thesis I find it the most difficult to express my gratitude to those whose support meant (and means) the most to me: my family. I fear that my words will be hopelessly inadequate.

Heinz and Cherril, thank you for welcoming me into your family and for the trust you have in me. Elianne, Timon, Sarah, and Willam, I thank you for being brothers and sisters to me and Miriam while our biological siblings are so far away and for the sense of belonging that comes with having family close by. And thank you, Sarah, for your help with the Dutch parts of this thesis.

André, thank you for your love and respect, for being older brother and good friend in unison. Thank you, Katrin, for being such a great partner to him and for helping me see many things in different perspectives. I thank you both for being there when I could not.

I cannot begin to describe how much the love and appreciation of my wife Miriam, our daughter Hannah, and our son Peter mean to me and how instrumental they were in the completion of this thesis. They kept me going in difficult times and helped me stay (mostly) sane. Stress, fatigue, and lack of sleep can do strange things to a person. Miriam, you have seen me through some tough moments. Thank you for your unwavering support, for your seemingly unlimited trust, for your encouragement, and for always trying to make things better. I love you too.

The last words of this thesis, however, I reserved for my parents, Sabine and Eberhard Seifert. Wann immer ich innehalte um über diese Dinge nachzudenken bin ich fasziniert und erstaunt mit welcher Selbstverständlichkeit und scheinbaren Mühelosigkeit ihr es geschafft habt mir in allem die Freiheit zu geben meine Möglichkeiten und Grenzen selbst zu entdecken und meine eigenen Fehler zu machen. Dass ich mich beim Entdecken und beim Fehler machen immer auf eure sichere Rückendeckung verlassen konnte, empfinde ich als besonders wertvoll. Aber wie bedankt man sich für eine Lebenszeit voller vorbehaltloser Unterstützung und Hingabe? An dieser Stelle fehlen mir nun endlich die Worte. Danke für alles.

Stefan Seifert
October 2012

Curriculum Vitae

Stefan Seifert was born in Schlema (German Democratic Republic) in 1979. He obtained his secondary school degree at the *Pestalozzi-Gymansium*, Aue (Sachsen, Germany) in 1998. In alternative to compulsory military service he spend a period of 13 months tending to residents of the *Wohnheim für Behinderte–Lebenshilfewerk gGmbH*; a home for individuals with mental disabiliaties. In 1999 he joined the physics program at the *Chemnitz University of Technology*. He graduated in 2005 with his thesis "Spectroscopy of Occupied and Unoccupied States in Bio-Molecular Layers". Subsequently, he was employed in the *semiconductor physics* section at the *Chemnitz University of Technology* as a research assistant. In 2007, he started his PhD research at the *Delft University of Technology* in *Radiation Detection and Medical Imaging* section of the *Faculty of Applied Sciences*. The results of this research are presented in this thesis.

List of Publications

Peer-Reviewed Journal Papers

Glowatzki H, Gavrila G N, Seifert S, Johnson R L, Rader J, Mullen K, Zahn D R T, Rabe J P and Koch N 2008 Hexa-peri-hexabenzocoronene on Ag(111): Monolayer/multilayer transition of molecular orientation and electronic structure *J Phys Chem C* **112** 1570-1574

Huizenga J, Seifert S, Schreuder F, van Dam H T, Dendooven P, Löhner H, Vinke R and Schaart D R 2011 A fast preamplifier concept for SiPM-based time-of-flight PET detectors *Nuclear Instruments and Methods in Physics Research Section A: Accelerators, Spectrometers, Detectors and Associated Equipment* in press

Schaart D R, van Dam H T, Seifert S, Vinke R, Dendooven P, Löhner H and Beekman F J 2009 A novel, SiPM-array-based, monolithic scintillator detector for PET *Physics in Medicine and Biology* **54** 3501-3512

Schaart D R, Seifert S, Vinke R, van Dam H T, Dendooven P, Löhner H and Beekman F J 2010 LaBr$_3$:Ce and SiPMs for time-of-flight PET: achieving 100 ps coincidence resolving time *Physics in Medicine and Biology* **55** N179-N189

Seifert S, Gavrila G N, Zahn D R T and Braun W 2007 The molecular orientation of DNA bases on H-passivated Si(111) surfaces investigated by means of near edge X-ray absorption fine structure spectroscopy *Surf Sci* **601** 2291-2296

Seifert S, van Dam H T, Huizenga J, Vinke R, Dendooven P, Löhner H and Schaart D R 2009 Simulation of Silicon Photomultiplier Signals *IEEE Trans. Nucl. Sci.* **56** 3726-3733

Seifert S, van Dam H T, Vinke R, Dendooven P, Löhner H, Beekman F J and Schaart D R 2012a A Comprehensive Model to Predict the Timing Resolution of SiPM-Based Scintillation Detectors: Theory and Experimental Validation *IEEE Trans. Nucl. Sci.* **59** 190-204

Seifert S, van Dam H T and Schaart D R 2012b The lower bound on the timing resolution of scintillation detectors *Physics in Medicine and Biology* **57** 1797-1814

Seifert S, van Dam H T, Huizenga J, Vinke R, Dendooven P, Löhner H and Schaart D R 2012c Monolithic LaBr$_3$:Ce crystals on silicon photomultiplier arrays for time-of-flight positron emission tomography *Physics in Medicine and Biology* **57** 2219–2233

Seifert S, Steenbergen J H L, van Dam H T and Schaart D R 2012 Accurate

measurements of the rise and decay times of fast scintillators with solid state photon counters *Journal of .Instrumentation* to be printed.

van Dam H T, Seifert S, Vinke R, Dendooven D, Löhner H, Beekman F J and Schaart D R 2010 A Comprehensive Model of the Response of Silicon Photomultipliers *IEEE Trans. Nucl. Sci.* **57** 2254-2266

van Dam H T, Seifert S, Vinke R, Dendooven P, Löhner H, Beekman F J and Schaart D R 2011a Improved Nearest Neighbor Methods for Gamma Photon Interaction Position Determination in Monolithic Scintillator PET Detectors *IEEE Trans. Nucl. Sci.* **58** 2139-2147

van Dam H T, Seifert S, Vinke R, Dendooven P, Löhner H, Beekman F J and Schaart D R 2011b A practical method for depth of interaction determination in monolithic scintillator PET detectors *Physics in Medicine and Biology* **56** 4135-4145

van Dam H T, Seifert S, Drozdowski W, Dorenbos P and Schaart D R 2012 Optical absorption length, scattering length, and refractive index of LaBr$_3$:Ce *submitted to IEEE Transactions on Nuclear Science*

Vinke R, Löhner H, Schaart D R, van Dam H T, Seifert S, Beekman F J and Dendooven P 2009 Optimizing the timing resolution of SiPM sensors for use in TOF-PET detectors *Nucl Instrum Meth A* **610** 188-191

Vinke R, Löhner H, Schaart D R, van Dam H T, Seifert S, Beekman F J and Dendooven P 2010 Time walk correction for TOF-PET detectors based on a monolithic scintillation crystal coupled to a photosensor array *Nucl Instrum Meth A* **621** 595-604

Zahn D R T, Seifert S, Gavrila G and Braun W 2007 Investigation of bio-organic/inorganic semiconductor interfaces *J Optoelectron Adv M* **9** 522-526

Conference Proceedings

Schaart D R, van Dam H T, Seifert S, Vinke R, Dendooven P, Löhner H and Beekman F J 2008a SiPM-Array Based PET Detectors with Depth-of-Interaction Correction *IEEE Nuclear Science Symposium and Medical Imaging Conference (2008 NSS/MIC)* (Dresden) 2856-2860

Schaart D R, Seifert S, van Dam H T, de Boer M R, Vinke R, Dendooven P, Löhner H and Beekman F J 2008b First Experiments with LaBr$_3$:Ce Crystals Coupled Directly to Silicon Photomultipliers for PET Applications *IEEE Nuclear Science Symposium and Medical Imaging Conference (2008 NSS/MIC)* (Dresden) 3266-3269

Seifert S, Schaart D R, van Dam H T, Huizenga J, Vinke R, Dendooven P, Löhner H and Beekman F J 2008 A High Bandwidth Preamplifier for SiPM-Based TOF PET Scintillation Detectors *IEEE Nuclear Science Symposium and Medical Imaging Conference (2008 NSS/MIC)* (Dresden) 891-894

Seifert S, Vinke R, van Dam H T, Löhner H, Dendooven P, Beekman F J and Schaart D R 2009 Ultra Precise Timing with SiPM-Based TOF PET Scintillation Detectors *IEEE Nuclear Science Symposium and Medical*

Imaging Conference (2009 NSS/MIC) (Orlando, Florida) 2329-2333

Seifert S, Steenbergen J H L, van Dam H T, Vinke R, Dendooven P, Löhner H, Beekman F J, Dorenbos P, van der Kolk E and Schaart D R 2010 Accurate measurements of the rise and decay times of fast scintillators with solid state photon counters *IEEE Nuclear Science Symposium and Medical Imaging Conference (2010 NSS/MIC)* (Knoxville, Tn) 1736-1739

van Dam H T, Drozdowski W, Seifert S, Dorenbos P and Schaart D R 2008 Experimental Determination of Optical Scattering and Absorption in LaBr$_3$:Ce^{3+} *IEEE Nuclear Science Symposium and Medical Imaging Conference (2008 NSS/MIC)* (Dresden) 3245-3247

van Dam H T, Seifert S, Vinke R, Dendooven P, Löhner H, Beekman F J and Schaart D R 2009 Silicon Photomultiplier Response Model *IEEE Nuclear Science Symposium and Medical Imaging Conference (2009 NSS/MIC)* (Orlando, Florida) 2362-2364

van Dam H T, Seifert S, Vinke R, Dendooven P, Löhner H, Beekman F J and Schaart D R 2010 An improved nearest neighbor method for the estimation of the gamma photon entry point in monolithic scintillator detectors for PET *IEEE Nuclear Science Symposium and Medical Imaging Conference (2010 NSS/MIC)* (Knoxville, Tn) 3088-3092

Vinke R, Löhner H, Schaart D R, van Dam H T, Seifert S, Beekman F J and Dendooven P 2008 Optimizing timing resolution for TOF PET detectors based on monolithic scintillation crystals using fast photosensor arrays *IEEE Nuclear Science Symposium and Medical Imaging Conference (2008 NSS/MIC)* (Dresden) 3229-3235

Vinke R, Seifert S, Schaart D R, Schreuder F P, de Boer M R, van Dam H T, Beekman F J, Löhner H and Dendooven P 2009 Optimization of Digital Time Pickoff Methods for LaBr$_3$-SiPM TOF-PET Detectors *IEEE Nuclear Science Symposium and Medical Imaging Conference (2009 NSS/MIC)* (Orlando, Florida) 2962-2968

Vinke R, van Dam H T, Seifert S, Beekman F J, Löhner H, Schaart D R and Dendooven P 2010 Thick monolithic scintillation crystals for TOF-PET with depth-of-interaction measurement *IEEE Nuclear Science Symposium and Medical Imaging Conference (2010 NSS/MIC)* (Knoxville, Tn) 1981-1984